ABSTRACT

Title of Dissertation:	ASSESSMENT OF MECHANICAL CUES TO ENHANCE THE CLINICAL TRANSLATION OF EXTRACELLULAR VESICLES
	Stephanie Marie Kronstadt Doctor of Philosophy, 2022
Dissertation directed by:	Associate Professor, Dr. Steven M. Jay, Fischell Department of Bioengineering

Mesenchymal stem cells (MSCs) are a common source for cell-based therapies due to their innate regenerative properties. However, these cells often die shortly after injection and, if they do survive, run the risk of forming tumors. Cell-secreted nanoparticles known as extracellular vesicles (EVs) have been identified as having therapeutic effects similar to those of their parental cells without the safety risks. Specifically, MSC EVs have emerged as a promising therapeutic modality in a multitude of applications, including autoimmune and cardiovascular diseases, cancer, and wound healing. Despite this promise, low levels of naturally occurring EV cargo may necessitate repeated doses to achieve clinical benefit, countering the advantages of EVs over MSCs. The current techniques to combat low EV potency (e.g., loading external molecules or using chemicals) are not agreeable to large-scale manufacturing techniques and would substantially increase the regulatory burden associated with EV translation. Fortunately, mechanical cues within the microenvironment have potential to overcome these translational barriers as they can alter EV

therapeutic effects but are also cost-effective and can be precisely manipulated in a reproducible manner. The goal of this project is to understand how these cues impact MSC EV secretion and physiological effects. We showed that flow-derived shear stress applied to MSCs seeded within a 3D-printed scaffold (i.e., the bioreactor) can significantly upregulate EV production (EVs/cell) while maintaining the *in vitro* pro-angiogenic effects of MSC EVs. Interestingly, we demonstrated that MSC EVs generated using the bioreactor system significantly improved wound healing in a diabetic mouse model, with increased CD31+ staining in wound bed tissue compared to animals treated with flask cell culture-generated MSC EVs. Furthermore, for the first time, we showed that mechanical confinement of MSCs within micropillars could augment MSC EV production and bioactivity. Lastly, we demonstrated that soft substrates composed of various polydimethylsiloxane (PDMS) formulations could increase MSC EV production and activity as well. Through the work performed here, we have laid the groundwork to elucidate the relationship between cell mechanobiology and EV activity that will ultimately enable an adaptable and scalable EV therapeutic platform.

ASSESSMENT OF MECHANICAL CUES TO ENHANCE THE CLINICAL TRANSLATION OF EXTRACELLULAR VESICLES

by

Stephanie Marie Kronstadt

Dissertation submitted to the Faculty of the Graduate School of the
University of Maryland, College Park, in partial fulfillment
of the requirements for the degree of
Doctor of Philosophy
2022

Advisory Committee:
Associate Professor Dr. Steven M. Jay, Chair
Professor Dr. John P. Fisher
Assistant Professor Dr. Katharina Maisel
Associate Professor Dr. Kimberly Stroka
Associate Professor Dr. Ryan Sochol, Dean's Representative

© Copyright by
Stephanie Marie Kronstadt
2022

Dedication

I would like to dedicate this dissertation to my father, Samuel Wayne Kronstadt. He has always been the person I most admire and look up to for his unrelenting work ethic, his capacity to master anything he puts his mind to, and his ability to overcome adversity. Dad, you are my inspiration. I love you.

Acknowledgements

I am extremely grateful for the support I received throughout the completion of this dissertation project. First and foremost, I want to thank my advisor, Dr. Steven Jay. Coming into the program as a marine biologist, I had very little experience in the techniques used in his lab. With his patience and encouragement, I was able to learn things I never thought I had the capacity to learn. He enabled me the freedom to pursue what I was truly interested in and he was always available for one-on-one meetings when I needed to talk. These meetings were not only instrumental in guiding me in my research, but also in keeping my sanity. He always offered sage advice that helped keep things in perspective even when I felt like everything was falling apart. I always left these interactions, no matter how brief they were, feeling renewed and refreshed. On top of everything, he was always on the search for opportunities that would help me become competitive for the career in industry I wanted. I truly appreciate his genuine interest and investment in not only my research, but my development as a well-rounded person.

I am also grateful to my committee members and collaborators. First, I am thankful to Dr. John Fisher for sharing his expertise and lab resources, without which I would have never been able to complete my experiments utilizing the perfusion bioreactor. No matter how busy he was he was also always happy to supply me with advice and recommendation letters for the countless awards and fellowships I applied to throughout the years. I'm also thankful to Dr. Fisher's lab members, specifically

Shannon McLoughlin for her willingness to help with 3D printing. I want to thank Dr. Katharina Maisel and Dr. Ryan Sochol for taking the time to meet with me and share their thoughts about my research. They helped show me a perspective that allowed me to see other aspects I had not considered. I would like to thank Dr. Wei Chao for his help with early experiments during my research and advice on my proposed project. I am also deeply indebted to Dr. Kimberly Stroka for opening her lab and resources which allowed me to master the techniques I needed to complete a majority of my thesis.

My experience during my time at UMD would not have been the same without my lab mates, past and present. I'd like to thank Dan Levy for always making the lab a fun and friendly place. He was always down for happy hour when I needed to vent or willing to help with experiments. On top of this, he always took his lab duties seriously and kept the lab running smoothly. I could not have asked for a better friend and co-worker. I'm thankful to our newest lab members Nick Pirolli, Emily Powsner, and Talia Solomon. Specifically, I'd like to thank Nick for taking the time to teach me some new techniques when he had no obligation to do so. And a special shout out to Emily for helping me finish up the loose ends of my research. I truly appreciate my mentees, Lauren Hoorens Van Heyningen and Amaya Aranda, who were always willing and ready to help with any and all of my experiments, no matter how tedious. I want to thank former lab members Drs. Eli Pottash, Louis Born, Divya Patel, and Anjana Jeyaram for their advice and support. Specifically, I thank Divya for laying the groundwork for my first aim and Louis for help conducting the animal studies. And

Anjana's guidance helped me keep everything in perspective during the final push of my research.

I'd also like to thank Ian Smith in Dr. Stroka's lab for his help and advice which allowed me to successfully complete a majority of my thesis work. He was not only an essential person in my research but also an incredible friend who always had a smile on his face. No matter what topic we were discussing, I always learned something new. Additionally, I'm grateful to former members of his lab, Drs. Rebecca Moriarty and Mary Doolin, for their help and advice.

I'd like to thank all my family, friends, and countless mentors, some of which are not mentioned here, for their continuous advice and support. Specifically, I'd like to thank my father, Samuel, and my step-mother, Kathy, for providing me a place to live and countless home-cooked meals as I pursued my dreams. I'm grateful to my boyfriend, Evan, for always understanding and supporting me during my late nights at the lab. His support has been unwavering and has allowed me to pursue my goals guilt-free. Finally, I'd like to thank Dr. Keith Herold for his support and kind words early on when I was applying to graduate school as it ultimately convinced me to pursue a PhD at UMD.

This work was supported by the National Institutes of Health (HL141611, NS110637, GM130923, HL141922, HL159590 to SMJ; AI089621 to SMK; EB023833 to JPF), the National Science Foundation (1750542 to SMJ; 1856350 to JPF), and the University of Maryland.

Table of Contents

Dedication ii
Acknowledgements iii
Table of Contents vi
List of Figures ix
List of Commonly Used Abbreviations xi
Chapter 1: Introduction 1
1.1 Extracellular Vesicles as Novel and Multifunctional Therapeutics 1
1.2 Limitations to MSC EV Clinical Translation 2
1.3 Enhancing MSC EV Translational Potential by Modulating Mechanical Cues 2
1.3.1. Flow-derived Shear Stress 3
1.3.2. Cell Confinement 3
1.3.3. Substrate Stiffness 3
1.4 Summary and Potential Impact 4
Chapter 2: Therapeutic Potential of Extracellular Vesicles 5
2.1 Introduction 5
2.2 Biology of Extracellular Vesicles 7
2.2.1. EV Secretion 8
2.2.2. EV Composition 10
2.2.3. EV Uptake 12
2.2.4. EVs in Disease 13
2.3 EV Isolation and Characterization 15
2.4 EVs as Therapies 17
2.5 Major Barriers to Clinical Translation and Possible Solutions 18
2.4.1. Cargo Loading 19
2.4.2. Manipulation of the Producer Cell Environment 21
2.6 The Potential of Mechanical Cues in the Development of EV Therapies 25
2.5.1. Shear Stress 25
2.5.2. Substrate Architecture 29
2.7 Conclusions 32
Chapter 3: Mesenchymal Stem Cell Culture Within Perfusion Bioreactors Incorporating 3D-Printed Scaffolds Enables Improved Extracellular Vesicle Yield with Preserved Bioactivity 34
3.1 Introduction 34
3.2 Methods 36
3.2.1. Cell Culture 36
3.2.2. 3D-printed Scaffold Design and Fabrication 38
3.2.3. Scaffold Sterilization, Coating, and Cell Seeding 39
3.2.4. Perfusion Bioreactor Assembly 40
3.2.5. Cell Staining and Imaging 40
3.2.6. EV Isolation and Characterization 41
3.2.7. Gap Closure Assay 43
3.2.8. Tube Formation Assay 44

3.2.9. EV Uptake via Flow Cytometry and Confocal Imaging 44
3.2.10. MALDI-TOF Mass Spectrometry 47
3.2.11. mRNA Isolation and Profiling 48
3.2.12. *In vivo* Studies 48
3.2.13. Histology 49
3.2.14. Statistics 51
3.3 Results 52
3.3.1. Culture of MSCs in 3D-printed Scaffold-Perfusion Bioreactor 52
3.3.2. MSC EV Production is Enhanced by Perfusion Bioreactor Culture 54
3.3.3. Enhanced EV Production in Perfusion Bioreactor Culture is Not Specific to MSCs 58
3.3.4. MSC EV *in vitro* Angiogenic Bioactivity is Maintained Following Perfusion Bioreactor Culture 60
3.3.5. *In vivo* MSC EV Wound Healing Bioactivity is Enhanced via Perfusion Bioreactor Culture 64
3.3.6. Assessment of Perfusion Bioreactor Culture-Induced Enhancement of in vivo MSC EV Bioactivity 66
3.4 Discussion 70
Chapter 4: Mechanical Confinement of Mesenchymal Stem Cells Enhances Production and Pro-Angiogenic Bioactivity of Extracellular Vesicles 77
4.1 Introduction 77
4.2 Methods 79
4.2.1. Cell Culture 79
4.2.2. Micropillar Device Fabrication 80
4.2.3. Cell Seeding and MSC EV Collection 84
4.2.4. Immunofluorescence Staining and Imaging 85
4.2.5. MSC EV Isolation 86
4.2.6. MSC EV Characterization 88
4.2.7. Tube Formation Assay 89
4.2.8. mRNA Isolation and Profiling in Recipient Cells 90
4.2.9. Statistics 92
4.3 Results 92
4.3.1. Validation of MSC Culture in Micropillar Devices 92
4.3.2. Culturing MSCs within Micropillar Devices Increases EV Production 94
4.3.3. MSC Confinement Impacts EV Bioactivity 96
4.3.4. EVs from Confined MSCs Alter Gene Expression in Recipient Cells 102
4.4 Discussion 104
Chapter 5: Culturing Mesenchymal Stem Cells on Polydimethylsiloxane of Various Elastic Moduli Improves Extracellular Vesicle Production and *in vitro* Bioactivity 111
5.1 Introduction 111
5.2 Methods 113
5.2.1. Cell Culture 113
5.2.2. PDMS Substrate Fabrication and Characterization 114
5.2.3. MSC Seeding and MSC EV Collection 115
5.2.4. MSC Viability Assay 116
5.2.5. MSC Identity Verification 117

5.2.6. MSC EV Isolation and Characterization 118
5.2.7. Tube Formation Assay 120
5.2.8. Gap Closure Assay 121
5.2.9. mRNA Isolation and Profiling in Recipient HUVECs 122
5.2.10. miRNA Isolation and Profiling in MSC EVs 126
5.2.11. Statistics 127
5.3 Results 127
5.3.1. Altering Base to Crosslinker Reagent Ratio of Sylgard 184 PDMS Changes the Elastic Modulus and is Non-toxic to Cells 127
5.3.2. Culturing MSCs on Softer Sylgard 184 PDMS Substrates Improves EV Production 130
5.3.3. Culturing MSCs on the Softest Sylgard 184 PDMS Substrate (0.3 MPa) Enhances MSC EV *in vitro* Angiogenic Bioactivity 132
5.3.4. Additional Dilution of Crosslinker Reagent Reduces Elastic Moduli of Sylgard 184 PDMS without Inducing Cytotoxicity 136
5.3.5. Culture Conditions Do Not Impact Sylgard 184 PDMS Elastic Moduli 138
5.3.6. Further Reduction of Sylgard 184 PDMS Elastic Modulus Maintains MSC EV *in vitro* Angiogenic Bioactivity 139
5.3.7. Mixing Sylgard 184 and Sylgard 527 Allows for a Finer Elastic Modulus Gradient that is Non-Toxic to Cells 143
5.3.8. Culture Conditions Do Not Influence the Elastic Moduli of the Sylgard 184:Sylgard 527 PDMS Mixtures 145
5.3.9. Culturing MSCs on Mixtures of Sylgard 184 and Sylgard 527 Maintains the Trend of Increased EV Production and Angiogenic Bioactivity with Decreasing Elastic Moduli 146
5.3.10. Substrate Stiffness Alters MSC EV Cargo and Gene Expression in Recipient Cells 152
5.3.11. MSC Phenotype is Maintained Across the PDMS Substrates 156
5.4 Discussion 157
Chapter 6: Summary, Conclusions, and Future Directions 169
6.1 Summary and Conclusions 169
6.2 Future Directions 171
6.3 Scientific Contributions to the Field and to the Jay Lab 176
6.4 Peer-Reviewed Journal Publications 178
Appendix A: Assessment of Anti-Inflammatory Bioactivity of Extracellular Vesicles is Susceptible to Error via Media Component Contamination 180
Bibliography 211

List of Figures

Figure 2.1. Schematic representation of the reported advantages of utilizing EVs as a clinical therapy 6
Figure 2.2. Schematic depicting EV biogenesis 8
Figure 3.1. Size exclusion chromatography (SEC) can effectively remove PKH67 dye aggregates 46
Figure 3.2. Perfusion bioreactor setup and scaffold characterization……..53
Figure 3.3. MSC EV production can be maximized in the bioreactor with a 5 mL/min flow rate. 56
Figure 3.4. Flow-induced increase in MSC EV production is maintained across donors and tissue of origin……...57
Figure 3.5. HEK293 EV production increases when cultured in perfusion bioreactor. 59
Figure 3.6. EVs from MSCs cultured in the static scaffolds and flasks perform similarly in the gap closure assay 61
Figure 3.7. Perfusion bioreactor culture maintains in vitro pro-angiogenic activity of MSC EVs. 62
Figure 3.8. Angiogenic bioactivity is maintained across donors of bone marrow-derived MSCs……...63
Figure 3.9. Perfusion bioreactor culture improves healing in a diabetic mouse excisional wound healing model 65
Figure 3.10. Assessment of HUVEC uptake and protein profile of flask and bioreactor MSC EVs 67
Figure 3.11. MALDI-TOF mass spectra of three separately prepared batches of flask and bioreactor EVs 68
Figure 3.12. RNA profiling of HDMECs treated with MSC EVs from flask vs perfusion bioreactor culture…….69
Figure 4.1. Verification of micropillar dimensions 82
Figure 4.2. MSCs can be cultured within PDMS micropillar devices. 93
Figure 4.3. EV production is augmented when MSCs are cultured within the micropillar devices. 95
Figure 4.4. Mechanical confinement during MSC culture augments in vitro tube formation activity of MSC EVs 97
Figure 4.5. EV isolation strategy has no effect on the observed tube formation enhancement facilitated by confinement 99
Figure 4.6. EVs from confined MSCs had no effect on the migratory potential and viability of recipient HUVECs 101
Figure 4.7. Angiogenic gene expression in HUVECs treated with EVs from MSCs cultured in PDMS devices with micropillar spacings of 5 μm. 103
Figure 4.8. Gene expression of TIE1, COL4A1, and COL18A1 in EV-treated HUVECs 104
Figure 5.1. Varying the elastomer base to crosslinker reagent ratio of Sylgard 184 PDMS changes the elastic modulus without inducing cytotoxicity 129
Figure 5.2. Culturing MSCs on the softest Sylgard PDMS formulation increases MSC EV production.. 131

Figure 5.3. Soft Sylgard 184 PDMS enhances MSC EV in vitro cell migration..... 133
Figure 5.4. Soft Sylgard 184 PDMS improves tube formation in recipient HUVECs……135
Figure 5.5. Further dilution of the crosslinker reagent (50:1) reduces the elastic modulus of the PDMS without inducing cell death.. 137
Figure 5.6. Sylgard 184 PDMS substrates maintain elastic modulus despite exposure to culture conditions……...138
Figure 5.7. Enhanced effect of MSC EVs in the gap closure assay is maintained as elastic modulus is reduced 140
Figure 5.8. Enhanced effect of MSC EVs in the tube formation assay is maintained as elastic modulus is reduced 142
Figure 5.9. Varying the ratio of Sylgard 184 to Sylgard 527 produces a refined range of elastic moduli that is non-toxic to cells 144
Figure 5.10. Substrates composed of varying ratios of Sylgard 184 to Sylgard 527 maintain elastic modulus despite exposure to culture conditions..... 145
Figure 5.11. Culturing MSCs on the softer Sylgard 184/527 mixtures increases MSC EV production.. 147
Figure 5.12. Enhanced effect of MSC EVs in the gap closure assay is maintained as elastic modulus is reduced by mixing Sylgard 184 and Sylgard 527 149
Figure 5.13. Enhanced effect of MSC EVs in the tube formation assay is maintained as elastic modulus is reduced by mixing Sylgard 184 and Sylgard 527..... 151
Figure 5.14. Substrate alters the MSC EV miRNA profile..... 152
Figure 5.15. Angiogenic gene expression in HUVECs treated with EVs from MSCs cultured in flasks or the softest PDMS substrate 154
Figure 5.16. Gene expression of E-selectin, PLAU, and PARD3 in EV-treated HUVECs 155
Figure 5.17. MSC phenotype is retained when cultured on PDMS of various elastic moduli 156
Figure 6.1. Mechanical cues investigated..... 170
Figure 6.2. Cellular processes governed by the mechanical cues of interest..... 174
Figure A.1. Culture conditions and isolation techniques do not impart significant effects on size or morphology of HEK293T EVs……..195
Figure A.2. Culture conditions and isolation techniques alter the immunomodulatory activity of HEK293T EVs……..198
Figure A.3. Unconditioned media subjected to each isolation technique alter cytokine secretion in stimulated macrophages in a similar manner to HEK293T EV preparations……200
Figure A.4. Unconditioned media do not elicit any significant response in *in vitro* angiogenic assays……...202
Figure A.5. Fetal bovine serum (FBS) may be responsible for observed immunomodulatory responses of stimulated macrophages……...204
Figure A.6. EV-depletion protocol of media supplements alter the results of the stimulated macrophage assay…….205

List of Commonly Used Abbreviations

EVs	Extracellular vesicles
ESCRT	Endosomal sorting complex required for transport
NTA	Nanoparticle tracking analysis
BCA	Bicinchoninic acid assay
RT-qPCR	Real-time quantitative polymerase chain reaction
UC	Ultracentrifugation
TFF	Tangential flow filtration
SEC	Size-exclusion chromatography
PDMS	Polydimethylsiloxane
MSCs	Mesenchymal stem/stromal cells
HUVECs	Human umbilical vein endothelial cells
HDMECs	Human dermal microvascular endothelial cells
HEK293/T	Human embryonic kidney cells
DNA	Deoxyribonucleic acid
RNA	Ribonucleic acid
miRNA	MicroRNA
YAP/TAZ	Yes-associated protein and transcriptional coactivator with PDZ-binding motif

Chapter 1: Introduction

1.1 Extracellular Vesicles as Novel and Multifunctional Therapeutics

Cell therapies (i.e., transplantation of stem/progenitor cells) have proven to be a multifaceted, promising approach in numerous disease applications but are hindered by short survival times after administration and risk of tumorigenesis [1, 2]. Recently, cell-derived nanoparticles known as extracellular vesicles (EVs) have been identified as a crucial factor underpinning the therapeutic value of cell therapies through the transfer of bioactive cargo (i.e., DNA, RNA, lipids, and proteins) with the additional benefit of reduced safety and immunogenicity concerns [3, 4]. Moreover, EVs are reported to cross biological barriers and efficiently traverse various tissue microenvironments [5-7]. This has spurred an increase in EV-based research that has since implicated EVs not only as diagnostically and prognostically informative biomarkers, but also as potential therapeutics and drug delivery vehicles [8]. In particular, EVs secreted from mesenchymal stem cells (MSCs) have demonstrated multifunctional potential as they often enact immunomodulatory, anti-fibrotic, pro-angiogenic, anti-apoptotic, antimicrobial, and/or antioxidant effects in recipient cells [9]. Ultimately, MSC EVs are poised for therapeutic utility in a multitude of chronic and deadly applications, including autoimmune and cardiovascular diseases, cancer, sepsis, and chronic wounds [9-13].

1.2 Limitations to MSC EV Clinical Translation

Despite the promise of MSC EV therapies, there are still many challenges that limit MSC EV efficacy and translation, including a lack of scalable production methods and low therapeutic efficiency (i.e., low levels of endogenous therapeutic cargoes). Common techniques to combat low EV potency, such as exogenous cargo loading and biochemical cell priming, have their merits, but they are generally fundamentally limited with respect to scalability and would substantially increase production costs and the regulatory burden associated with EV translation. Alternatively, mechanical cues can be used to regulate and enhance EV therapeutic effects [14, 15]. Compared to other approaches, mechanical cues are easily characterized, cost-effective, and can be manufactured with high reproducibility and scalability [16]. However, there is inadequate knowledge as to exactly how these cues alter the EVs, as well as the extent to which these cues can be used to control EV therapeutic efficacy. Thus, understanding the relationship between mechanobiology and EV production and activity will enable a rationally designed, scalable EV manufacturing process and help unlock the full potential of EVs.

1.3 Enhancing MSC EV Translational Potential by Modulating Mechanical Cues

Here, we investigated the individual effect of several mechanical cues (i.e., flow-derived shear stress, cell constraint, and substrate stiffness) on the production and bioactivity of MSC EVs. To assess bioactivity, we specifically focused on wound healing abilities due to the well-documented pro-angiogenic effects of EVs from traditionally-cultured MSCs [17, 18].

1.3.1. Flow-derived Shear Stress

Previous work conducted in our lab demonstrated that human dermal microvascular endothelial cell (HDMEC) EV production can be significantly increased using a 3D-printed scaffold-perfusion bioreactor [15]. In the present study, we modified this 3D-printed scaffold-perfusion bioreactor and showed that flow-derived shear stress, specifically at $3x10^{-3}$ dyn/cm^2, can be used to enhance MSC EV production while maintaining MSC EV pro-angiogenic bioactivity both *in vitro* and *in vivo*.

1.3.2. Cell Confinement

Cell morphology is a well-known regulator of cell phenotype, function, and migration [19]. Importantly, cell morphology is a clinically relevant cue as it is a function of the physical confinement that can occur within the *in vitro* and *in vivo* microenvironments [20]. To our knowledge, only two studies have explored the association between cell confinement and EV activity and thus this remains a largely unexplored relationship, especially when studying MSCs [21, 22]. Presently, we demonstrated that physically confining MSCs significantly increased EV production and EV bioactivity.

1.3.3. Substrate Stiffness

Finally, we investigated the effect of substrate stiffness on MSC EVs. Substrate stiffness is an important mechanical cue capable of driving cell behavior and fate [23]. Tissue stiffness has been found to have profound implications in many pathologies including cancer [24, 25], cardiovascular disease [26], and fibrosis

[23]. Here, we found that as substrate softened, MSC EV production increased and that softer substrates (< 0.3 MPa) produced MSC EVs with enhanced bioactivity.

1.4 Summary and Potential Impact

The results of this study inform a method to increase the production and potency of MSC EVs through the manipulation of flow-derived shear stress, cell confinement, or substrate stiffness. Overall, this work establishes a promising solution to major EV translational issues (i.e., scalability and low potency) with potential for adaptation to various EV-based therapeutics and capacity for improvement alongside the continuous advancements in biomanufacturing technologies.

Chapter 2: Therapeutic Potential of Extracellular Vesicles[†]

2.1 Introduction

Cell-based therapies demonstrate a broad potential that blankets numerous disorders from cancer to autoimmune diseases [27]. These cell-based therapeutics are equipped with the ability to target multiple pathways through parallel mechanisms, demonstrating an innate biological intellect seemingly unobtainable with traditional therapeutics. Unfortunately, cell-based therapies face various challenges to clinical translation that have yet to be resolved, including immunogenicity, short survival times after administration, and risk of tumorigenesis, as well as several other considerations [1, 2]. However, it is now widely recognized that cells exert much of their biological function through trophic mechanisms, especially the secretion of lipid-delimited nanoparticles known as extracellular vesicles (EVs) [28, 29]. In terms of translational therapeutic potential, EVs possess several potential advantages compared with traditional cell therapies, including increased safety (EVs do not divide or differentiate after administration) and possibly reduced immunogenicity (studies indicate EVs can be administered across species and may not require donor-matching) [3, 4]. Moreover, EVs are reported to cross biological barriers and efficiently traverse various tissue microenvironments (**Figure 2.1**) [5-7]. Cells are known to selectively load EVs with a variety of bioactive molecules and dictate EV surface characteristics (e.g., tetraspanins and lipids), allowing EVs to behave as an extension of the original cell – targeting and

[†] A portion of this work was adapted from **Kronstadt, S.M.**, A.E. Pottash, D. Levy, S. Wang, W. Chao, S.M. Jay. 2021. Therapeutic potential of extracellular vesicles for sepsis treatment. Advanced Therapeutics. DOI: 10.1002/adtp.202000259.

modifying near or distant tissues [30-32]. Thus, the utilization of EVs as an alternative therapeutic to cells has become an intriguing new strategy. However, the biological and malleable nature of EVs can present issues during biomanufacturing involving heterogeneity, potency, and scalable production. Understanding the interactions among the microenvironment, cells, and their subsequently secreted EVs will lay the necessary foundation for an adaptable and clinically translatable EV therapeutic platform that will prove invaluable in many chronic and deadly diseases.

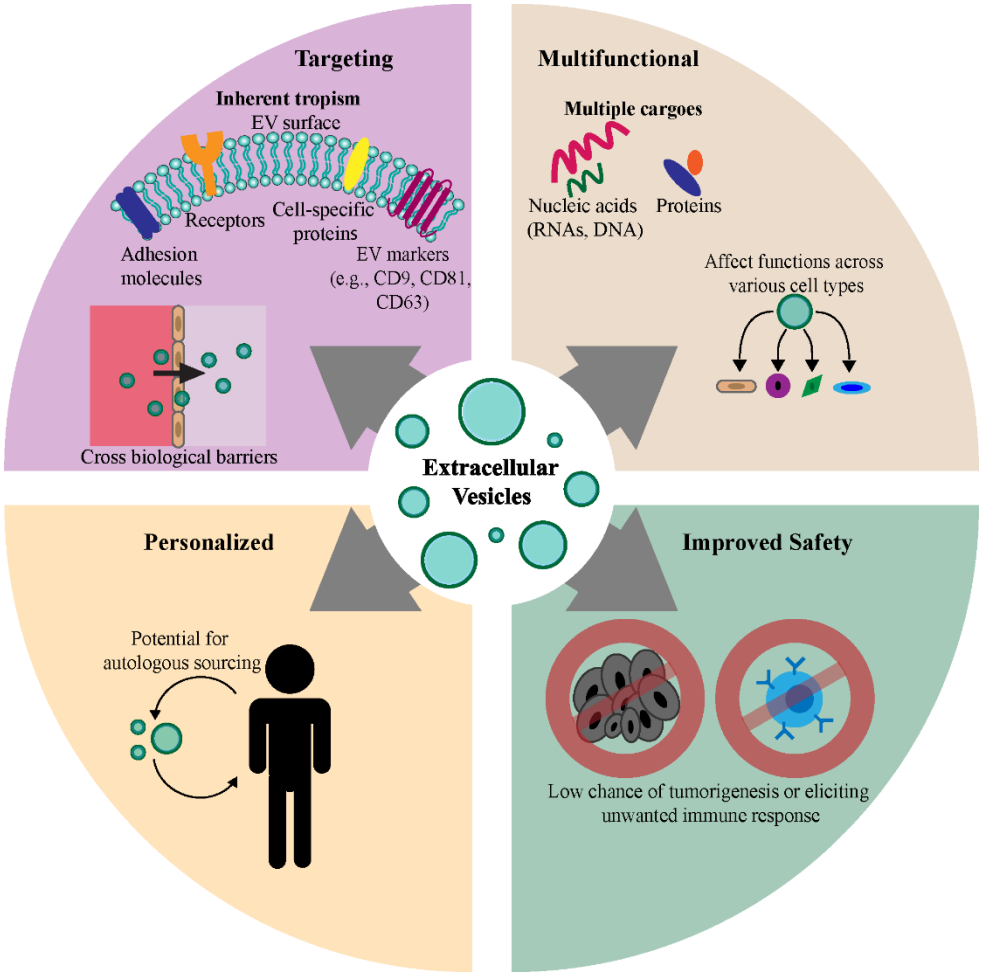


Figure 2.1. Schematic representation of the reported advantages of utilizing EVs as a clinical therapy

2.2 Biology of Extracellular Vesicles

The term EVs encompasses different subpopulations of vesicles that can be characterized on the basis of their size, biochemical composition, and/or the cell of origin [33]. These subpopulations – including exosomes, microvesicles, and others – can arise from either the outward budding of the plasma membrane or from the endosomal system as intra-luminal vesicles that are secreted after the fusion of the multivesicular body with the cell membrane (**Figure 2.2**) [33]. Unfortunately, overlapping size ranges coupled with the lack of unique molecular markers makes it unclear how to accurately differentiate among these subpopulations. Overall, EVs constitute an endogenous system for paracrine and endocrine intercellular communication via cell-to-cell transfer of their bioactive cargo (i.e., DNA, RNA, lipids, and proteins) and/or the activation of target cell surface receptors [34-36]. This integral involvement in cellular communication along with their ubiquitous presence throughout the body [32], portends a multifunctional role of EVs in a diverse array of physiological processes, both healthy and pathological, that is driven by EV secretion dynamics, composition, and uptake.

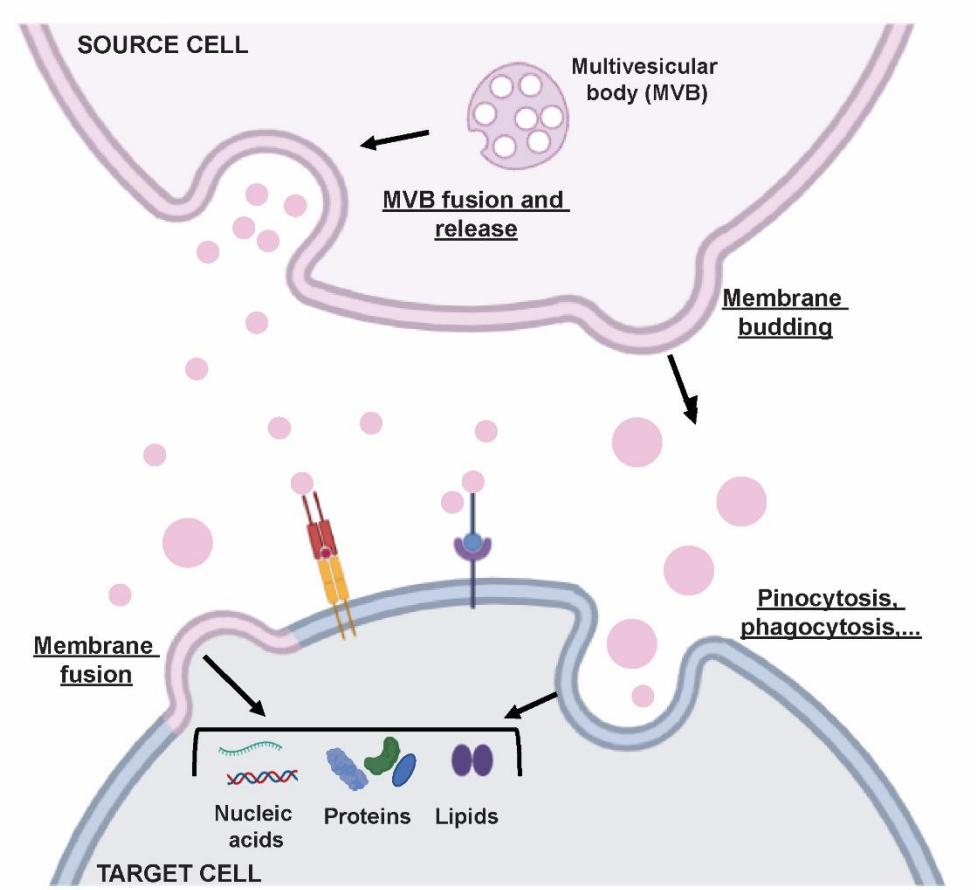


Figure 2.2. Schematic depicting EV biogenesis.

2.2.1. EV Secretion

The mechanisms behind EV secretion remain poorly understood as they are complex and can vary depending on cell-type [37-39]. The best characterized cellular mechanism proposed is known as the endosomal sorting complex required for transport (ESCRT) [38]. The ESCRT machinery consists of twenty proteins that form multiple sub-complexes (i.e., ESCRT-0, -I, II, and -III). ESCRT-0 is responsible for sequestering ubiquitinated proteins into the endosomal membrane, while ESCRT- I and -II deform the membrane to form buds and initiates the uptake of cytosolic cargo, and ESCRT-III then drives vesicle scission [37, 38]. This process is facilitated by ESCRT accessory

proteins including tumor susceptibility gene 101 (TSG101) and ALG-2 interacting protein-X (ALIX), which are often used as identifying markers of EVs [38]. Select ESCRT proteins are also required for the formation of EVs from the cell membrane [40]. However, depletion of the ESCRT components has failed to stop EV secretion from either the endosome or the plasma membrane, suggesting an ESCRT-independent biogenesis pathway. While less characterized, different modes of ESCRT-independent pathways are known to involve the self-organization of lipids (e.g., sphingomyelin, cholesterol, phosphatidic acid), the interactions of tetraspanins (e.g., CD9, CD63), or the influx of calcium, all of which can promote regional membrane remodeling and subsequent vesicle formation [38, 41, 42]. Intracellular trafficking of EVs is largely governed by Rab GTPases (e.g., Rap27a/b) which brings the EVs to the plasma membrane. Once at the membrane, soluble N-ethylmaleimide-sensitive fusion attachment protein receptors (SNAREs) as well as altered actin polymerization are integral in facilitating EV fusion and release. As it is likely that these pathways and components work in concert, there is a need for complementary methods to determine the exact origin of specific EV populations.

The ability to establish the mode of biogenesis of a specific EV population would be beneficial in understanding pathological conditions. It is known that EV secretion is often deregulated during human disease; a characteristic that is exemplified in cancer [43]. Cancerous cells have been shown to generate EVs

at levels magnitudes higher than healthy cell counterparts. Additionally, these cancer cell derived EVs have been identified as vital in promoting cell cancer expansion, potentiating metastasis, and establishing resistance to anticancer treatments [44, 45]. As biogenesis is thought to influence EV cargo composition and thus ultimately EV function [46], a complete understanding of EV biogenesis could help elucidate the connection between EV origin and specific functional outcomes, allowing the identification of potential therapeutic targets.

2.2.2. EV Composition

It is known that nucleic acids as well as proteins and lipids can naturally co-occur within a single population of EVs [46, 47]. Some proteins (e.g., CD63, CD9, TSG101) and lipids (e.g., phosphatidylserine and sphingomyelin) seem to be universally present in EVs while others are cell-type specific. In 2007, the discovery that EVs are capable of transferring functional RNAs to recipient cells spurred an increase in EV-based research that has since implicated EVs not only as diagnostically and prognostically informative biomarkers [8, 48], but also as potential therapeutics and drug delivery vehicles in a multitude of chronic and deadly diseases [49-53]. Specifically, EVs are known to ferry microRNA (miRNAs), which are molecules capable of epigenetic reprogramming of cells under normal and pathological conditions [54], and have been associated with the development of numerous disorders including sepsis [55], cancer [56], and cardiovascular disease [57]. miRNAs are one of the most abundant regulatory molecules within the human body and, with the ability to target various messenger RNAs (mRNAs), they can effectively

control multiple levels of a pathological process [58, 59]. Additionally, it is important to note that miRNAs, while powerful on their own, often work together as a regulatory network to ensure precise physiological responses [60, 61]. For instance, numerous miRNAs have been noted as critical in regulating the nuclear factor kappa-light-chain-enhancer of activated B cells (NF-κB) pathway [60, 62-64], which performs a central role in the regulation of both innate and adaptive immunity and has emerged as an important therapeutic target in numerous diseases [65, 66]. In 2017, Mann et al. demonstrated a combined positive and negative feedback network governed by the interplay between miR-146a and miR-155 that effectively controlled the activity of the NF-κB pathway in murine macrophages [60]. It was demonstrated that this miRNA interaction was essential in enabling an effective yet controlled inflammatory response crucial for functional immunity. Importantly, numerous miRNAs that have been implicated in the regulation of NF-κB (i.e., miR-146a, -155, -223, -21) [60, 62-64], have been shown to co-exist in EV populations derived from numerous sources (e.g., blood, urine, cerebral fluid). Moreover, EV-associated miRNA transfer is not only important in mediating the inflammatory response but has been implicated as an important driver in other physiological processes including muscle cell differentiation, follicular maturation, and osteogenic differentiation of human bone marrow-derived mesenchymal stem cells (MSCs) [46]. In terms of disease, EV-associated miRNA transfer is well-documented in pathological settings including various pulmonary diseases (e.g., acute lung injury, asthma) [67], cancer [68], and

sepsis [69]. While, miRNAs are indispensable in normal and pathological processes, it should be noted that EVs can also be associated with many other RNAs (e.g., long non-coding RNAs, transfer RNAs, ribosomal RNAs, circular RNAs, messenger RNAs, etc.) [70]. Overall, further dissection of EV composition will prove to enhance the understanding of the molecular mechanisms in both health and disease.

2.2.3. EV Uptake

The manner of EV uptake dictates the interaction with the recipient cell and the subsequent delivery of EV cargo, ultimately shaping functional outcomes. Routes for internalization include phagocytosis, macropinocytosis, receptor-mediated endocytosis, and membrane fusion and seem to be cell-type dependent [71, 72]. Although, the most commonly-reported route of EV uptake seems to be clathrin/caveolin-mediated endocytosis [71]. Furthermore, numerous molecules are known to be involved in EV uptake including tetraspanins, integrins, immunoglobulins, proteoglycans, lectins, and lipids [71]. Notably, EV internalization is not always necessary as receptor-ligand interactions on the cell surface has been shown to be sufficient in inducing functional responses in the recipient cell. In addition, EVs may be degraded or re-secreted, which could have powerful implications for the inferred functional effects of EV cargo [73]. Thus, just like the knowledge of EV biogenesis, the understanding of EV uptake is limited and requires further exploration to precisely understand EV fate and function.

2.2.4. EVs in Disease

During the development of diseases, endogenous EVs often undergo fluctuations in relative quantities, composition, and functional effects, making them integral in the progression of pathophysiological conditions [74-78]. For example, in sepsis and subsequent organ damage, endogenous EVs have been implicated as critical immunomodulatory factors that can regulate inflammation [79-88], coagulation [87, 89-97], apoptosis [95], and vascular dysfunction [84, 97-101]. The ability of EVs to trigger, amplify, and sometimes suppress immune responses during disease can be attributed to the presence of distinct membranous proteins or lipids (e.g., phosphatidylserine, integrins, major histocompatibility complexes) and to differential luminal cargo (e.g., miRNAs, proteins) [49, 102]. There is much research dissecting these attributes and the mechanisms through which they work, as it can prove not only beneficial in the development of an EV therapeutic but also in clarifying the complex pathophysiology of the disease in question. For example, Xu et al. showed that circulating plasma EVs in a cecal ligation and puncture (CLP) murine model of sepsis were not only more abundant when compared with healthy mice but also contained different miRNA and had pro-inflammatory effects on bone marrow-derived macrophages (BMDMs) [69]. This immunomodulation was shown to be partially mediated by EV-associated miRNAs (i.e., miR-34a, miR-122, miR-146a) that signal via a TLR 7-myeloid differentiation primary response 88 (TLR7-MyD88)-dependent mechanism [69]. This research led to further investigation of the TLR7 signaling mechanism using a loss-of-function

approach by Jian and colleagues that showed TLR7 signaling contributes to inflammation, organ injury, and mortality in murine sepsis [103]. Thus, this type of research is important in revealing insights into EV functions and is essential in exposing the cellular mechanisms contributing to chronic disease.

In addition to disease progression, endogenous EVs can also lend protection during illness. A study by Gao and colleagues found that administration of murine septic EVs into a CLP mouse model suppressed inflammatory cytokine production (i.e., tumor necrosis factor-alpha; TNF-α), alleviated liver and lung tissue injury, and significantly prolonged survival [104]. In rheumatoid arthritis patients, neutrophil derived EVs were increased in concentration and enriched with the anti-inflammatory protein Annexin A1 (AnxA1). When applied in a murine model of arthritis, these $AnxA1^{+}$ EVs were shown to significantly reduce cartilage degradation through induction of transforming growth factor beta 1 (TGF-β1) production and extracellular matrix (ECM) deposition, and inhibition of apoptosis of chondrocytes [105]. In a separate study, patients with inflammatory bowel disease demonstrated an increased release of $AnxA1^{+}$ EVs and these EVs were found to activate wound repair cascades [106]. Overall, the clear importance of endogenous EVs in both the progression and mitigation of disease demonstrates the efficacy of targeting or exploiting EVs as a potent treatment platform.

2.3 EV Isolation and Characterization

There are numerous methods when it comes to isolating EVs, each with its own advantages and shortcomings. The most common is ultracentrifugation, which separates particles based on their size [107, 108]. This high-speed centrifugal method results in co-isolation of contaminants, demanding further filtration and washing steps, which can decrease EV yield. Additionally, it may induce deformation of EV membranes and there is a risk for EV aggregation or fusion. The process is also time-intensive and requires expensive equipment [108]. However, ultracentrifugation demands relatively few consumables and requires no addition of extraneous reagents which ultimately simplifies the downstream purification process. Filtration methods such as ultrafiltration, tangential flow filtration (TFF), and size exclusion chromatography (SEC) are also used [109-111]. They require less time, result in less contaminants, and are scalable, but typically must be paired with low-speed centrifugation and concentration steps [107]. Notably, pairing these methods together (i.e., ultrafiltration followed by SEC) can produce a high yield of relatively pure EVs with functional effects [110]. Precipitation methods using polymers, specifically polyethylene glycol (PEG), are relatively quick and easy to perform but often leads to retention of the polymer within the final EV sample [108]. Isolation by immunoaffinity entails separating EVs using antibodies tailored to specific EV surface proteins, allowing for high selectivity. However, as many EV subpopulations overlap in membrane markers, more information about specific EV characteristics and about what EV subpopulations are most desired will be needed to take full advantage of this method [112]. Importantly, isolation methods have been shown to result in EV

populations with significantly different membrane markers, RNA cargo [113, 114], purity [115], uptake potential [116], and bioactivity [117]. And recently, it was shown that isolation artifacts can even lead to misinterpretation of observed bioactivity as being exclusively dependent on EVs [118]. Thus, while isolation is a downstream procedure in the development process, it may be critically beneficial to consider the possible effects of the chosen methods much earlier in the course of therapeutic development.

The characterization of isolated EVs is also challenging due to a high degree of physicochemical heterogeneity. Basic characterization involves immunoblotting for common EV markers (i.e., CD9, CD63, CD81) to attempt to differentiate EVs from co-isolated contaminants like lipoproteins and cellular debris. EV morphology is visualized using scanning or transmission electron microscopy techniques (i.e., TEM or SEM), atomic force microscopy (AFM), or small angle x-ray scattering. The size and concentration of EVs can be measured via several platforms. Dynamic light scattering (DLS) and nanoparticle tracking analysis (NTA) utilizes laser beam light scattering and Brownian motion to calculate the hydrodynamic radius of EVs. NTA has become the most common method used as it can directly visualize individual EVs and calculate concentration. However, this method suffers inaccuracies which arise from a detection sensitivity that is limited to diameters greater than 50-70 nm. Additionally, as it is label-free, NTA cannot distinguish from contaminants such as lipoproteins. Other emerging techniques include an electrical based method known as tunable resistance pulse sensing (TRPS) and special flow cytometry setups [119, 120].

In addition to size, concentration, surface markers, and morphology, EV subpopulations can possess and be characterized by different optical properties (e.g., refractive index), buoyant densities, zeta potentials, and various biomolecular cargoes [119, 121]. It is important to note that the results and accuracy of the aforementioned characterization methods rely heavily on the isolation method utilized. For instance, a study by Sharma and colleagues found that the EV size, particle count, and EV topography (i.e., surface roughness) of breast cancer-derived EVs differed significantly across four methods of isolation (i.e., ultracentrifugation, sucrose density ultracentrifugation, immune affinity, and polymeric precipitation) [122].

Much of what is thought to be known about EV biology is highly dependent on the isolation and characterization methods. Thus, future EV therapies depend on a deeper understanding of the relationship between EV properties and functions alongside continuous advancement of characterization and isolation methods.

2.4 EVs as Therapies

The diverse functions of endogenous EVs in disease, as well as their ability to cross biological barriers [5-7], have spurred pre-clinical investigations in anticipation of EVs as a forthcoming therapeutic in various disorders. Furthermore, the ubiquity of EVs has directed this research to span multiple cell sources in search of an effective defense. EVs derived from wide range of cell types including endothelial progenitor cells, dendritic cells, and cardiosphere derived cells have been reported to demonstrate therapeutic effects in numerous applications including pulmonary fibrosis, myocardial infarction, and vascular repair [123]. Although some EV functions seem to be cell-type

specific, it is important to mention that a single source of EVs, potentially due to the presence of multiple intraluminal cargoes, can have the capacity to modulate pleiotropic functions across various target cells. As an example, regenerative medicine has focused on the utilization of MSCs, which carry intrinsic clinical value due to their multi-lineage differentiation capacity and natural regenerative abilities which confer on them anti-fibrotic, anti-apoptotic, pro-angiogenic, and immunosuppressive properties [124]. Subsequently, much pre-clinical EV research focuses on MSC EVs which have been shown to reduce the inflammatory response in multiple cell types, including macrophages and cardiomyocytes [125, 126]. Moreover, MSC EVs are also powerful regulators of oxidative stress, proliferation, and phenotype in various recipient cells, including endothelial cells and immune cells [127-130]. Following from this pre-clinical work, MSC EVs have shown clinical promise in several applications including steroid refractory graft-versus host disease, chronic kidney disease, refractory macular holes, and acute ischemic stroke [131] and are actively being tested as therapies several indications including COVID-19 associated acute respiratory distress syndrome (ARDS) (NCT04657458), dystrophic epidermolysis bullosa (NCT04173650), retinitis pigmentosa (NTC05413148), and wound healing (NCT05475418). Still, a number of reparable obstacles to clinical translation have left promising EV therapies stalled in development.

2.5 Major Barriers to Clinical Translation and Possible Solutions

Several challenges limit efficacy and translation of EV therapies, including low therapeutic efficiency as well as a lack of scalable and standardized production methods. Research has shown that advancements in the EV biomanufacturing process,

such as the manipulation of EV cargo and EV production conditions, can potentially overcome these obstacles. These, along with simultaneous advancements in the mechanistic understanding of disease pathologies, present ample opportunities for the development of a powerful and clinically translatable EV treatment platform.

2.4.1. Cargo Loading

As natural intercellular communicators, EVs have been targeted as vehicles for the delivery of both native and non-native molecules (i.e., RNAs, DNA, proteins, and non-biologic small molecule drugs) in numerous therapeutic applications [132-135]. In comparison with current synthetic drug delivery systems such as liposomes, lipid nanoparticles, and polymeric nanoparticles, EVs may provide a platform that offers several advantages including increased biocompatibility, minimal toxicity issues, and intrinsic targeting abilities [136]. However, therapeutic molecules within EVs, such as miRNAs, may only be present at relatively low levels (e.g., 1 miRNA per ~100 EVs) [137]. Additionally, knockdown studies of a single cargo (e.g., a singular miRNA) to affirm the protective EV mechanism never fully abolish the beneficial effects [125], implicating the role of multiple cargoes. To overcome these issues, specific therapeutic molecules can be loaded singularly or simultaneously into EVs either endogenously or exogenously. Endogenous methods involve manipulation of the loading machinery of the parental cells (e.g., via transduction or transfection). However, in addition to being expensive, transfection reagent residues may affect cargo functions [138]. Furthermore, the efficiency of these methods depends heavily on the biogenesis which could vary

greatly among different cell types. But, these methods may become more attractive as mechanisms of biogenesis are revealed. For instance, by incorporating specific peptide motifs (i.e., KFERQ), proteins can be translocated by chaperons (i.e., LAMP2A) to multi-vesicular bodies where they can be packaged into EVs [139]. Exogenous loading methods entail physically disrupting the EV membrane (e.g., via sonication, electroporation, heat shock, or freeze-thaw cycles) [135, 140], which can produce high loading efficiencies (e.g., 1,000 - 3,000 siRNA copies per EV) [141], but often induces degradation and aggregation leading to reduced cargo functionality [142].

Recently, a less disruptive loading method involving a transmembrane pH gradient, originally used for loading liposomes [143], was modified for use in EVs [144]. Using this technique, Jeyaram and colleagues demonstrated the ability to load small interfering RNA (siRNA), single-stranded DNA (ssDNA), and miRNA into EVs derived from HEK293T cells. Similar to other exogenous loading methods, the pH modification method allowed the loading of thousands of RNA molecules per EV [144]. Additionally, due to the lack of introduction of high energy into the loading process, the pH method preserved the integrity of the unloaded cargo and allowed the molecules to be recycled for successive loading procedures [144]. This eliminates the loss of excess cargo resulting in a more practical loading process. Furthermore, as dendritic cell EVs naturally contain miR-146a that is capable of inhibiting endotoxin-induced inflammation in mice [145], HEK EVs were loaded with double-stranded (ds)-miR-146a and

applied to BMDMs. Consequently, the BMDMs exhibited a significant decrease in the expression of the proinflammatory enzyme interleukin-1 receptor-associated kinase 1 (IRAK1), a key adaptor molecule in the TLR4/MD-2/MyD88/NF-κB pathway [146], as well as a reduction in the secretion of the inflammatory cytokine IL-6 [144]. This study demonstrated an improved EV loading technique as well as the successful embedding of a desired, but previously nonexistent, function (i.e., anti-inflammatory) into HEK EVs using miR-146a. Despite the promising attributes of this method, the potential for scale-up using this technique remains to be seen.

2.4.2. Manipulation of the Producer Cell Environment

EV activity can be impacted by stress-induced adaptive responses of parental cells to their environment, whether in a physiological setting or in a controlled EV production environment [211]. This phenomenon provides an opportunity during the biopharmaceutical development process to control EV efficacy through the manipulation of upstream parameters (i.e., cell culture parameters), which would potentially lessen the need to load synthetic drugs or non-native biological components (e.g., nucleic acids or proteins) into EVs during downstream procedures. This is significant as many loading methods, as mentioned previously, require disrupting the EV membrane, potentially damaging native structures and targeting features of EVs [142]. Furthermore, various loading techniques require the addition of process-related impurities (i.e., unencapsulated cargoes) to the previously purified EV preparation, demanding the implementation of supplementary purification procedures which

can be costly, time-consuming, and risk even further loss and possible deformation of target EV material [108].

Importantly, modification of cell culture parameters has previously been shown to significantly reshape EV intraluminal cargo composition [147-156], augment EV production (e.g., number of EVs produced per cell) [147, 148, 152, 157-159], and increase EV potency in a diverse array of applications including neurological disorders and injuries, wound healing, cartilage repair, kidney disease, ischemia/reperfusion (I/R) injury, myocardial infarction, and sepsis [15, 116, 157, 158, 160-164]. These changes can be produced through the adjustment of numerous upstream variables including cell seeding density [164], media composition (i.e., serum-free media) [149, 155, 158], collection frequency of EVs [164], architecture of the culture vessel (i.e., two-dimensional versus three-dimensional; 2D vs 3D) [15, 116, 157, 160, 162, 165-167], fluid shear stress (i.e., static versus dynamic flow) [15, 168-171], mechanical stimulation (e.g., cyclic stretch) [172-175], exposure to hypoxia [155, 161, 176], heat [177], oxidative stress [177, 178], electrical stimulation [179], substrate stiffness [180], or co-incubation with soluble signals (e.g., cytokines, growth factors) [15, 148, 156, 159, 181].

While the breadth of upstream factors affecting EV therapeutic potential is extensive, each can be described as either biochemical or mechanical in nature. Biochemical priming consists of exposing cells to specific molecules (e.g.,

growth factors, cytokines, hormones, soluble gases, and pharmacological compounds) that are capable of modulating particular intracellular signaling pathways and ultimately directing cell phenotype and behavior. Numerous studies have demonstrated the power of biochemical priming in enhancing MSC EV therapeutic effects in a number of applications including tendon repair [182], sepsis [125, 183], diabetic cutaneous wounds [148], myocardial infarction [184], and acute radiation syndrome [185]. Nevertheless, the biochemical priming method is riddled with barriers to clinical translation. First, ligand characteristics (e.g., type, concentration, duration of exposure), cell origin (i.e., human or mouse), cell source (e.g., bone marrow, adipose, or umbilical cord derived MSCs), and culture conditions (e.g., medium) all vary considerably among studies which makes any beneficial effects difficult to characterize and reproduce [186]. Secondly, as the elicited effects of priming on the bioactivity of MSCs varies between donors [187, 188], it is highly likely this variability would be perceptible in the secreted EVs. Third, these priming reagents can be expensive and may persist at low levels in the final EV product even after purification [189], hampering adherence to good manufacturing practices (GMPs) and ultimately slowing movement into the clinic. Finally, it has been demonstrated that despite eliciting different cell phenotypes specifically in MSCs (i.e., either anti-inflammatory or inflammatory), biochemical priming can produce EVs with the same immunosuppressive qualities. As there are conflicting reports as to which types of biochemical stimuli leads to which MSC phenotype [186, 190, 191], detailed analyses and

consistent reporting of the effects of priming on MSCs will be critical in not only understanding the immunomodulatory mechanisms of MSCs but also in informing the most efficient way to produce therapeutic EVs.

A potential solution to these issues can be found in the aggregate structural and mechanical properties of the surrounding microenvironment and adjacent cells, which comprises a wide range of mechanical cues originating both endogenously (e.g., substrate dimensionality, topography, stiffness) and exogenously (e.g., shear stress, electromagnetic fields, tensile and compressive strain) [192, 193]. Research investigating the impact of these cues has contributed immensely to the fields of mechanotransduction and cell behavior and has the potential to bolster the translation of clinical therapies [194]. With such an overwhelming effect on cells, it should come as no surprise that mechanical cues have been shown to alter MSC EV secretion dynamics and MSC EV molecular cargoes [169-171]. Thus, in comparison to biochemical cues, mechanical cues demonstrate the capacity to modify downstream EV therapeutic efficacy without the addition of external molecules. Moreover, mechanical cues are often cost-effective, longer lasting, easily characterized, and can be manufactured with high reproducibility and scalability [16]. The burgeoning research investigating these cues and their effects on EVs demonstrates the integral need to understand the complexity of the cellular microenvironment when developing future EV therapies.

2.6 The Potential of Mechanical Cues in the Development of EV Therapies

In the body, cells are continuously exposed to mechanical forces (i.e., stress, strain, and stretch) and substrate architectures that can vary spatiotemporally during normal physiological functions (e.g., blood vessel dilation, lung inflation, eye blinking) as well as pathological conditions (e.g., atherosclerosis, hypertension). Therefore, implementing mechanical cues in cell culture supports the ability to mimic the *in vivo* niche more closely, permitting more physiologically relevant cell-to-cell and cell-to-extracellular matrix interactions and a more accurate recapitulation of cell behavior [14]. Fortunately, the culture systems employed thus far have come equipped with tunable characteristics (e.g., stiffness, specific architecture) enabled by engineering advancements (e.g., 3D printing) that has allowed a reductionist approach in determining how mechanical cues are ultimately converted into inter- and intracellular signaling cascades. These advancements are important because there exist numerous contributing parameters, particularly shear stress and substrate architecture, that need to be carefully dissected to fully understand the relationship between the physical environment and cell activity. As EVs serve as an important mechanism in intercellular communication, understanding the effects of these cues on subsequently secreted EVs will be critical.

2.5.1. Shear Stress

Due to its ubiquitous presence in multiple fluid compartments of the body (i.e., intravascular and interstitial) and its ability to influence other potential effectors (i.e., cellular stretch), the effect of shear stress on cells has been particularly well-studied in a variety of contexts [195, 196]. This research has shown that

shear stress is an important regulator of gene expression, differentiation, and cell phenotype and is thus imperative in normal and pathological cellular function [196], demonstrating promise for the manipulation of cultured cells. In one such study, Liu et al. revealed that by applying intermittent fluid shear stress to human bone marrow derived MSCs seeded in 3D poly lactic-co-glycolic acid (PLGA) scaffolds they were able to upregulate the activity of focal adhesion kinase (FAK) [197]. In another study, the application of an "on/off" flow regime (i.e., 5 min of flow/5 min of no flow), stimulated the production of prostaglandin E2 (PGE2), a principal mediator of inflammation and a primary product of cyclooxygenase 2 (COX2) [198]. Indeed, COX2 has been shown to indicate the ability of MSCs to attenuate neuroinflammation in traumatic brain injury [199]. Moreover, FAK is a primary regulator of COX2 expression and the mechanical stimulation of FAK is crucial in triggering the immunosuppressive abilities of MSCs [200]. Protective effects of fluid shear stress application (e.g., anti-inflammatory, antioxidant) have also been demonstrated extensively in endothelial cells (ECs) [201]. A study by Lee and colleagues showed that shear stress was able to suppress the inflammatory EC phenotype via inhibition of TAK1, a key mediator of the inflammatory TGF-β1 signaling pathway [202]. Importantly, the type of flow (e.g., oscillatory vs pulsatile), force of fluid flow (typically measured in dynes/cm^2), and timing (e.g., continuous or intermittent application) can influence the subsequent cell response [201, 203-205]. As an example, Hwang et al. found that, compared with pulsatile shear stress, oscillatory shear stress significantly upregulated the

mRNA and protein expression of two subunits of the reactive oxygen species (ROS)-producing endothelial NADPH oxidase, Nox4 and $Gp91^{phox}$, in bovine aortic ECs [203]. Consequently, a significant increase in superoxide production as well as low density lipoprotein oxidation was observed, implicating oscillatory shear stress as an important contributor to EC inflammation [203]. Overall, these studies demonstrate a potentially powerful control mechanism for the immunomodulatory potential of MSCs and ECs in the form of flow-derived shear stress that warrants further investigation.

With the important role demonstrated in cell biology, there is evidence to believe that the effects of shear stress can be used to control secreted EVs. Previous work in our lab showed dynamic culture can significantly enhance EV production from human ECs [15]. Additionally, it was shown that, when paired with ethanol conditioning, this dynamic culture environment induced pro-vascularization EV bioactivity that was associated with increased EV levels of pro-angiogenic lncRNAs HOTAIR and MALAT1 [15]. It has also been shown dynamic culture increases EV release [147, 206-208] and has been shown to dictate EV intraluminal content and EV function [169-171, 206]. In addition, specific shear stress characteristics, such as magnitude, can be important in controlling EV function. Devue et al. showed that the magnitude of flow that the producer cells experienced could affect the uptake of the EVs by other cells (i.e., B and T lymphocytes) [208]. Furthermore, the strength of flow also dictated the miRNA content of EVs, with lower flow resulting in an increased

packaging of miR-24 into EVs [208]. This is notable as miR-24 is an important molecule in cardiovascular diseases and other inflammatory-based disorders due to its ability to block the NF-κB pathway effectively regulating the inflammatory response in endothelial cells [209].

It should be emphasized that, although they are intimately connected, flow and shear stress are two separate phenomena. Shear stress (tau; τ) is defined as the force per unit area that is applied parallel or tangential to a surface and can be calculated using Poiseulle's Law ($\tau = 4\eta Q/ \pi r^3$; where τ is shear stress, Q is flow rate, η is viscosity of the culture medium, and r is the radius of the culture vessel) [210]. While flow generates shear stress, it can also create tensile and compressive stresses across the cell membrane [211]. Additionally, besides inducing stress on the cell surface, flow can modulate the surrounding environment by augmenting diffusive exchanges (i.e., oxygen, nutrient, waste metabolites) [212, 213], which can in turn affect cellular metabolism. Importantly, previous work in our lab has shown that, in 3D static culture, inhibition of glycolysis and oxidative phosphorylation reduced both MSC EV production capacity and EV pro-angiogenic activity (unpublished data). Therefore, further investigation is needed to understand the extent to which each component (i.e., flow or shear stress) contributes to EV composition and therapeutic effects.

2.5.2. Substrate Architecture

While most cell research utilizes monolayer cell culture in two-dimensional (2D) flasks, the use of 3D-based architecture is gaining traction as it allows the development of an extracellular matrix (ECM) resembling that which is found in native tissue [14]. Subtle variances in microarchitectural features like grooves, pores, and pillars have been shown to influence crosstalk among cell types [214, 215], gene expression, and cellular adhesion, ultimately manifesting downstream as changes in cell growth, phenotype, migration, and differentiation [216, 217]. Additionally, 3D substrates developed with bio-inspired topographic features can constrain cells into spatial arrangements that can dictate morphology and how the cells experience various mechanical cues, including shear stress and strain [215, 218]. Specifically, cell morphology can determine cytoplasmic organization and has been shown to be a potent mediator of cell physiology and function [19, 219, 220]. In fact, morphology has been used to accurately predict the immunosuppressive abilities [221] and osteogenic potential of MSCs [222]. The ability to engineer cell shape using mechanical cues would enable explicit control over functional effects and significant improvement in the ability to develop cellular therapies tailored to specific clinical applications.

Importantly, the implementation of 3D culture systems (e.g., bioreactors, microcarrier-based systems, spheroid culture) has been proven to markedly increase EV production when compared with cells cultured in a traditional 2D

system [15, 116, 147, 223], demonstrating a more promising avenue to scale-up. Strikingly, in one study it was estimated that 53 T175 culture flasks producing 800 mL of media would be needed to match the amount of EVs produced in a single collection from a hollow-fiber bioreactor system [147]. Furthermore, 3D culture has exhibited the ability to substantially boost the purity of EVs (i.e., ratio of number of EVs to µg of protein) when compared with their 2D counterparts [15, 158]. As large doses of EVs are typically needed to achieve biological outcomes in mouse models (i.e., 10^9- 10^{11} EVs per mouse) and purity can affect EV bioactivity [116, 224], 3D culture may prove integral in the clinical translation of an EV therapy in many disease applications.

Significantly, the effects of EVs can be conserved and translated from 2D to 3D culture systems where the EV therapeutic efficacy is often enhanced. EVs produced from 3D conditions have often demonstrated the ability to strengthen the angiogenic [15], anti-inflammatory [162], anti-apoptotic [158], reparative and regenerative (e.g., cognitive and osteochondral) [158, 162, 225] effects observed with EVs generated from 2D culture. As an example, Lamichhane and colleagues found that exposing human dermal microvascular endothelial cells (HDMECs) and human umbilical vein endothelial cells (HUVECs) to ethanol significantly enhanced EC-derived EV vascularization bioactivity. Moreover, they found that in HUVECs this effect was largely mediated by the upregulation of lncRNAs HOTAIR and MALAT1 [163]. The same research group was then able to recreate the ethanol-induced lncRNA EV cargo changes while

enhancing pro-angiogenic abilities and yield of EVs by culturing HDMECs in a perfusion bioreactor [15]. Even so, it is critical to note that 3D culture can also transform the therapeutic profile of EVs. For instance, EVs from MSCs derived from human exfoliated deciduous teeth cultured on laminin-coated 3D alginate micro-carriers in a bioreactor were able to alleviate oxidative stress-induced apoptosis in human dopaminergic neurons, an effect that was not elicited by EVs isolated from the same cells grown under standard 2D conditions [166]. The observed shift in therapeutic effect may be due to the enhanced delivery of alternate molecular cargo, as 3D cell culture has been recognized to considerably modify the intraluminal contents of EVs as well as augment cellular uptake [116]. However, any change of this caliber during research and development would certainly hinder progress in the manufacturing pipeline. The study also portends the potential to overlook specific contributions of EVs to an efficient therapy during traditional pre-clinical research and emphasizes the importance of considering how the mechanical cues experienced during the inevitable scale-up process (i.e., the shift in culture systems) may affect the therapeutic quality of EVs.

Lastly, with its prominent role in cell function, morphology has also been proven valuable in EV activity. In 2020, Liang and colleagues manipulated ECs into an elongated shape by culturing them on polydimethylsiloxane (PDMS) membrane surfaces decorated with microgrooves. They showed that in comparison with ECs with a more cobblestone form, the spindle-shaped ECs

were able to suppress the activation of monocytes. Further investigation revealed that this anti-inflammatory effect was regulated by EV-associated miR-10a [21]. This study was the first to demonstrate the ability to control EV functional outcomes through manipulation of cell shape and, with further investigation, promises a unique and powerful opportunity in the regulation of EV therapies.

2.7 Conclusions

The intrinsic capability of EVs to shuttle bioactive compounds and the advantages they possess over cell therapies has generated a surge in EV research that has uncovered numerous therapeutic applications. Despite promising preliminary data, FDA-approved EV-based therapies remain elusive. This translational bottleneck seems to be largely driven by low therapeutic efficiency (e.g., low levels of specific cargo) and the lack of a scalable biomanufacturing platform.

To date, most EV biomanufacturing approaches utilize platforms originally designed for whole cell expansion (e.g., hollow-fiber, multi-layered culture vessels, stirred-tank bioreactors), during which cells can experience numerous mechanical stressors. As EVs can reflect the physiological status of cells, each of these stressors must be considered when optimizing EV manufacturing techniques. However, a limited understanding of the relationship between cellular mechanobiology and EVs hinders the rational design of an effective EV-specific biomanufacturing platform.

The connection between mechanobiology and EVs is evident based on the physiological roles of EVs and the growing indication that EVs are impacted by mechanical cues experienced by cells. Prior research has demonstrated that flow-derived shear stress and substrate architecture can be used to augment the production as well as alter composition and functional effects of EVs [15, 168-171, 206, 208]. This level of control over EVs is important as it is thought that the endogenous EV cargoes are heterogenous and present at exceptionally low levels (e.g., <1 miRNA per EV) [137], likely requiring multiple high doses to achieve therapeutic effects. Unfortunately, the commonly used techniques to combat low EV potency typically induce membrane damage, involve extraneous reagents, or are not conducive to scale-up techniques. The utilization of mechanical cues like shear stress or substrate architecture to alter EVs is advantageous as they can be precisely manipulated within a controlled setting in a reproducible manner. Therefore, a deep understanding of the relationship between the mechanical environment and EVs will help alleviate EV potency issues without sacrificing scalability and will be essential in the advancement of EV therapies.

Chapter 3: Mesenchymal Stem Cell Culture Within Perfusion Bioreactors Incorporating 3D-Printed Scaffolds Enables Improved Extracellular Vesicle Yield with Preserved Bioactivity[‡]

3.1 Introduction

Extracellular vesicles (EVs), specifically those from mesenchymal stem/stromal cells (MSCs), have emerged as an intriguing therapeutic alternative to whole-cell therapies in a multitude of applications (e.g., sepsis, cancer, wound healing) with additional promise as efficient drug delivery vehicles [135, 226]. With an improved safety profile [4], favorable storage requirements [227], and the ability to traverse biological barriers [228, 229], MSC EVs represent a promising and effective alternative to their parental cells. However, there exist fundamental obstacles that hinder the translation of MSC EVs, including a lack of a rationally designed production platform and low therapeutic potency (i.e., low levels of endogenous EV cargos).

Numerous methods have been employed to attempt to combat these issues, including MSC EV cargo loading and biochemical priming of parental cells [11, 159, 230]. These approaches have their merits, but they are generally limited with respect to scalability

[‡] A portion of this work is adapted from **Kronstadt, S.M.**, D.B. Patel, L.J. Born, D. Levy, M. Lerman, B. Mahadik, S. McLoughlin, A. Fasuyi, L. Fowlkes, L.H. Van Heyningen, A. Aranda, S.N. Abadchi, K.H. Chang, A.T.W. Hsu, S. Bengali, J.W. Harmon, J.P. Fisher, S.M. Jay. 2022. Mesenchymal stem cell culture within perfusion bioreactors incorporating 3D-printed scaffolds enables improved extracellular vesicle yield with preserved bioactivity. Biomaterials. Submitted.

and could substantially increase production costs and the regulatory burden associated with MSC EV translation. Alternatively, mechanical cues, such as flow-derived shear stress, intrinsically exist in established biomanufacturing set-ups and can be utilized in a highly reproducible and cost-effective manner [16]. Importantly, dynamic culture conditions have been shown to augment stem cell EV production and bioactivity. For example, using GMP-compliant serum- and xeno-free cell culture media, Gobin and colleagues were able to utilize a hollow-fiber bioreactor system to significantly increase MSC EV production across multiple donors while maintaining the functionality of the parental cells [171]. In a separate study, EVs from human dental pulp stem cells (DPSCs) grown in dynamic conditions on a fiber-based scaffold significantly increased axonal sprouting in neurons when compared with DPSC EVs from static conditions [170]. However, in addition to flow-derived shear stress, these systems introduce other cues as the topographical, chemical, and mechanical attributes of the membrane itself can affect cellular behavior, which ultimately convolutes the true effectors at play [231]. Recent studies have utilized simpler systems (e.g., flat-plate bioreactors) [169], allowing a more precise approach to understanding and harnessing flow-derived shear stress but still lack the tunability necessary for dynamic manufacturing and exploratory research needs.

A promising solution exists in 3D-printing technology, which, with the ability to precisely control scaffold geometry and architecture [232], allows for more adaptable systems as well as more precise computational fluid modeling. As the therapeutic profiles of EVs are often shaped by the stress-adaptive responses of their parental cells

[177, 233], a tunable platform is vital in the ability to understand these responses and subsequently adjust EV formulations for specific applications. In a previous study, we employed a 3D-printed, biocompatible scaffold coupled with a peristaltic pump, which we termed the bioreactor, to enhance the production of human dermal microvascular endothelial cell (HDMEC) EVs [15]. We also demonstrated that ethanol conditioning-mediated pro-angiogenic effects of HDMEC EVs, previously demonstrated using conventional culture techniques [163], were maintained when cells were cultured in the bioreactor. In the current investigation, we utilized a similar bioreactor to assess the effects of flow-derived shear stress on the production and bioactivity of EVs secreted by bone marrow-derived MSCs as they are a common therapeutic cell source [234]. We specifically focused on wound healing abilities due to the well-documented pro-angiogenic effects of EVs from traditionally-cultured MSCs [17, 18]. Our results suggest that this particular bioreactor set-up can be used to increase MSC EV production while maintaining pro-angiogenic bioactivity, effectively increasing the potency of the EV formulation. Given the tunability of this system, the methods used here have the potential to be applied to various EV-based formulations with the ability to increase effectiveness without sacrificing scalability.

3.2 Methods

3.2.1. Cell Culture

Bone marrow-derived mesenchymal stem cells (MSCs; passage 2) and human embryonic kidney cells (HEK293) were purchased from ATCC (MSC: PCS-500-012; HEK293: CRL-1573). A kit of MSCs from three different donors was

also purchased from RoosterBio to assess donor variability (KT-014). All MSCs were cultured in Dulbecco's Modification of Eagle's Medium (DMEM) (Corning, 10-013-CV) supplemented with 10% fetal bovine serum (FBS; VWR, 89510-186), 1% non-essential amino acids (NEAA; Fisher Scientific, 11-140-050), and 1% penicillin-streptomycin (P/S; Corning, 30-002-CI). All MSCs were expanded so they were at passage 4 upon seeding into the experiments. HEK293 cells were cultured in DMEM supplemented with 10% FBS and 1% P/S. During experiments, MSC or HEK293 culture media was switched to media containing 10% EV-depleted FBS (referred to as EV-depleted media). EV-depleted FBS was produced by centrifuging heat-inactivated FBS at 118,000 × g for 16 h and filtering the supernatant through a 0.2 μm bottle-top filter for later use in media supplementation. Human umbilical vein endothelial cells (HUVECs) pooled from multiple donors (C-12203) and human dermal microvascular endothelial cells (HDMECs) (C-12212) were obtained from PromoCell. HUVECs or HDMECs were cultured on tissue culture polystyrene flasks coated with 0.1% gelatin at 37 $^{\circ}$C for 1 h prior to seeding. HUVECs and HDMECs were cultured in complete endothelial growth medium-2 (EGM2; PromoCell C-22111) supplemented with 1% P/S and used at passages 3-5 in experiments. During experiments, HUVECs and HDMECs were maintained in endothelial basal medium-2 (EBM2; PromoCell, C-22221) supplemented with 0.1 % FBS and 1% P/S.

3.2.2. 3D-printed Scaffold Design and Fabrication

The scaffold design involved a series of small pillars that were 1 mm in diameter and situated 2.5 mm apart in a 50 cm^2 cell growth area within a 12 cm^3 volume construct. This design was chosen to provide a sufficient culture surface area in a highly-ordered pillared array that was amenable to cell removal and immunofluorescence imaging. The architecture also allowed for media to perfuse the circuit around and in-between the pillars, facilitating active transport of nutrients and gases from gas permeable tubing, and provided a mechanism to control fluid characteristics predictably throughout. Computational fluid modeling was accomplished using the SolidWorks (Dassault Systèmes, Velizy-Villacoublay, France) Flow Simulation add-in. Fluid flow was analyzed at flow rates of 1, 5, and 10 mL/min by modulating the inlet volume rate with surface shear stress, flow profiles, and fluid velocity (computed and recorded).

Scaffold designs were exported into stereolithography (.stl) files following computational design and scaffold models were oriented, fixed, and supported using Magics 18 (Materialise, Leuven, Belgium). Solid objects were fabricated out of a clear, biocompatible, acrylate-based material (E-Shell 300; EnvisionTEC, Inc.) using a commercially available stereolithography apparatus (EnvisionTEC Perfactory 4 Mini Multilens; Gladbeck Germany). Excess resin was removed by submerging printed objects in 99% isopropanol (Pharmco-Aaper, Shelbyville, KY) for 5 min, followed by flowing 99% isopropanol

through the scaffolds, and blowing the interior dry with filtered air. The process was repeated until all excess material was removed from the interior of the object. Complete resin curing was achieved with 2000 flashes of broad-spectrum light (Otoflash, EnvisionTEC, Inc.). Scaffolds were cleaned in 100% ethanol (Pharmco-Aaper, Shelbyville, KY) for >30 min to leach any remaining soluble contaminants before proceeding to the sterilization and rehydration steps described below.

3.2.3. Scaffold Sterilization, Coating, and Cell Seeding

3D-printed scaffolds were submerged in fresh 100% ethanol and sterilized in an ultraviolet sterilizer (Taylor Scientific, 17-1703) for 10 min. Scaffolds were gradually rehydrated by submerging in sterile solutions with a progressively increasing volume of pH 7.4 sterile 1X PBS (i.e., 25:75 PBS:EtOH for 5 min, 50:50 PBS:EtOH for 5 min, 75:50 PBS:EtOH for 5 min) and placed in 100% sterile 1X PBS in the fridge until use. Once ready to use, scaffolds were coated with 0.5 μg/cm^2 fibronectin in sterile water for 30 min at 37˚C. Open ends of the scaffolds were closed using platinum-cured tubing and binder clips to prevent leakage. Scaffolds were drained and passage 4 MSCs were seeded into the scaffolds at a seeding density of 2.5×10^3 cell/cm^2 in 15 mL of EV-depleted MSC media. Cells were allowed to attach for 24 h at 37°C before connecting the scaffold to the bioreactor or replacing the media and keeping the scaffold detached as a static control. In parallel, cells were also seeded in 75 cm^2 tissue culture flasks at the same density as within the scaffolds in EV-depleted MSC media as an additional static control.

3.2.4. Perfusion Bioreactor Assembly

After initial cell seeding, the 3D-printed scaffolds were connected to a Masterflex L/S Digital Drive (Cole-Parmer) coupled with a pump head to circulate medium at 1, 5, or 10 mL/min. Open ends of the tubing on either end of the scaffold were affixed to a media reservoir with 50 mL of EV-depleted MSC media. The pump head allowed for up to 4 lines to be connected at a time at a single flow rate. The assembly was then placed within a cell culture incubator at 37°C with 5% CO_2, with the scaffold chamber secured on the incubator sidewall with flow anti-parallel to gravity. The complementary flask and scaffold controls were also incubated at 37°C with 5% CO_2. Scaffolds were situated vertically to ensure complete submergence in medium.

3.2.5. Cell Staining and Imaging

After 24 h culture in the bioreactor, MSCs were fixed in the scaffolds with 4% paraformaldehyde (PFA) and 1% sucrose for 15 min and washed three times with 1X PBS. Prior to staining, cells were permeabilized for 5 min with a 300 µM sucrose, 100 µM sodium chloride, 6 µM magnesium chloride, 20 µM HEPES, and 0.5% Triton-X-100 solution. Cellular actin was stained in a 1:100 dilution of AlexaFluor 488 Phalloidin (Invitrogen, A12379) in 1X PBS for 20 min and visualized on a Nikon Ti2 Microscope (Nikon, Minato City, Tokyo, Japan).

3.2.6. EV Isolation and Characterization

Conditioned media from MSCs cultured in EV-depleted media were collected and underwent a series of differential centrifugation steps which entailed a final centrifugation step of 118,000 × *g* for 2 h as previously described [133, 235]. After resuspending the pelleted EVs in 1X PBS, they were transferred to a Nanosep 300 kDa MWCO spin column (Pall, OD300C35) and centrifuged at 8,000 × *g* until all PBS was removed (~8-12 min). The EVs were washed two more times in a similar fashion. EVs collected at the top of the column were then resuspended in a desired volume of 1X PBS and sterile filtered using 0.2 µm syringe filters. The total surface protein concentration of the washed EVs was measured by BCA. EV size distribution and concentration were evaluated using a NanoSight LM10 (Malvern Instruments; Malvern, UK) with Nanoparticle Tracking Analysis (NTA) software version 2.3. Each sample was measured three times with a camera level set at 14 and acquisition time of 30 s. Approximately, 20-100 objects per frame with more than 200 completed tracks were analyzed for each video. The detection threshold was set at the beginning of each sample and kept constant for each repeat. EVs were also quantified based on the amount of total immunoreactive CD63 within isolated EV samples using the ExoELISA-ULTRA Complete Kit (System Biosciences, EXEL-ULTRA-CD63-1) per the manufacturer's protocol. Briefly, 10-25µg of EVs (based on BCA analysis) were used for the analysis. The number of EVs was obtained using an exosomal CD63 standard curve calibrated against NTA data.

Total number of EVs was then calculated based on resuspension volume and final data was expressed as total # of EVs/cell.

Immunoblotting was then performed to confirm the presence of EVs and purity of each sample. Based on the BCA analysis, 10 μg of protein from each EV sample was used for analysis and compared with cell lysate. The presence of various EV-associated proteins was assessed using primary antibodies for Alix (Abcam, ab186429), TSG101 (Abcam, ab125011), CD9 (Abcam, ab92726), CD63 (Proteintech, 25682-1-AP), actin (Cell Signaling Technology, 4970), and GAPDH (Cell Signaling Technology, 2118), while the absence of contaminating proteins were confirmed using antibodies for calnexin (Cell Signaling Technology, 2679), HSP90 (Abcam, ab13492), and AGO2 (Abcam, ab186733). All primary antibodies were added at a 1:1,000 dilution, except GAPDH which was diluted 1:2,000. A goat anti-rabbit secondary (LI-COR Biosciences, 926-32211) was added at a 1:10,000 dilution. Protein bands were detected using a LI-COR Odyssey CLX Imager. All EVs were used within three days or frozen at -20°C and used within 2 weeks with no more than 1 freeze/thaw cycle.

A portion of each EV sample (10 μl) was fixed using 4% EM-grade PFA (10 μl) for 30 min at room temperature. Following fixation, a carbon-coated copper grid with type 200 mesh (Electron Microscopy Sciences, CF200-Cu-25) was allowed to adsorb to the EV/PFA mixture for 20 min. The grid was then placed

on a drop of PBS to wash and then laid upon a drop of 1% glutaraldehyde in 1X PBS for 5 min. The grid was washed extensively (5-7 times x 2 min) on deionized water droplets, blotting gently in between each wash at a 45° angle on a piece of filter paper. The grid was then placed on a droplet of uranyl acetate replacement stain (Electron Microscopy Sciences, 22405) and let sit for 10 min. The grid was allowed to completely dry prior to imaging at 200 kV on a JEOL JEM 2100 LaB6 TEM.

3.2.7. Gap Closure Assay

P4 HUVECs were seeded in gelatin-coated 96-well plates at 1.5×10^4 cells/well in EGM2 and allowed to grow until a uniform monolayer was formed (24 h). The cell monolayer was denuded using an AutoScratch (BioTek Instruments; Winooski, VT, USA). Cells were then washed once with 1X PBS and incubated with endothelial cell basal medium (EBM2; PromoCell C-22221) supplemented with 0.1% FBS for 2 h to serum starve the cells. After serum starvation, medium was replaced with fresh EGM2 (positive control), EBM2 (0.1% FBS) without EVs (negative control), or EBM2 with the addition of EVs at 5×10^9 EVs/mL based on NTA quantification or 200 μg/mL of EVs based on BCA quantification of surface protein. EBM2 or EGM2-treated cells were used as negative or positive controls, respectively. The closure of the cell gap was imaged at 0 h and 20 h using a Nikon Eclipse Ti2 Microscope at 2x magnification. The change in the gap area was measured using ImageJ as previously described [164].

3.2.8. Tube Formation Assay

24-well plates were coated with 100 µl of growth factor reduced Matrigel (Corning, 354230) and incubated at 37°C for 30 min. P4 HUVECs were then seeded at 6×10^4 per well with EGM2 media (positive control), EBM2 media (0.1% FBS) devoid of EVs (negative control), or EBM2 media (0.1% FBS) with EVs (5×10^9 EVs/mL) on top of the Matrigel. At six hours, cells were imaged using a Nikon Eclipse Ti2 Microscope at 2x magnification. The number of fully-closed loops formed by the HUVECs were counted and recorded as a proxy for the formation of capillary-like structures in wound healing.

3.2.9. EV Uptake via Flow Cytometry and Confocal Imaging

MSC EVs from flask and bioreactor culture were labeled separately with lipid membrane PKH67 dye (Sigma-Aldrich, PKH67GL) as previously described [235]. Briefly, EVs in PBS suspension were spun down at 8,000 × g in a 300 kDa MWCO filter and resuspended in 200 µl of Diluent C to wash away buffer-related salts. EVs were then spun down again at 8000 × g and resuspended in 250 µl of Diluent C per 200 µg of EVs. A mock dye treatment was prepared by mixing PBS devoid of EVs with diluent C. EVs and the mock dye solution were labeled at 1:1 ratio using 4 µM of PKH67 dye diluted in diluent C solution and incubated for 5 min with frequent mixing at room temperature every minute. 1% BSA prepared in diluent C was added to the EV or PBS/PKH67 dye mix at 1:1:1 ratio and incubated for another 1 min at room temperature to quench any leftover dye. Samples were then concentrated using protein concentrators (100

kDa MWCO; ThermoFisher Scientific, 88524) to 500 µl and centrifuged at 10,000 × *g* for 10 min at 4°C to remove any protein aggregates formed during concentration. To remove any non-EV associated dye aggregates, the samples were then run through size exclusion columns (Izon; qEV original 35 nm, ICO-35) per the manufacturer's instructions. The first four fractions after the void volume were collected and used in further experiments (**Figure 3.1**). These fractions were concentrated (100 kDa MWCO), resuspended in 1X PBS, and sterile filtered (0.2 µm). Particle concentration was determined via NTA. Approximately 5×10^5 HUVECs in a 6-well plate were treated with 5×10^9 EVs/mL of labeled flask or bioreactor EVs or equal volume of mock dye solution in duplicates, while untreated HUVECs (PBS vehicle) were used as a negative control. HUVECs treated with the mock dye solution were used to assess uptake of any dye aggregates. After 24 h at 37˚C, media were collected from each treatment to collect nonadherent cells. Adherent cells were detached using 1 mL of Accutase (ThermoFisher Scientific, A1110501), then added to the collected nonadherent cells, and spun down at 220 × *g* for 5 min. Cells were washed twice in 500 µl of FACS buffer (1% BSA in 1X PBS) and then resuspended in 250 µl of FACS buffer and strained through a cell strainer (40 µm) for further analysis. Samples were analyzed on an Amnis ImageStream X Mark II Imaging flow cytometer and analyzed using the IDEAS software. Live cell gating was done first in forward light scatter/side scatter, and PKH67 populations were gated from the live cell population.

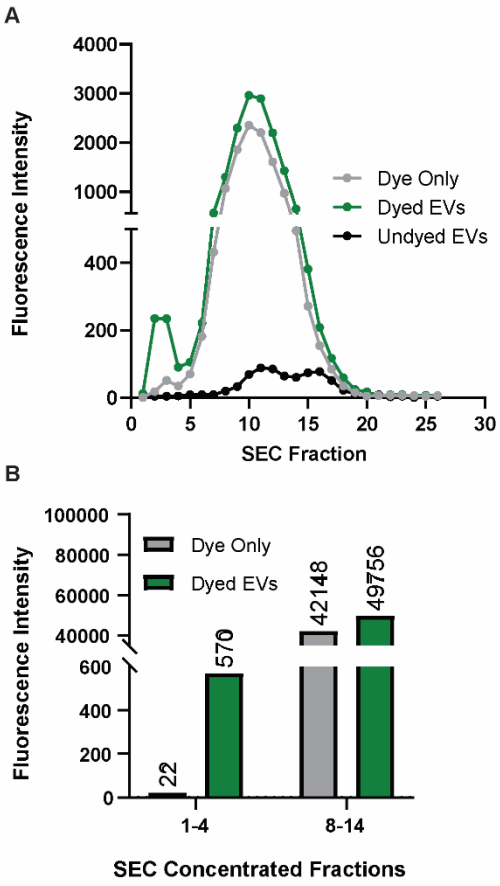


Figure 3.1. Size exclusion chromatography (SEC) can effectively remove PKH67 dye aggregates(A) Fluorescence readings of each fraction from dye only (no EVs), dyed EVs, and undyed EVs (no PKH67) subjected to SEC. EVs elute in the first four fractions. (B) Fluorescence readings from the pooled fractions. Dye aggregates appear to elute in later fractions.

In a concurrent experiment, HUVECs were seeded onto gelatin-coated coverslips (0.1%) in a 6-well plate. After 16 h, cells were treated with the PKH67 mock dye solution or PKH67-labeled flask or bioreactor EVs (5×10^9 EVs/mL). Cells treated with PBS devoid of dye or EVs acted as an additional control. After a 24 h incubation, HUVECs were fixed with 4% PFA for 15 min. Cells were washed three times with 1X PBS and then permeabilized for 5 min

using a 0.5% Triton-X-100 solution. Following permeabilization, HUVECs were washed three times with 1X PBS and then blocked at room temperature for 1 h with a 2.5% goat serum (Abcam, ab7481) solution. Cellular actin was stained in a 1:100 dilution of Alexa Fluor Plus 647 Phalloidin (Invitrogen, A30107) coupled with a nuclear stain using a 1:10,000 dilution of DAPI (Cayman Chemical Company, 14285) for 30 min at room temperature. HUVECs were then washed three times in 1X PBS and imaged using an Olympus FLUOVIEW FV3000 confocal laser scanning microscope (Olympus, Shinjuku City, Tokyo, Japan) at 60x magnification.

3.2.10. MALDI-TOF Mass Spectrometry

Fresh MSC EVs from the flask and perfusion bioreactor (5 mL/min) conditions were washed in sterile deionized water to minimize the presence of buffer-related salts and were resuspended in a final volume of 300 µl of deionized water. BCA and NTA were performed and EVs were subjected to MALDI-TOF analysis on a MicroFlex LRF MALDI-TOF mass spectrometer (Bruker, Bremen, Germany). Each EV sample was mixed 1:1 with sinapic acid matrix (Millipore Sigma, 85429; 20 mg/mL in 50% acetonitrile, 50% water, 0.1% trifluoracetic acid v/v/v) and 1 µl of the sample/matrix solution was deposited on a MicroFlex AnchorChip plate (Bruker, Bremen, Germany) in triplicate and dried in a vacuum. The analysis was performed under linear positive mode using the following parameters as previously described [236]: 70% laser intensity, laser attenuator with 35% offset and 40% range, accumulation of 500 laser shots, and 10.3 detector gain. Mass calibration was completed using

cytochrome c (2 mg/mL; Sigma Aldrich, C8857) and myoglobin (2 mg/mL; Sigma Aldrich, M0630).

3.2.11. mRNA Isolation and Profiling

P4 HDMECs were treated with PBS (control) or 200 µg/mL MSC EVs from flask or bioreactor (5mL/min) culture. After 24 h, HDMEC RNA was isolated using RNeasy kits (Qiagen, 74106) and cDNA was prepared using the iScript cDNA synthesis kit (Bio-Rad, 1708891). Following the manufacturer's protocol, approximately 5 ng of RNA converted to cDNA was used per 10µL well reaction in the Wound Healing PCR Array (Bio-Rad, 10034601). Real-time PCR reaction was prepared using SsoAdvanced Universal SYBR Green Supermix (Bio-Rad, 1725271). Quantitative PCR was performed using an ABI 7900 Fast HT machine, with recommended thermal cycler settings for the SYBR Green Supermix. Data were analyzed using the ΔΔCt method. β-actin mRNA was used as a housekeeping control (ΔCt = Ct target gene – Ct β-actin) and results were normalized to PBS (ΔΔCt = ΔCt Bioreactor or Flask – ΔCt PBS). Data are shown in a heat map, where negative values indicate higher expression and positive values indicate lower expression compared to PBS treated group.

3.2.12. *In vivo* Studies

All animal experimental protocols were approved by the Johns Hopkins University Animal Care and Use Committee and followed the Johns Hopkins University ACUC (Protocol RA18M86). A total of 24 db/db mice (40-50 g)

from Jackson Laboratory (Bar Harbor, ME) were utilized (eight mice per treatment). All mice were anesthetized with 1.5% isoflurane (Baxter Healthcare Corporation, Deerfield, IL) and had their entire dorsum shaved where a singular 8 mm punch biopsy (Integra, Plainsboro, NJ) was performed. Buprenorphine (0.05 mg/kg) was given subcutaneously on days 0, 1, and 3 to help reduce any unnecessary discomfort. Treatments (i.e., flask EVs, perfusion bioreactor EVs, or PBS devoid of EVs) were injected four times around the wound in a cross pattern on day 3. Each dose contained 50 μg of EVs in a total volume of 50 μl or 50 μl of PBS without EVs. Photographs of the wounds were taken on days 0, 3, 7, 10, 12, and 14 and wound size was quantified by digital processing using Adobe Photoshop. On days 7, 10, 12, and 14, the wounds were debrided of the eschar to allow clear visualization. Wound size was calculated as the percentage of area of the wound versus the wound size on day 0.

3.2.13. Histology

On day 21, healed tissues were biopsied using a 12 mm punch biopsy. The tissue was then cut down the center of the wound area and placed in a cryomold (Tissue Tek, 4557), where it was covered with OCT medium (Leica, 3801480). The tissue-containing cryomold was then placed onto a metal surface and cooled with dry ice and ethanol until the OCT medium solidified. The samples were stored at -80°C for less than 1 week prior to sectioning (10 μm thick) using a CM1950 Cryostat (Leica, Wetzlar, Germany). Tissue sections were fixed and permeabilized in 1:1 methanol:acetone solution at -20°C. Sections were then

stained with H&E using a previously described protocol [11]. In brief, sections were washed for 2 min in deionized water, hematoxylin (VWR, 75810-352) for 3 min, deionized water for 1 min, differentiated in 4% HCl in 95% ethanol for 1 min, washed for 1 min in deionized water, bluing for 1 min in 1% NaCO3, washed for 1 min in deionized water, 95% ethanol for 1 min, eosin (VWR, 75810-354) for 45 s, 95% ethanol for 1 min, 100% ethanol for 1 min twice, and xylene for 2 min twice. Sub-X Mounting Medium (Leica, 3801740) was used to add a No. 1.5 micro cover slip (VWR, 48393-195) on top of the tissue section and was sealed using clear fingernail polish. The tissue sections were then imaged using a Nikon Ti2 Microscope at 10x magnification.

In addition, 10 µm tissue sections were subjected to CD31 staining in order to detect newly formed blood vessels using a previously established protocol [11]. In short, slides were washed with tris-buffered saline (TBS) for 2 min, pre-blocked with 1% bovine serum albumin (Sigma Aldrich, A2058)/5% donkey serum (Sigma Aldrich, D9663) in TBS for 30 min, incubated with CD31 primary antibody (Abcam, 28364) at 1:50 in blocking solution for 60 min at room temperature, washed with TBS for 5 min twice, incubated with Alexa Flour 647 donkey anti-rabbit secondary antibody (Invitrogen, A31573) for 60 min at room temperature, and washed with TBS for 5 min twice. Coverslips were mounted over the tissue section as described in the previous section. Fluorescent images were taken using a Nikon Eclipse Ti2 Microscope at 10x

magnification. The numbers of vessels were counted, and the area of tissue was quantified using ImageJ.

3.2.14. Statistics

Data are presented as mean ± standard error of the mean (SEM). Normality of each data set was tested and, when appropriate, parametric tests were used to determine statistical differences ($p < 0.05$) among groups. Specifically, one-way ANOVA with Tukey's or Šídák's multiple comparisons tests were used to determine statistical differences ($p < 0.05$) among groups in the EV characterization data, the *in vitro* tube formation assays, and *in vivo* vessel density data. Two-way ANOVA with Tukey's or Holm-Šídák's multiple comparisons tests were used to detect statistical differences ($p < 0.05$) among groups across dosing schemes in the *in vitro* gap closure assay, across donors within the different culture conditions, and among groups in the *in vivo* wound healing experiments over time. All statistical analyses were performed using Prism 9.1 (GraphPad Software, La Jolla, CA, USA). Notation for significance in figures are as follows: ns – $p > 0.05$: #, *, or § - $p < 0.05$; §§ or ** - $p < 0.01$; *** - $p < 0.001$; ****, §§§§, ####, or †††† - $p < 0.0001$.

3.3 Results

3.3.1. Culture of MSCs in 3D-printed Scaffold-Perfusion Bioreactor

MSCs are physiologically subjected to interstitial flow that exerts low levels of shear stress that has been shown to impact their growth kinetics as well as differentiation [237, 238]. We designed and 3D-printed scaffolds with a total surface area of 50 cm^2 consisting of a pillared array (**Figure 3.2.A**) that permitted medium and gas flow through gas permeable tubing (**Figure 3.2.C**). Computational fluid modeling was carried out for 1, 5, and 10 mL/min to evaluate shear stress (**Figure 3.2.D**) and flow trajectories (**Figure 3.2.E**) throughout the scaffold. Shear stress and flow trajectory heat maps show the distribution of shear stresses across the scaffold growth surfaces, with highest values found closed to the entrance and exit of the scaffold. Average shear stress values for 1, 5, and 10 mL/min were calculated to be $1.6x10^{-4}$, $3x10^{-3}$, and $1.2x10^{-2}$ dyn/cm^2, respectively, all of which are below physiological interstitial shear stress levels of 0.01 Pa (0.1 dyn/cm^2) [239]. For cell viability analysis, MSCs were fixed and stained with AlexaFluor 488 Phalloidin after exposure to dynamic culture at 0, 1, 5, or 10 mL/min. Images confirmed the presence of live cells throughout the scaffold base and along the side walls of the pillars (**Figure 3.2.F**) that were subjected to no flow or flow rates of 1 and 5 mL/min. At a flow rate of 10 mL/min flow rate, very few cells remained adhered to the scaffold.

flow rate, very few cells remained adhered to the scaffold.

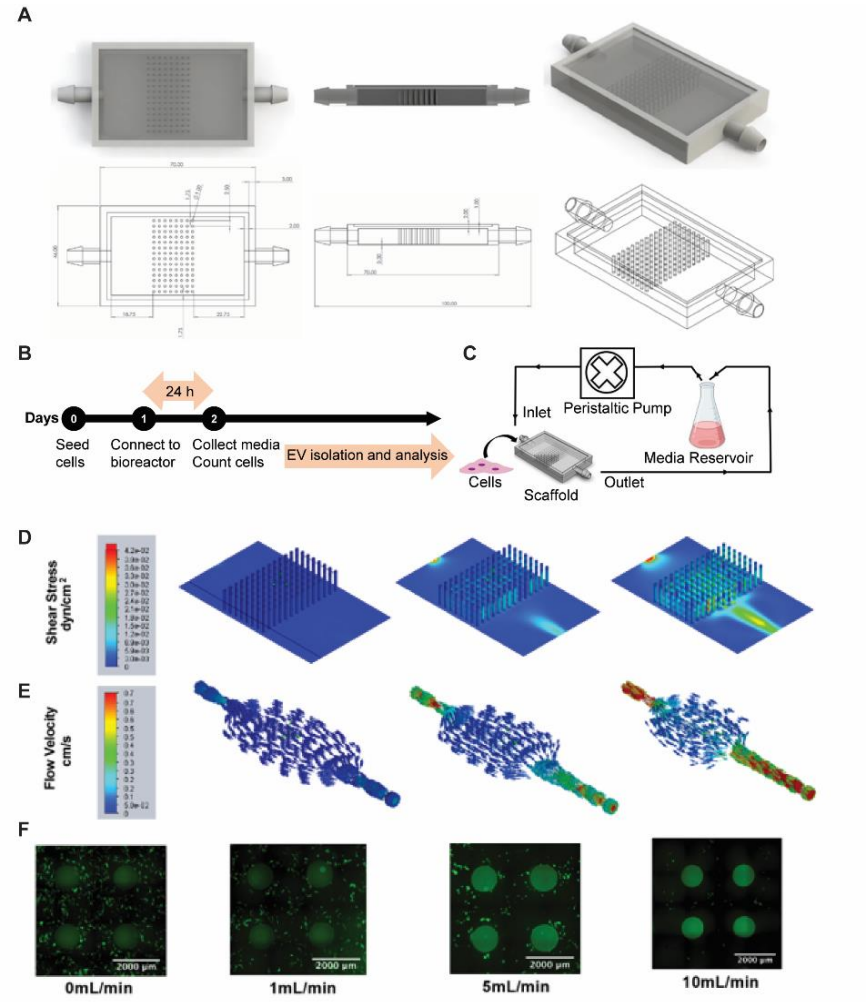


Figure 3.2. Perfusion bioreactor setup and scaffold characterization. (A) Cross-sectioned image of the scaffold generated in SolidWorks showing dimensions of the scaffold as well as individual pillar height, diameter, and spacing. (B) Timeline of the perfusion bioreactor experimental procedure. (C) Schematic representation of the perfusion bioreactor setup. A scaffold seeded with cells is connected to a peristaltic pump and media reservoir using gas-permeable tubing. Inlet and outlet of the media circulates at 1, 5, or 10 mL/min flow rate. (D) Visual representation of varying levels of shear stress and (E) flow trajectories at different areas within the scaffold as evaluated by computational flow simulation are shown for 1, 5, and 10 mL/min. (F) Images of the phalloidin-stained scaffold seeded with MSCs after 24 h of dynamic culture. Images courtesy of Dr. Divya Patel.

3.3.2. MSC EV Production is Enhanced by Perfusion Bioreactor Culture

We first aimed to assess the impact of increasing flow rates on MSC EV production. EVs were isolated from MSCs cultured in flask, scaffold (0 mL/min), or perfusion bioreactor conditions (1, 5, or 10 mL/min) for 24 h. The flow rates were selected based on CFD analysis to determine maximum shear stress to not exceed physiological interstitial levels of 0.1 dyn/cm^2, which has been shown to induce MSC differentiation into osteogenic phenotype [238]. NTA revealed no significant difference in EV size distribution. Peak size values for EVs from all culture conditions were approximately 160 nm (**Figure 3.3.A**). More than 90% of the total EV populations from all culture conditions were within the typical exosome diameter range (40-200nm) (**Figure 3.3.A**) [34]. The highest level of EV production per cell occurred when MSCs were exposed to a 5 mL/min flow rate (9.8E5 ± 9E4), which was 83-fold, 28-fold, 3-fold, and 2.5-fold higher than flask, 0, 1, and 10 mL/min, respectively (flask: 1.18E4 ± 9.3E3; 0 mL/min: 3.5E4 ± 5.2E3; 1 mL/min: 3.0E5 ± 2.7E4; 10 mL/min: 3.9E5 ± 4.6E4) (**Figure 3.3.B**). This trend of elevated EV production as determined by NTA was retained across various tissue origins (i.e., bone-marrow and adipose-derived MSCs) as well as different donors (**Figure 3.4**). EV production per cell was also evaluated using a CD63-specific ExoELISA, which confirmed the significant increase in EV output in the bioreactor culture system at 1, 5, and 10 mL/min compared to flask culture (25-fold, 43-fold, and 47-fold) and 0 mL/min (23-fold, 39-fold, and 43-fold), respectively (**Figure 3.3.C**). Interestingly, exoELISA results showed higher CD63$^+$ EV production per cell

at 10 mL/min compared to the total EV population per cell assessed by NTA (**Figure 3.3.C**). As measured by BCA, average protein content per EV decreased 2-fold in the 5 mL/min bioreactor compared to the flask culture, but was not significant ($p > 0.05$). Protein content per EV was inversely proportional to EV production rates (**Figure 3.3.D**).

We observed a 2-fold, 5-fold, and 4-fold decline in protein content per EV compared to 0 mL/min in the 1, 5, and 10 mL/min cultures, respectively. TEM images revealed no observable changes in MSC EV morphology when MSCs were cultured within the bioreactor (i.e., 5 mL/min) (**Figure 3.3.E**). Immunoblot analyses confirmed the presence of EV markers (Alix, TSG101, CD63, and CD9) and absence of cellular debris markers (Calnexin, HSP90, and Ago2) in MSC EV samples for flask, and 0, 1, 5, and 10 mL/min culture conditions (**Figure 3.3.F**). The 5 mL/min flow rate was determined to be optimal as it was able to significantly increase EV production without dislodging cells (**Figures 3.2.F and 3.3.B**), and was thus used for further experiments.

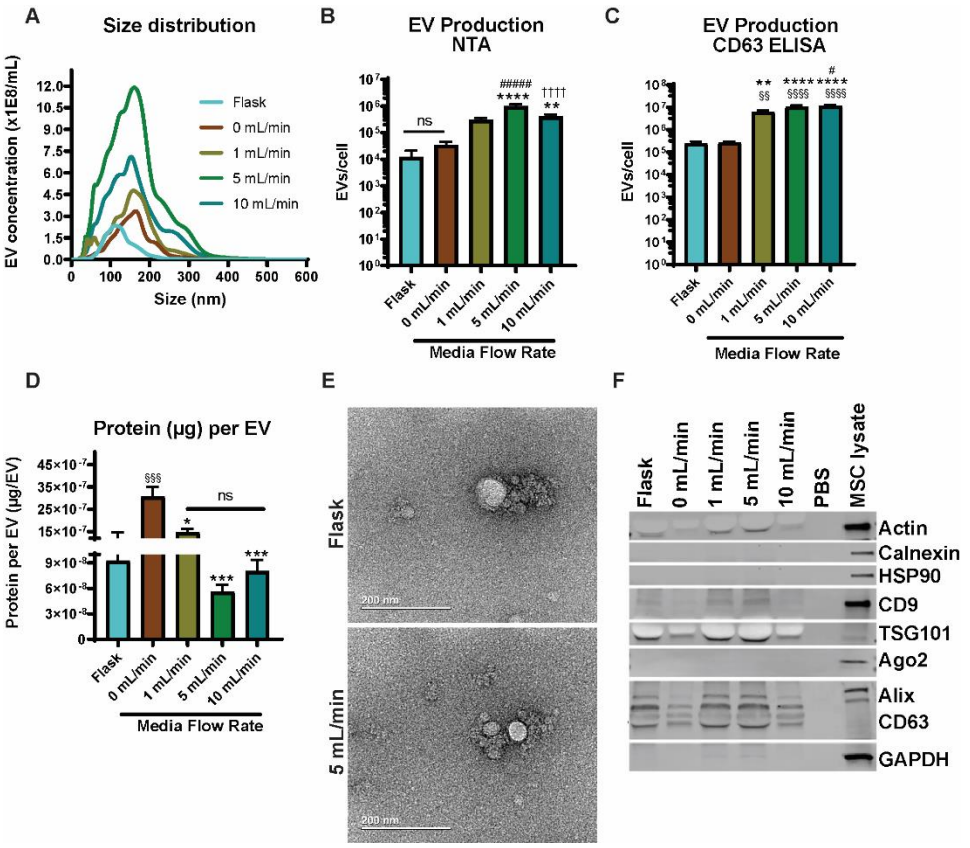


Figure 3.3. MSC EV production can be maximized in the bioreactor with a 5 mL/min flow rate. (A) Size distribution of MSC-derived EVs produced in the various culture conditions. Number of EVs produced per cell as measured using (B) nanoparticle tracking analysis (NTA) and (C) a CD63-specific ExoELISA. (D) The ratio of total surface protein amount (µg) to total number of EVs are shown. A significant increase in EV production (§ - compared to flask, * - compared to 0 mL/min, # - compared to 1 mL/min, † - compared to 5 mL/min) was recorded, but a decrease in protein content ($p < 0.001$) was observed for the 5 mL/min condition when compared with the 0 mL/min condition. (E) TEM images of EVs from MSCs either cultured in the flask or 5 mL/min conditions. (F) Immunoblots of MSC EVs from the various culture conditions for EV markers (CD63, Alix, TSG101, CD9), cell markers (Calnexin, HSP90, and Ago2), and control markers (Actin and GAPDH). Data representative of at least three independent experiments (N = 3). Statistical significance was calculated using a one-way ANOVA using Tukey's multiple comparison tests (ns – $p > 0.05$: #, *, or § - $p < 0.05$; §§ or ** - $p < 0.01$; *** - $p < 0.001$; ****, §§§§, ####, or †††† - $p < 0.0001$). Panels A, B, C, D, and F courtesy of Dr. Divya Patel.

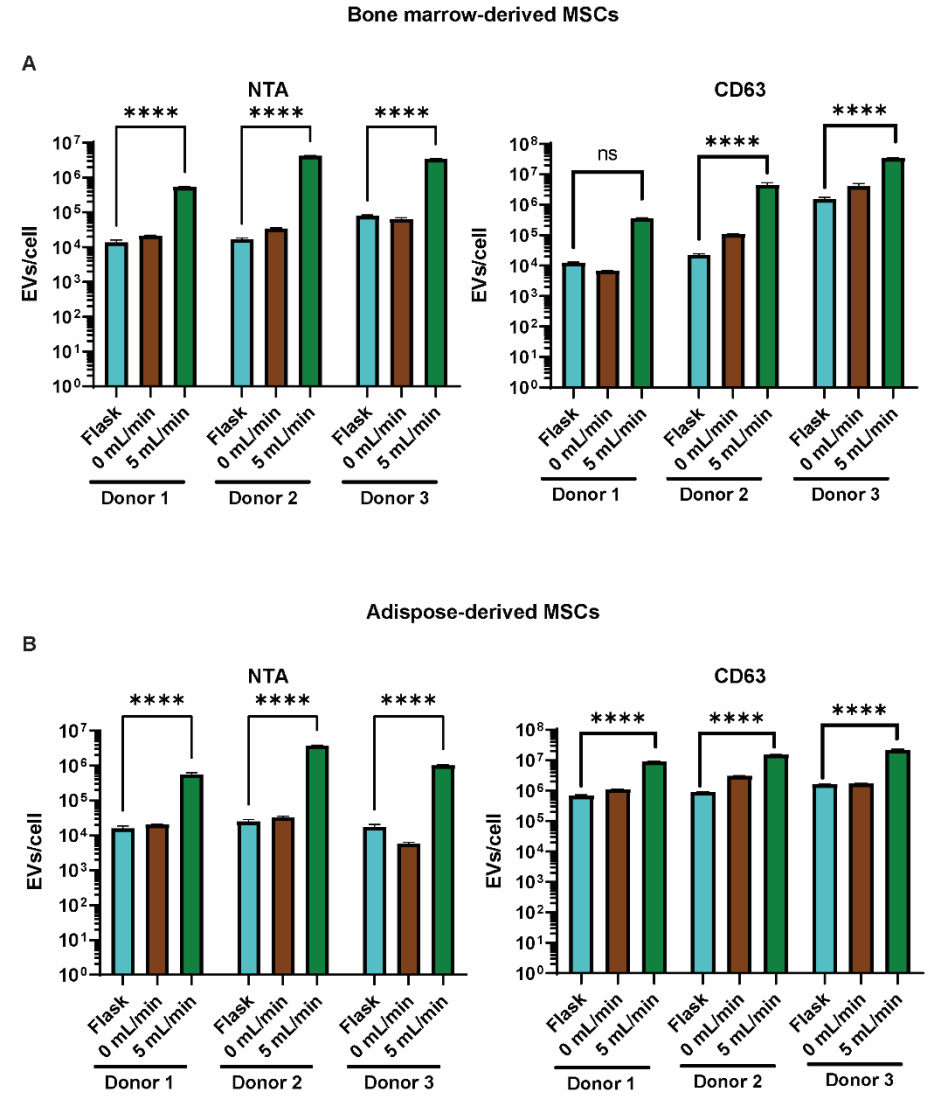


Figure 3.4. Flow-induced increase in MSC EV production is maintained across donors and tissue of origin. EV production from three donors of (A) bone marrow-derived MSCs and three donors of (B) adipose-derived MSCs as measured by NTA and a CD63 ELISA. A significant increase in EV production occurred when cells were cultured in the 5 mL/min bioreactor when compared with those maintained in flasks regardless of donor or tissue origin. Data representative of three independent experiments (N = 3). Statistical significance was calculated using a two-way ANOVA using Tukey's multiple comparison tests (ns – $p > 0.05$: * - $p < 0.05$; ** - $p < 0.01$; *** - $p < 0.001$; ****- $p < 0.0001$). Data courtesy of Dan Levy.

3.3.3. Enhanced EV Production in Perfusion Bioreactor Culture is Not Specific to MSCs

In an attempt to understand whether the observed boost in MSC EV production is the result of a cell-driven mechanoresponse, we cultured HEK293 cells within the system as they lack the abundance of mechanoreceptors inherently present in MSCs [240-242]. Interestingly, the HEK cells demonstrated a similar and significant uptick in EV production as well as a decreasing trend in protein per EV as flow rate increased (**Figure 3.5.A, B**). HEK EV morphology was not altered by the culture conditions (**Figure 3.5.C**). And immunoblotting confirmed the presence of EV markers (CD63, Alix, TSG101) and the absence of the cellular debris marker calnexin (**Figure 3.5.D**).

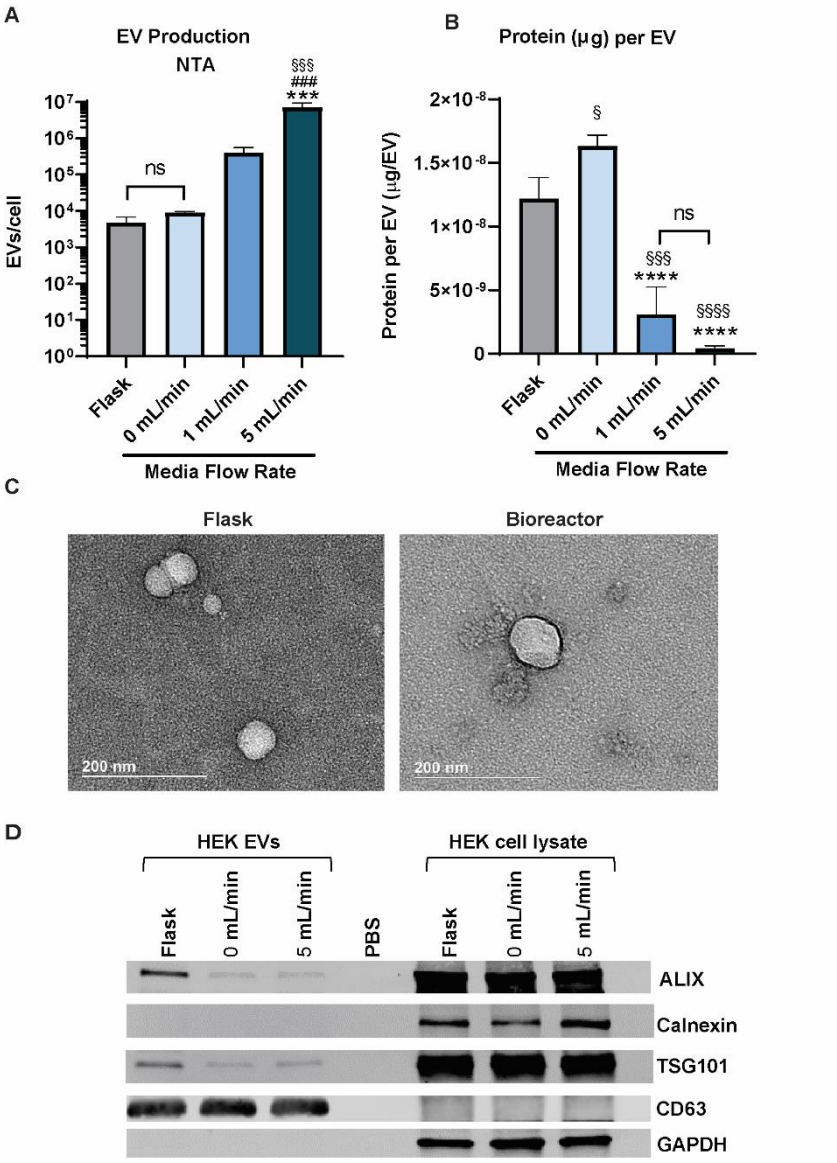


Figure 3.5. HEK293 EV production increases when cultured in perfusion bioreactor. (A) Size distribution of HEK-derived EVs produced in the various culture conditions. (B) Number of EVs produced per cell as measured using nanoparticle tracking analysis (NTA). (C) The ratio of total surface protein amount (µg) to total number of EVs are shown. A significant increase in EV production (§ - compared to flask, * - compared to 0 mL/min, # - compared to 1 mL/min) was recorded, and a decrease in protein content ($p < 0.0001$) was observed for the 5 mL/min condition when compared with the 0 mL/min condition. (C) TEM images of EVs from HEK cells maintained in the flask or bioreactor conditions. (F) Immunoblots of HEK EVs from the various culture conditions for EV markers (CD63, Alix, TSG101) and cell markers (Calnexin, GAPDH). Data representative of at least three independent experiments (N = 3). Statistical significance was calculated using a one-way ANOVA using Tukey's multiple comparison tests (ns – $p > 0.05$: # , *, or § - $p < 0.05$; ***, §§§, or ### - $p < 0.001$; **** or §§§§- $p < 0.0001$).

3.3.4. MSC EV *in vitro* Angiogenic Bioactivity is Maintained Following Perfusion Bioreactor Culture

Bioactivity of MSC EVs isolated from the flask and optimal perfusion bioreactor condition (5 mL/min) was subsequently assessed using an *in vitro* gap closure assay and a tube formation assay. In the gap closure assay, we found that there was no significant difference between the activity induced by flask-derived MSC EVs and those from the scaffolds without flow (i.e., 0 mL/min), regardless of dosing scheme (i.e., particles per mL or protein concentration) (**Figure 3.6**). Thus, in all subsequent experiments we compared the bioreactor to flask conditions. When treated with flask-derived MSC EVs based on EV count (i.e., 5×10^9 EVs/mL), HUVECs had significantly higher gap closure when compared with the negative control that was treated with basal media only ($p < 0.01$) (basal media: 22.23 ± 3.659; flask at 5×10^9 EVs/mL: 48.49 ± 1.737) (**Figure 3.7.A, B**). Using the same dosing scheme, bioreactor-derived MSC EVs also significantly improved gap closure in comparison with the negative control ($p < 0.0001$) and the flask-derived EVs ($p < 0.05$) (bioreactor at 5×10^9 EVs/mL: 65.26 ± 5.926). When dosed at 200 μg/mL, MSC EVs derived from both the flask and bioreactor conditions significantly augmented gap closure in HUVECs when compared with the negative control ($p < 0.01$ and $p < 0.0001$; respectively) (flask at 200 μg/mL: 42.31 ± 2.746; bioreactor at 200 μg/mL: 52.72 ± 1.318). This trend of maintained EV bioactivity was retained across donors of bone marrow-derived MSCs, whereas we observed no angiogenic activity from adipose-derived MSCs (**Figure 3.8**). Importantly, there was no

significant difference between the dosing schemes in the respective culture conditions. Therefore, in all subsequent experiments, MSC EVs were dosed at 5×10^9 EVs/mL.

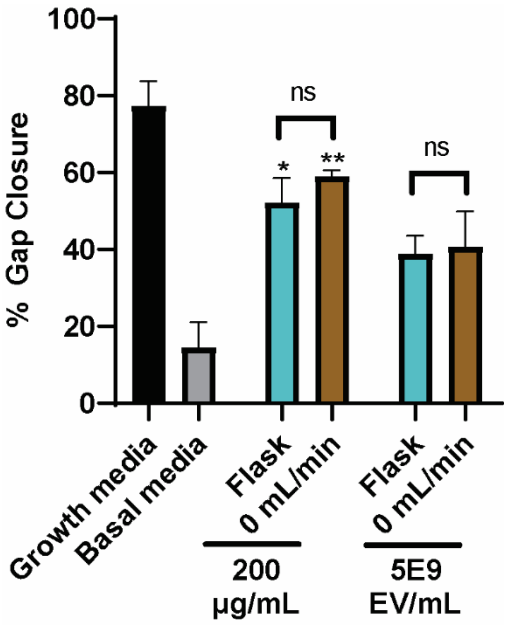


Figure 3.6. EVs from MSCs cultured in the static scaffolds and flasks perform similarly in the gap closure assay. Cell gap area after 20 h as a percentage of gap area at 0 h. A significant increase in gap closure was observed when HUVECs were treated with either flask or static scaffold (i.e., 0 mL/min) MSC EVs when dosed at 200 µg/mL (* - compared to basal). There were no significant differences detected between flask-derived or static scaffold-derived MSC EVs ($p > 0.05$). All data are representative of three independent experiments (N = 3). Statistical significance was calculated using two-way with Tukey's multiple comparisons test (ns – $p > 0.05$; * - $p < 0.05$; ** - $p < 0.01$).

In the tube formation assay, both flask- and bioreactor-derived MSC EVs significantly enhanced the number of capillary-like structures formed by the HUVECs (i.e., number of loops) when compared with the negative control ($p < 0.01$ and $p < 0.05$, respectively; basal: 18.67 ± 3.93; flask: 43.00 ± 6.110; bioreactor: 35.67 ± 2.300) (**Figure 3.7.C, D**). There was no significant difference between the flask and bioreactor EVs.

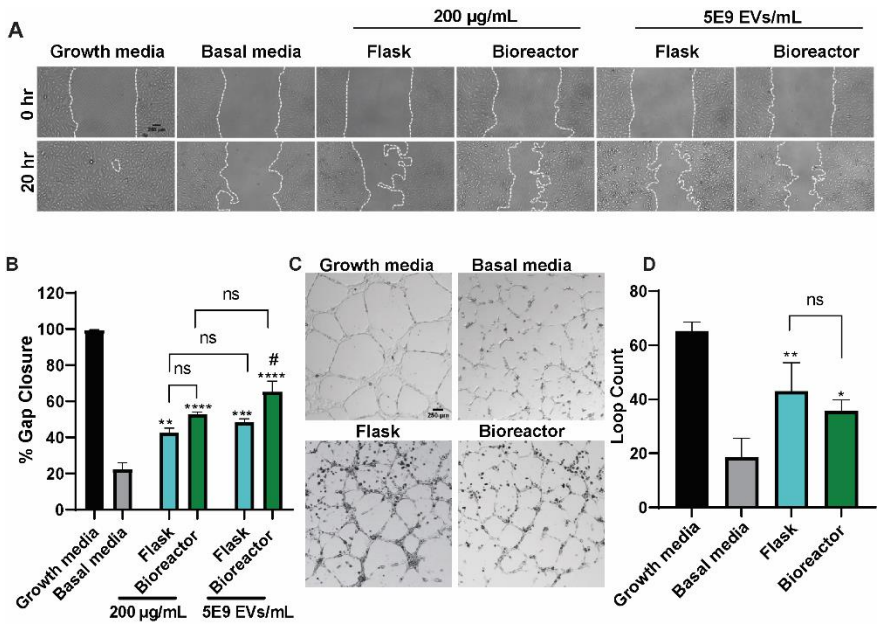


Figure 3.7. Perfusion Bioreactor culture maintains *in vitro* pro-angiogenic activity of MSC EVs. (A) Representative images of HUVECs in the gap closure assay at 0 and 20 h after treatment with growth media (positive control), basal media (negative control), or 5E9 EVs/mL or 200 µg/mL EVs isolated from MSCs in the flask or bioreactor (5 mL/min) culture conditions. (B) Cell gap area after 20 h as a percentage of gap area at 0 h. A significant increase in gap closure was observed when cells were treated with either flask or bioreactor EVs at 5E9 EVs/mL or 200 µg/mL (* - compared to basal, # - compared to flask). There were no significant differences detected between dosing schemes. (C) Representative images HUVECs in the tube formation assay 6 h after application of growth media (positive control), basal media (negative control), or 5E9 EVs/mL EVs from MSCs maintained in flasks or the bioreactor. (D) Results of the tube formation were quantified as the number of complete loops formed by HUVECs. Both flask and bioreactor EVs significantly increased the number of loops with no differences between flask and bioreactor EVs (* - compared to basal). All images and data are representative of three independent experiments (N = 3). Statistical significance was calculated using either a two-way (B) or one-way ANOVA (D) with Tukey's multiple comparisons test (ns – $p > 0.05$; * or # - $p < 0.05$; ** - $p < 0.01$; *** - $p < 0.001$; ****- $p < 0.0001$).

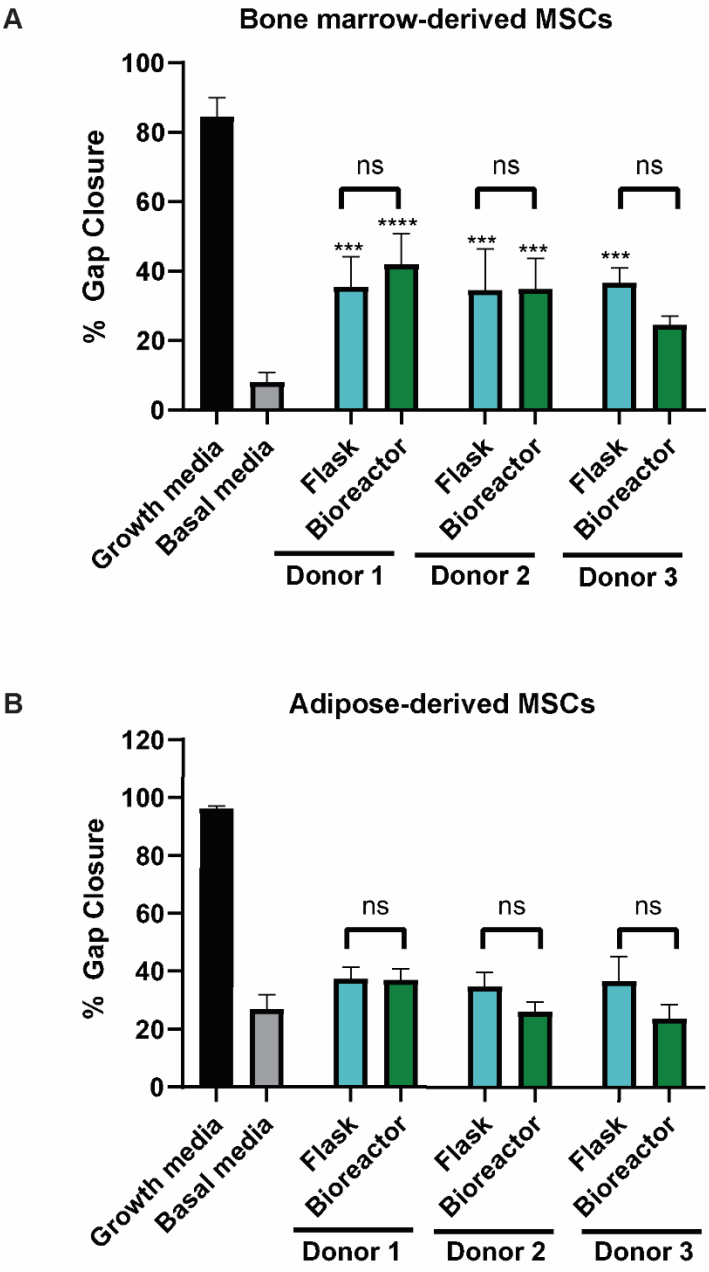


Figure 3.8. Angiogenic bioactivity is maintained across donors of bone marrow-derived MSCs. Cell gap area after 20 h as a percentage of gap area at 0 h. (A) A significant increase in gap closure was observed when HUVECs were treated with 200 μg/mL of EVs from three donors of bone marrow-derived MSC when compared with basal media (negative control). (B) EVs from adipose-derived MSCs had no effect on gap closure regardless of culture conditions. There were no significant differences between flask- or bioreactor-derived EVs from either tissue source. Data representative of three independent experiments (N = 3). Statistical significance was calculated using a two-way ANOVA using Tukey's multiple comparison tests (ns – $p > 0.05$; *** - $p < 0.001$; ****- $p < 0.0001$). Data courtesy of Dan Levy.

3.3.5. *In vivo* MSC EV Wound Healing Bioactivity is Enhanced via Perfusion Bioreactor Culture

The wound healing bioactivity of EVs from flask and bioreactor culture was assessed *in vivo* using a diabetic mouse wound healing model. An 8 mm punch biopsy excisional wound was created on the dorsum of each mouse. Three days post-injury, mice were injected four times around the wound with 50 μg of flask MSC EVs, bioreactor MSC EVs, or a PBS vehicle control. EVs isolated from MSCs cultured in the bioreactor generated a significant improvement in healing overall when compared with the vehicle control ($p < 0.05$) (**Figure 3.9.A, B**). CD31 immunohistochemistry revealed that mice treated with bioreactor MSC EVs had significantly more CD31+ vessel structures when compared with animals treated with flask MSC EVs or PBS ($p < 0.05$; PBS: 4.7 ± 0.984; flask: 5.876 ± 1.636; bioreactor: 12.02 ± 2.423). There was no significant difference between the vehicle control and flask MSC EVs (**Figure 3.9.C, D**).

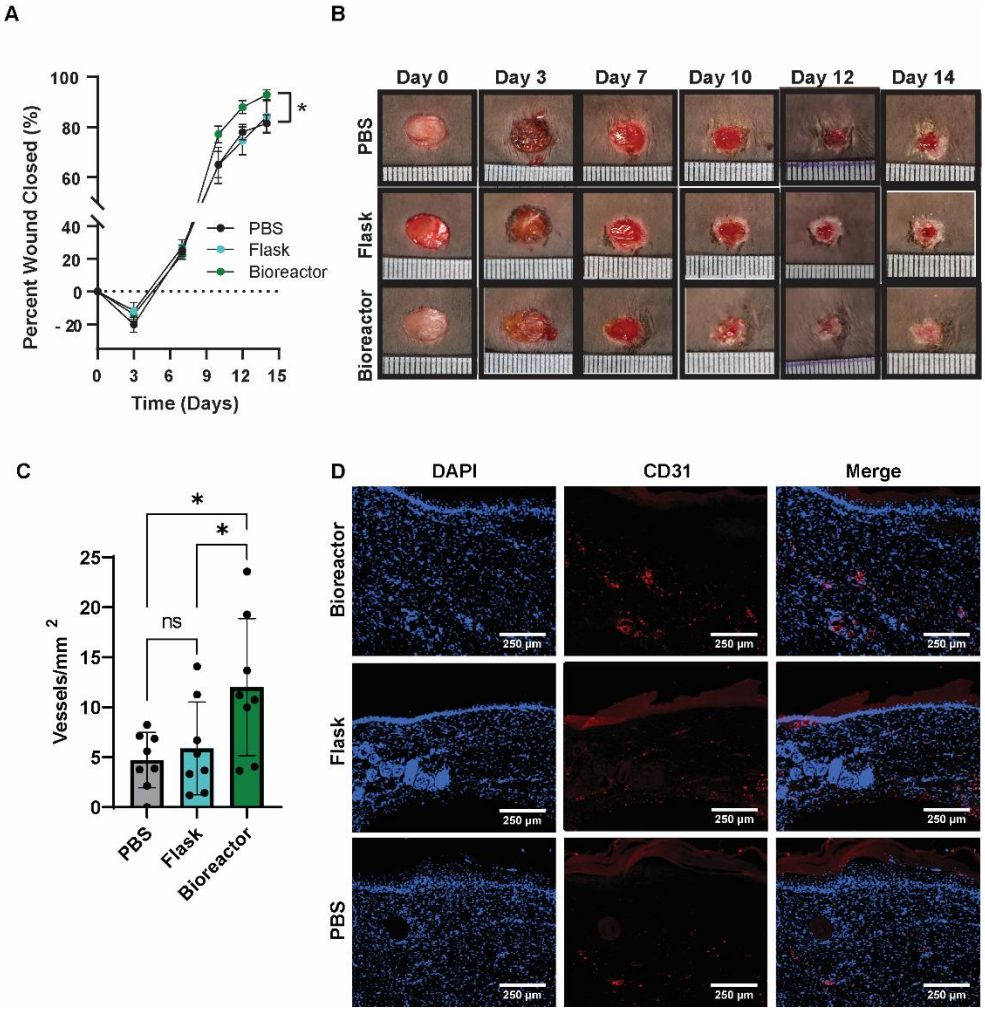


Figure 3.9. Perfusion bioreactor culture improves healing in a diabetic mouse excisional wound healing model. (A) Closure evaluated for wounds treated with flask MSC EVs, bioreactor MSC EVs, or PBS. Bioreactor MSC EVs improved overall wound healing compared with the PBS control ($p < 0.05$). (B) Representative images of mice wounds over the length of the experiment. (C) Number of CD31+ vessels in healed tissues isolated from mice on day 21 with (D) representative immunohistochemistry images. A significant enhancement of CD31+ vessels was apparent in mice treated with bioreactor MSC EVs ($p < 0.05$). Statistical significance was calculated using a (A) two-way ANOVA or (C) one-way ANOVA with Holm-Šídák's multiple comparisons test (*$p < 0.05$; $n = 8$). Data courtesy of Dr. Louis Born.

3.3.6. Assessment of Perfusion Bioreactor Culture-Induced Enhancement of in vivo MSC EV Bioactivity

To determine whether any differences in MSC EV bioactivity observed *in vivo* could be attributed to disparate internalization into recipient cells, we evaluated EV uptake. HUVECs were treated with PKH67-labeled MSC EVs from flask or bioreactor culture for 24 h (**Figure 3.10.A**). There was no difference in uptake of the EVs from the bioreactor culture (96.7%) compared to flask culture (98.6%) (**Figure 3.10.B**), which was visually confirmed with confocal images of the recipient cells (**Figure 3.10.C**). As flow has been shown to alter protein corona composition of nanoparticles which can in turn affect uptake [243, 244], we assessed the EV surface proteins using MALDI-TOF. However, the resulting spectra showed no apparent differences between the flask and bioreactor MSC EVs (**Figure 3.10.C**). MALDI-TOF spectra of MSC EVs were highly reproducible over time (**Figure 3.11**).

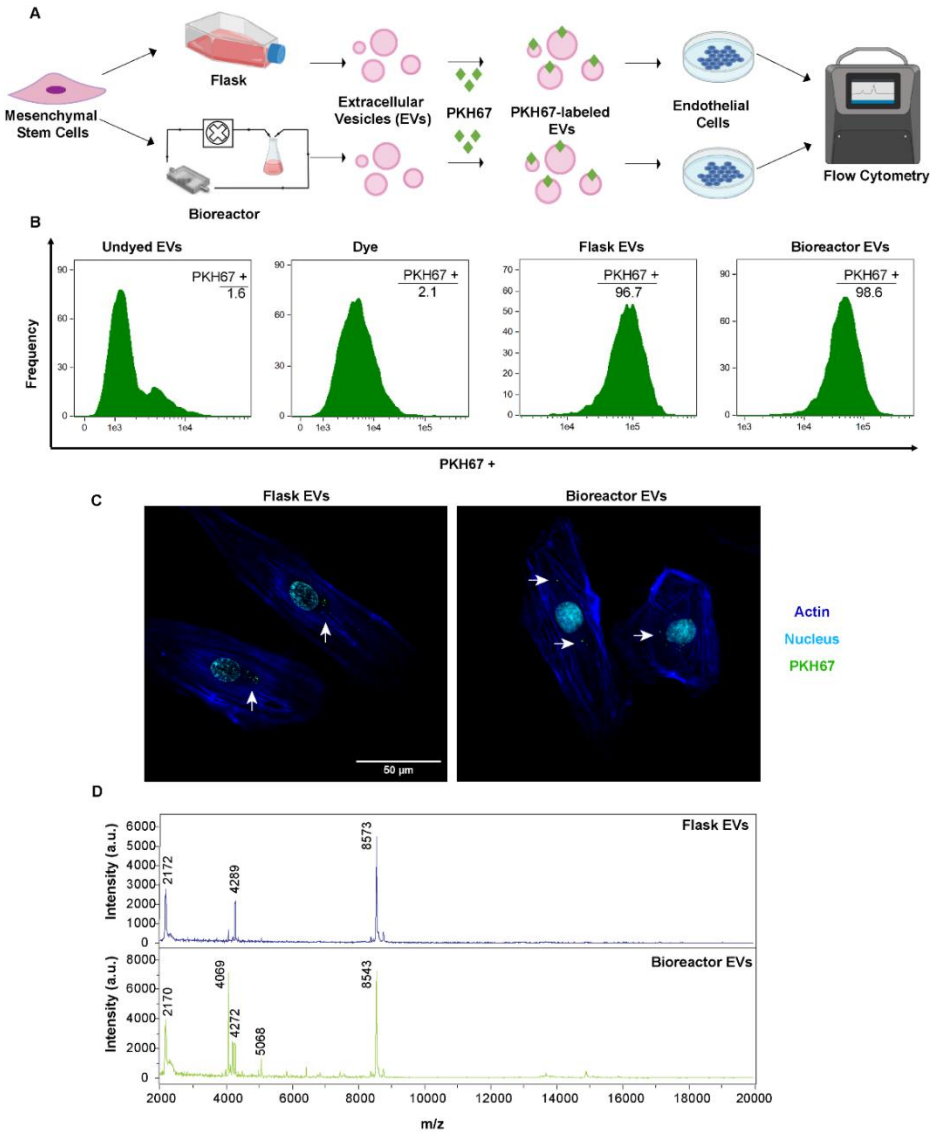


Figure 3.10. Assessment of HUVEC uptake and protein profile of flask and bioreactor MSC EVs. To assess EV uptake, flow cytometry analysis of PKH67-labeled EVs from MSCs cultured in flask vs. bioreactor conditions was conducted as shown in (A). (B) Histograms of frequency vs fluorescence intensity are shown for HUVECs that were treated with undyed EVs (no PKH67), just dye (no EVs), dyed flask EVs, or dyed bioreactor EVs. (C) Representative images of HUVECs after treatment with labeled EVs. White arrows denote the location of PKH67-labeled EVs. (D) MALDI-TOF mass spectra of flask and bioreactor-derived EVs. Data represent at least 2 independent experiments (N = 2).

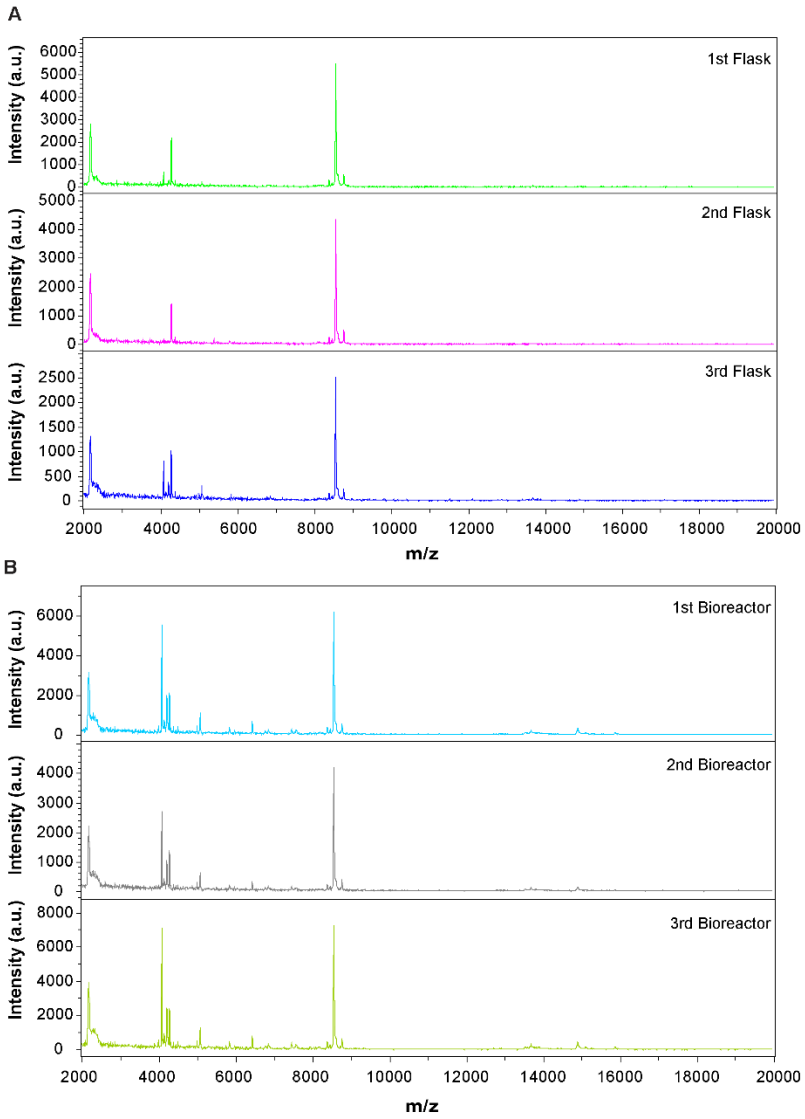


Figure 3.11. MALDI-TOF mass spectra of three separately prepared batches of flask and bioreactor EVs.

Next, to assess any variance in RNA profiles of recipient HDMECs due to flask vs. bioreactor MSC EVs, we analyzed expression of 88 genes associated with wound healing (**Figure 3.12.A**). Among the 88 genes, 34 were upregulated and only 2 were downregulated more than 2-fold compared to PBS for both flask and bioreactor EV groups. Between flask and bioreactor EV groups, 3 were upregulated (EGF, FGF, and COL5A3) and 3 were downregulated (VTN, ITGB6, and IL2) in the bioreactor EV group by more than 2-fold, though none showed significance ($p > 0.05$) (**Figure 3.12.B**).

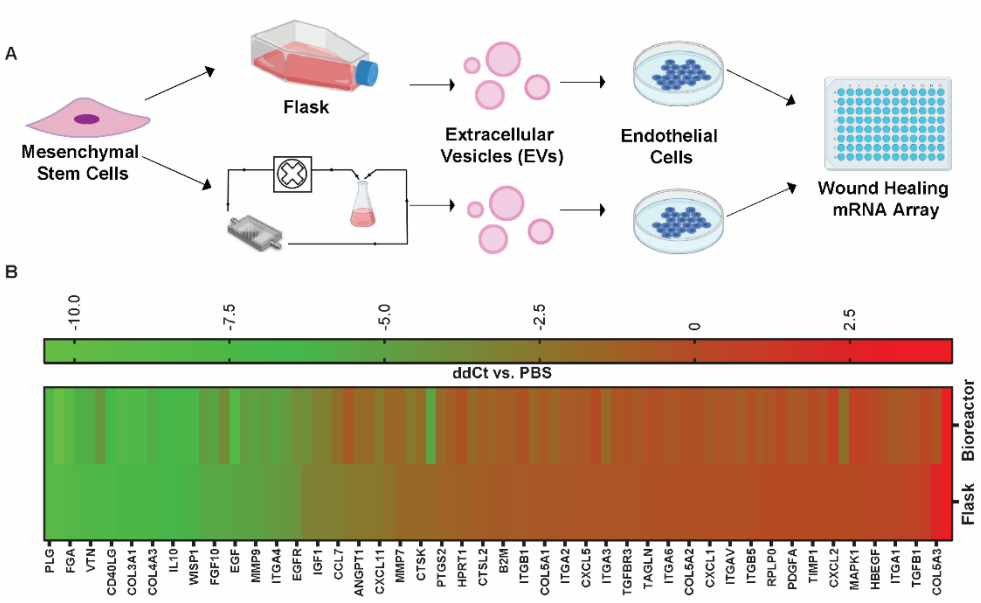


Figure 3.12. RNA profiling of HDMECs treated with MSC EVs from flask vs perfusion bioreactor culture. (A) Experimental schematic of wound healing specific gene expression in HDMECs treated with MSC EVs from flask or bioreactor culture. (B) Heat map representing gene regulation profile of 88 genes associated with wound healing. Data shown as $\Delta\Delta Ct = (\Delta Ct$ Flask or Bioreactor – ΔCt PBS), where $\Delta Ct = (Ct$ target gene – Ct β-actin). No significant difference between RNA profiles of HDMECs treated with flask or bioreactor derived MSC EVs was observed (data not shown). Significance was tested using one-way ANOVA with Bonferroni's multiple comparison test. Data are representative of two independent experiments (N = 2). Data courtesy of Dr. Divya Patel.

3.4 Discussion

The lack of a scalable manufacturing platform has remained a substantial hindrance to the clinical translation of EV-based therapies [171, 245, 246]. The most commonly employed solution to this problem is the use of hollow-fiber technology, which is highly effective for optimizing yield [171, 247], but has limited versatility with regard to control of the various mechanical cues that can most influence EV properties, such as shear stress and substrate architecture. Engineering advancements, such as 3D printing, can allow for a more reductionist and tunable approach that enables control over these cues in a manner amenable to large-scale production. In a previous study, we leveraged 3D-printing to create a scaffold-perfusion bioreactor that significantly increased the secretion of EVs from human dermal microvascular endothelial cells (HDMECs) [15]. Inspired by these results, we attempted to use the perfusion bioreactor to enhance the therapeutic efficacy of MSC EVs, as MSCs are another mechanosensitive cell type with many therapeutic applications [234, 248]. In this study, the scaffold was redesigned to incorporate a pillar configuration previously implemented to create a highly-adaptable and physiologically-relevant microenvironment specifically for human MSCs [249]. In addition, when perfused with media, this design allowed for the use of flow rates that produced shear stress values well below levels previously reported for the *in vivo* stem cell niche (i.e., 0.1 – 1 dyn/cm^2) and well below values known to induce MSC differentiation [237, 239, 250] (**Figure 3.2.D**).

While implementing the bioreactor system, we found that a flow rate of 5 mL/min ($3x10^{-3}$ dyn/cm^2) appeared optimal as it significantly increased MSC EV production by 83-fold when compared with flask culture and by 2.5-fold when compared with a flow rate of 10 mL/min ($1.2x10^{-2}$ dyn/cm^2) (**Figure 3.3.B**) without causing the significant cell detachment that was observed in the 10 mL/min condition (**Figure 3.2.F**). However, when an ELISA was used to examine the levels of tetraspanin CD63, which is considered an indicator of EVs originating from the multi-vesicular body (i.e., exosomes) [33], the 5 mL/min produced only a 43-fold increase in CD63$^+$ EVs while the 10 mL/min condition produced a very similar 47-fold increase in CD63$^+$ EVs when compared with flask culture (**Figure 3.3.C**). We also show a significant reduction in total protein content per EV as flow rate is increased from 0 to 5 mL/min, which seemed to saturate at 10 mL/min (**Figure 3.3.D**). Protein per EV is often used as a proxy for EV purity, with less protein per EV being considered a gauge of higher purity [251]. We have previously reported similar phenomena in which HDMECs within a perfusion bioreactor produced a significant yet smaller increase in CD63$^+$ EVs in comparison with total EVs along with a purer EV population [15]. Altogether, these results indicate that the bioreactor favors the secretion of other EV sub-populations such as microvesicles, which are known to originate from the cell membrane and may be composed of a relatively lower amount of CD63 [41, 252]. Indeed, shear stress is known to increase cell membrane tension which results in augmented exocytotic activity [253, 254]. Overall, the increased MSC EV production we observed mirrors the results of previous studies by other groups that have used dynamic culture conditions to increase EV production [147, 170, 253, 255, 256]. It is important to note

that TEM images revealed no significant changes in morphology or size (**Figure 3.3.E**). Furthermore, immunoblotting revealed no presence of the endoplasmic reticulum protein calnexin (**Figure 3.3.F**), signifying that it is unlikely that the levels of shear stress used in this study were causing physical disruption to the cell membrane and/or instigating the release of apoptotic bodies.

MSCs monitor mechanical cues within their microenvironment in order to initiate adaptive and reparative responses; a capability governed by countless mechanosensors including, but not limited to, adherens junctions, focal adhesions, integrins, and ion channels [257-259]. Flow-derived shear stress is a mechanical cue pervasive throughout the physiological niche as well as many scalable manufacturing processes. However, flow and shear stress are two separate phenomena in that, besides inducing various stresses on the cell surface (i.e., shear, tensile, and compressive stresses), flow can also modulate the surrounding environment by augmenting diffusive exchanges (i.e., oxygen, nutrients, and waste metabolites) [212, 213]. After culturing the relatively mechanically-inert HEK293 cell line [242], we found a similar increase in both EV production and EV purity as was seen in MSCs (**Figure 3.5.A, B**). HEK293 cells are often used in overexpression studies investigating mechanically-activated channels (e.g., Piezo2 and TRPV4) due to their low abundance of endogenous channels [242]. Coupled with our data, this could mean that the increased EV production we observed in this bioreactor system is a result of fluid dynamics rather than a specific mechanoresponse of the cells. However, in a recent study, while culturing MSCs in a flat-plate perfusion bioreactor, Kang et al. found that flow increased intracellular

calcium as well as calcium-related proteins, and thus could be a mechanism behind the increase in EV biogenesis [169]. Separately, Guo and colleagues found that the increased MSC EV production present within their perfusion bioreactor was dependent on the expression of yes-associated protein (YAP), a well-known cellular mechanotransducer [170, 260, 261]. As both of these proposed mechanisms exist across cell-types (including HEK293), it would be of interest to probe these particular pathways within our system in future studies.

Of the various therapeutic applications of MSCs and MSC EVs elucidated thus far, the role they play in tissue reparative processes (e.g., angiogenesis) has been well-documented [262-265]. Moreover, it is known that flow-derived shear stress can be used to influence the regenerative properties of both MSCs and their secreted EVs [169]. Across two orthogonal angiogenic assays (i.e., cell migration and tube formation), we found that the angiogenic properties of MSC EVs derived from the perfusion bioreactor were at least as effective as those from flask-grown MSCs (**Figure 3.7**). We found that the same bioactivity pattern was apparent when using bone marrow-derived MSC EVs from several donors, but not when using MSC EVs derived from adipose tissue (**Figure 3.8**). This emphasizes the impact and importance of choosing the optimal EV source for the desired application [266]. The observed similarity in angiogenic activity between the flask- and bioreactor-derived MSC EVs were supported by similar cellular uptake of the EVs by HUVECs and comparable surface protein fingerprints (**Figure 3.10**). Previous works have shown that cell culture conditions (e.g., bioreactor vs. flask or 2D vs. 3D culture) can enhance EV efficacy,

alter EV uptake by recipient cells, and change the EV proteome profile [223, 256, 267]. Importantly, proteomic profiling of EVs utilizing the technique used in the current investigation (i.e., MALDI-TOF MS) can be sensitive. A study by Han and colleagues demonstrates the utility of this methodology by using the MALDI-TOF mass spectra of plasma-derived EVs to distinguish osteosarcoma lung metastasis from non-lung metastasis [236]. While we reveal possible slight differences in the protein make-up (**Figure 3.10.D**), we only investigated the surface proteins of undigested EV samples and thus further proteomic analyses (i.e., LC-MS) may reveal more significant differences. Additionally, it would be interesting to gauge how perfusion bioreactor culture can alter the proteome of MSC EVs in comparison with parental cells, which would be valuable information for the continued development of EVs in general for both diagnostic and therapeutic applications. It is also important to consider that any nuances caused by shear stress may alternatively lie within the EV metabolome, lipidome, and/or transcriptome, all of which are known to be dynamic with changing culture conditions [14, 154].

As described above, the flask- and bioreactor-derived MSC EVs were similar in numerous ways. However, there was a significant decrease in protein content per EV from the perfusion bioreactor. Consequently, dosing by protein entailed applying 5-7 times more bioreactor EVs (according to NTA data) than flask EVs. Taking this into account, we also dosed by EV count and found a similar pattern in the angiogenic activity assays, indicating a possible saturation point and equal efficacy of the two EV preparations (**Figure 3.7.B**). This agrees with previous research showing that

bioactivity of EVs can be maintained within bioreactor culture systems [15]. Critically, with the exaggerated EV production from the perfusion bioreactor, dosing by EV count allowed the application of a much smaller volume to achieve the same effect (e.g., 8 µl of bioreactor EVs vs 80 µl of flask EVs). Altogether, these results indicate that our perfusion bioreactor system may not enhance MSC EV efficacy but can be used to increase MSC EV potency and thus has important implications in scale-up efforts needed for clinical administration.

Intriguingly, when applied in a diabetic mouse wound healing model and compared to a vehicle control, EVs from the perfusion bioreactor system significantly improved healing in terms of percent wound closed and the number of new blood vessels formed, while those from flask culture had no effect (**Figure 3.9.A, C**). The disparate results between the *in vitro* and *in vivo* data are not to be unexpected as the physiological niche is much more complex than anything that can be recapitulated in a laboratory setting. Particularly, wound healing is a highly regulated process that requires a dynamic yet balanced interplay among various cell types, including macrophages, fibroblasts, endothelial cells, and keratinocytes [262, 268]. Notably, MSC EVs are internalized by all of these cell types and have been documented to influence critical events during wound healing such as inflammation, collagen deposition, apoptosis, and re-epithelialization [262]. The *in vivo* results suggest that bioreactor MSC EVs may be more efficacious in any number of these wound healing processes and thus, further work is required to understand the exact role the MSC EVs play at the physiological wound site. It is also important to note that the bioreactor MSC EVs were able to alter

the gene expression of HDMECs, although not significantly (**Figure 3.12.B**). While the altered gene expression did not seem to impart any significant pro-angiogenic benefits in the *in vitro* validation assays, it remains to be seen how this translates to physiological wound healing.

Overall, the perfusion bioreactor utilized in the current study embodies a means to both enhance MSC EV potency while providing the opportunity to explore the effects of scale-up procedures necessary for clinical translation. The modularity of the system allows significant ability to tune the system to various needs, including the ability to alter other important attributes such as the stiffness and architecture of the 3D-printed scaffold. This investigation and further exploration of the system will ultimately inform the design of a manufacturing platform capable of producing a potent MSC EV wound healing therapeutic at the scale necessary for clinical use.

Chapter 4: Mechanical Confinement of Mesenchymal Stem Cells Enhances Production and Pro-Angiogenic Bioactivity of Extracellular Vesicles[§]

4.1 Introduction

Within the body, cells experience various levels of mechanical confinement through interaction with a dynamic microenvironment consisting of neighboring cells, tissues, and the extracellular matrix (ECM) [269]. Specifically, MSCs undergo mechanical confinement in the physiological space as they migrate through the ECM to sites of injury or in the biomanufacturing space as they move through structures internal of engineered scaffolds and *in vitro* assays [270]. Cell confinement often leads to cytoskeletal reorganization as well as changes in cell and nuclear morphologies which ultimately result in variations in cell function [271]. Although EVs have been implicated as a critical factor underlying many cell functions [246], confinement remains uninvestigated in terms of the effects specifically on MSC EVs.

The investigation of confinement on EVs in general is scarce. To our knowledge, only two studies have explored the relationship between cell confinement and EV functionality. In 2020, Liang and colleagues were able to confine endothelial cells (ECs) by culturing them on polydimethylsiloxane (PDMS) surfaces etched with

[§] Figure 4.1 and a portion of figure 4.2 were adapted from Doolin, M.T. and K.M. Stroka. 2019. Integration of Mesenchymal Stem Cells into a Novel Micropillar Confinement Assay. Tissue Engineering: Part C. DOI: 10.1089/ten.tec.2019.0083.

microgrooves. They showed that in comparison with unconfined ECs, the ECs cultured within the microgrooves were able to suppress the activation of monocytes. Further investigation revealed that this anti-inflammatory effect was regulated mainly by EV-associated miR-10a [21]. In a different study, the same research group then went on to show that two different confinement conditions (i.e., electrospun nano-fibrous scaffolds with aligned fibers or microgrooved PDMS) produced EC EVs capable of regulating the phenotype of recipient smooth muscle cells [22]. Altogether, these two studies demonstrate the significant impact confinement can have on the resulting EV population as well as the utility of this information for tissue engineering applications.

In addition to tissue engineering applications, cell confinement may be leveraged directly as a strategy to enhance EV therapies. Specifically, the effect of confinement on MSC EVs would prove invaluable in understanding and overcoming translational issues facing MSC EVs, including low potency and the lack of an adequate manufacturing scheme. Previously, Doolin and Stroka designed a PDMS-based device with micropillars distanced 5, 10, 20, or 50 μm apart that they then optimized for the physical confinement of bone-marrow derived human MSCs [272]. While methods to induce confinement can vary widely [269, 271], this particular device offers multiple benefits over other confinement systems. First, a wide range of micropillar spacings can be used to successfully culture MSCs over long periods of time (i.e., 3 weeks), theoretically allowing for long-term EV collection. Moreover, the device allows seeding of the cells directly onto the micropillar array. This feature enables tighter control over the mechanical cues experienced by the cells, as the device can be placed

into a non-adherent plate, essentially ensuring that no cells are experiencing 2D culture conditions [272]. Here, we have utilized these same devices to examine the influence of mechanical confinement on MSC EVs. Our results suggest confinement can be used to increase both MSC EV production and alter MSC EV bioactivity. Given the tunability of the device itself, variations on the micropillar spacing as well as possible geometries can be readily explored. The framework of this work (i.e., using micropillars to confine cells) can be recapitulated using other techniques such as 3D printing. Thus, the results here lay the foundation for the implementation of microenvironments conducive to desired EV functionality within a biomanufacturing platform.

4.2 Methods

4.2.1. Cell Culture

Bone marrow-derived mesenchymal stem cells (MSCs; passage 2) and human umbilical vein endothelial cells (HUVECs; pooled donors) were obtained commercially from ATCC (MSC: PCS-500-012; HUVEC: C-12203). MSCs were maintained in Dulbecco's Modification of Eagle's Medium (DMEM) (Corning, 10-013-CV) with 10% fetal bovine serum (FBS; VWR, 89510-186), 1% non-essential amino acids (NEAA; Fisher Scientific, 11-140-050), and 1% penicillin-streptomycin (P/S; Corning, 30-002-CI). MSCs were expanded so they were at passage 3 upon seeding into the experiments. HUVECs were cultured on tissue culture polystyrene flasks coated with 0.1% gelatin at 37 $^{\circ}$C for 1 h prior to seeding. HUVECs were maintained in complete endothelial

growth medium-2 (EGM2; PromoCell C-22111) supplemented with 1% P/S and expanded so they were at passages 3-5 in all studies. During experiments, HUVECs were kept in endothelial basal medium-2 (EBM2; PromoCell, C-22221) supplemented with 0.1 % FBS and 1% P/S.

During MSC EV collection, cell culture media was switched to media containing 10% EV-depleted FBS (referred to as EV-depleted media). To EV-deplete the FBS, heat-inactivated FBS was centrifuged at 118,000 × g for 16 h after which the supernatant was carefully decanted and filtered through a 0.2 μm bottle-top filter. The EV-depleted FBS was then aliquoted and stored at -20°C for later use in media supplementation.

4.2.2. Micropillar Device Fabrication

Polydimethylsiloxane (PDMS) devices adorned with micropillars of various spacings were fabricated as previously described [272-274]. Dr. Kimberly Stroka supplied a mask representing the desired micropillar configurations as she and her lab have previously verified that the following fabrication protocol produced devices of the desired dimensions (i.e., micropillars space 5, 10, 20, or 50 μm apart) (**Figure 4.1**) [272]. After obtaining the mask, a photoresist silicon master (University Wafer, 452; 100 mm diameter, 0-100 Ohm-cm, 500 μm thick) detailing the micropillar geometry was then created using photolithography. First, the silicon master underwent a sequential cleaning with acetone, methanol, and isopropanol, followed by water. The master was then

dried with filtered air and baked at 150°C on a hot plate for 5-10 min to allow complete dehydration and adhesion of the subsequent photoresist. After cooling to room temperature, a layer of SU-8 3010 negative photoresist (Kayaku Advanced Materials, Y311060 0500L1GL) was spin-coated onto the silicon master. The silicon master was then soft baked on a hot plate to reduce the residual solvent concentration of the photoresist film and prepare the master for ultraviolet (UV) light exposure. To do this, the temperature was ramped to 95°C at 1°C/min, held at 95°C for 5 min, and then cooled to room temperature. Then, using a MA-4 Suss mask aligner (SUSS MicroTec, Garching, Germany), the micropillar mask was placed over the coated silicon master and exposed to UV light to enable crosslinking. Excess SU-8 3010 was removed using SU-8 developer (Kayaku Advanced Materials, Y020100 4000L1PE) and the master was rinsed with isopropanol, water, dried with filtered air, and hard baked at 200°C for 10 min to stabilize the micropillars. The height of the micropillars was measured using a Tencor Alpha Step 200 Profilometer (KLA Corporation, Milpitas, CA, USA). Next, the master was silanized overnight in a vacuum desiccator using trichloro(1H,1H,2H,2H-tridecafluoro-n-octyl)silane (FOTS, 97%) (TCI Chemicals, T2577-5G).

A

Pillar spacing (theorized)	Pillarspacing (mean± SD)	Pillar diameter (mean± SD)	Pillar height (mean± SD)
5 µm	5.861 ± 0.21 µm	9.160 ± 0.16 µm	12.82 ± 0.29 µm
10 µm	10.95 ± 0.30 µm	8.622 ± 0.19 µm	14.27 ± 0.21 µm
20 µm	20.35 ± 0.25 µm	9.217 ± 0.25 µm	13.26 ± 0.20 µm
50 µm	51.57 ± 0.60 µm	9.011 ± 0.51 µm	16.94 ± 0.92 µm

B

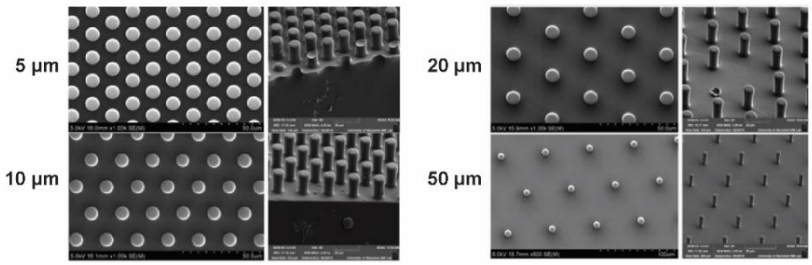


Figure 4.1. Verification of micropillar dimensions. (A) Measurements of SEM images of micropillar devices with spacing of 5, 10, 20, or 50 µm (B) Representative SEM images. Adapted from Doolin and Stroka [272].

The silanized master consisted of micropillars that were 14-16 µm in height and had spacings of 5, 10, 20, and 50 µm. This configuration was previously designed and optimized by Doolin and Stroka for the mechanical confinement of MSCs [272]. Using the silanized master, PDMS micropillar devices were fabricated as previously described [272]. PDMS (~50 g) (Sylgard 184; Krayden, DC2065622) was mixed at a 10:1 base:curing agent ratio and poured over the silicon master. To remove air bubbles, the PDMS and master were placed into a vacuum desiccator for ~45 min. Once air bubbles were removed, the PDMS-covered master was baked at 80°C for 1 h. After the PDMS cooled, the master was cut out and carefully peeled from the PDMS to create a negative PDMS mold. The negative PDMS mold was then plasma treated for 3 min in a plasma cleaner (Harrick Plasma, Ithaca, NY, USA) and silanized using FOTS (97%) in a vacuum desiccator overnight. After silanization, 10 g of PDMS (10:1 base:curing agent ratio) was poured over the silanized mold and degassed in the desiccator. Once air bubbles were removed, the PDMS was baked at 80°C for

1 h. The PDMS with the micropillar constructs was carefully removed from the mold and micropillar devices about the size of a glass coverslip were cut from the PDMS and stored until use.

To deter cell adhesion to the top of the pillars, a thin layer of surfactant (Pluronic F127) was applied using a PDMS stamp using a previously described microcontact technique [272, 275]. To create a PDMS stamp, 15 g of PDMS (10:1) was poured into a 150 mm petri dish and allowed to coat evenly. The stamp was then degassed and baked for 1 h at 80°C. Once cooled, the stamp was rinsed with ethanol, DI water, then ethanol, and dried with filtered air. The stamp was coated with 8% Pluronic F127 (Sigma-Aldrich, P2443-250G) in water. Then, the petri dish was sealed using parafilm and let sit overnight at room temperature to allow the Pluronic to adsorb to the PDMS surface. The next day, micropillar devices were cleaned with ethanol, DI water, ethanol, and dried with filtered air. They were then plasma treated with oxygen for 5 min. Meanwhile, the stamp was rinsed with DI water and dried with filtered air. The plasma-treated micropillar devices were immediately placed in conformal contact with the cleaned stamp so that the top of the pillars were exposed to the surfactant and let sit for 5 min. The micropillar devices were then placed individually into six-well plates and UV sterilized (Taylor Scientific, 17-1703) for 10 min. Immediately following sterilization, devices were coated with 20 μg/mL collagen I (Sigma-Aldrich, C3867-1VL) in PBS. The plates were then sealed using parafilm and let sit overnight at 4°C.

4.2.3. Cell Seeding and MSC EV Collection

After sufficient coating, the collagen was removed and the devices were washed twice with PBS before seeding MSCs at a density of 2.5×10^4 cells/well in EV-depleted media. At the same time, MSCs were seeded into T175 tissue culture flasks (VWR, 29185-308) either un-coated or coated with 20 μg/mL collagen I as well as featureless PDMS devices (i.e., PDMS without micropillars) as controls. After 24 h, the media in the flasks were discarded and replaced with fresh EV-depleted media. The seeded devices were transferred to compartmentalized petri dishes (100 mm×15 mm; Celltreat, 229684) with 4 mL of EV-depleted media per compartment. Devices were moved from the six-well plates to the compartments to maximize the volume of conditioned media while keeping the device contained and restricted from excessive movement. Conditioned media was collected and replaced every 24 h for three days.

For count data (i.e., to determine number of EVs produced per cell), four of each type of device were seeded, along with one coated and uncoated flask. 24 h after the initial media discard and replacement, conditioned media of the groups designated for count data were collected and kept separate. Cells within the devices were fixed, stained, and counted as described in section 4.2.4. Cells from the flasks were detached using trypsin (0.25%) EDTA (1X) (VWR, 02-0154-0100) and counted as the average of three cell counts that were made using a Countess 3 Automated Cell Counter (Invitrogen, Waltham, MA, USA).

For imaging purposes, two of each type of device were seeded. MSCs were also seeded directly on two #1.5 high resolution glass coverslips. 24 h after seeding the media was replaced and after another 24 h the cells were fixed, stained, and imaged as described in section 4.2.4.

4.2.4. Immunofluorescence Staining and Imaging

24 h after the initial media discard and replacement, cells within the devices (with and without pillars) and those seeded directly onto coverslips that were designated for imaging, as well as those cells designated for count data, were fixed in cold 4% PFA diluted in PBS for 20 min on ice with gentle agitation. PFA solution was removed and the cells were washed three times with PBS (10 min washes). Cells were permeabilized with 0.5% Triton X-100 in PBS for 7 min at room temperature with gentle agitation. The permeabilization solution was then removed, the cells were washed three times with PBS (10 min washes), and blocked for nonspecific binding for 1 h at room temperature using 2.5% goat serum (Abcam, ab7481) prepared in PBS. For those being used for count data, after blocking the cells were then stained using a Hoechst (Thermo Scientific, 62249; 1:10,000) solution in PBS and incubated at room temperature for 30 min with gentle agitation. The cells were then washed three times with PBS and imaged using an Olympus IX83 microscope (Olympus, Shinjuku City, Tokyo, Japan). Images were imported into ImageJ and cells were counted using the BioInformant macro. These cell counts were later used to calculate the total # of EVs/cell. For the rest of the fixed cells, after blocking, a rabbit anti-

phospho-paxillin (Cell Signaling Technology, 69363; 1:100) was diluted in 1% goat serum in PBS, added to the cells, and incubated at 4°C overnight on a shaker.

24 h later, the primary antibody was removed and cells were washed three times in PBS (10 min washes) and incubated with Hoechst (Thermo Scientific, 62249; 1:10,000), Alexa Fluor Plus 647 Phalloidin (Thermo Scientific, A30107; 1:150), and a fluorescent secondary antibody for 1 h at room temperature with gentle agitation. The secondary antibody used to detect paxillin was Alexa Fluor 488 goat anti-rabbit at a 1:200 dilution (Thermo Scientific, A32731). Cells were then washed three times in PBS. The devices were inverted onto a #1.5 high resolution coverslip, placed onto a microscope slide, and imaged using a 60× objective on an Olympus FLUOVIEW FV3000 laser scanning confocal microscope (Olympus, Shinjuku City, Tokyo, Japan).

4.2.5. MSC EV Isolation

Conditioned media from MSCs cultured in EV-depleted media were subjected to a sequence of differential centrifugation steps to clear the media of debris as previously described [11, 144]. Briefly, the media was centrifuged at 1,000 × g for 10 min to eliminate any intact cells that may have been collected. The supernatant was then collected and centrifuged at 2,000 × g for 20 min to extract any larger pieces of cellular debris. This supernatant was then centrifuged at 10,000 × g for 30 min to remove any large organelles and apoptotic bodies. The EVs from the clarified conditioned media were then isolated using either

ultracentrifugation (UC) or tangential flow filtration (TFF) as described below. Purified EV samples were kept at 4°C and were evaluated within three days of isolation.

For UC, the conditioned media underwent a final centrifugation step at 118,000 × *g* for 2 h at 4°C in a Type 70 Ti ultracentrifuge rotor (Beckman Coulter). The pelleted EVs were resuspended in PBS and transferred to a Nanosep 300 kDa MWCO spin column (Pall, OD300C35) and spun at 8,000 × *g* until all PBS passed through the membrane (~10-12 min). EVs were washed by resuspension two more times using PBS, resuspended in PBS, and sterile filtered through a 0.2 μm syringe filter.

Isolation using TFF was completed via a KrosFlo KR2i TFF system (Spectrum Labs, Los Angeles, CA, USA) equipped with a 300 kDa MWCO hollow fiber filter made of a modified polyethersulfone membrane (Spectrum Labs, D02-E100-05-N). To remove the bacteriostatic reagent, the filter was first cleaned with at least three volumes of PBS. Samples were then processed at a transmembrane pressure (TMP) of 5 psi and the shear rate was kept at 4000 s^{-1} by keeping the flow rate at a continuous 106 mL/min. The samples were first concentrated to a volume of ~25 mL and diafiltrated five times in PBS to change buffers. After buffer exchange, the sample was then further concentrated to a volume of 8-12 mL. The sample was removed from the reservoir and further concentration was performed using a 100 MWCO centrifugal concentrator

(Corning, 431486) to obtain a final volume of ~0.5 mL which was then sterile filtered through a 0.2 μm syringe filter.

4.2.6. MSC EV Characterization

Total EV protein concentration of the washed EVs was measured using BCA per the manufacturer's protocol. Particle concentration and size distribution were assessed using a NanoSight LM10 (Malvern Instruments; Malvern, UK) with Nanoparticle Tracking Analysis (NTA) software version 2.3. Each sample was measured three times with a camera level set at 12 and acquisition time of 30 s and a uniform detection threshold set across samples. For each video, at least 200 completed tracks were analyzed with 20-100 objects per frame. The total number of EVs was then calculated based on resuspension volume. Final data was expressed as total number of EVs per cell.

Immunoblotting was then performed to confirm the presence of EVs and purity of each sample. Based on the BCA analysis, 7 μg of protein from each EV sample was used for analysis and compared with cell lysate. The presence of various EV-associated proteins was assessed using primary antibodies for Alix (Abcam, ab186429), TSG101 (Abcam, ab125011), CD63 (Proteintech, 25682-1-AP), and GAPDH (Cell Signaling Technology, 2118), while the absence of cell debris from EV samples was confirmed using an antibody for calnexin (Cell Signaling Technology, 2679). All primary antibodies were added at a 1:1,000 dilution, except GAPDH which was diluted 1:2,000. A 1:15,000 dilution of a

goat anti-rabbit secondary (LI-COR Biosciences, 926-32211) was added and protein bands were imaged using a LI-COR Odyssey CLX Imager.

For transmission electron microscopy (TEM) images, 10 µl of each EV sample was fixed using 4% EM-grade PFA (10 µl) for 30 min at room temperature. After fixation, the EV/PFA mixture was adsorbed to a carbon-coated copper grid with type 200 mesh (Electron Microscopy Sciences, CF200-Cu-25) for 20 min. The grid was washed on top of a PBS drop and then placed on a drop of 1% glutaraldehyde in PBS for 5 min. The grid was washed extensively (5-7 times x 2 min) on deionized water droplets, blotting carefully in between each wash at a 45° angle on a piece of filter paper. The grid was then laid on top of a uranyl acetate replacement stain droplet (Electron Microscopy Sciences, 22405) for 10 min. After drying, the grid was imaged at 200 kV on a JEOL JEM 2100 LaB6 TEM.

4.2.7. Tube Formation Assay

Growth factor reduced Matrigel (100 µl) (Corning, 354230) was used to coat a 24-well plate which was then incubated at 37°C for 30 min. HUVECs were passaged at 80% confluency and seeded at 6×10^4 cells/well with complete growth media (EGM2 media; positive control), basal media (EBM2 media + 0.1% FBS) devoid of EVs (negative control), or basal media (EBM2 media + 0.1% FBS) with EVs (5×10^9 EVs/mL) on top of the solidified Matrigel. After six hours of incubation, cells were imaged using a Nikon Eclipse Ti2 Microscope with a 2× objective. The total number of fully-closed loops formed

by the HUVECs was used as a proxy for the formation of capillary-like structures in tissue regeneration.

4.2.8. mRNA Isolation and Profiling in Recipient Cells

P3 HUVECs were seeded at 4×10^4 cells per well in a 24-well plate that was previously coated with 0.1% gelatin at 37 ˚C for 1 h. After 24 h, HUVECs were treated in quadruplicate using basal media (+ 0.1% FBS) spiked with EVs from MSCs cultured on devices without pillars (i.e., no pillars) or devices with micropillars spaced 5 μm apart (5×10^9 EVs/mL). 24 h later the cellular RNA was isolated. To ensure that detached cells were analyzed, the media from each condition was collected and placed into labeled conical tubes. HUVECs were then washed once with warmed PBS and the PBS was placed into the same conical tubes. The media/PBS solution was spun at 220 × *g* for 5 min at room temperature to pellet the cells. While the cells were spinning, the cells in each treatment were quickly lysed with 700 μl of QIAzol lysis reagent (Qiagen, 79306) and pipetted into labeled 2 mL centrifuge tubes. Once pelleted, the supernatants on top of the cells that were spun were discarded, the cells were resuspended in warmed PBS to remove all media components, and then spun again. The PBS supernatants were then removed and the resulting cell pellets were lysed using the same QIAzol reagent from the appropriate treatments.

The HUVEC RNA was isolated using a miRNeasy kit (Qiagen, 217004) and cDNA was prepared using the iScript cDNA synthesis kit (Bio-Rad, 1708891).

Per the manufacturer's instructions, approximately 50 ng of cDNA was used per 20 µl reaction in the Taqman™ Array Human Angiogenesis (Thermo Scientific, 4414071). The reactions were prepared using Taqman™ Fast Advanced Master Mix (Thermo Scientific, 4444556) and real-time PCR was performed using the QuantStudio 7 Flex Real-Time PCR System (Applied Biosystems, Waltham, MA, USA) with recommended thermal cycler settings for the Taqman™ Fast Advanced Master Mix. The ΔΔCt method was used to analyze the data. GAPDH mRNA was used as the housekeeping gene (ΔCt = Ct target gene – Ct GAPDH) and results were normalized to the HUVECs treated with the no pillar device EVs (ΔΔCt = ΔCt 5 µm micropillar device – ΔCt no pillar device). Normalized fold change was calculated as $2^{-\Delta\Delta Ct}$. Results of the array were confirmed using the three most upregulated genes through qPCR as described above. Primer sequences are shown below.

Primer sequences for qPCR of TIE1:

Forward: ATGGCTGCTCTTGTGGATCTGG

Reverse: CGGTCACAAGTGCCACCATTCT

Primer sequences for qPCR of COL4A1:

Forward: TGTTGACGGCTTACCTGGAGAC

Reverse: GGTAGACCAACTCCAGGCTCTC

Primer sequences for qPCR of COL18A1:

Forward: GGAGAGATTGGCTTTCCTGGAC

Reverse: CCTCATGCCAAATCCAAGGCTG

Primer sequences for qPCR of GAPDH:

Forward: AACTTTGGCATTGTGGAAGG

Reverse: GGATGCAGGGATGATGTTCT

4.2.9. Statistics

Data are displayed as mean ± standard error of the mean (SEM). Normality of each data set was tested and, when appropriate, parametric tests (one or two-way ANOVA with Šídák's or Tukey's multiple comparisons tests) were used as appropriate to determine statistical differences ($p < 0.05$) among groups, unless otherwise stated in figure captions. All statistical analyses were completed using Prism 9.1 (GraphPad Software, La Jolla, CA, USA). Notation for significance in figures are as follows: ns – $p > 0.05$: * - $p < 0.05$; ** - $p < 0.01$; *** - $p < 0.001$; ****- $p < 0.0001$.

4.3 Results

4.3.1. Validation of MSC Culture in Micropillar Devices

The design of the micropillar device utilized in this investigation was previously generated by Doolin and Stroka [272]. The spacings between the micropillars (i.e., 5, 10, 20, or 50 μm) were chosen as they represent typical dimensions of *in vivo* tracks and *in vitro* scaffolds [272, 276]. Doolin and Stroka were able to verify, using scanning electron microscopy, that the fabrication protocol produced devices of the desired dimensions and that the devices could be used to significantly alter MSC morphology [272]. Using confocal microscopy, we were able to confirm that, in our hands, MSCs could fully infiltrate into all of

the micropillar designs and cause a visually perceptible change in MSC morphology (**Figure 4.2**).

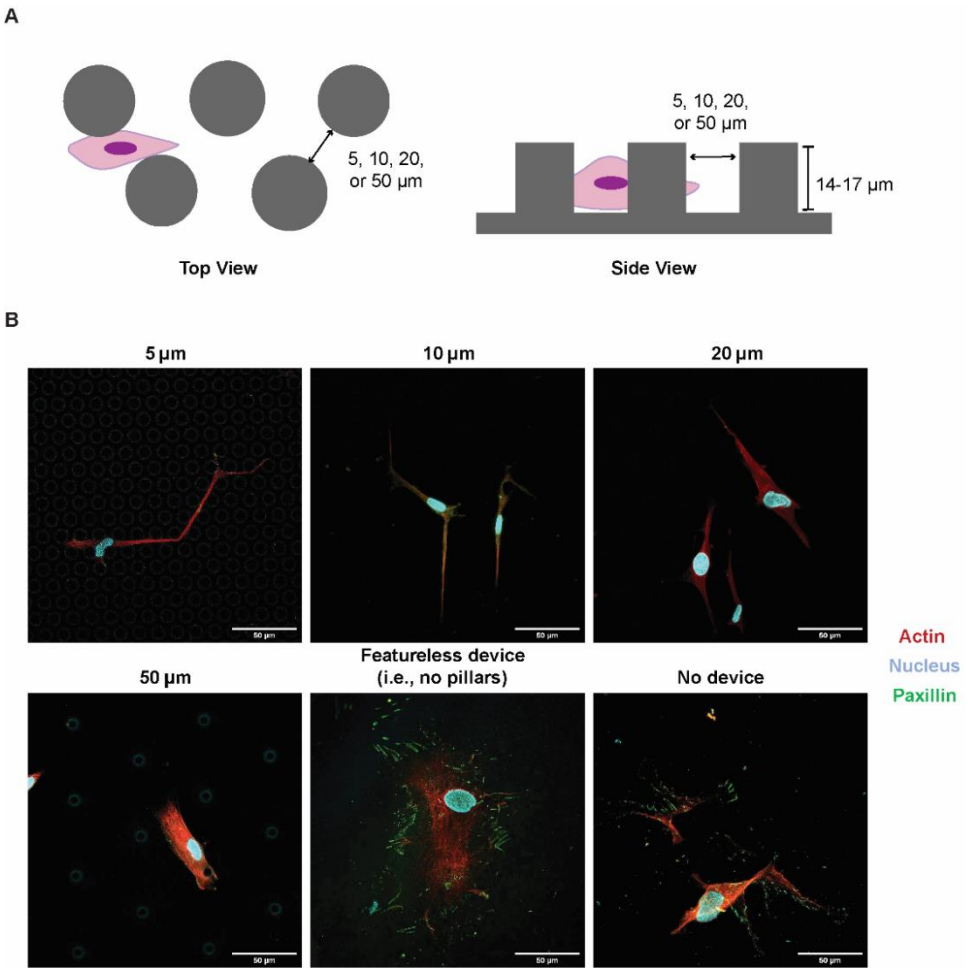


Figure 4.2. MSCs can be cultured within PDMS micropillar devices. (A) Schematic depicting the top view (left) and side view (right) of the PDMS micropillar device in which MSCs were cultured. (B) Confocal images of MSCs cultured within the micropillar devices with spacings of 5, 10, 20, or 50 µm as well as on devices without pillars and without any device. All surfaces were coated with collagen. After 24 h, MSCs were fixed and stained for actin (red), paxillin (green), and the nucleus (blue). Scale bars represent 50 µm.

4.3.2. Culturing MSCs within Micropillar Devices Increases EV Production

First, we investigated the influence of confined culture on MSC EV production. After 24 h, EVs were isolated from control culture conditions (uncoated flask, collagen-coated flask, collagen-coated PDMS without pillars) and confined culture conditions (collagen-coated PDMS devices fabricated with micropillars spaced 5, 10, 20, or 50 μm apart) using ultracentrifugation. It is important to note that there were considerably less cells within the devices when compared with flask controls (10-15,000 cells per device vs 250,000 cells per flask) due to the fact that not all of the cells infiltrated the pillars upon seeding and were subsequently removed from the experiments. Despite this, cells within the devices produced similar amounts of EVs, leading to an augmented EV/cell measurement which was used as a proxy for EV production (**Figure 4.3.A**). NTA showed no significant difference in EV size distributions with 100 nm being the approximate mode size for all conditions (5 μm: 101.9 ± 6.9 nm; 10 μm: 96 ± 5.7 nm; 20 μm: 94.1 ± 8.1 nm; 50 μm: 96.6 ± 1.8 nm; no pillars: 92.5 ± 11.1 nm; flask with collagen: 99.5 ± 7.4 nm; flask without collagen: 90.4 ± 2.6 nm) (**Figure 4.3.B**). Greater than 90% of each population of EVs was less than 140 nm in diameter; well within the characteristic exosome diameter range of 40-200 nm (**Figure 4.3.B**) [34]. Western blot analysis confirmed the presence of EV markers (CD63, TSG101, and Alix) and the absence of the

cellular debris marker, calnexin, in all EV preparations (**Figure 4.3.C**). TEM images showed no observable change in MSC EV morphology (**Figure 4.3.D**).

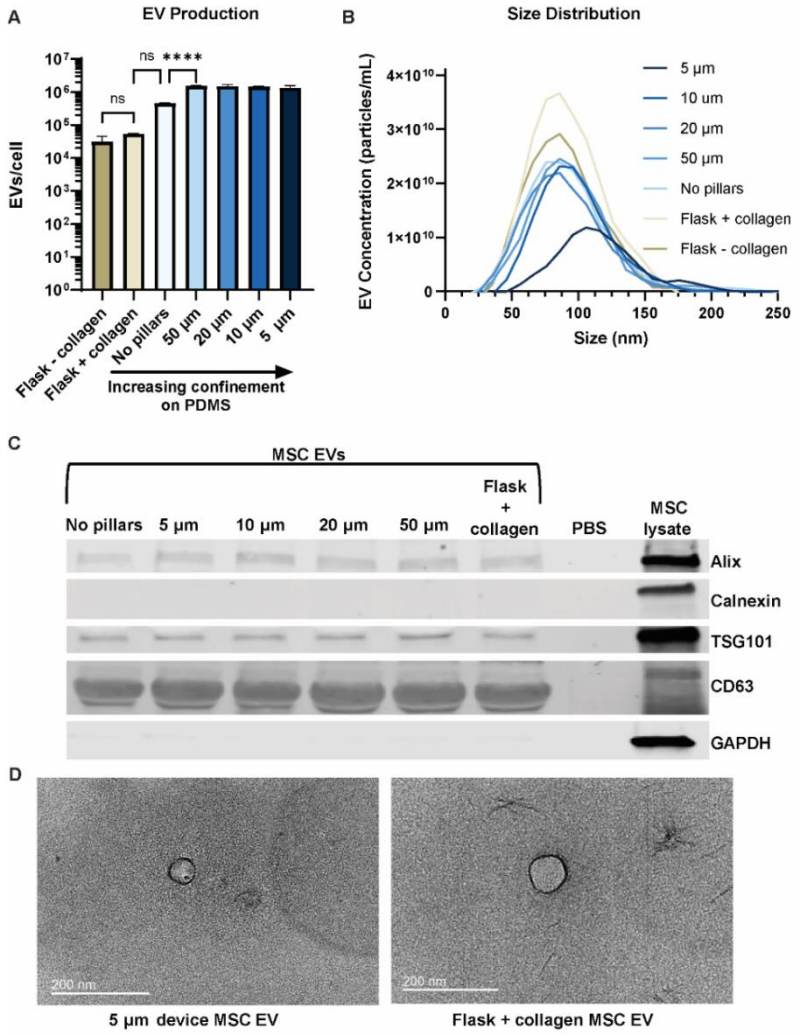


Figure 4.3. EV production is augmented when MSCs are cultured within the micropillar devices. (A) Number of EVs produced per MSC as measured using nanoparticle tracking analysis (NTA). (B) Size distribution of EVs from MSCs cultured in the various confinement conditions. (C) Immunoblots of MSCs and MSC EVs from the various confinement conditions for EV markers (CD63, TSG101, Alix), cell marker (Calnexin), and control marker (GAPDH). (D) Representative transmission electron microscopy images of EVs from MSCs cultured within the most confined condition (i.e., 5 µm micropillar device) and one of the least confined conditions (i.e., flask with collagen coating). All PDMS devices were coated with collagen. Scale bars represent 200 nm. Data representative of three independent experiments (N = 3). Statistical significance was calculated using a one-way ANOVA using Šídák's multiple comparisons tests (ns – $p > 0.05$; **** - $p < 0.0001$).

4.3.3. MSC Confinement Impacts EV Bioactivity

Bioactivity of MSC EVs isolated from all culture conditions was then evaluated using an *in vitro* tube formation assay, a gap closure assay, and a cell viability assay. In the tube formation assay, EVs from the uncoated flask culture significantly increased the number of capillary-like structures formed by the HUVECs (i.e., number of loops) when compared with the basal media negative control ($p < 0.001$; basal: 12.00 ± 3.210; flask without collagen: 49.00 ± 6.658) (**Figure 4.4**). Compared with the flask without collagen, there was a significant increase in the number of tubes formed when HUVECs were treated with EVs from MSCs cultured on the flask coated with collagen ($p < 0.05$; flask with collagen: 75.00 ± 5.568). There was no significant differences in HUVEC tube formation among the MSC EV preparations from flasks with collagen, PDMS devices without pillars, and PDMS devices with micropillars spaced 50 μm apart ($p > 0.05$; device without pillars: 70.67 ± 2.848; 50 μm device: 65.3 ± 4.33). MSC EVs collected from the PDMS devices with micropillars 20 μm apart significantly increased the number of loops formed by HUVECs when compared with EVs from PDMS without pillars ($p < 0.05$; 20 μm device: 94.67 ± 2.404) and with those from the 50 μm device ($p < 0.01$). This elevated effect was maintained when HUVECs were treated with the EVs derived from MSCs cultured in the devices with 5 and 10 μm micropillar spacings with no significant difference between these two conditions ($p > 0.05$; 5 μm: 103.3 ± 2.186; 10 μm: 112 ± 8.889). Interestingly, the 5, 10, and 20 μm micropillar devices produced MSC EVs that significantly improved tube formation relative

to the positive control ($p < 0.01$, $p < 0.0001$, $p < 0.05$, respectively; growth media: 68.33 ± 4.667) (**Figure 4.4**).

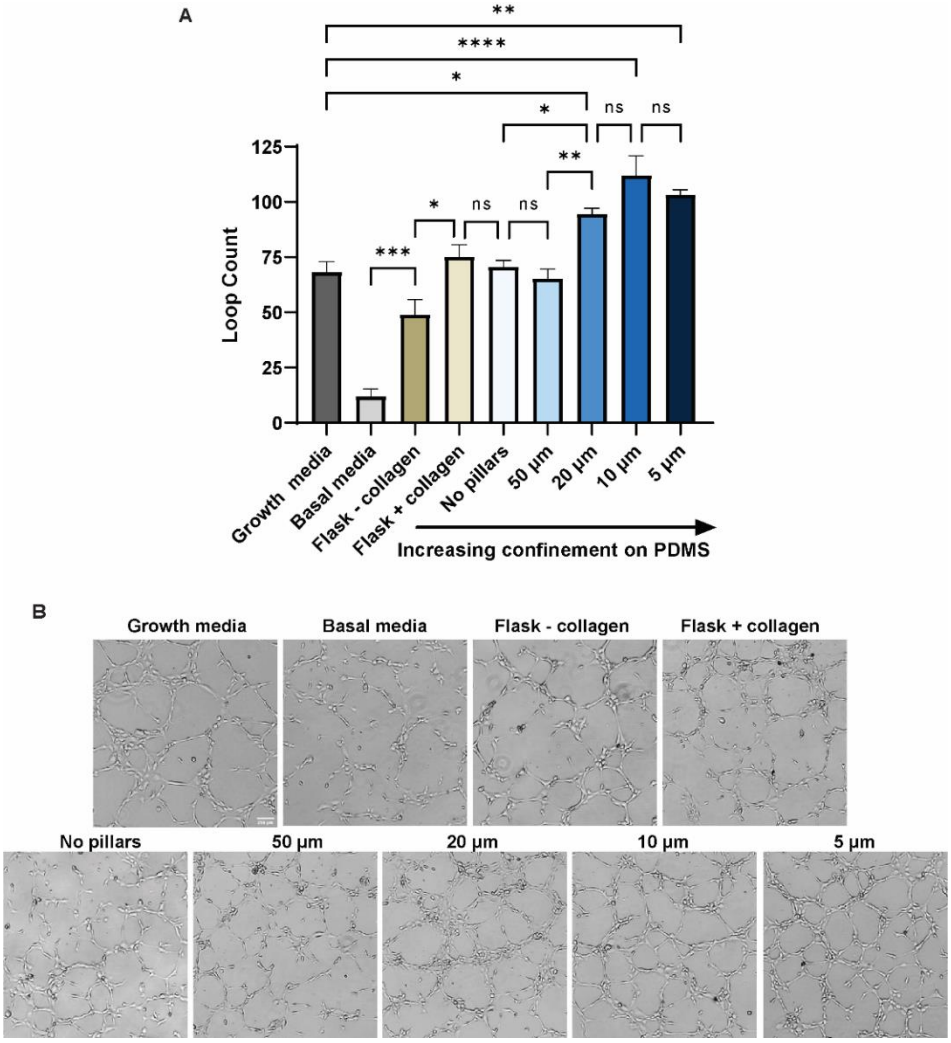


Figure 4.4. Mechanical confinement during MSC culture augments in vitro tube formation activity of MSC EVs. (A) Tube formation results were quantified as the number of complete loops formed by HUVECs. EVs from the MSCs cultured in the PDMS devices with micropillar spacings of 5, 10, and 20 µm significantly increased the number of loops when compared with EVs from MSCs cultured on PDMS devices without pillars and when compared with growth media (positive control). All PDMS devices were coated with collagen. (B) Representative images of HUVECs in the tube formation assay 6 h after application of growth media (positive control), basal media (negative control), or basal media with EVs from MSCs maintained in the various culture conditions (5×10^9 EVs/mL). Scale bar represents 250 µm. All images and data are representative of three independent experiments (N = 3). Statistical significance was calculated using a one-way ANOVA with Šídák's multiple comparisons tests (ns – $p > 0.05$; * - $p < 0.05$; ** - $p < 0.01$; *** - $p < 0.001$, **** - $p < 0.0001$).

Since the bioactivity of EVs has been known to be dependent on the chosen isolation strategy [116, 117], we investigated whether or not the augmented tube formation activity observed when isolating via ultracentrifugation (UC) was lost when isolating using utilizing tangential flow filtration (TFF); an emerging scalable technique for EV isolation [277]. Conditioned media was collected from MSCs in the flasks with collagen and from MSCs within the 5 μm micropillar devices. The media from each condition was split and half was isolated using UC while the other half was isolated using TFF. Results showed that MSC EVs from the flask culture and isolated using UC significantly improved tube formation when compared with the negative control ($p < 0.0001$; basal: 17.67 ± 2.028; UC flask: 44 ± 2.082) (**Figure 4.5**). This effect was not lost when the flask MSC EVs were isolated using TFF ($p > 0.05$; TFF flask: 52 ± 1.155). Again, we found that EVs from MSCs grown in the 5 μm micropillar devices and isolated via UC were able to augment tube formation in HUVECs when compared with EVs from the unconfined culture condition isolated using UC ($p < 0.0001$; UC 5 μm: 80.67 ± 2.333). There was a slight decline in bioactivity when the MSC EVs from the 5 μm micropillar devices were isolated using TFF when compared with those isolated using UC ($p < 0.05$; TFF 5 μm: 92 ± 1.528). However, they were still shown to significantly upregulate tube formation activity when compared with the flask MSC EVs isolated using TFF ($p < 0.0001$). The results also showed that, regardless of isolation strategy, MSC EVs from the 5 μm micropillar devices significantly improved the number of

loops formed by HUVECs in comparison with the positive control (UC – $p < 0.0001$; TFF – $p < 0.01$; growth media: 65 ± 3.512) (**Figure 4.5**).

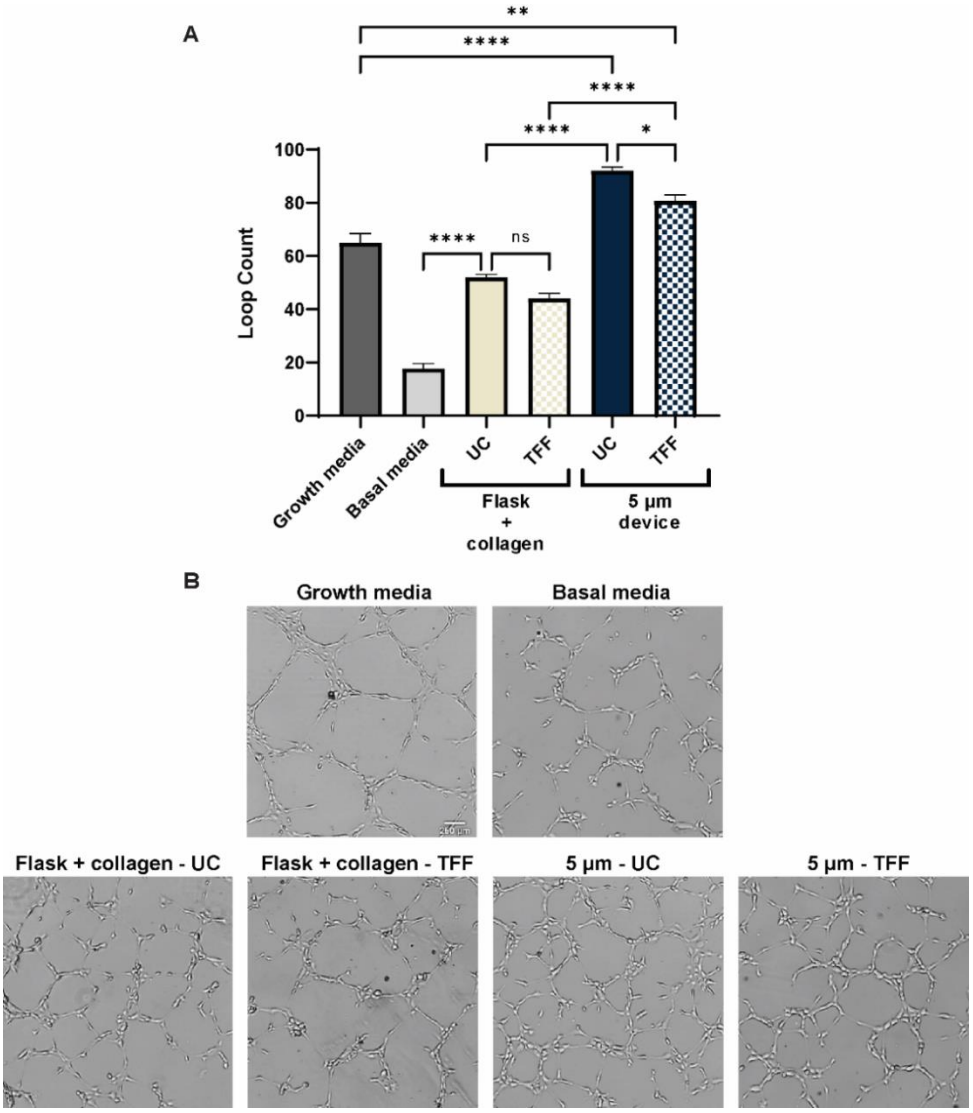


Figure 4.5. EV isolation strategy has no effect on the observed tube formation enhancement facilitated by confinement. (A) Tube formation results were quantified as the number of complete loops formed by HUVECs. Regardless of isolation strategy (i.e., ultracentrifugation – UC or tangential flow filtration – TFF), EVs from the MSCs confined within the PDMS devices with micropillar spacings of 5 µm significantly increased the number of tubes formed when compared with those cultured in flasks. All PDMS devices were coated with collagen. (B) Representative images of HUVECs in the tube formation assay 6 h after application of growth media (positive control), basal media (negative control), or EVs from MSCs maintained in the various culture conditions (5×10^9 EVs/mL). Scale bar represents 250 µm. All images and data are representative of three independent experiments (N = 3). Statistical significance was calculated using a one-way ANOVA with Šídák's multiple comparisons tests (ns – $p > 0.05$; * - $p < 0.05$; ** - $p < 0.01$; **** - $p < 0.0001$).

In the gap closure assay, when treated with uncoated flask-derived MSC EVs, HUVECs had a significantly higher gap closure when compared with the negative control that consisted of basal media devoid of MSC EVs ($p < 0.01$; basal: 29.37 ± 3.081; flask without collagen: 43.53 ± 2.031) (**Figure 4.6.A**). However, there was no significant difference among any of the MSC EVs from the various culture conditions ($p > 0.05$). Additionally, there was no improvement in viability when HUVECs were co-incubated with each of the MSC EV preparations for 48 h compared with the basal media negative control ($p > 0.05$) (**Figure 4.6.B**).

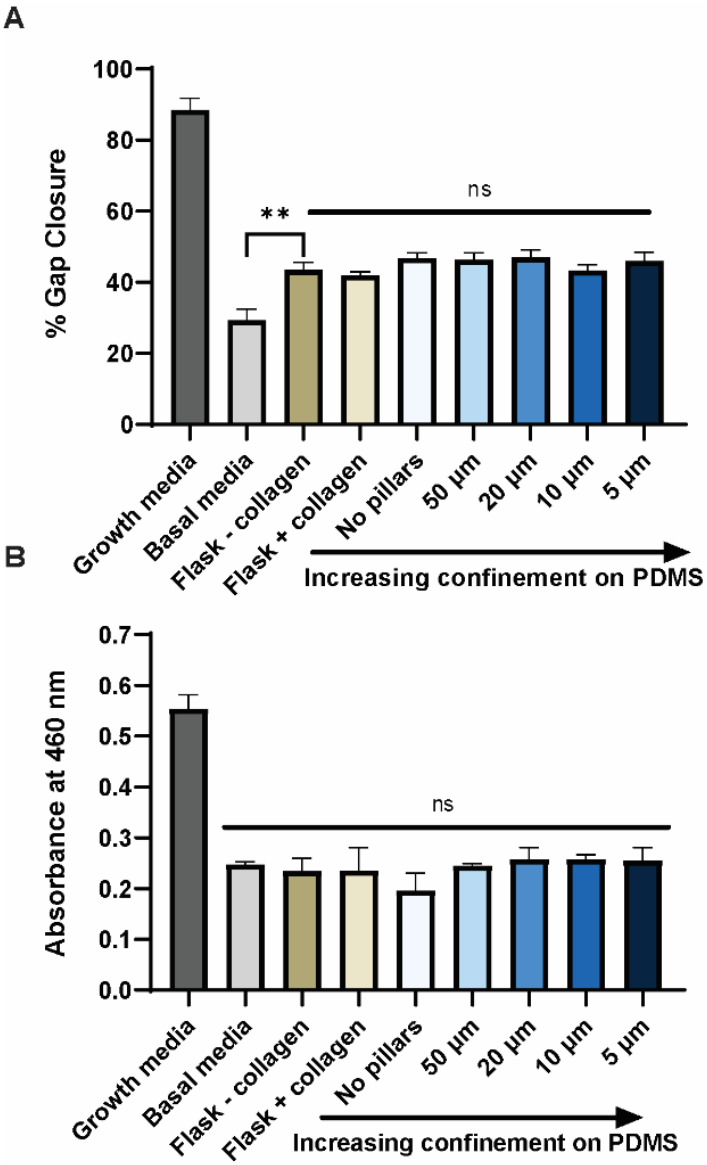


Figure 4.6. EVs from confined MSCs had no effect on the migratory potential and viability of recipient HUVECs. (A) Gap closure assay results quantified as cell gap area after 20 h as a percentage of gap area at 0 h. There were no significant difference in gap closure among the EV treatments. (B) HUVEC viability was measured using a WST-8 assay. MSC EVs did not alter HUVEC viability after co-incubation for 48 h when compared with the negative control (i.e., basal media). All PDMS devices were coated with collagen. Data are representative of three independent experiments (N = 3). Statistical significance was calculated using a one-way ANOVA with Šídák's multiple comparisons tests (ns – $p > 0.05$; ** - $p < 0.01$).

4.3.4. EVs from Confined MSCs Alter Gene Expression in Recipient Cells

In an attempt to understand the mechanism underlying the apparent enhanced bioactivity in the tube formation assay, we screened for the expression of 72 genes associated with angiogenesis in recipient HUVECs (**Figure 4.7.A**). When HUVECs were treated with EVs from the MSCs cultured within the 5 μm micropillar devices, 20 of the evaluated genes were upregulated while 6 were down regulated more than 2-fold compared with HUVECs treated with EVs from the MSCs cultured on the PDMS without pillars (**Figure 4.7.B**). Logistically constrained by the array setup, only one technical replicate was performed per gene, thus no statistical analysis was able to be performed. Despite this, we moved forward and specifically analyzed several of the genes (i.e., TIE1, COL4A1, and COL18A1) using qPCR but were not able to replicate the results from the array (**Figure 4.8**). TIE1, COL4A1, and COL18A1 were significantly upregulated in HUVECs treated with MSC EVs from the no pillar devices or the 5 μm micropillar devices in comparison with PBS-treated HUVECs ($p < 0.0001$). However, contrary to the mRNA array performed, there were no significant differences in the expression of TIE1 and COL18A1 between the two groups of EVs ($p > 0.05$). Additionally, the expression of COL4A1 in HUVECs treated with EVs from the devices without pillars were significantly upregulated when compared with those treated with 5 μm micropillar device EVs ($p < 0.01$) (**Figure 4.8**).

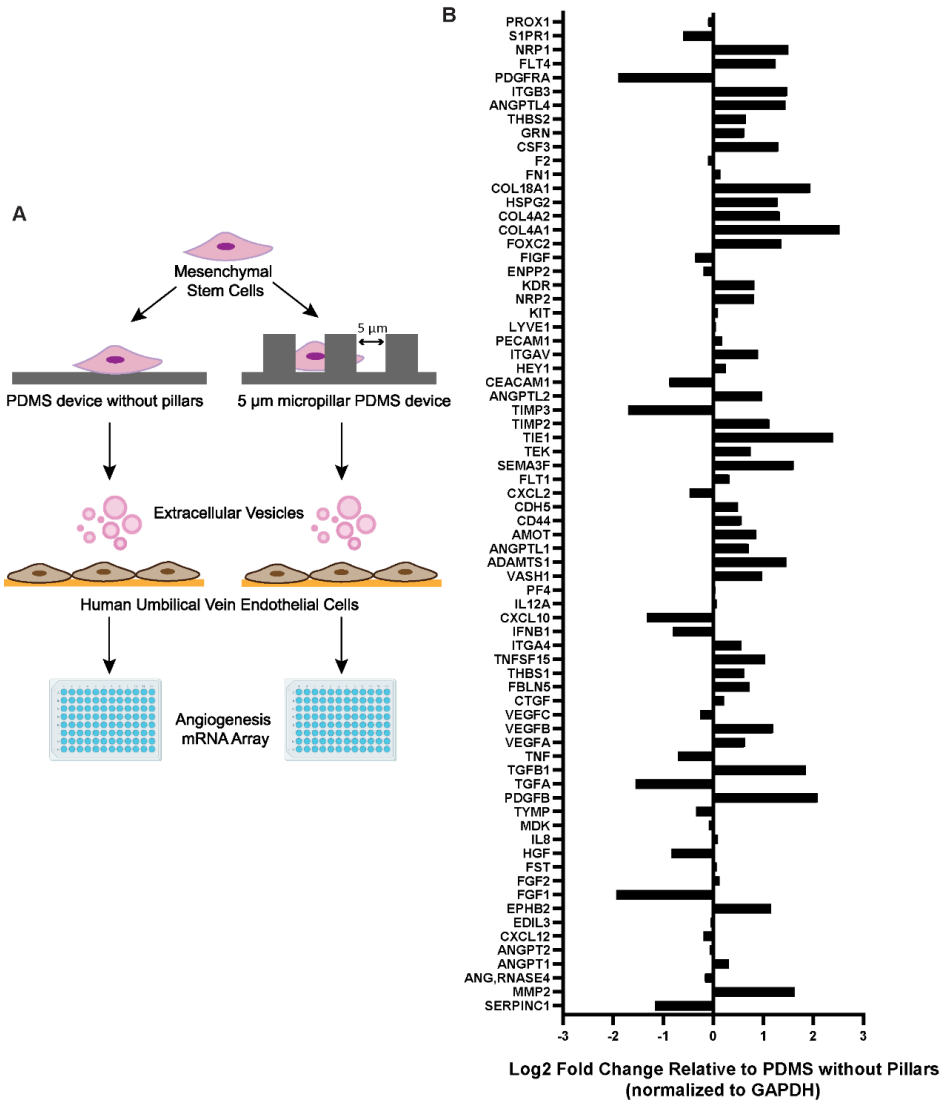


Figure 4.7. Angiogenesis-related gene expression in HUVECs treated with EVs from MSCs cultured in PDMS devices with micropillar spacings of 5 µm. (A) Experimental schematic of angiogenesis-specific gene expression analysis in HUVECs treated with EVs from MSCs cultured on the PDMS devices without pillars and in the 5 µm micropillar devices. All PDMS devices were coated with collagen. (B) Gene expression of 72 genes associated with angiogenesis in HUVECs after treatment with EVs from MSCs cultured in 5 µm micropillar device. Data shown as log2 of the fold change relative to EVs from MSCs cultured on PDMS without pillars. Data was calculated using the ΔΔCt method. ΔΔCt = (ΔCt target gene – ΔCt GAPDH), where ΔCt target gene = (Ct 5 µm device – Ct no pillar device).

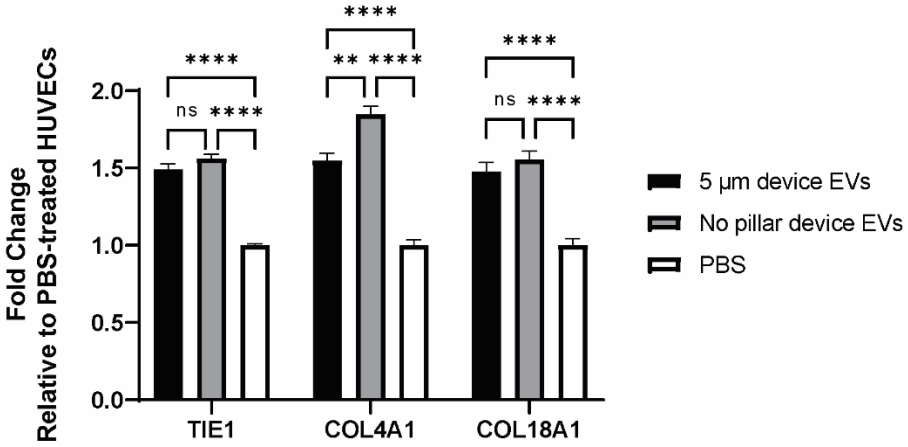


Figure 4.8. Gene expression of TIE1, COL4A1, and COL18A1 in EV-treated HUVECs. HUVECs were analyzed after being treated with PBS (vehicle control), EVs from MSCs in the devices without micropillars, or EVs from the MSCs cultured within the 5 µm micropillar devices. All PDMS devices were coated with collagen. Data shown as fold change relative to HUVECs treated with PBS and normalized to GAPDH. Data was calculated using the ΔΔCt method. = (ΔCt 5 µm device or no pillar device – ΔCt PBS), where ΔCt = (Ct target gene – Ct GAPDH). Data is representative of one biological replicate with 3 technical replicates. Statistical significance was calculated using a two-way ANOVA using Šídák's multiple comparisons tests (ns – $p > 0.05$; ** - $p < 0.01$; **** - $p < 0.0001$).

4.4 Discussion

Mechanical confinement can alter numerous aspects of MSC physiology known to regulate cell function and phenotype, including morphology, metabolism, differentiation, and the cell secretome [271, 272, 278]. Here, we aimed to understand how confinement influences the production and bioactivity of MSC EVs. To do so, we utilized a device previously optimized for the confinement of MSCs [272] which consisted of PDMS decorated with micropillars spaced 5, 10, 20, or 50 µm apart. Our results suggest that culturing MSCs in the presence of the micropillars significantly increased MSC EV production (i.e., number of EVs per cell) (**Figure 4.3.A**). This can be expected as confinement has been shown to increase cell membrane tension which,

in turn, can result in amplified exocytotic activity [253, 254, 279]. Some studies have found that this mechanically-induced exocytotic activity is connected to the activation of calcium-ion channels. For instance, a recent study by Li and colleagues showed that activation of the mechanosensitive transient receptor potential vanilloid 4 (TRPV4) channel enhanced exocytosis in melanoma cells and was dependent on the influx of calcium ions from the extracellular space [280]. Indeed, TRPV4 channels are abundant in MSCs, along with other mechanically-activated calcium ion channels like Piezo 1 [281] and increased intracellular calcium has been shown to augment EV biogenesis in MSCs [169]. In addition to mechanoreceptor stimulation, confinement can induce nuclear membrane protein reorganization [271, 278]. It has been shown that this reorganization can alter key regulators of gene expression, specifically Yes-associated protein/transcriptional co-activator with PDZ-binding motif (YAP/TAZ), which has been shown to be localized to the nucleus in physically confined MSCs [282]. In a study by Guo and colleagues, mechanically-activated YAP was responsible for the observed uptick in EV secretion when MSCs were cultured in dynamic conditions [170]. For future studies, it would be interesting to see if YAP/TAZ and/or calcium ion channels play a similar role in the increased MSC EV production observed when MSCs are confined as in the present investigation.

Furthermore, there were no differences in EV production among the cells grown within the different micropillar spacings, indicating more of a threshold-based response rather than a dose-response to increased level of confinement (**Figure 4.3.A**). This may be explained by the fact that multiple pathways may be activated during MSC confinement

(e.g., YAP/TAZ, calcium signaling, etc.) with possible additive effects on EV secretion, and thus a saturation in EV production could be expected. Future studies should probe multiple pathways in order to understand the relative contributions to confinement-induced MSC EV production. Additionally, experiments should confirm the increase in EV production by quantifying known EV markers (i.e., CD63) via ELISA. NTA and TEM images of MSC EVs from the different culture conditions revealed similar size distributions and morphologies, respectively (**Figure 4.3.B, D**). Western blot analysis confirmed the absence of the cellular debris marker calnexin, indicating that the confinement conditions were not promoting the release of apoptotic bodies (**Figure 4.3.C**).

In terms of bioactivity, we found that, in general, MSC EVs significantly increased the tube formation capacity of HUVECs (**Figure 4.4**). This is in line with numerous previous studies that have depicted similar results when applying MSC EVs in the tube formation assay [127, 283, 284]. Interestingly, there was a significant increase in tube formation when using MSC EVs from the flask coated with collagen compared with those derived from the uncoated flask condition. In the present investigation, collagen I was dissolved in pH 7.4 PBS; as is often done in cells studies utilizing PDMS [272, 285]. However, a study by Stanton and colleagues revealed that, in comparison to pH 3.4 acetic acid, collagen solutions of 7.4 pH PBS tended to form fibrous bundles and exhibited greater heterogeneity when coated onto PDMS substrates [286]. The same study showed that, depending on the solvent used, collagen could alter the localization of the transcriptional regulator YAP – a well-known mechanotransducer in MSCs [287]

– and may affect how cells sense substrate stiffness [286]. In the present investigation, we used the collagen-coated flasks and collagen-coated featureless PDMS devices (i.e., PDMS without pillars) as a means to decouple any effect of collagen coating. Nevertheless, it would be interesting and important to investigate the effects of various preparations of extracellular matrices on the bioactivity of MSC EVs in future studies.

The results from this study also indicate that confinement of MSCs significantly increases the effect of subsequently-secreted EVs on endothelial cell tube formation ability. This enhancement was observed when MSCs were cultured within devices with micropillar distances of 5, 10, or 20 μm (**Figure 4.4**). Notably, MSC EVs from the 50 μm micropillar devices and the featureless devices performed similarly to those from the collagen-coated flask condition, suggesting that the observed increase in bioactivity was not solely due to the PDMS substrate itself or to the collagen coating. The loss of this enhanced bioactivity occurred between the 20 and 50 μm micropillar devices, likely due to the inability of the MSCs to appropriately sense the pillars in the 50 μm configuration. In a study by Mills et al., it was discovered that MSC migration within channels was only altered when the width of the channel approached the diameter of a single cell [288]. As MSCs range from 15-30 μm in diameter [289], the 50 μm device may have been at too large of a scale to have this specific effect on the MSC EVs. The level of confinement needed to elicit increased effect on tube formation (i.e., 20 μm) was different from the level necessary for increased EV production (i.e., 50 μm). This may indicate that these two phenomena require disparate levels of mechanical stimulation and/or that they work through different mechanisms. Interestingly,

previous research implicates that YAP and mechanoreceptors, both of which can also be linked to increased EV production, can alter angiogenic properties of MSCs. For instance, in a study by Bandaru et al., it was shown that the secretion of the pro-angiogenic factor VEGF from MSCs is dependent on YAP activity [290], which, as previously discussed, has been shown to be upregulated in confined MSCs [282]. In another study, mechanical stimulation of Piezo calcium ion channels in adipose-derived MSCs was found to significantly enhance their therapeutic effect on vascular density in a diabetic erectile dysfunction rat model [291]. Thus, future knockdown and inhibition studies should be performed to determine if these same pathways play a role in both the increased EV production and augmented EV bioactivity observed in the present investigation.

Next, as the MSC EVs were isolated using ultracentrifugation, we wanted to assess whether the observed bioactivity in the tube formation assay could be retained using a disparate method of isolation. TFF was chosen as it is a highly scalable and GMP-compatible technique that holds promise in the production of clinical-grade EVs [277]. We found that, regardless of isolation technique, EVs from MSCs cultured in the most confined micropillar devices (i.e., 5 μm) preserved their ability to significantly augment tube formation in HUVECs (**Figure 4.5**). This implies that the observed effect is indeed due to the MSC EVs themselves and not an artefact of isolation.

Surprisingly, despite the improved activity observed in the tube formation assay, MSC EVs from the various confinement conditions had no effect on endothelial cell

migration in the gap closure assay (**Figure 4.6.A**) or viability in the WST-8 assay (**Figure 4.6.B**). Although these assays (specifically the tube formation and gap closure) are typically used in conjunction to evaluate the *in vitro* effects of EVs on angiogenesis, it is important to note that the underlying mechanics of each assay are different. For instance, the formation of tubes in the tube formation assay depends on the differentiation of the endothelial cells [292], an event that does not take place when these cells are cultured in a monolayer on tissue culture plastic as is done in the gap closure and WST-8 assays. Thus, the MSC EVs prepared in the present study may be specifically influencing endothelial cell differentiation more so than endothelial cell migration or viability. This, along with the fact that the tube formation assay involves the use of basement membrane matrix (i.e., Matrigel) that is meant to simulate the *in vivo* process, may be contributing to the discrepancy in the results.

Finally, we showed that, when compared with EVs from MSCs cultured on the PDMS without micropillars, MSC EVs from the 5 μm micropillar PDMS device altered angiogenic gene expression in recipient HUVECs (**Figure 4.7**). Specifically, TIE1, COL4A1, and COL18A1, were a few of the most upregulated genes. TIE1 is essential in angiogenesis and vascular integrity [293] while the deposition of COL4A1 by endothelial cells has been shown to be critical for vascular survival and maturation *in vivo* [294]. Interestingly, a proteolytic fragment of COL18A1, known as endostatin, is recognized as an anti-angiogenic factor [295]. However, angiogenesis is controlled by intricate pathways regulated by both pro- and anti-angiogenic factors [296]. Regardless, we were unable to recapitulate the array results using qPCR. This could be

due to deficits in the quality of the genetic material used as well as the relatively low accuracy and specificity which are both known issues inherent to microarray analyses [297]. More direct strategies such as proteomics or RNA-seq on the MSC EVs themselves, coupled with knockdown studies, should be used to identify the specific EV cargoes responsible for the observed bioactivity.

To our knowledge, this study is the first to highlight the influence of MSC confinement on the production and bioactivity of subsequently secreted EVs. By culturing MSCs within PDMS micropillar devices, we demonstrated that confinement can be used to increase MSC EV production and alter MSC EV angiogenic bioactivity. Additionally, as many cells experience confinement within the physiological niche, these micropillar devices can be used investigate the effect of this mechanical cue on EVs from various cell types. This research and future work will be instrumental in the design of optimal EV biomanufacturing strategies as well as the fine tuning of tissue-engineered constructs that enable cell phenotypes maximized for a given therapeutic application.

Chapter 5: Culturing Mesenchymal Stem Cells on Polydimethylsiloxane of Various Elastic Moduli Improves Extracellular Vesicle Production and *in vitro* Bioactivity

5.1 Introduction

Within the body, tissue stiffness has been found to have profound implications in many pathological conditions including cancer [24, 25], cardiovascular diseases [26], fibrosis [23], and chronic wounds [298]. This has spawned an interest in how substrate stiffness, typically described as the elastic modulus, affects cellular behavior; much of which is often focused on MSCs [299]. These studies have revealed that substrate stiffness can be a powerful driver of the immunosuppressive and angiogenic potential of MSCs [300-302]. Numerous additional studies have demonstrated that substrate stiffness can also control MSC proliferation, morphology, and differentiation [303-305]. Despite the clinical relevance and effect of substrate stiffness on MSC biology, to our knowledge, only one study has directly looked at the effect of substrate stiffness on MSC EVs. Lenzini and colleagues found that culturing MSCs on soft hydrogels (3 kPa) increased MSC EV production while maintaining therapeutic activity in an LPS-induced acute lung injury mouse model when compared to EVs from MSCs cultured on stiff (20 kPa) hydrogels and tissue culture plastic (0.1 GPa) [180]. Given these results and the clinical relevance of substrate stiffness, further investigation into the effect of stiffness on MSC EV activity is warranted.

In Chapter 4, we demonstrated that mechanical confinement in a PDMS-based micropillar device was able to significantly alter MSC EV production and bioactivity. Notably, PDMS has been utilized in numerous cell mechanotransduction studies evaluating substrate stiffness [303, 306-308]. In several of these studies, the PDMS (i.e., Sylgard 184) was tuned by adjusting the ratio of the elastomer base to crosslinker reagent to produce elastic moduli reaching from 570 kPa to 3.7 MPa [309]. An even wider range of elastic moduli (i.e., 5 kPa to 1.72 MPa) was obtained when two different types of PDMS (i.e., Sylgard 184 and Sylgard 527) were mixed [306, 308]. In the present investigation, we used these techniques to examine the effect of substrate stiffness on MSC EVs. Our results suggest that PDMS stiffness can be harnessed to augment MSC EV bioactivity and enhance MSC EV angiogenic bioactivity. As a cost-effective, biocompatible, and non-toxic material, PDMS has a history of use in many biomedical and biomanufacturing applications including microfluidic devices and bioreactor design [310-312]. As such, the results obtained here will contribute to the optimization of an appropriate MSC EV biomanufacturing protocol as well as help elucidate the interface between material science and EV-based therapeutic development.

5.2 Methods

5.2.1. Cell Culture

Bone marrow-derived mesenchymal stem cells (MSCs; passage 2) were purchased from ATCC (PCS-500-012) and maintained in Dulbecco's Modification of Eagle's Medium (DMEM) (Corning, 10-013-CV) with 10% fetal bovine serum (FBS; VWR, 89510-186), 1% non-essential amino acids (NEAA; Fisher Scientific, 11-140-050), and 1% penicillin-streptomycin (P/S; Corning, 30-002-CI). MSCs were seeded into experiments at passage 3 in media containing 10% EV-depleted FBS (referred to as EV-depleted media). To EV-deplete the FBS, heat-inactivated FBS was centrifuged at 118,000 × *g* for 16 h after which the supernatant was carefully decanted and filtered through a 0.2 μm bottle-top filter.

Human umbilical vein endothelial cells (HUVECs; pooled donors) from ATCC (C-12203) were cultured on tissue culture polystyrene flasks (T75) coated with 0.1% gelatin at 37 ˚C for 1 h prior to seeding. HUVECs were maintained in complete endothelial growth medium-2 (EGM2; PromoCell C-22111) supplemented with 1% P/S and expanded so they were at passages 3-5 in all studies. During experiments, HUVECs were kept in endothelial basal medium-2 (EBM2; PromoCell, C-22221) supplemented with 0.1 % FBS and 1% P/S.

5.2.2. PDMS Substrate Fabrication and Characterization

PDMS (Sylgard 184; Krayden, DC2065622) base and crosslinker reagent were mixed at five different ratios by weight (5:1, 10:1, 20:1, 33:1, and 50:1), where the 10:1 ratio represented the suggested formulation by the manufacturer. Each mixture (~2 g) was poured into one of four compartments of a compartmentalized petri dish (Cell Treat, 229684) and allowed to coat evenly. Care was taken to maintain 2 g within each compartment to keep thickness the same across substrates. The compartmentalized dishes were utilized to allow for collection of an adequate amount of conditioned media (~4 mL per compartment) while still maintaining access to the substrate for surface treatment procedures that were performed immediately prior to cell seeding (see Section 5.2.3). The dishes with the PDMS were then placed into a vacuum desiccator for ~30 min to remove all air bubbles and then baked at 80°C for 1 h. The dishes were then removed from the oven and let rest until experiments.

Additional experiments in which two types of PDMS, Sylgard 184 (Krayden, DC2065622) and Sylgard 527 (Krayden, DC1696742), were then performed. First, each type of PDMS was made according to the manufacturer's protocol: Sylgard 184 was mixed at a 10:1 base to crosslinker reagent ratio and Sylgard 527 was mixed at a 1:1 base to crosslinker reagent ratio (by weight). Then, the Sylgard 184 and Sylgard 527 were mixed at various weight ratios (10:1, 5:1, 1:1, 1:5, 1:10). Each mixture (~2 g) was poured into one of four compartments of a compartmentalized petri dish and allowed to coat evenly. The PDMS-filled

dishes were then placed into a vacuum desiccator for ~30 min to remove air bubbles. All PDMS substrates were cured at 65°C overnight and then let cool. All substrates were used within one week of fabrication.

After fabrication and prior to cell seeding, PDMS substrates were cleaned with ethanol, DI water, ethanol, and dried with filtered air. They were then plasma treated with oxygen for 5 min. The plasma-treated substrates were sterilized in a UV sterilizer (Taylor Scientific, 17-1703) for 10 min. Directly after sterilization, devices were coated with 20 μg/mL collagen I (Sigma-Aldrich, C3867-1VL) in PBS. The dishes were then sealed using parafilm and let sit overnight at 4°C.

5.2.3. MSC Seeding and MSC EV Collection

The collagen coating was discarded and the PDMS substrates were washed twice with PBS before seeding MSCs at a density of 10×10^3 cells/compartment in EV-depleted media. At the same time, MSCs were seeded into T175 tissue culture flasks (VWR, 29185-308) either un-coated or coated with 20 μg/mL collagen I at the same seeding density (~700 cells/cm^2) and acted as controls. After 24 h, the media in all conditions were discarded and replaced with fresh EV-depleted media. Conditioned media from each PDMS substrate was collected and replaced every 24 h for three days.

For count data (i.e., to determine number of EVs produced per cell), four compartments of each type of substrate were seeded, along with one coated and uncoated flask. 24 h after the initial media discard and replacement, conditioned media of the groups designated for count data were collected and kept separate. Cells from all conditions were detached using trypsin (0.25%) EDTA (1X) (VWR, 02-0154-0100) and counted as the average of three cell counts that were made using a Countess 3 Automated Cell Counter (Invitrogen, Waltham, MA, USA).

5.2.4. MSC Viability Assay

To assess if the PDMS mixtures were toxic to MSCs, 50 µl of PDMS substrates prepared as in Section 5.2.3 were pipetted into a 96-well plate in sextuplicate. Following plasma treatment and UV sterilization, substrates were collagen-coated overnight as in Section 5.2.3 as well as six wells without PDMS (collagen control). MSCs were seeded into three of the wells coated with each type of PDMS substrate, three of the collagen-coated wells without PDMS, and three of the uncoated wells without PDMS at 3×10^3 cells/well in 200 µl of EV-depleted MSC media. Three additional wells were also seeded as a negative control (i.e., DMSO treatment). Three wells of each treatment were left without cells to serve as normalization controls for the assay. Additionally, a standard curve ranging from 0 – 10,000 cells/well in duplicate was seeded using serial dilutions in order to quantify the number of cells/well at any point during the assay if desired. The following day, the cells were checked for adequate seeding

and a WST-8 assay (Abcam; ab228554) was performed per the manufacturer's protocol. In short, the WST-8 reagent was diluted 10X in EV-depleted MSC media and warmed to 37°C. The medium within the wells was discarded and 115 µl of the diluted WST-8 reagent was added to all of the wells (i.e., the wells with cells and the correlating blank wells, as well as the standard curve wells). The plate was then incubated for 4 h at 37°C. After incubation, 100 µl of each well was carefully removed as to not disturb the cells and pipetted into the wells of a new 96-well plate. The remaining WST-8 medium on the cells was discarded and 200 µl of fresh EV-depleted MSC media was carefully pipetted into each well. For the negative control, EV-depleted MSC media supplemented with 10% DMSO was added to induce cell death. All cells were then placed back into the incubator. The plate with the cell-conditioned WST-8 media was centrifuged at 1,000 × g to remove all air bubbles and then the absorbance of each well was read at 460 nm. This process was repeated every 24 h for 4-5 days on all wells, except the standard curve which was only completed on the first day.

5.2.5. MSC Identity Verification

As substrate stiffness has been known to differentiate MSCs [304], immunoblotting was performed to confirm that the identity and multipotency status of the MSCs remained relatively the same across substrates. To do so, MSCs were cultured for three days (i.e., the longest time of any experiment in the current investigation) on collagen-coated flasks, all of the Sylgard 184 base to crosslinker reagent ratio substrates (i.e., 5:1, 10:1, 20:1, 33:1, and 50:1), and

the Sylgard 527 substrate. The cells were then washed once with 1X PBS and lysed using RIPA lysis buffer (Thermo Scientific, 89901) supplemented with 1% protease inhibitor, 1% EDTA, and 1 mM phenylmethylsulfonyl fluoride (PMSF). A BCA was performed to determine the cell lysate protein concentration and 25 μg of cell lysate was loaded into each well. The presence of MSC markers were probed using primary antibodies for CD90 (Abcam, ab92574), CD73 (Abcam, ab133582), and CD105 (Abcam, ab169545) as well as GAPDH (Cell Signaling Technology, 2118). Primary antibodies for a negative MSC marker (CD45; Abcam, ab281586) and a marker of multipotency (SOX2; Abcam, ab133337) were also employed. All primary antibodies were added at a 1:1,000 dilution, except GAPDH which was added at a 1:2,000 dilution. A goat anti-rabbit secondary (LI-COR Biosciences, 926-32211) was added at a dilution of 1:15,000 and bands were imaged using a LI-COR Odyssey CLX Imager.

5.2.6. MSC EV Isolation and Characterization

MSC-conditioned media collected from each culture condition was subjected to several differential centrifugation steps to remove any unwanted debris as previously described [11, 144]. Briefly, the media was centrifuged at 1,000 × g for 10 min to remove any whole cells that may have detached from the substrate during media collection. The supernatant was then centrifuged at 2,000 × g for 20 min to pellet any larger pieces of cellular debris. This supernatant was then centrifuged at 10,000 × g for 30 min to remove any organelles and apoptotic bodies. Finally, the supernatant from this spin underwent a final centrifugation

step at 118,000 × *g* for 2 h at 4°C in a Type 70 Ti ultracentrifuge rotor (Beckman Coulter). The EV pellet was then resuspended in PBS, pipetted into a Nanosep 300 kDa MWCO spin column (Pall, OD300C35), and spun at 8,000 × *g* until all PBS passed through the membrane (~10-12 min). EVs were washed by resuspension two more times using PBS, resuspended in PBS, and sterile filtered through a 0.2 μm syringe filter. All EV preparations were store at 4° C and used within three days of isolation.

Protein concentration of each of the final EV preparations was measured using BCA according to the manufacturer's protocol. Particle concentration and size distribution were measured using a NanoSight LM10 (Malvern Instruments; Malvern, UK) with Nanoparticle Tracking Analysis (NTA) software version 2.3. Three videos of each sample were captured with a camera level set at 14 and acquisition time of 30 s and a detection threshold of 3. A minimum of 200 completed tracks were analyzed per video with 20-100 objects per frame. The total EV count was then determined based on resuspension volume. Final data was represented as total number of EVs/cell using the cell counts previously measured.

Western blot analysis was completed to verify the presence of EVs and purity of each sample. Based on the BCA results, 6 μg of protein from each EV sample or cell lysate was loaded into each well. The presence of various EV-associated proteins was evaluated using primary antibodies for Alix (Abcam, ab186429),

TSG101 (Abcam, ab125011), CD63 (Proteintech, 25682-1-AP), and GAPDH (Cell Signaling Technology, 2118), while the absence of cell debris from EV samples was confirmed using an antibody for calnexin (Cell Signaling Technology, 2679). All primary antibodies were incubated with samples at a 1:1,000 dilution, except GAPDH which was diluted at 1:2,000. A goat anti-rabbit secondary (LI-COR Biosciences, 926-32211) at a dilution of 1:15,000 was added and bands were visualized using a LI-COR Odyssey CLX Imager.

To prepare samples for transmission electron microscopy (TEM), 10 µl of each EV sample was fixed using 4% EM-grade PFA (10 µl) for 30 min at room temperature. After fixation, 10 µl of the EV/PFA mixture was placed on a carbon-coated copper grid with type 200 mesh (Electron Microscopy Sciences, CF200-Cu-25) and was allowed to adsorb for 20 min. The grid was washed on top of a PBS drop and then placed on a drop of 1% glutaraldehyde in PBS for 5 min. The grid was thoroughly washed (5-7 times x 2 min) using droplets of deionized water, blotting carefully in between each wash at a 45° angle on a piece of filter paper. The grid was then laid on top of a uranyl acetate replacement stain droplet (Electron Microscopy Sciences, 22405) for at least 10 min. After drying completely, the grid was imaged at 200 kV on a JEOL JEM 2100 LaB6 TEM.

5.2.7. Tube Formation Assay

In preparation for the tube formation assay, a 24-well plate was coated with growth factor reduced Matrigel (Corning, 354230) by adding 100 µl to the

center of each well. Care was taken to ensure even coating of the Matrigel without the formation of bubbles. The plate was then placed into an incubator at 37°C for 30 min. HUVECs were passaged using trypsin and resuspended in basal media (EBM2 media + 0.1% FBS) for cell counting. To ensure full deactivation of the trypsin, basal media supplemented with 10% FBS was added to the cells prior to spinning and resuspension in EBM2 + 0.1% FBS. Cells were then seeded with complete growth media (EGM2 media; positive control), basal media (EBM2 media + 0.1% FBS) devoid of EVs (negative control), or basal media (EBM2 media + 0.1% FBS) with EVs (5×10^9 EVs/mL) on top of the solidified Matrigel at 6×10^4 cells per well. Images of the cells were taken 4-6 h later using a Nikon Eclipse Ti2 Microscope with a 2× objective. The number of fully-closed loops the HUVECs formed were counted and used to measure HUVEC ability to form capillary-like structures.

5.2.8. Gap Closure Assay

A 96-well plate was coated with 0.1% gelatin and incubated at 37°C for 1 h. The gelatin was then discarded and HUVECs were seeded at 1.5×10^4 cells/well in EGM2 complete growth medium. 24 h later, a scratch was made down the center of each well using an AutoScratch (BioTek Instruments; Winooski, VT, USA). Cells were then gently washed one time with 1X PBS and incubated for 2 h with endothelial cell basal medium supplemented with 0.1% FBS and 1% P/S to serum starve the cells. After serum starvation, medium was replaced with fresh EGM2 (positive control), EBM2 (0.1% FBS) without EVs (negative control), or EBM2 with EVs spiked in for a final concentration of 5×10^9

EVs/mL. The cell gap was imaged at 0 h and 20 h using a Nikon Eclipse Ti2 Microscope at 2x magnification. The change in the gap area from 0 to 20 h was determined using ImageJ as previously described [164].

5.2.9. mRNA Isolation and Profiling in Recipient HUVECs

A 24-well plate was coated with 0.1% gelatin and incubated at 37 ˚C for 1 h. The gelatin was then discarded and HUVECs were seeded at 4×10^4 cells per well and allowed to attach overnight. The next day, HUVECs were treated in quadruplicate with just PBS, EVs from MSCs cultured on collagen-coated flasks, or EVs from MSCs grown on the softest PDMS substrate (Sylgard 527; 3 kPa) in basal media supplemented with 0.1% FBS and 1% P/S (5×10^9 EVs/mL). 24 h later, HUVEC RNA was isolated. To ensure that all cells were included in the analysis (i.e., attached and detached cells), the media from each condition was collected and placed into labeled conical tubes. The HUVECs were washed one time with warmed PBS and the PBS was collected and placed into the same conical tubes. The media and PBS solution within the conical tubes was spun at 220 × *g* for 5 min at room temperature to pellet the cells. While the cells were spinning, the cells in the wells were quickly lysed with 700 µl of QIAzol lysis reagent (Qiagen, 79306) and placed into labeled 2 mL centrifuge tubes. Once pelleted, the supernatant on top of the cells was discarded, the cell pellet was washed with ~1 mL of warm PBS, and spun again to ensure the removal of all media components which could disrupt downstream analyses. The PBS supernatant was discarded and the pelleted cells were lysed

in the same QIAzol reagent from the appropriate treatments. The RNA was then isolated immediately as detailed below.

Immediately after collection, the HUVEC RNA in QIAzol was homogenized by vortexing each sample for 1 min. The samples were then allowed to sit at room temperature for 5 min to allow disassociation of the nucleoprotein complexes. The RNA was then isolated using a miRNeasy kit (Qiagen, 217004). cDNA was prepared using 1 μg of RNA from each sample following the instructions in the iScript cDNA synthesis kit (Bio-Rad, 1708891). Then, in alignment with the manufacturer's recommendation, approximately 170 ng of cDNA was used per 20 μl reaction in the GeneQuery™ Human Angiogenesis qPCR Array Kit (ScienCell, GK017). The reactions were prepared using GoldNStart TaqGreen qPCR Master Mix (ScienCell, MB6018) with ROX reference dye spiked in so as to obtain a final concentration of 50 nM of ROX in each reaction of the qPCR analysis. As this procedure required running multiple plates, an adequate volume of master mix with ROX dye for all plates (plus 12% overage) was made and maintained on ice and protected from light. The cDNA from each sample (enough for 170 ng per well) was mixed thoroughly with the appropriate amount of master mix (including 12% overage) immediately prior to loading onto the plate. The plate was allowed to reach room temperature and the samples were loaded (20 μl) using a multi-channel pipette and carefully pipetted up and down 3-5 times within the wells to mix (except the no-template control well). Care was taken to completely dispense

all sample into the wells and change tips between each well so as to not introduce cross-contamination. The plate was then tightly sealed with an optical plate seal and spun in a chilled centrifuge at 1,500 × *g* for 2 min to remove any air bubbles. After confirming that all air bubbles were removed, the cover was checked to ensure a very tight seal, and the plate was covered with foil to protect from light. Immediately prior to analysis, the bottom of the plate was cleaned with isopropanol to remove any dust particles. Real-time PCR was performed using the QuantStudio 7 Flex Real-Time PCR System (Applied Biosystems, Waltham, MA, USA) with the recommended thermal cycler settings (Initial denaturation: 95°C for 10 min; denaturation: 95°C for 20 s; annealing: 65°C for 20 s; extension: 72°C for 20 s). Immediately prior to the run completion, the next plate was prepared in a similar manner and this was continued until all samples were processed. The ΔΔCt method was used to analyze the data as detailed by the array manufacturer's instructions. In brief, the mRNA of actin, GAPDH, NONO, LDHA, and PPIH were used as housekeeping genes (ΔCt HKG = Ct HKG, PDMS or flask sample – Ct HKG, PBS sample; ΔCt ref for PDMS or flask sample = average ΔCt HKG1, ΔCt HKG2…ΔCt HKG5). The results were relative to the PBS-treated HUVECs for each gene of interest (GOI) (ΔCt GOI, PDMS or flask sample – ΔCt GOI, PBS sample; ΔΔCt = ΔCt GOI, PDMS or flask sample – ΔCt ref of PDMS or flask sample). Normalized fold change was calculated as $2^{-\Delta\Delta Ct}$. Results of the array were displayed as log2 of the normalized fold change.

Further analysis of the three most upregulated genes from the array was completed using qPCR methods. First, the HUVEC experiment and RNA isolation was repeated as detailed above. 33 ng of cDNA from each sample was used for each of the qPCR reactions (10 μl) which were prepared using SsoAdvanced Universal SYBR Green Supermix (Biorad, 172-5270) per the manufacturer's instructions. The plate was loaded and bubbles were removed by centrifugation as described above. Real-time PCR was then performed using the QuantStudio 7 Flex Real-Time PCR System. The reaction cycle was 95°C for 2 min, followed by 40 cycles of 95°C for 15 s and 60°C for 1 min. Expression was normalized to GAPDH and was made relative to HUVECs treated with PBS. Fold change was calculated as $2^{-\Delta\Delta Ct}$. Primer sequences are shown below.

Primer sequences for qPCR of E-selectin:

Forward: TCAAGGGCAGTGGACACAGCAA

Reverse: GGAAACTGCCAGAAGCACTAGG

Primer sequences for qPCR of PLAU:

Forward: GGCTTAACTCCAACACGCAAGG

Reverse: CCTCCTTGGAACGGATCTTCAG

Primer sequences for qPCR of PARD3:

Forward: CGGTCAAAAGAGAACCACGCAG

Reverse: CATTCACCCGAAGCCTTCCATC

Primer sequences for qPCR of GAPDH:

Forward: AACTTTGGCATTGTGGAAGG

Reverse: GGATGCAGGGATGATGTTCT

5.2.10. miRNA Isolation and Profiling in MSC EVs

RNA of EVs from the MSCs cultured in collagen-coated flasks and MSCs cultured softest PDMS substrate (Sylgard 527, 2 kPa) was isolated and the miRNA fraction was enriched following the appropriate protocols in the miRNeasy kit (Qiagen, 217004). cDNA was prepared using the miRCURY LNA RT kit (Qiagen, 339340) following the 40 µl protocol and using the maximum volume of RNA. Per the manufacturer's instructions, cDNA was diluted by 10X using sterile, nuclease-free water. Reactions were prepared using the recommended All-in-One™ qPCR Mix (Genecopoeia, QP002) with ROX reference dye spiked in for a final concentration of 50 nM in each reaction well. As this procedure required running multiple plates, an adequate volume of master mix with ROX dye for all plates (plus 12% overage) was made and maintained on ice and protected from light. The diluted cDNA from each sample (enough for 1 µl per well) was mixed thoroughly with the appropriate amount of master mix (including 12% overage) immediately prior to loading (20 µl per well) into the miProfile™ Human MSC Exosome qPCR Array plate (Genecopoeia, qm046-A6) using a multi-channel pipette. As the sample was loaded, care was taken to thoroughly mix by pipetting 3-5 times and fully dispense the sample into each well. Tips were changed between wells to avoid contamination. Real-time PCR was performed using the QuantStudio 7 Flex Real-Time PCR System (Applied Biosystems, Waltham, MA, USA) with the recommended thermal cycler settings for the All-in-One™ qPCR Mix (Initial

denaturation: 95°C for 10 min; denaturation: 95°C for 10 s; annealing: 60°C for 20 s; extension: 72°C for 20 s). The ΔΔCt method was used to analyze the data as detailed by the array manufacturer's instructions.

5.2.11. Statistics

Data are displayed as mean ± standard error of the mean (SEM). Normality of each data set was tested and, when appropriate, parametric tests (one or two-way ANOVA with Šídák's or Tukey's multiple comparisons tests) were used as appropriate to determine statistical differences ($p < 0.05$) among groups, unless otherwise stated in figure captions. All statistical analyses were completed using Prism 9.1 (GraphPad Software, La Jolla, CA, USA). Notation for significance in figures are as follows: ns – $p > 0.05$: * - $p < 0.05$; ** - $p < 0.01$; *** - $p < 0.001$; ****- $p < 0.0001$.

5.3 Results

5.3.1. Altering Base to Crosslinker Reagent Ratio of Sylgard 184 PDMS Changes the Elastic Modulus and is Non-toxic to Cells

Varying the elastomer base to crosslinker reagent ratio allowed for PDMS substrates with a range of elastic moduli. The stiffest PDMS (5:1) resulted in an average approximate elastic modulus of 3.0 MPa, the medium-stiff PDMS (10:1) 2.4 MPa, the medium-soft PDMS (20:1) 1.2 MPa, and the softest PDMS (33:1) 0.3 MPa (**Figure 5.1.A**).

To examine the impact of PDMS manipulation on MSC viability, MSCs were cultured on the different PDMS substrates and a WST-8 cell viability assay was performed. MSCs were able to grow in all conditions, as demonstrated by the positive slope of absorbance values, which contrasted those MSCs within the condition meant to induce cell death (i.e., 10% DMSO). On the final day of culture, there was a significant difference between the MSCs grown in coated and uncoated flasks ($p < 0.05$) and between those cultured in coated flasks and those grown on any PDMS substrate ($p < 0.0001$) (**Figure 5.1.B**).

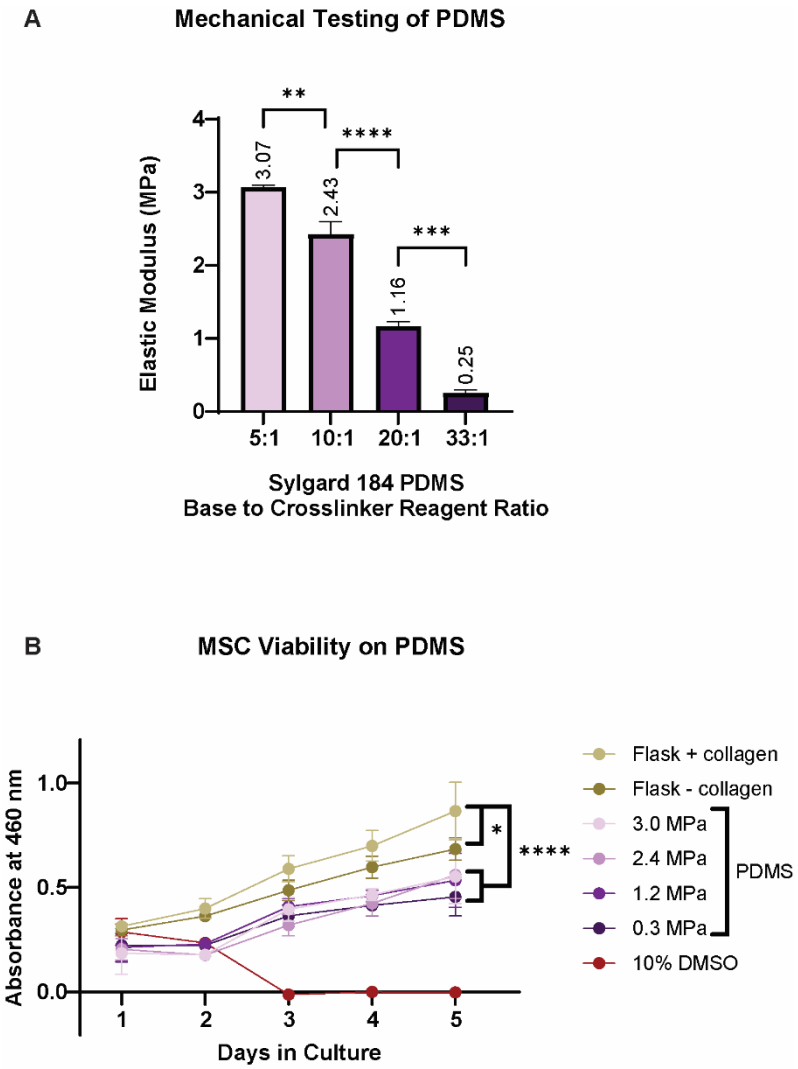


Figure 5.1. Varying the elastomer base to crosslinker reagent ratio of Sylgard 184 PDMS changes the elastic modulus without inducing cytotoxicity. (A) Elastic modulus of each of the four different PDMS formulations was measured using a Q800 Dynamic Mechanical Analyzer. Data is representative of two different fabrications of the substrates with three measurements per formulation. (B) WST-8 colorimetric cell viability results of MSCs cultured on the various PDMS formulations. All PDMS substrates were coated with collagen. Data is representative of three independent experiments (N = 3). Statistical differences were calculated using either (A) a one-way ANOVA with Šídák's multiple comparisons tests or (B) a two-way ANOVA with Tukey's multiple comparisons tests or a (* - $p < 0.05$; ** - $p < 0.01$; *** - $p > 0.001$; **** - $p < 0.0001$).

5.3.2. Culturing MSCs on Softer Sylgard 184 PDMS Substrates Improves EV Production

We then examined the effect of the different PDMS substrates on MSC EV production. Following 24 h of culture, the EVs were collected and isolated and the cells were counted. Similar to the PDMS micropillar devices in Chapter 4, there were less cells cultured on the PDMS substrates compared with flasks as the growth area of each compartment with PDMS (14.1 cm^2) was much less than one flask (175 cm^2). Regardless, the MSCs cultured on the PDMS substrates produced a similar amount of EVs leading to EV/cell measurements that increased as the elastic modulus of the substrate decreased (**Figure 5.2.A**). Although MSC EV production (i.e., EVs/cell) increased when cultured on the stiffest PDMS (3.0 MPa) (1E5 ± 4E3), the increase was not found to be significant until MSCs were cultured on the medium-soft PDMS (1.2 MPa) (2.6E5 ± 2.5E4), which was 16-fold higher than those cultured in the collagen-coated flask (1.7E4 ± 6E2). This increase was comparable to what was observed on the softest PDMS (0.3 MPa) (2.3E5 ± 5.5E4), which was 13-fold higher than the collagen-coated flask (**Figure 5.2.A**). Analysis of EV size using NTA showed no significant difference in EV size distributions with 95 nm being the approximate mode size for all conditions (flask - collagen: 89.8 ± 6.4 nm; flask + collagen: 97.2 ± 3.1 nm; 3.0 MPa: 93.6 ± 3.2; 2.4 MPa: 98.9 ± 6.0 nm; 1.2 MPa: 98.1 ± 7.2 nm; 0.3 MPa: 94.5 ± 10 nm). More than 90% of each EV population was less than 145 nm in diameter and within the range of typical exosomal diameter (**Figure 5.2.B**) [34]. Immunoblotting established the

presence of EV markers (CD63, TSG101, and Alix) as well as the absence of the cellular debris marker, calnexin (**Figure 5.2.C**). TEM images showed no perceptible change in EV morphology (**Figure 5.2.D**).

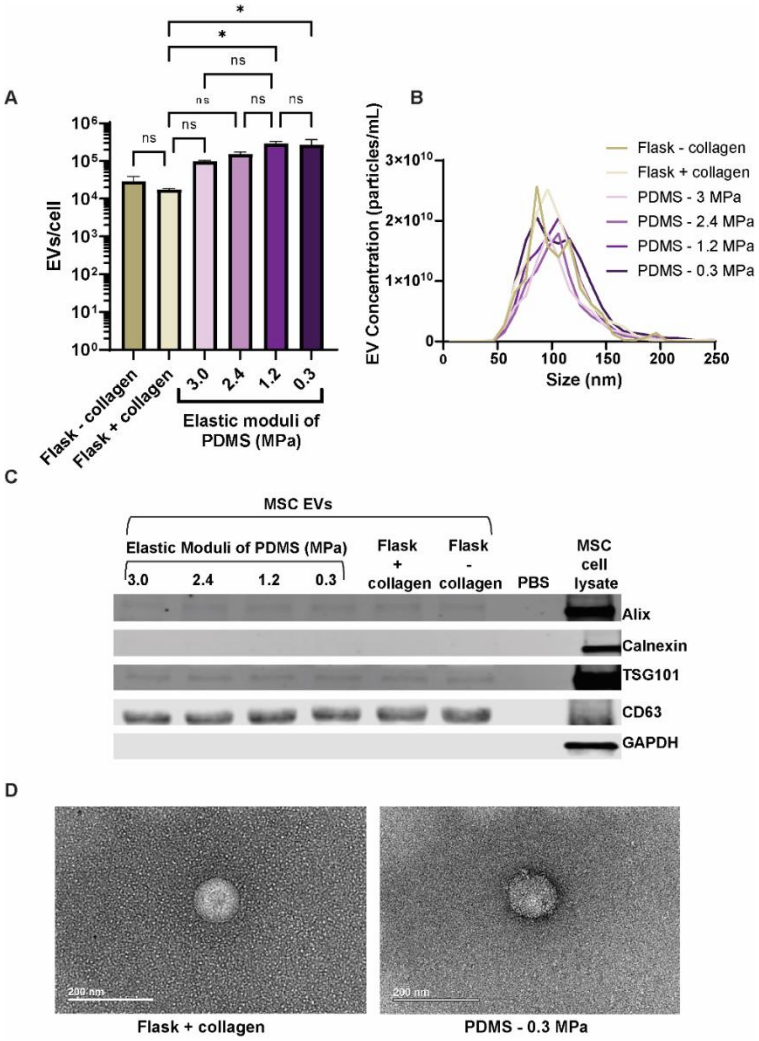


Figure 5.2. Culturing MSCs on the softest Sylgard PDMS formulation increases MSC EV production. (A) Number of EVs produced per MSC as measured using nanoparticle tracking analysis (NTA). (B) Size distribution of EVs from MSCs cultured on the various PDMS formulations. All PDMS substrates were coated with collagen. (C) Immunoblots of MSCs and MSC EVs from the various confinement conditions for EV markers (CD63, TSG101, Alix), cell marker (Calnexin), and control marker (GAPDH). (D) Representative transmission electron microscopy images of EVs from MSCs cultured on collagen-coated flasks and the softest PDMS formulation (0.3 MPa). Scale bars represent 200 nm. Data representative of three independent experiments (N = 3). Statistical significance was calculated using a Kruskal-Wallis with Dunn's multiple comparisons test (ns – $p > 0.05$; * - $p < 0.05$).

5.3.3. Culturing MSCs on the Softest Sylgard 184 PDMS Substrate (0.3 MPa) Enhances MSC EV *in vitro* Angiogenic Bioactivity

MSC EV bioactivity was then assessed using an *in vitro* gap closure assay and a tube formation assay. While all MSC EV formulations significantly improved gap closure in HUVECs (basal media: 26.69 ± 2.913; flask – collagen: 37.46 ± 2.536; flask + collagen: 35.01 ± 1.332; 3.0 MPa: 46.75 ± 3.718; 1.2 MPa: 40.34 ± 3.884; 0.3 MPa: 49.82 ± 1.852), only the EVs from the MSCs grown on the softest Sylgard 184 PDMS formulation (0.3 MPa) resulted in significantly higher gap closure when compared with the collagen-coated flask ($p < 0.05$) (**Figure 5.3**).

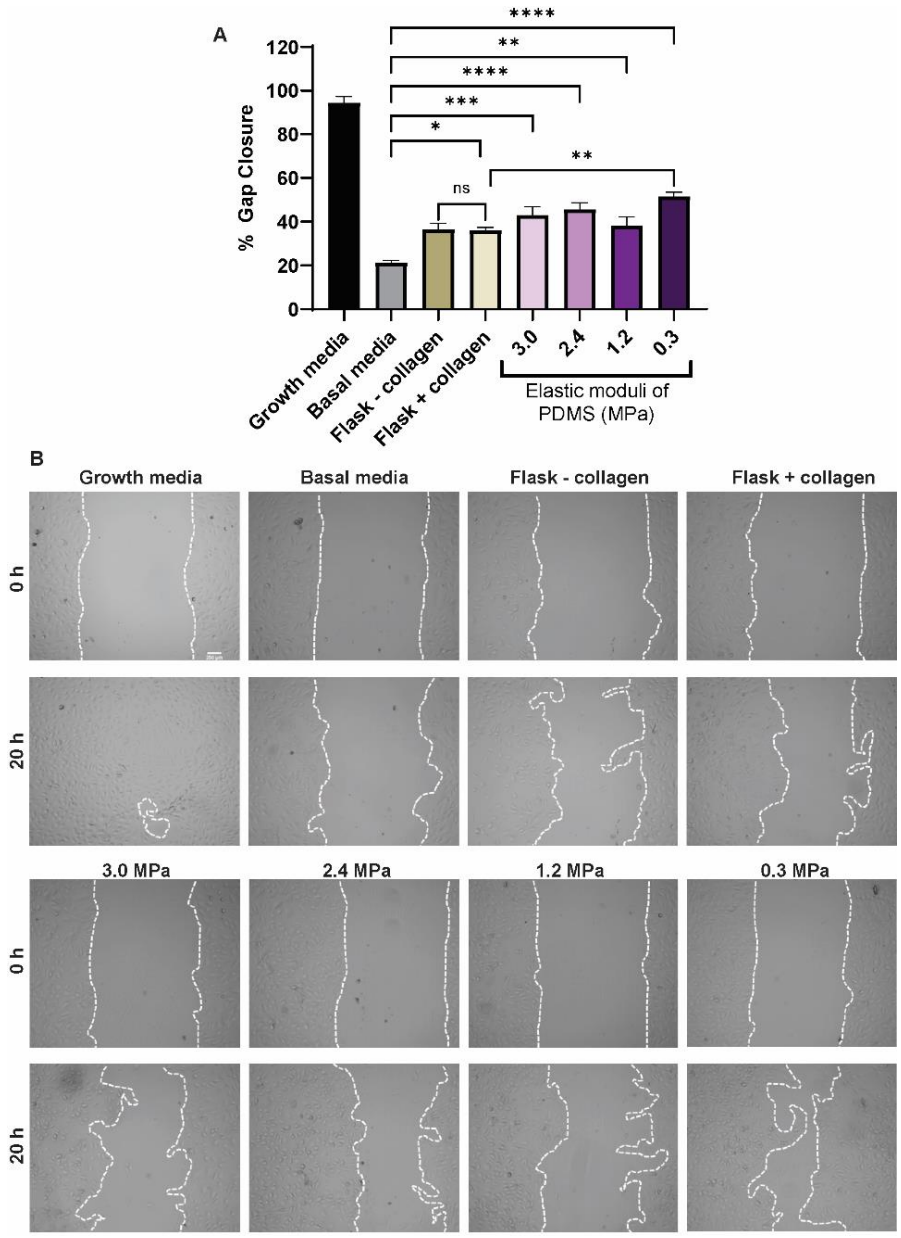


Figure 5.3. Soft Sylgard 184 PDMS enhances MSC EV in vitro cell migration. (A) Cell gap area after 20 h as a percentage of gap area at 0 h. EVs from MSCs cultured on the softest Sylgard 184 PDMS formulation (0.3 MPa) significantly increased the gap closure of HUVECs. All PDMS substrates were coated with collagen. (B) Representative images of HUVECs in the gap closure assay at 0 and 20 h following treatment with growth media (positive control), basal media (negative control) or 5E9 EVs/mL of EVs isolated from MSCs grown on the different Sylgard 184 PDMS substrates. All images and data are representative of three independent experiments (N = 3). Statistical significance was calculated using a one-way ANOVA with Šídák's multiple comparisons tests (ns – $p > 0.05$;* - $p < 0.05$; ** - $p < 0.01$; ****- $p < 0.0001$).

In the tube formation assay, EVs from every culture condition significantly enhanced the number of loops formed by the HUVECs when compared with the basal media negative control (basal: 8.50 ± 1.67; flask - collagen: 23.5 ± 2.60; flask + collagen: 18 ± 3.51; 3.0 MPa: 24.0 ± 3.06; 2.4 MPa: 23 ± 1.15; 1.2 MPa: 19.5 ± 3.61; 0.3 MPa: 37.5 ± 0.88). However, just as in the gap closure assay, only the EVs from the MSCs cultured on the softest substrate (0.3 MPa) were able to significantly improve tube formation when compared with those from the collagen-coated flask condition (**Figure 5.4**)

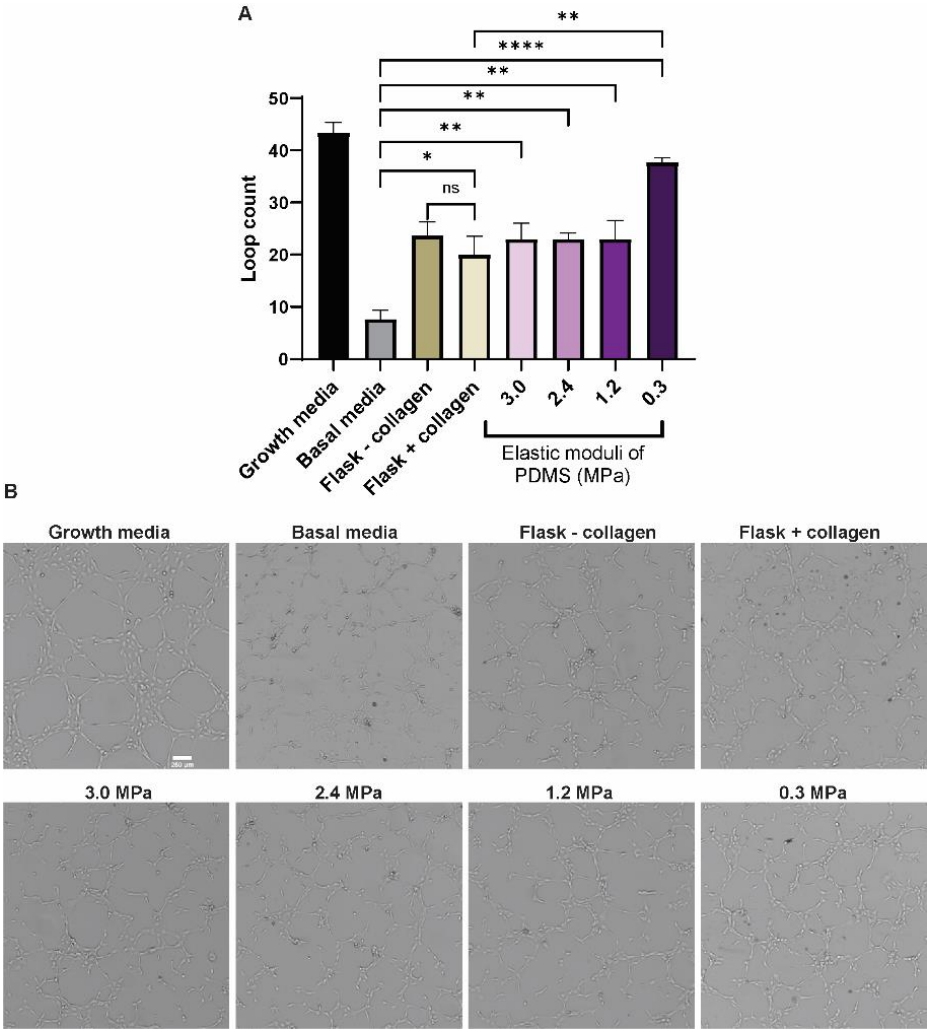


Figure 5.4. Soft Sylgard 184 PDMS improves tube formation in recipient HUVECs. (A) Tube formation results were quantified as the number of complete loops formed by HUVECs. EVs from the MSCs cultured on the soft PDMS formulation (0.3 MPa) were the only ones to significantly increase the number of loops formed by HUVECs when compared with EVs from MSCs cultured on collagen-coated flasks. All PDMS substrates were coated with collagen. (B) Representative images of HUVECs in the tube formation assay 6 h after application of growth media (positive control), basal media (negative control), or basal media with EVs from MSCs maintained in the various culture conditions (5×10^9 EVs/mL). Scale bar represents 250 μm. All images and data are representative of three independent experiments (N = 3). Statistical significance was calculated using a one-way ANOVA with Šídák's multiple comparisons tests (ns – $p > 0.05$; * - $p < 0.05$; ** - $p < 0.01$; **** - $p < 0.0001$).

5.3.4. Additional Dilution of Crosslinker Reagent Reduces Elastic Moduli of Sylgard 184 PDMS without Inducing Cytotoxicity

To test the limits of the observed effects on MSC EVs, the crosslinker was further diluted with the base reagent (50:1). Following mechanical testing, it was found that the 50:1 could reduce the elastic modulus to 0.005 MPa, although this was not significantly different from the 33:1 (0.3 MPa) (**Figure 5.5.A**). Next, we confirmed that the formulation was not inherently toxic to the cells using a WST-8 cell viability assay. Again, MSCs were able to grow in all conditions, as shown by the positive slope of absorbance values, which juxtaposed those MSCs within the negative control (i.e., 10% DMSO). On the final day of culture, there was a significant difference between the MSCs grown in coated and uncoated flasks ($p < 0.01$) and between those cultured in coated flasks and those grown on any PDMS substrate ($p < 0.0001$) (**Figure 5.5.B**).

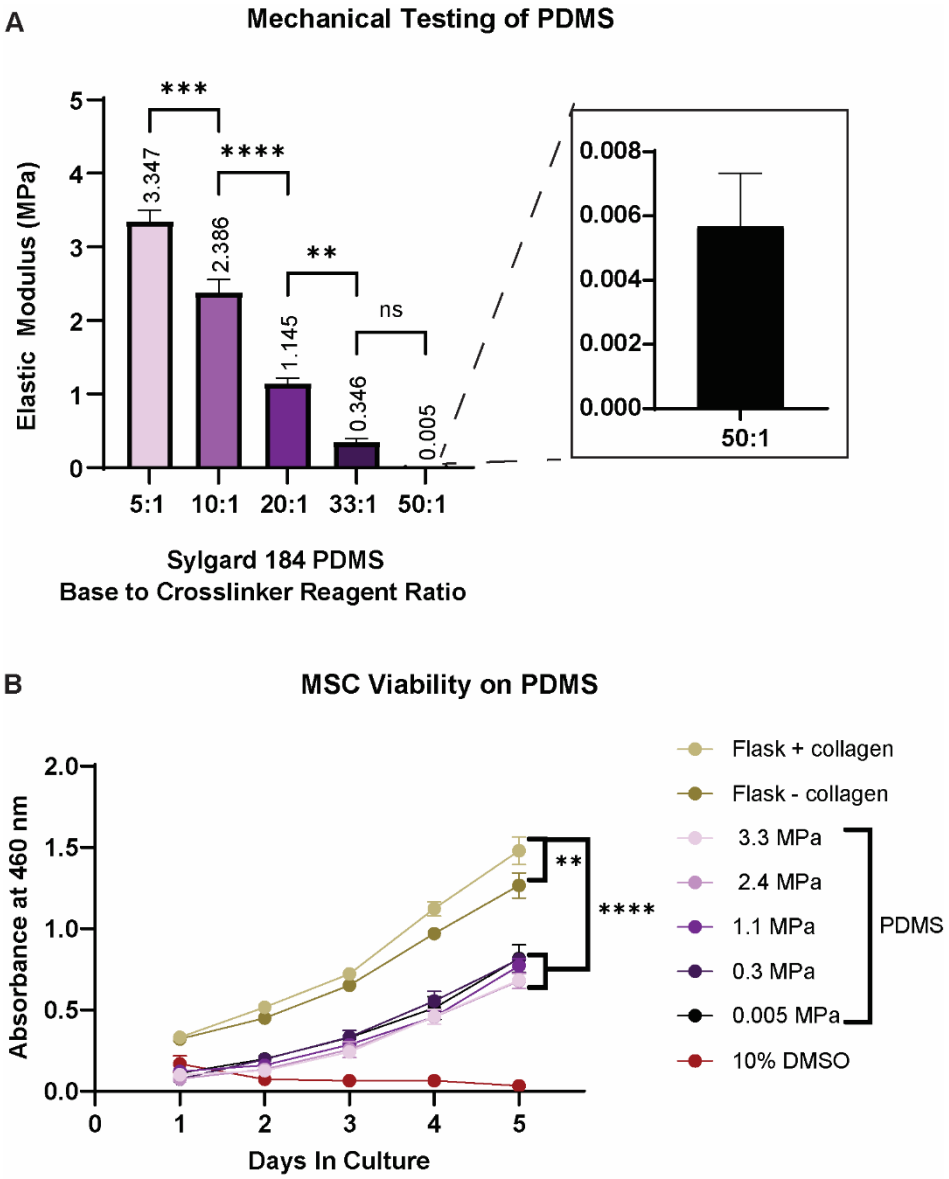


Figure 5.5. Further dilution of the crosslinker reagent (50:1) reduces the elastic modulus of the PDMS without inducing cell death. (A) The elastic modulus of each of the five PDMS formulations was measured using a Q800 Dynamic Mechanical Analyzer. Data is representative of two different fabrications of the substrates with three measurements per formulation. (B) WST-8 colorimetric cell viability results of MSCs cultured on the various PDMS formulations. All PDMS substrates were coated with collagen. Data is representative of three independent experiments (N = 3). Statistical differences were calculated using a (A) one-way ANOVA with Šídák's multiple comparisons tests or a (B) two-way ANOVA using Tukey's multiple comparisons tests (ns – $p > 0.05$; ** - $p < 0.01$; *** - $p > 0.001$; **** - $p < 0.0001$).

5.3.5. Culture Conditions Do Not Impact Sylgard 184 PDMS Elastic Moduli

To ensure that culture conditions did not impact the elastic modulus of the PDMS, the elastic modulus of each PDMS substrate was measured and then the substrates were submerged in cell culture media and incubated at 37°C for three days, followed by a final elastic modulus measurement. Results showed that there were no significant changes in the elastic modulus of each formulation following incubation with cell culture media (**Figure 5.6**).

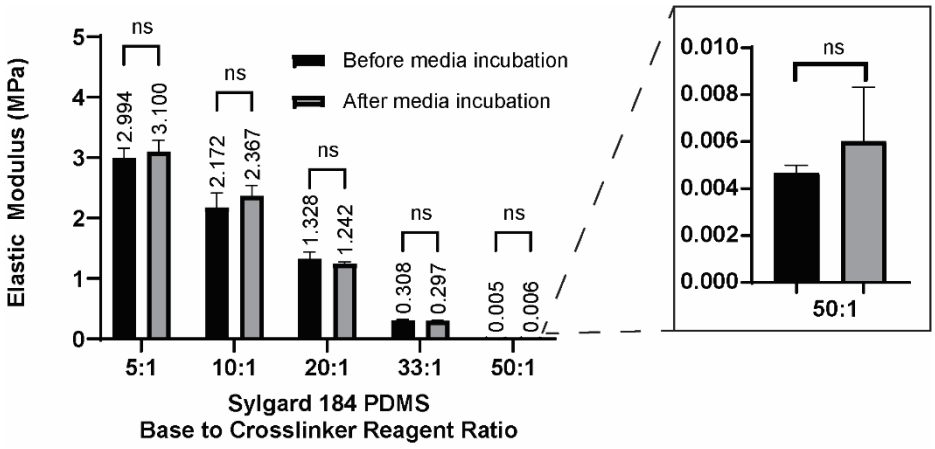


Figure 5.6. Sylgard 184 PDMS substrates maintain elastic modulus despite exposure to culture conditions. The elastic modulus of each of the five PDMS formulations was measured using a Q800 Dynamic Mechanical Analyzer. The elastic modulus of each substrate was not affected by submersion in cell culture media and incubation at 37°C for three days. Data is representative of two different fabrications of the substrates with three measurements per formulation. Statistical significance was calculated using a two-way ANOVA with Šídák's multiple comparisons tests (ns – $p > 0.05$).

5.3.6. Further Reduction of Sylgard 184 PDMS Elastic Modulus Maintains MSC EV *in vitro* Angiogenic Bioactivity

In the gap closure assay, when treated with any MSC EV preparation, HUVECs had significantly higher gap closure when compared with the negative control which consisted of basal media only (basal media: 23.98 ± 3.704; flask - collagen: 36.81 ± 2.903; flask + collagen: 37.04 ± 2.563, 3.3 MPa: 42.73 ± 5.441; 2.4 MPa: 45.62 ± 2.669; 1.1 MPa: 47.19 ± 2.090; 0.3 MPa: 63.70 ± 1.411; 0.005 MPa: 60.87 ± 0.848). Only MSC EVs from cells grown on the softest PDMS substrates (0.3 and 0.005 MPa) were able to significantly improve gap closure compared with MSC EVs from collagen-coated flasks ($p < 0.001$ and $p < 0.01$, respectively) (**Figure 5.7**).

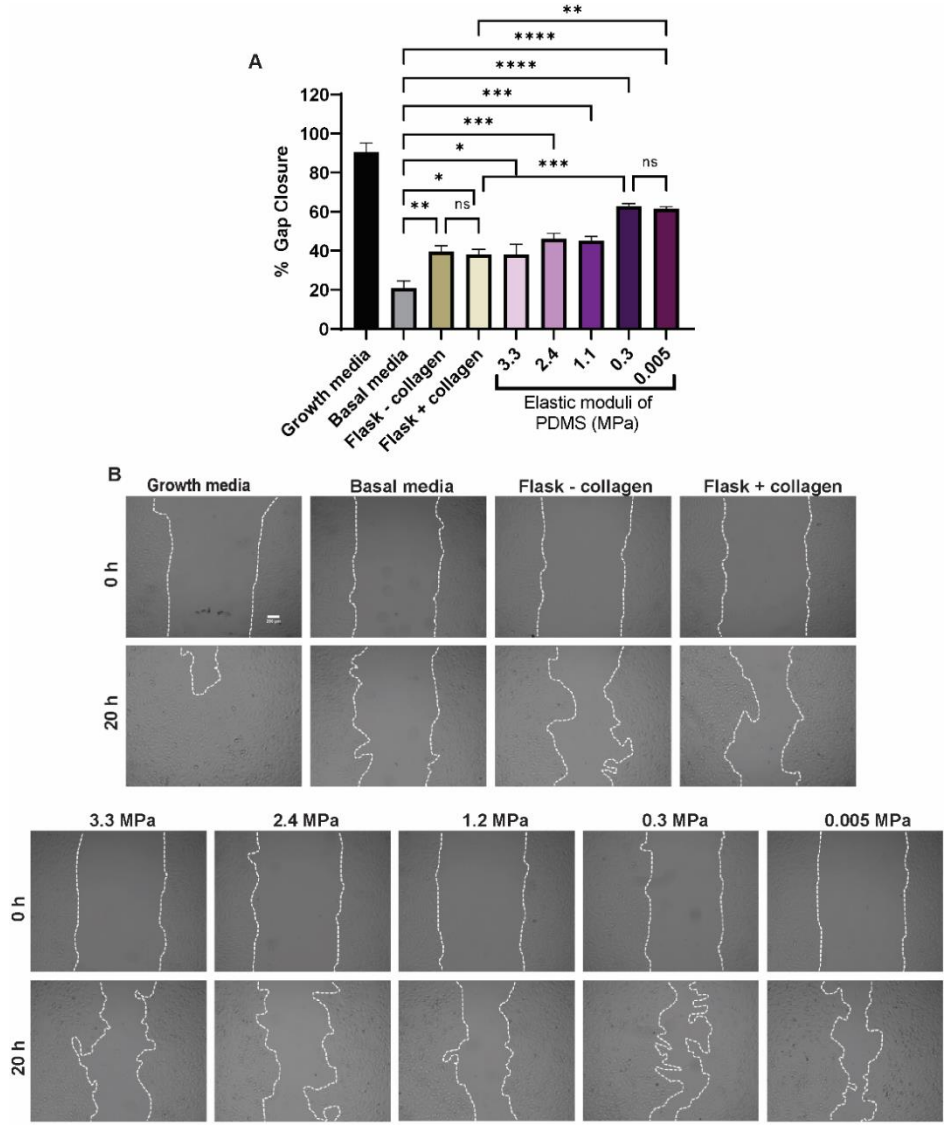


Figure 5.7. Enhanced effect of MSC EVs in the gap closure assay is maintained as elastic modulus is reduced. (A) Cell gap area after 20 h as a percentage of gap area at 0 h. EVs from MSCs cultured on the softest Sylgard 184 PDMS formulations (0.3 and 0.005 MPa) significantly increased the gap closure of HUVECs. All PDMS substrates were coated with collagen. (B) Representative images of HUVECs in the gap closure assay at 0 and 20 h following treatment with growth media (positive control), basal media (negative control) or 5E9 EVs/mL of EVs isolated from MSCs grown on the different Sylgard 184 PDMS substrates. All images and data are representative of three independent experiments (N = 3). Statistical significance was calculated using a one-way ANOVA with Šídák's multiple comparisons tests (ns – $p > 0.05$;* - $p < 0.05$; ** - $p < 0.01$; *** - $p < 0.001$; ****- $p < 0.0001$).

A similar trend was seen in the tube formation assay with all EV preparations significantly augmenting the number of loops formed by the HUVECs when compared with the negative control (basal media: 16.5 ± 2.33; flask – collagen: 46.0 ± 1.86; flask + collagen: 46.5 ± 1.45; 3.3 MPa: 43.0 ± 1.33; 2.4 MPa: 50.0 ± 2.03; 1.1 MPa: 45.5 ± 4.58; 0.3 MPa: 76.5 ± 7.23; 0.005 MPa: 75 ± 5.51). Only those EVs from the softest PDMS substrates (0.3 and 0.005 MPa) were able to improve tube formation when compared with EVs from collagen-coated flask culture ($p < 0.01$ and $p < 0.05$, respectively) (**Figure 5.8**).

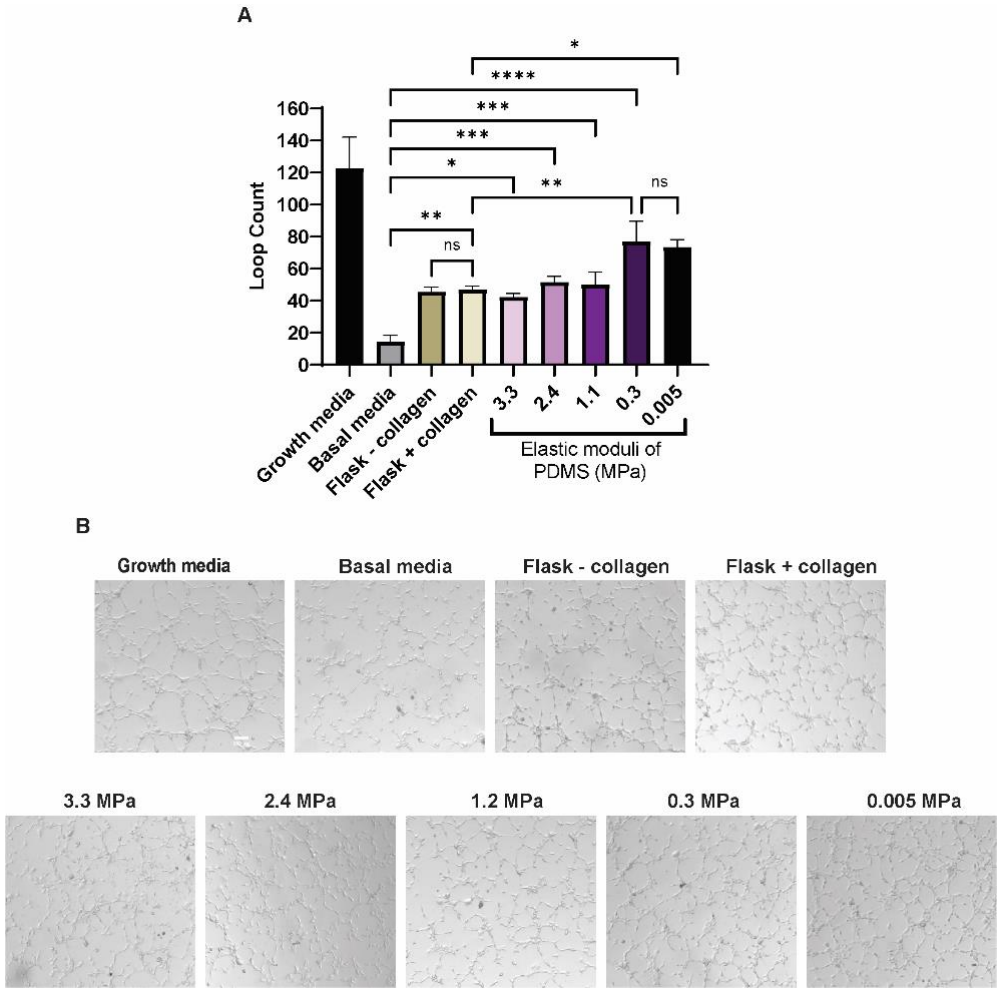


Figure 5.8. Enhanced effect of MSC EVs in the tube formation assay is maintained as elastic modulus is reduced. (A) Tube formation results were quantified as the number of complete loops formed by HUVECs. EVs from the MSCs cultured on the softest PDMS formulations (0.3 MPa and 0.005 MPa) significantly increased the number of loops formed by HUVECs when compared with EVs from MSCs cultured on collagen-coated flasks. All PDMS substrates were coated with collagen. (B) Representative images of HUVECs in the tube formation assay 6 h after application of growth media (positive control), basal media (negative control), or basal media with EVs from MSCs maintained in the various culture conditions (5×10^9 EVs/mL). Scale bar represents 250 μm. All images and data are representative of three independent experiments (N = 3). Statistical significance was calculated using a one-way ANOVA with Šídák's multiple comparisons tests (ns – $p > 0.05$; * - $p < 0.05$; ** - $p < 0.01$; *** - $p < 0.001$; **** - $p < 0.0001$).

5.3.7. Mixing Sylgard 184 and Sylgard 527 Allows for a Finer Elastic Modulus Gradient that is Non-Toxic to Cells

To obtain a more refined gradient of elastic moduli, we mixed two different types of PDMS (Sylgard 184 and Sylgard 527) at various ratios, as has been previously done [306, 308]. We were able to obtain a more detailed range of elastic moduli from 2 MPa (pure Sylgard 184) down to 0.003 MPa (pure Sylgard 527) (**Figure 5.9.A**). Using a WST-8 cell viability assay, we demonstrated that MSCs were able to grow in all conditions, as shown by the positive slope of absorbance values, which contrasted those MSCs treated with 10% DMSO meant to induce cell death. On the final day of culture, there was no significant differences among the MSCs grown in any of the conditions ($p > 0.05$) (**Figure 5.9.B**).

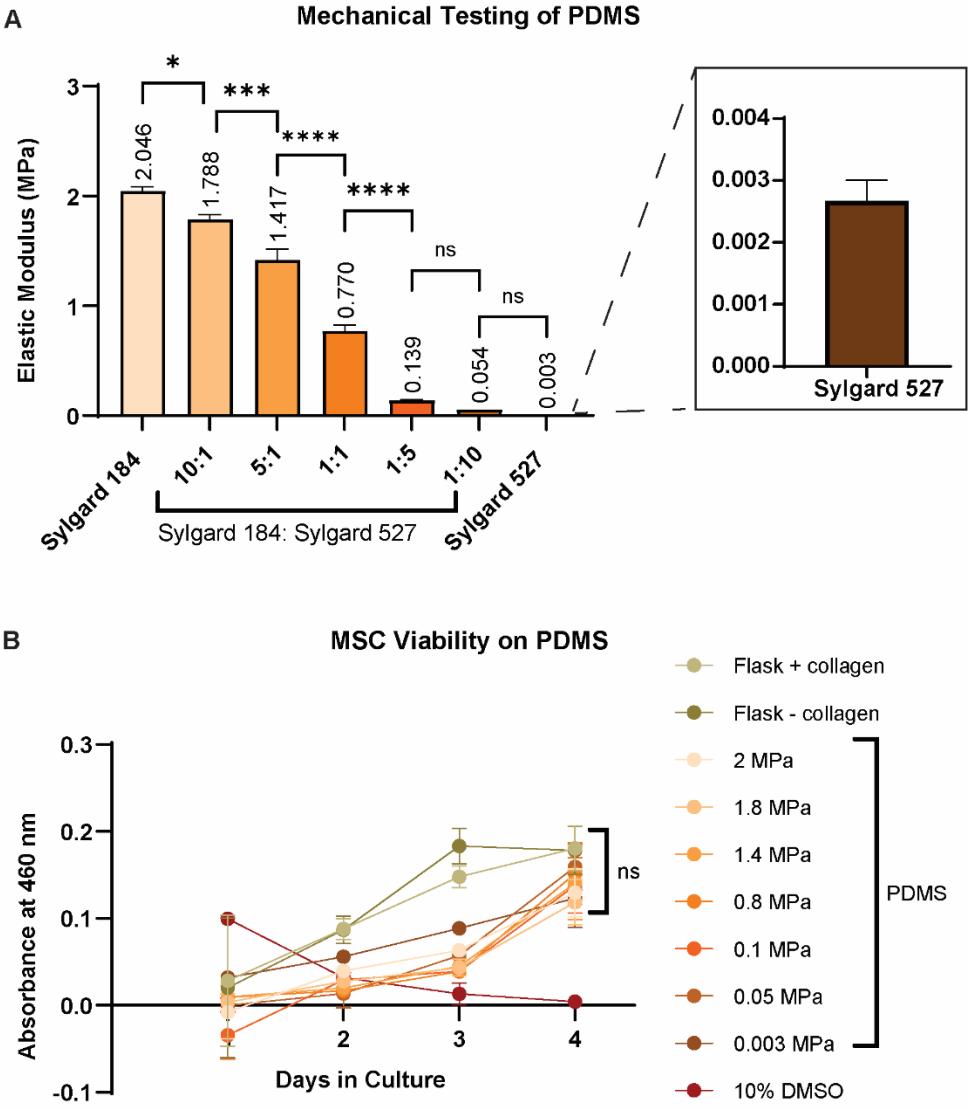


Figure 5.9. Varying the ratio of Sylgard 184 to Sylgard 527 produces a refined range of elastic moduli that is non-toxic to cells. (A) Elastic modulus of each of the seven different PDMS formulations was measured using a Q800 Dynamic Mechanical Analyzer. Data is representative of two different fabrications of the substrates with three measurements per formulation. (B) WST-8 colorimetric cell viability results of MSCs cultured on the various PDMS formulations. All PDMS substrates were coated with collagen. Data is representative of two independent experiments (N = 2). Statistical differences were calculated using a (A) one-way ANOVA with Šídák's multiple comparisons tests or a (B) two-way ANOVA with Tukey's multiple comparisons test (ns – $p > 0.05$; *- $p < 0.05$; *** - $p > 0.001$; **** - $p < 0.0001$). Data courtesy of Emily Powsner.

5.3.8. Culture Conditions Do Not Influence the Elastic Moduli of the Sylgard 184:Sylgard 527 PDMS Mixtures

To ensure that culture conditions did not impact the elastic modulus of the PDMS, the elastic modulus of each PDMS substrate was measured and then the substrates were submerged in cell culture media and incubated at 37°C for three days, followed by a final elastic modulus measurement. Results showed that there were no significant changes in the elastic modulus of each formulation following incubation with cell culture media (**Figure 5.10**).

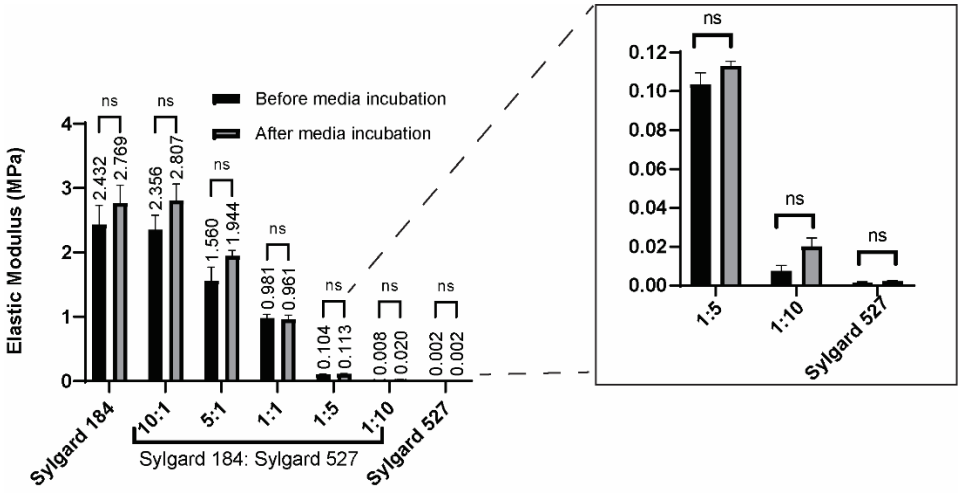


Figure 5.10. Substrates composed of varying ratios of Sylgard 184 to Sylgard 527 maintain elastic modulus despite exposure to culture conditions. The elastic modulus of each of the five PDMS formulations was measured using a Q800 Dynamic Mechanical Analyzer. The elastic modulus of each substrate was not affected by submersion in cell culture media and incubation at 37°C for three days. Data is representative of two different fabrications of the substrates with three measurements per formulation. Statistical significance was calculated using a two-way ANOVA with Šídák's multiple comparisons tests (ns – $p > 0.05$). Data courtesy of Emily Powsner.

5.3.9. Culturing MSCs on Mixtures of Sylgard 184 and Sylgard 527 Maintains the Trend of Increased EV Production and Angiogenic Bioactivity with Decreasing Elastic Moduli

After 24 h, the EVs from every PDMS mixture culture condition were collected and isolated and the cells were counted. As was reported in Section 5.3.2, the amount of EVs produced per cell increased as substrate softened. Specifically, MSC EV production was significantly upregulated at a substrate stiffness of 1.4 MPa (6.7E5 ± 6E4), which was approximately 9-fold greater than those cultured in collagen-coated flasks (7.2E4 ± 1.5E3) and was comparable to the threshold of 1.2 MPa reported in Section 5.3.2. This increase in EV production was maintained when MSCs were cultured on the 0.8, 0.1, 0.05, and 0.003 MPa PDMS substrates (0.8 MPa: 7.7E5 ± 1.0E4; 0.1 MPa: 7.1E5 ± 5.4E4; 0.05 MPa: 4.3E5 ± 1.6E5; 0.003 MPa: 6.2E5 ± 7.5E3), which were 11-, 10-, 6-, and 9-fold higher, respectively, than EV production by MSCs in the collagen-coated flasks (**Figure 5.11.A**). NTA analysis revealed no significant difference in EV size distribution (flask – collagen: 85.6 ± 8.5 nm; flask + collagen: 104.8 ± 5.5 nm; 2.0 MPa: 93.8 ± 6.9; 1.8 MPa: 88.6 ± 7.7 nm; 1.4 MPa: 76.3 ± 2.7 nm; 0.8 MPa: 85.3 ± 7.7 nm; 0.1 MPa: 79.7 ± 1.5; 0.05 MPa: 83.5 ± 6 nm; 0.003 MPa: 80.7 ± 8.2), with more than 90% of each population lying within the typical exosomal diameter range (40-200 nm) [34] (**Figure 5.11.B**).

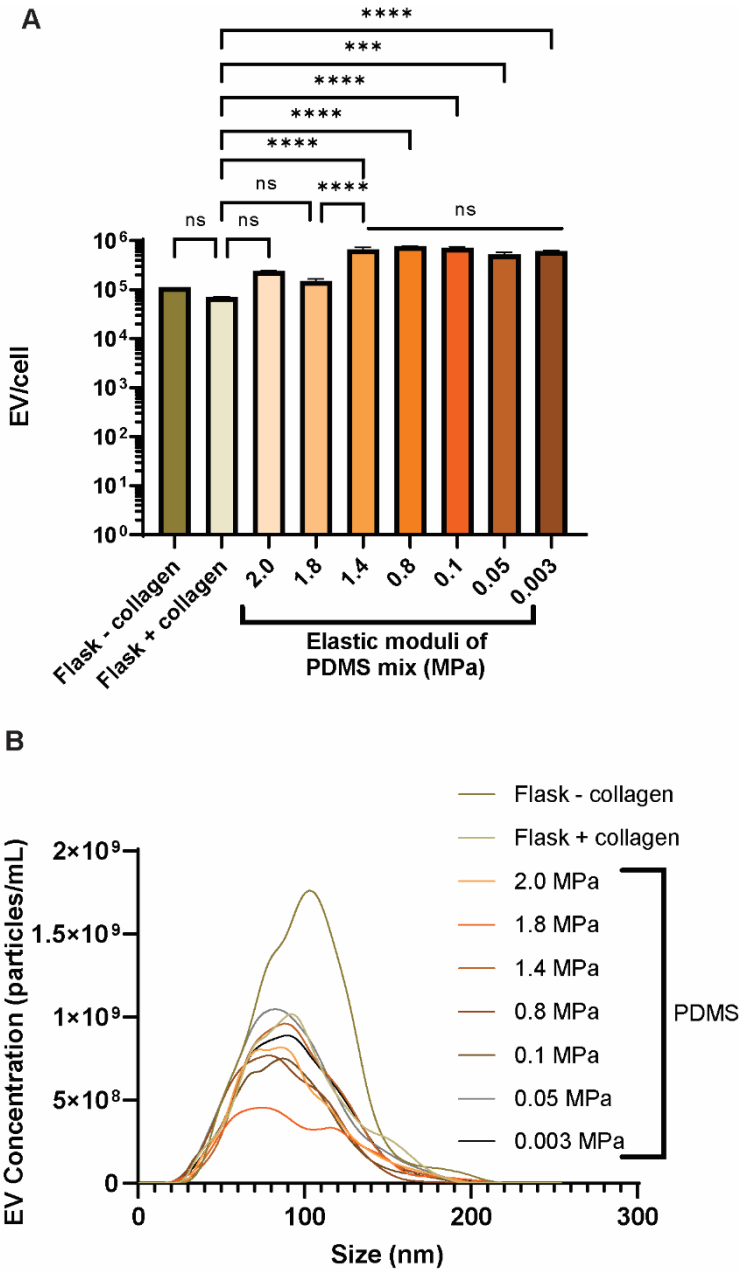


Figure 5.11. Culturing MSCs on the softer Sylgard 184/527 mixtures increases MSC EV production. (A) Number of EVs produced per MSC as measured using nanoparticle tracking analysis (NTA). (B) Size distribution of EVs from MSCs cultured on the various PDMS formulations. All PDMS substrates were coated with collagen. Data representative of three independent experiments (N = 3). Statistical significance was calculated using a one-way ANOVA with Tukey's multiple comparisons tests (ns – $p > 0.05$; *** - $p < 0.001$; **** - $p < 0.0001$).

In the gap closure assay, HUVECs demonstrated significantly higher gap closure when treated with any of the MSC EV preparations and compared with the negative control (basal media: 36.94 ± 1.609; flask - collagen: 42.66 ± 1.508; flask + collagen: 43.30 ± 1.016, 2.0 MPa: 43.02 ± 4.774; 1.8 MPa: 48.15 ± 0.826; 1.4 MPa: 41.91 ± 2.782; 0.8 MPa: 55.77 ± 1.070; 0.10 MPa: 58.89 ± 1.096; 0.05 MPa: 58.17 ± 1.805; 0.003 MPa: 62.44 ± 4.137). Only when EVs were derived from MSCs cultured on substrates of 0.8 MPa or less was gap closure in HUVECs significantly increased when compared with HUVECs treated with EVs from MSCs in collagen-coated flasks (**Figure 5.12**).

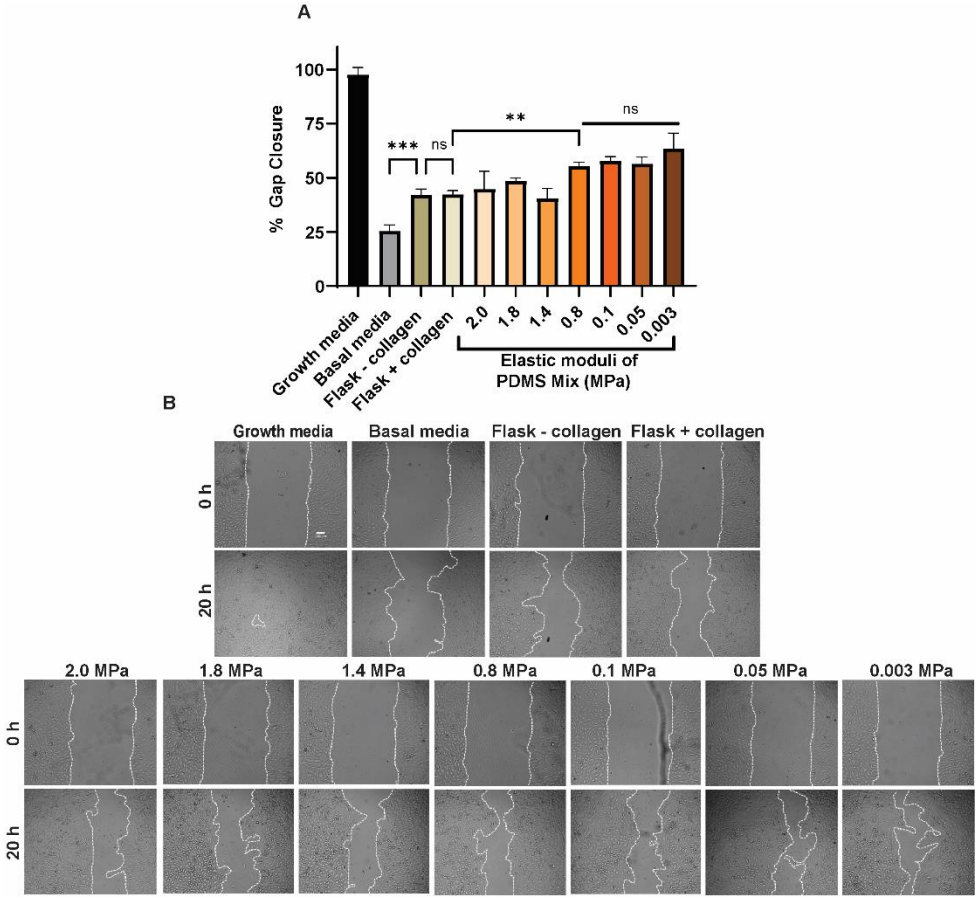


Figure 5.12. Enhanced effect of MSC EVs in the gap closure assay is maintained as elastic modulus is reduced by mixing Sylgard 184 and Sylgard 527. (A) Cell gap area after 20 h as a percentage of gap area at 0 h. EVs from MSCs cultured on the 1.4, 0.8, 0.05, and 0.003 MPa substrates significantly increased the gap closure of HUVECs when compared with MSC EVs from collagen-coated flask culture. All PDMS substrates were coated with collagen. (B) Representative images of HUVECs in the gap closure assay at 0 and 20 h following treatment with growth media (positive control), basal media (negative control) or 5E9 EVs/mL of EVs isolated from MSCs grown on the different Sylgard 184 PDMS substrates. All images and data are representative of three independent experiments (N = 3). Statistical significance was calculated using a one-way ANOVA with Šídák's multiple comparisons tests (ns – $p > 0.05$; ** - $p < 0.01$; *** - $p < 0.001$).

Similarly, in the tube formation assay, EVs from every culture condition significantly improved tube formation (i.e., loop count) when compared with just basal media (basal: 17 ± 2.91; flask - collagen: 55.5 ± 1.67; flask + collagen: 48.5 ± 4.93; 2.0 MPa: 75.5 ± 5.17; 1.8 MPa: 68.5 ± 3.18; 1.4 MPa: 84.5 ± 3.38; 0.8 MPa: 103 ± 6.24; 0.1 MPa: 107.5 ± 19.7; 0.05 MPa: 93.5 ± 2.85; 0.003 MPa: 118.5 ± 2.19). However, only when the elastic modulus reached 1.4 MPa or lower did the EVs significantly improve tube formation when compared with those from the collagen-coated flask condition (**Figure 5.13**).

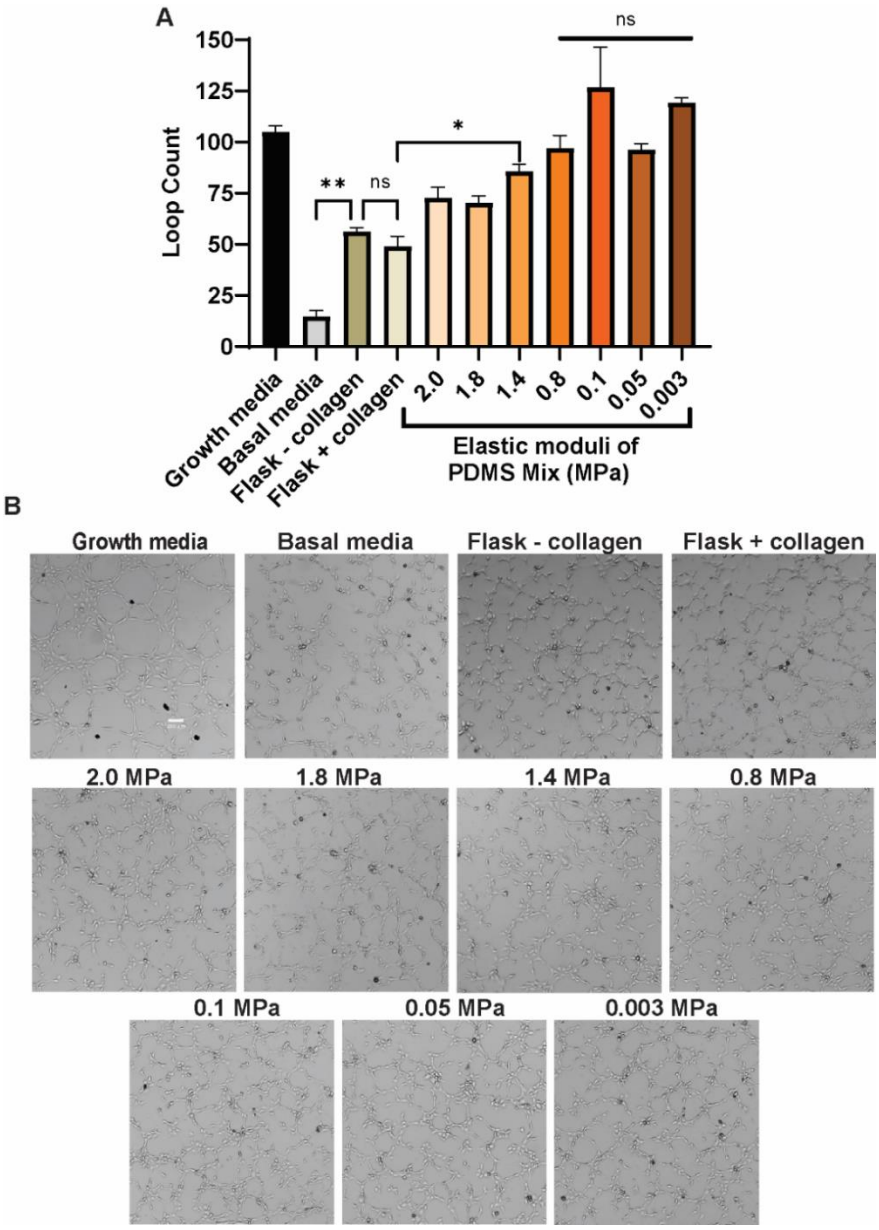


Figure 5.13. Enhanced effect of MSC EVs in the tube formation assay is maintained as elastic modulus is reduced by mixing Sylgard 184 and Sylgard 527. (A) Tube formation results were quantified as the number of complete loops formed by HUVECs. EVs from the MSCs cultured on the 1.4, 0.8, 0.1, 0.05, and 0.003 MPa substrates were the only ones to significantly increase the number of loops formed by HUVECs when compared with EVs from MSCs cultured on collagen-coated flasks. All PDMS substrates were coated with collagen. (B) Representative images of HUVECs in the tube formation assay 6 h after application of growth media (positive control), basal media (negative control), or basal media with EVs from MSCs maintained in the various culture conditions (5×10^9 EVs/mL). Scale bar represents 250 μm. All images and data are representative of three independent experiments (N = 3). Statistical significance was calculated using a one-way ANOVA with Šídák's multiple comparisons tests (ns – $p > 0.05$; * - $p < 0.05$; ** - $p < 0.01$).

5.3.10. Substrate Stiffness Alters MSC EV Cargo and Gene Expression in Recipient Cells

To investigate the mechanism underlying the enhanced MSC EV *in vitro* angiogenic bioactivity, we screened for the expression of MSC-specific miRNAs in the flask- and PDMS-derived EVs (Sylgard 527; 0.003 MPa). Relative to the flask MSC EVs, the EVs from the PDMS culture showed considerable increase in the levels of miR-10a-5p, miR-365a-3p, and miR-548ar-3p as well as downregulation of miR-3613-3p (**Figure 5.14**). Interestingly, miR-888-5p was well-expressed in the PDMS EVs but undetectable in the flask EVs. miR-154-5p, -130a-3p, -30e-5p, and -411-3p were expressed in flask EVs but undetectable in PDMS EVs (data not shown).

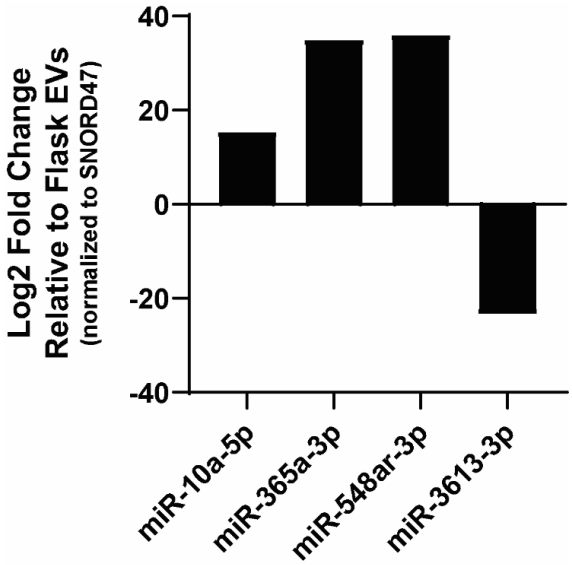


Figure 5.14. Substrate alters the MSC EV miRNA profile. Expression of MSC-specific miRNAs in EVs derived from MSCs cultured on the softest collagen-coated PDMS substrate (Sylgard 527; 0.003 MPa) relative to EVs derived from collagen-coated flask culture. Values were normalized to the small nuclear RNA, SNORD47. Data shown as log2 of the fold change and calculated using the ΔΔCt method. ΔΔCt = (ΔCt miRNA of interest – ΔCt SNORD47), where ΔCt miRNA of interest = (Ct PDMS EV – Ct flask EV).

Next, we collected genetic material from HUVECs treated with PBS (vehicle control), EVs from MSCs grown on flasks, or EVs from MSCs grown on the softest PDMS substrate (Sylgard 527; 0.003 MPa) and screened for the expression of 75 genes associated with angiogenesis (**Figure 5.15.A**). In comparison with PBS-treated HUVECs, the expression of many genes were altered when treated with MSC EVs. However, we were particularly interested in the relative changes between the two EV formulations (flask vs PDMS). The array showed that several genes were more upregulated in HUVECs when they were treated with PDMS EVs, including E-selectin, PLAU, and PARD3; all of which showed at least a two-fold difference from HUVECs treated with the flask EVs or PBS. Notably, PTGS2 was downregulated more than two-fold in the HUVECs treated with the PDMS EVs than those treated with the PBS or flask EVs (**Figure 5.15.B**). Logistically constrained by the array setup, only one technical replicate was performed per gene, thus no statistical analysis was performed.

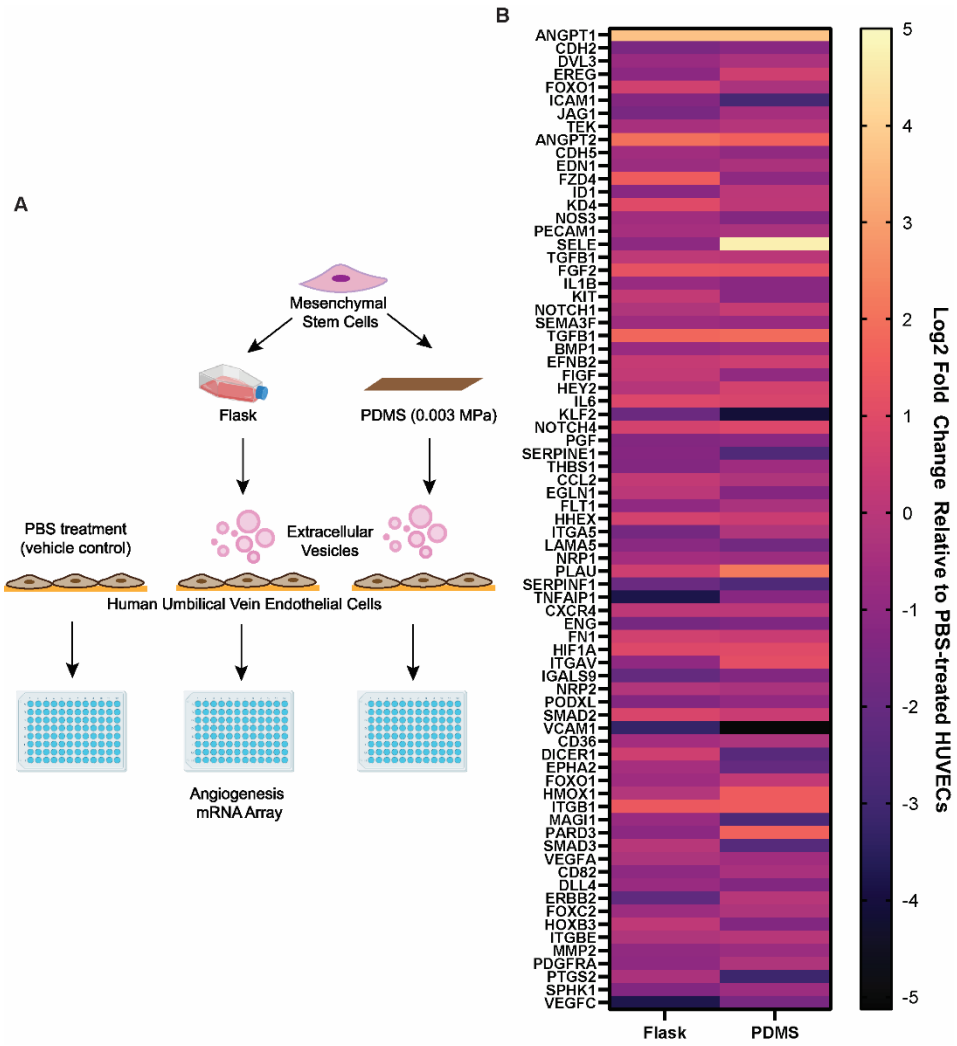


Figure 5.15. Angiogenic gene expression in HUVECs treated with EVs from MSCs cultured in flasks or the softest PDMS substrate. (A) Experimental schematic of angiogenesis-specific gene expression analysis in HUVECs treated with just PBS (vehicle control), EVs from MSCs cultured in collagen-coated flasks, or EVs from MSCs cultured on the softest collagen-coated PDMS substrate (Sylgard 527; 0.003 MPa). (B) Gene expression of 75 genes associated with angiogenesis in HUVECs after EV treatment. Values were normalized to five housekeeping genes (actin, GAPDH, NONO, LDHA, and PPIH). Data shown as log2 of the fold change relative to HUVECs treated with just PBS. Data was calculated using the ΔΔCt method per the array manufacturer's instructions.

We then specifically analyzed several of the genes (i.e., E-selectin, PLAU, PARD3) using qPCR to attempt to confirm the array results but were not able to replicate the results from the array. There were no differences in the expression of E-selectin, PLAU, and PARD3 across the different HUVEC treatments (**Figure 5.16**).

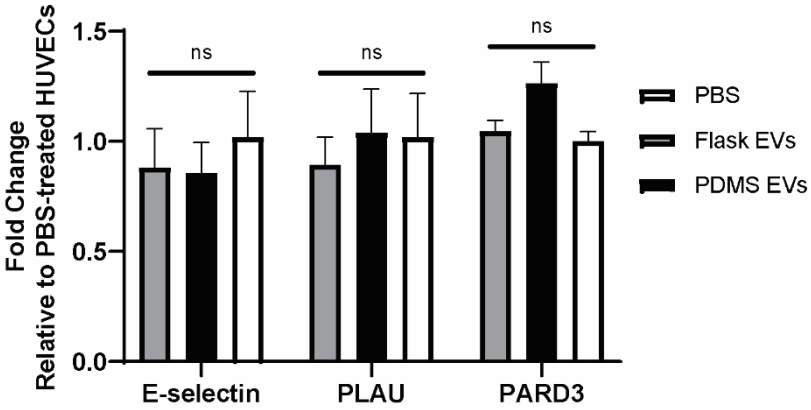


Figure 5.16. Gene expression of E-selectin, PLAU, and PARD3 in EV-treated HUVECs. HUVECs were analyzed after being treated with PBS (vehicle control), EVs from MSCs cultured in flasks, or EVs from the MSCs cultured on the softest collagen-coated PDMS substrate (Sylgard 527; 0.003 MPa). Data shown as fold change relative to HUVECs treated with PBS and normalized to GAPDH. Data was calculated using the ΔΔCt method. ΔΔCt = (ΔCt gene of interest– ΔCt GAPDH), where ΔCt gene of interest = (Ct flask or PDMS EV – Ct PBS). Data is from one biological replicate with three technical replicates. Statistical significance was calculated using a two-way ANOVA using Šídák's multiple comparisons tests (ns – $p > 0.05$).

5.3.11. MSC Phenotype is Maintained Across the PDMS Substrates

Finally, we wanted to confirm that the MSCs were not differentiating while on the PDMS substrates. Immunoblotting revealed a relatively stable presence of MSC markers (CD73, CD90, and CD105), a multipotency marker (SOX2), as well as the absence of the negative marker CD45 across the range of PDMS substrates (**Figure 5.17**).

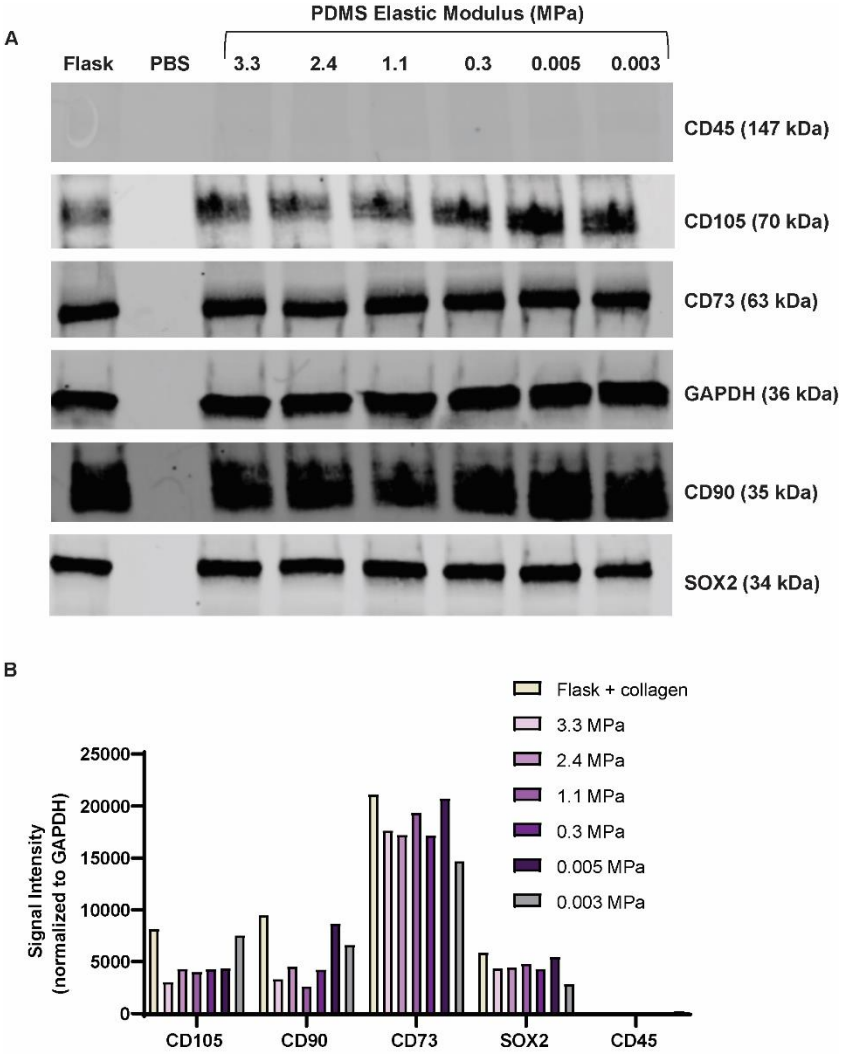


Figure 5.17. MSC phenotype is retained when cultured on PDMS of various elastic moduli. (A) Immunoblot showing the presence of MSC-specific markers (CD73, CD90, CD105) and the multipotency marker SOX2, as well as the absence of a negative marker (CD45). (B) Quantification of the immunoblot normalized to GAPDH.

5.4 Discussion

Substrate stiffness is a well-known regulator of MSC fate and function [313, 314] and is inherently present in the engineering of tissue-like constructs and the biomanufacturing space. Despite this, little is known about the effects on the therapeutic trophic factors secreted by MSCs, specifically MSC EVs. In the present investigation, we sought to understand how substrate stiffness can impact both secretion and bioactivity of MSC EVs. To do so, we cultured the MSCs on various PDMS substrates. Specifically, we varied the PDMS substrates by either changing the level of crosslinker in the PDMS (Sylgard 184) or by mixing two types of PDMS (Sylgard 184 and 527). Through this manipulation we were able to obtain a range of elastic moduli similar to previously conducted research (0.003 MPa – 3.0 MPa) [306-309] (**Figures 5.1.A, 5.5.A, 5.9.A**) and we were able to demonstrate that these values could be maintained through the entire length of the experiment (i.e., 3 days) in culture conditions (i.e., in media at 37°C and 5% CO_2) (**Figures 5.6 and 5.10**). Importantly, we showed that the MSCs were able to survive and proliferate on all PDMS substrates (**Figures 5.1.B, 5.5.B, 5.9.B**), which aligns with previous research [306]. However, despite equal seeding densities, MSCs cultured on any PDMS substrate seemed to have lower absorbance values in the cell viability assay. As all modified PDMS substrates had comparable values to the control PDMS substrates (i.e., Sylgard 184 and Sylgard 527 made according to the manufacturer's protocol), we suspect these differences had little to do with our manipulation of the PDMS. These results could reflect differences in the number of cells that were able to initially adhere to the PDMS. Inherently, PDMS has many surface characteristics that differ from traditional tissue culture plastic (e.g.,

roughness, wettability, surface charge), that could affect cell adhesion [315]. In addition, the silicon-oxygen links that make up the backbone of PDMS offer high mobility and thus promotes surface reorganization, making it difficult to maintain a cell-adhesive layer that persists over time [316, 317]. Future studies should involve cell adhesion assays as well as live/dead assays to fully understand the results of the cell viability experiments in the present investigation. Moreover, investigation of longer-term culture (i.e., > 3 days) will help elucidate the practicality of these techniques in boosting MSC EV production in a scaled-up platform. If the cell-adhesive properties prove to be too transitory, steps to induce covalent linkages between the ECM and PDMS can be taken (e.g., polydopamine or (3-aminopropyl) triethoxysilane coating prior to ECM coating) [318, 319].

When we examined MSC EV production (i.e., number of EVs secreted by each cell), our results suggest that, using either methodology, EV production significantly increased when the elastic modulus decreased below a certain threshold (**Figures 5.2.A and 5.11.A**). The threshold for the increase was between 2.4 and 1.2 MPa when varying the levels of crosslinker (**Figure 5.2.A**) and between 1.8 and 1.4 MPa when using the mixture of PDMS types (**Figure 5.11.A**). This indicates that perhaps the true elastic modulus threshold for the increased EV production is somewhere between 1.8 and 1.2 MPa. In Chapters 3 and 4, possible mechanisms proposed for the observed increase in EV production during the application of flow-derived shear stress or mechanical confinement were the increased nuclear translocation of YAP/TAZ and increased intracellular calcium signaling induced by the activation of mechanoreceptors and

cytoskeletal rearrangement. Interestingly, previous research has demonstrated that MSCs are often less mechanically-stimulated on soft substrates. In fact, a study by Kim et al. showed that MSCs cultured on soft polyacrylamide gels (<1 kPa) presented with diminished cytoplasmic calcium oscillations that were mediated by the RhoA pathway [320]. Additionally, it has been shown that on relatively soft substrates, cells often display a decreased formation of F-actin bundles and low contractile forces which causes inactivation of YAP/TAZ [321, 322]. Altogether, these studies indicate a mechanism of EV production that may diverge from those previously discussed in Chapters 3 and 4. A particularly interesting study conducted by Lenzini and colleagues found that MSC EV production was significantly upregulated when MSCs were cultured on soft alginate hydrogels (3 kPa) when compared with stiff hydrogels (20 kPa) or tissue culture plastic (0.1 GPa) [180]. It was shown that knocking down focal-adhesion kinase (FAK) in MSCs – a mediator of ligand-induced signaling – on the stiff substrates triggered an increase in EV secretion. They supported these results by showing that chemical interference with integrin binding as well as decreasing the amount of cell-adhesion peptide on the stiff hydrogels resulted in an increase in EV secretion. Using protein-fusion techniques, they were then able to show that soft hydrogels supported more rapid transport of MVBs throughout the cell and more MVB-plasma membrane fusion events. This MVB transport could be enhanced by inhibiting the actin related protein 2/3 (Arp2/3) complex, which is downstream of FAK. While the mechanisms probed in this study are interesting and should be considered in the present investigation, there a few things to note. First, the change in EVs per cell considered to be significant in the study are relatively very small (6E3) compared to

what we reported here (> 2E5). Additionally, they report that increased EV secretion is due to higher trafficking of $CD63^+$ MVBs but comment that the number of $CD63^+$ EVs across conditions were similar and that differences in EV secretion were only perceptible when larger EVs (e.g., microvesicles; presumably not secreted through MVB fusion) were included in the analysis. Contrary to Lenzini and the present investigation, one study showed that stiff polyacrylamide gels (5 kPa) enhanced breast cancer cell EV secretion in a YAP/TAZ-dependent manner relative to soft gels (0.5 kPa) [323]. While the stark contrast in these studies is likely due to the cell type studied (MSC vs breast cancer cell), it could also be due to the employment of different types of substrates (alginate hydrogels vs polyacrylamide gels vs PDMS), or the chosen method of EV quantification (NTA vs cryoSEM). Future work should include orthogonal methods of EV quantification and different substrates of similar elastic moduli to confirm the observed phenomenon, as well as probing of the suspected mechanisms (i.e., YAP/TAZ, actin cytoskeleton organization).

In terms of MSC EV bioactivity, we found that culturing MSCs on PDMS with an elastic modulus < 1 MPa resulted in MSC EVs with improved angiogenic activity in *in vitro* gap closure and tube formation assays (**Figures 5.3, 5.4, 5.7, 5.8, 5.12, 5.13**). Specifically, we observed that when varying the crosslinker amount, MSCs produced EVs with enhanced angiogenic activity when cultured on PDMS with an elastic modulus ≤ 0.3 MPa (**Figures 5.3, 5.4, 5.7, 5.8**). When mixing PDMS types to achieve various stiffnesses, we found that improvement in EV angiogenic activity in both assays occurred when MSCs were cultured on PDMS substrates with an elastic

modulus ≤ 0.8 MPa (**Figures 5.12, 5.13**). Importantly, angiogenic activity of the EVs does not increase further with incremental reduction in the elastic modulus. Taken together, these data suggest that enhanced EV angiogenic activity occurs at when MSCs are cultured on PDMS that is ~1 MPa and softer. The fact that we observed a threshold response in angiogenic activity rather than a gradient response may reflect either maximized loading of pro-angiogenic cargo into EVs or saturation of the HUVEC response to EVs. Interestingly, Lenzini and colleagues found that EVs from MSCs cultured on soft (3 kPa) hydrogels were shown to reduce edema and vascular permeability in LPS-treated mice to a greater extent than those from flask MSCs [180]. Looking specifically at angiogenic molecules, a study by Ji et al. found that when cultured on polyacrylamide gels of a low elastic modulus (0.5 kPa), MSCs produced significantly more pro-angiogenic factors (e.g., VEGF, HGF, bFGF, IGF-1) than those cultured on gels of a higher elastic modulus (200 kPa). Conditioned media from the 0.5 kPa condition was able to enhance tube formation and chemotactic migration in HUVECs when compared with the 200 kPa condition [300]. They went further and showed that the enhanced secretion of most of the angiogenic trophic factors (all except VEGF) could be recapitulated on the stiff substrate when cytoskeletal tension was inhibited using blebbistatin or Rho-associated protein kinase (ROCK) inhibitor Y27632. It is important to note that this study did not compare the gels to tissue culture plastic so it is unclear if this trend is evident when looking at a much larger range of elastic moduli. We did not show any further improvement of EV angiogenic properties below 1 MP. However, the lowest elastic modulus we were able to obtain was 0.003 MPa (i.e., 3 kPa), which is much higher than the 0.5 kPa achieved in this study.

Contrary to these results, a study by Nasser and colleagues, found that MSCs on medium-stiff hydrogel scaffolds (5 kPa) secreted the most VEGF and tubulogenic effect on HUVECs when compared to MSCs on gels with either higher (23 kPa) or lower (1 kPa) stiffness, demonstrating a sort of biphasic response to stiffness [302]. Given these contrasting results, further research will need to be conducted in order to confirm and understand the observed phenomena. Namely, the utilization of cytoskeletal inhibitors (e.g., blebbistatin) on MSC cultures on various PDMS substrates to examine downstream effects on MSC EVs would be an important place to start.

Next, as miRNA cargo has been implicated in EV bioactivity [324], we explored the miRNA profile of MSC EVs as well as the mRNA profile of recipient HUVECs using an unbiased array approach. Within the EVs, we found an upregulation of miR-10a-5p, miR-365a-3p, and miR-548ar-3p as well as a downregulation of miR-3613-3p in EVs derived from MSCs cultured on the softest PDMS (Sylgard 527; 0.003 MPa) when compared with those derived from flasks (**Figure 5.14**). Notably, EV-encapsulated miR-10a can promote angiogenesis both *in vitro* and *in vivo* [325, 326] as well as inhibit apoptosis [327]. But, it is also known to inhibit some angiogenesis pathways (i.e., TGFβ1/Smad) [328]. miR365a promotes cancer cell growth and invasion [329] while miR-3613 inhibits cell proliferation [330]. Although undetectable in flask-derived EVs, we found miR-888 – a potent promoter of cell proliferation and migration [331, 332] – to be highly expressed in PDMS EVs. Interestingly, miR-548ar was highly expressed in PDMS EVs but has a potent anti-angiogenic nature [333]. miR-30e-5p and miR-154-5p were found in flask EVs but not the PDMS EVs and are known for their anti-

proliferative and pro-apoptotic effects on cancer cells [334, 335]. On the other hand, other miRNAs known to be involved in promoting cell proliferation and migration were found in flask EVs but were not detected in PDMS EVs (i.e., miR-130a-3p, miR-411-5p) [336, 337]. Importantly, miRNAs often work together as a regulatory network to alter various mRNAs, sometimes even regulating other miRNAs to ensure precise physiological responses [60, 61]. Thus, it can often be hard to predict and understand the exact mechanism of action. The results of this analysis will need to be confirmed via RT-qPCR and overexpression and knockdown studies will need to be completed to confirm that the miRNAs detected are responsible for the effects seen in the recipient cells.

When looking at the gene expression in the recipient HUVECs, many genes were differentially expressed in the HUVECs across the two EV treatments (i.e., flask or PDMS-derived EVs) when compared with the PBS-treated HUVECs. However, only a few were substantially upregulated (more than two-fold) in the HUVECs treated with the PDMS-derived EVs, including pro-angiogenic factors E-selectin, PLAU, and PARD3 [338, 339] (**Figure 5.15**). While E-selectin is often correlated with endothelial cell activation, its expression in endothelial cells has also been found to increase in proliferating endothelial cells independently of activation [340, 341]. It is important to note that, in the present study, the expression of other genes often associated with endothelial cell activation (i.e., VCAM1 and ICAM1) were not upregulated across EV treatments (**Figure 5.15**). E-selectin expression has also been shown to correlate with the amount of soluble E-selectin shed from HUVECs in culture [342]. This soluble

form of E-selectin has been shown to induce tube formation in both endothelial progenitor cells and HDMECs *in vitro* [343-345]. PLAU, also known as urokinase-type plasminogen activator or uPA, contributes to proteolytic degradation of the ECM during wound healing and has been shown to increase the migration of HUVECs *in vitro* (Song et al. 2019). And PARD3 (par3 family cell polarity regulator), also known as PAR3, is vital to the tube formation ability of cultured HUVECs [339].

On the other hand, the anti-angiogenic PTGS2 was downregulated by more than two-fold [346] in the HUVECs treated with the PDMS EVs. This information can be tied back to the miRNA cargos detected in the EVs themselves. For instance, PTGS2 is known to be positively regulated by the activation of NF-κB and it just so happens that several NF-κB activators (i.e., interleukin-1 receptor-associated kinase 4, IRAK4; TGF-beta-activated kinase 1, TAK1; and β-transducing repeat-containing protein 1, BTRC) are all target genes of miR-10a [347]. Thus, the miR-10a in the PDMS EVs may be downregulating PTGS2 in the HUVECs via inhibition of NF-κB. The downregulation of NF-κB has been linked to increased tube formation in HUVECs and other pro-angiogenic effects [348]. Future studies using miR-10 inhibitors and overexpression plasmids will be required to confirm this mechanism. Finally, once the results of the array are confirmed using RT-qPCR, biocomputational methods should be utilized to understand the influence of each of the detected EV-encapsulated miRNAs, how they alter downstream gene expression in recipient HUVECs, and the extent to which these pathways may influence the physiological wound site.

Unfortunately, we were unable to recapitulate the HUVEC mRNA array results using RT-qPCR (**Figure 5.16**). This could be due to low-quality genetic material used as well as the relatively low accuracy and specificity which are known issues inherent to microarray analyses [297]. More direct strategies such as proteomics or RNA-seq on the MSC EVs themselves, coupled with knockdown studies, should be used to identify the specific EV cargoes responsible for the observed bioactivity.

Finally, we demonstrated that, regardless of substrate, MSCs were able to retain a relatively stable expression of MSC markers (CD73, CD90, and CD45) as well as the expression of SOX2, a well-known marker of stem cell differentiation potential (**Figure 5.17**). Importantly, SOX2 expression is often significantly decreased after differentiation [349]. Changes in phenotype were not expected as the MSCs were only cultured on the substrates for three days whereas, when cultured without specialized differentiation media, differentiation on substrates of various stiffnesses has been shown to take seven days [304]. Nevertheless, future work should confirm this undifferentiated state by examining the presence of adipogenic (lipoprotein lipase, LPL; peroxisome proliferator-activate receptor γ, PPARγ), osteogenic (runt-related transcription factor 2, RUNX2; alkaline phosphatase, ALP), and chondrogenic markers (collagen type 2 alpha 1, COL2A1; collagen type x alpha 1 chain, COL10A1) using RT-qPCR, flow cytometry, and immunocytochemistry.

The fact that we were able to produce similar results regarding MSC EV production and bioactivity across two different PDMS fabrication methodologies supports the fact

that substrate stiffness, rather than the other disparate characteristics of the substrates, was the stimulus. For instance, according to the materials safety data sheets (MSDS), while both Sylgard 184 and Sylgard 527 consist mostly of the same chemical components (i.e., dimethylvinyl-terminated dimethyl siloxane and dimethyl, methylhydrogen siloxane), Sylgard 184 has several additional chemicals including xylene, ethylbenzene, and silica nanoparticles. Varying the base to crosslinker ratio can result in an increased amount of non-crosslinked PDMS linear chains that then migrate to the surface of the material which could, theoretically, affect cell function [350]. In contrast, the mixing of the two PDMS types maintains proper stoichiometry and should result in the lowest amount of non-crosslinked material. Forthcoming work could examine the amount of non-crosslinked material in each preparation by weighing the substrate, extracting the non-crosslinked PDMS linear chains using hexane, removing the solvent, and then re-weighing [351]. Additionally, other mechanical properties of the PDMS along with the elastic modulus may be changing as the formulations are manipulated. Previous studies using the same methods have shown that surface wettability, which is often used as a proxy for surface energy and which ultimately affects protein adsorption, can change significantly among the formulations [307, 308]. However, these studies did not use any sort of ECM coating on the PDMS. Research by Pachelsko and colleagues found that differences in surface wettability among formulations only exist prior to ECM coating and once the PDMS was coated with fibronectin, these differences were lost and the wettability remained stable across PDMS preparations [306]. The same study also showed that fibronectin adsorption was virtually indistinguishable across PDMS substrates and that surface roughness was < 1

nm for all PDMS formulations; well below the detection limit for cells [352]. Another study by Brown et al. demonstrated that using polyelectrolyte multilayers to promote cell adhesion can alter the wettability among PDMS formulations; an observation that was lost when fibronectin was adsorbed to the surface [316]. While it seems coating with an ECM prior to cell seeding can help alleviate any significant deviations in mechanical properties other than the elastic modulus, our method of coating was slightly different (collagen). This is an important detail as seemingly innocuous traits, such as ligand density of the ECM coating, has been shown to enhance osteogenesis of MSCs on polyacrylamide gels regardless of substrate stiffness [353]. In the same study, at low (1 μg/mL) or high (10 μg/mL) fibronectin density, YAP translocation was dominated by ligand density irrespective of substrate stiffness [353]. Furthermore, in some cases, it has been shown that protein tethering can also change the cellular response to stiffness [354]. Thus, future work is needed to confirm that other material properties (i.e., surface energy, roughness, ligand density, and protein adsorption) do not differ significantly among the PDMS formulations. When comparing these different attributes, care must be taken in maintaining similar PDMS fabrication methods as the elastic modulus of PDMS can also be manipulated by curing time and temperature [355], as well as the method of sterilization (e.g., UV vs gamma irradiation) [318]. It would also be interesting to see if the results presented here change when culturing on different types of substrates (i.e., PDMS vs hydrogel) with similar elastic moduli or when using different ECM coatings.

This investigation demonstrates that PDMS of varying elastic moduli can be used to increase both the production of MSC EVs as well as *in vitro* EV angiogenic bioactivity, ultimately increasing both MSC EV potency and efficacy. Given the biocompatibility and cost-effective nature of PDMS, this system can be implemented in biomanufacturing processes to enable scalable production of therapeutically-relevant MSC EVs. This research also contributes to a deeper understanding of the interplay between EV biology and synthetic materials that will ultimately advance the engineering of tissue-like constructs for regenerative applications.

Chapter 6: Summary, Conclusions, and Future Directions

6.1 Summary and Conclusions

The intrinsic capability of EVs to shuttle bioactive compounds and the advantages they possess over cell therapies has generated a surge in EV research that has uncovered numerous therapeutic applications [4]. However, the translation of EVs as a clinical medicine is hindered by the lack of a rationally designed biomanufacturing system and low therapeutic potency (i.e., low levels of endogenous therapeutic cargos). To date, most EV biomanufacturing approaches utilize platforms originally designed for whole cell expansion (e.g., hollow-fiber, multi-layered culture vessels, stirred-tank bioreactors), during which cells can experience numerous mechanical stressors. As EVs can reflect the physiological status of cells, these stressors must be considered when optimizing EV manufacturing techniques. However, a limited understanding of the relationship between cellular mechanobiology and EVs hinders the design of an effective EV-specific biomanufacturing platform.

Thus, the studies carried forth during the completion of this dissertation project were meant to reveal how EVs, specifically those derived from therapeutic MSCs, are influenced by the mechanical cues most pervasive in scalable manufacturing processes. Specifically, we focused on establishing methods capable of altering flow-derived shear stress, cellular confinement, and substrate stiffness which we then used to

investigate the impact of the cues on the ability of MSCs to produce EVs (i.e., MSC EV production) and induce angiogenic effects in recipient cells (**Figure 6.1**).

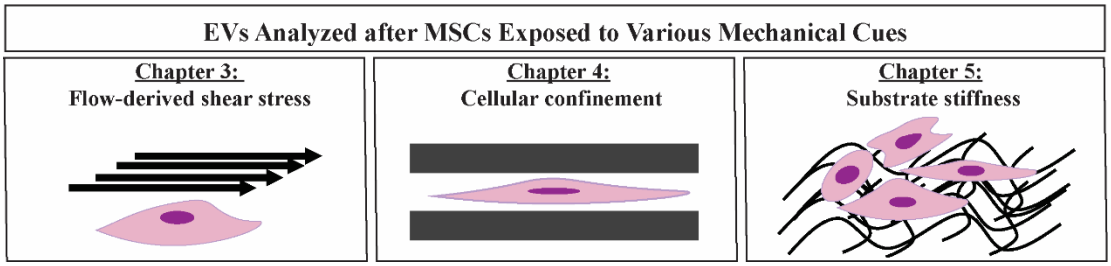


Figure 6.1. Mechanical cues investigated. MSCs were exposed to flow-derived shear stress (Chapter 3), confinement (Chapter 4), or substrates of various stiffnesses (Chapter 5) and the resulting EVs were analyzed.

Chapter 3 introduces a 3D-printed scaffold coupled with a peristaltic pump as a means to controllably expose MSCs to flow-derived shear stress. Previous research has demonstrated the utility of flow-derived shear stress in increasing MSC EV yield and activity [169, 170], but none have implemented a highly-tunable 3D-printing approach amenable to scalable manufacturing practices. We successfully demonstrated that applying flow to MSCs seeded within a 3D-printed scaffold can increase EV production (i.e., the number of EVs secreted per cells) while maintaining the pro-angiogenic effects of the EVs themselves. With the ability to adjust the scaffold features using 3D-printing techniques, this work lays the groundwork for future investigations into the synergistic effects of flow and substrate architecture. In **Chapter 4**, we implemented a PDMS-based micropillar device previously optimized for the mechanical confinement of MSCs [272] and found that cellular confinement leads to increased MSC EV production and changes in EV bioactivity. These experiments are the first to assess the effects of cellular confinement on the downstream potential of EVs. This portion of our work is not only relevant for the development of an EV

manufacturing process but also holds powerful implications for the design of tissue-like constructs for regenerative applications. Notably, PDMS is a polymer widely used in cell-based assays with an elastic modulus (i.e., stiffness) that is inherently different from traditional substrates used in cell culture (i.e., plastic) [312, 356]. This led us to investigate the effects of substrate stiffness on MSC EV production and bioactivity via the manipulation of PDMS formulations in **Chapter 5**. We revealed that PDMS with an elastic modulus ~1 MPa significantly increased MSC EV production while PDMS with an elastic modulus $\leq$ 0.3 MPa augmented MSC EV angiogenic bioactivity. As PDMS is biomanufacturing-friendly, soft PDMS substrates could be integrated within scale-up processes in order to increase MSC EV yield and therapeutic effects. Similar to the micropillar device work, these results will also inform improved tissue engineering techniques.

Overall, this work reveals how mechanical cues inherently present within the biomanufacturing process can be manipulated to enhance EV potency without sacrificing scalability. Given the ubiquitous nature of these cues and the tunability of the developed methodologies, the research conducted here will be applicable to essentially all EV-based formulations, regardless of the intended application and thus has far-reaching benefits throughout regenerative medicine.

6.2 Future Directions

The work presented here provides the foundational knowledge required for the design and implementation of an optimized biomanufacturing platform for MSC EVs. However, deeper investigations, specifically into the mechanisms underlying the

observed effects, are needed to truly harness the cellular microenvironment and ultimately enhance the clinical translation of therapeutic EVs. In general, future studies will need to probe the cargos (e.g., lipids, non-coding RNAs, proteins) of the EVs produced using RNA-seq, liquid chromatography/mass spectrometry (LC/MS)-based proteomics, and lipidomic techniques. This information will prove powerful when coupled with the analysis of the target genes in recipient cells as well as the evaluation of the related functional aspects of the recipient cells. It will also be interesting to see if the same effects can be obtained when utilizing induced pluripotent stem cell-derived MSCs as they have lower heterogeneity and greater clinical potential [357]. Then, comparing EV cargos and recipient cell gene expression across the stimuli may help pinpoint similar upstream regulators and pathways.

In terms of regulators and pathways, it is known that disparate mechanical stimuli can activate the same mechanotransduction pathways. Therefore, to understand the underlying mechanism(s) as well as the potential of each mechanical cue in the enhancement of EV therapeutics, a closer investigation of the results as a whole is required. Interestingly, the maximal number of EVs were produced when MSCs were exposed to low-level shear stress ($3x10^{-3}$ dyn/cm^2), confined conditions (cultured within micropillars; 5-50 μm), or softer substrates (PDMS ~1 MPa). Previous research utilizing bioreactor culture of MSCs has demonstrated that augmented EV secretion could be explained by an increase in intracellular calcium [169], which is known to trigger plasma-membrane EV biogenesis by initiating collapse of the membrane phospholipid asymmetry [358, 359]. The increase in EVs observed when MSCs are

placed under flow has also been shown to be dependent on an increase in the nuclear translocation of YAP [170]. But, previous work has also demonstrated the inhibitory effect of increased intracellular calcium levels on YAP/TAZ activity mediated by the Hippo signaling pathway [360]. Yet, a study by Franklin et al. found that YAP can re-enter the nucleus after an initial spike in calcium and stimulate YAP target genes [361], which demonstrates the complexity of the relationship. It is important to note that the previously mentioned mechanistic studies concerning MSC EV production under flow conditions utilized disparate systems to apply flow shear stress (i.e., flat-plate bioreactor vs fibrous scaffold bioreactor), thus other mechanical cues inherent to the different substrates may be at play. Nonetheless, just as the flow-induced increase in MSC EV secretion was associated with nuclear localization of YAP and calcium levels, a study by Bao and colleagues showed that confined MSCs display an increased nuclear localization of YAP/TAZ [282] and confinement has been shown to increase intracellular calcium [271]. These findings suggest that the mechanism for the increase in MSC EV production across flow or confinement conditions in the present study could be of a similar origin and warrants further investigation in future work. It is interesting to note that many of the same cellular processes are affected by both cellular confinement and flow-derived shear stress in a similar manner (**Figure 6.2**).

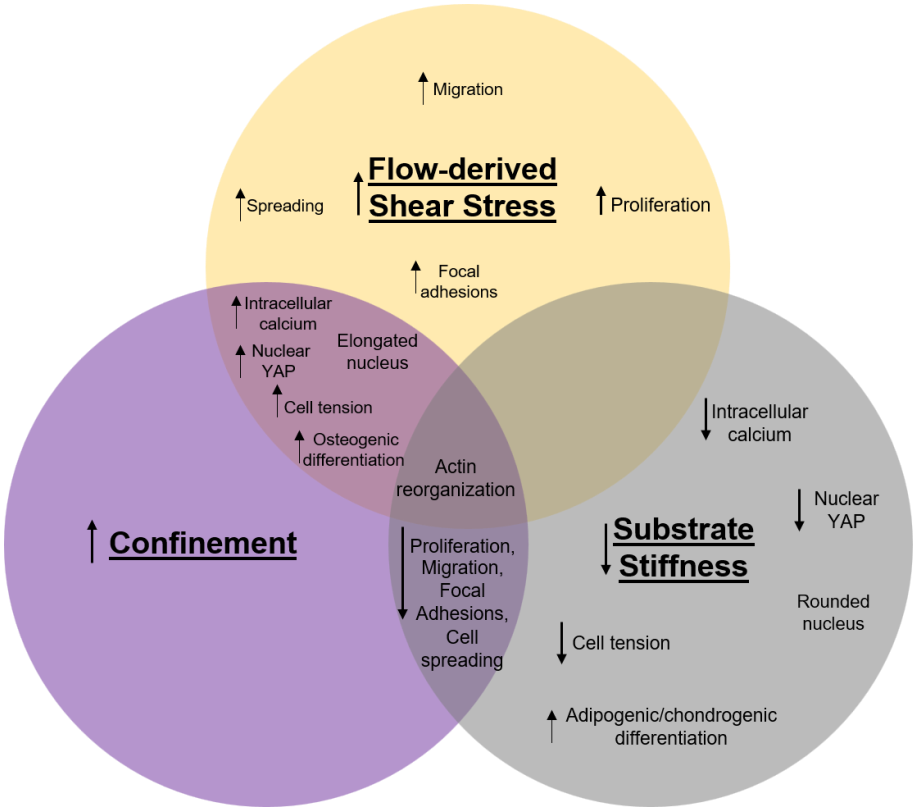


Figure 6.2. Cellular processes governed by the mechanical cues of interest.

In terms of substrate stiffness, previous research has indicated that intracellular calcium levels and YAP/TAZ nuclear translocation is increased with increasing stiffness [260, 362]. However, we found that MSC EV production increased as substrate stiffness decreased; effectively arguing against any shared mechanism with the flow and confinement cues discussed above. A recent study by Lenzini and colleagues also showed that MSCs cultured on soft hydrogels were capable of producing more EVs than those on tissue culture plastic [180]. Interestingly, they found that decreasing FAK could increase EV secretion. It would be interesting to see if a controlled depletion of focal adhesion in MSCs under flow would affect EV secretion. Remarkably, many processes governed by substrate stiffness are in exact opposition to those governed by flow and confinement (**Figure 6.2**). The only apparent shared characteristic among all

three seems to be that all involve some sort of actin reorganization. Given the contradictory nature of the possible mechanisms, it would be beneficial to profile the gene expression of the MSCs themselves under each mechanical stimulus. This type of investigation will also help explain the increase in angiogenic activity observed when MSCs were exposed to confined conditions (micropillars ≤ 20 μm) or soft substrates (PDMS ≤ 0.3 MPa) produced EVs with increased pro-angiogenic effects on endothelial cells, whereas those exposed to flow maintained a similar angiogenic profile to those derived from static culture.

Once the mechanisms of each mechanical cue are interrogated, the ultimate goal will be to synergize the mechanical cues into a singular optimized set-up. This can be done partially by 3D printing scaffolds mimicking the optimal micropillar spacings using a NanoScribe laser lithography system. However, as the softest resin we could use would only reach 15.3 MPa and may not retain microscale topographies, it may not be possible to integrate all three mechanical cues (i.e., flow, confinement, and soft substrate). Nonetheless, the combination of multiple cues (flow and confinement or flow and stiffness) could be investigated.

Finally, as each of these cues are inherently complex, it will be important to examine other cues that may be contributing to the results obtained here. For instance, flow and shear stress are distinct phenomena and they should be examined separately. Notably, shear stress experienced by cells can be controlled by the geometric features of the surrounding physical environment (i.e., architecture, pore size, and porosity) without

adjusting flow rate [363, 364]. Using CAD software and 3D-printing techniques, the geometry of the scaffold used here can be manipulated to induce varying levels of shear stress without altering the flow rate. The confinement within the micropillars may also be introducing other mechanical cues including curvature, which has been shown to alter MSC differentiation [365], so various pillar geometries could be investigated here as well. Lastly, as mentioned earlier, other properties of the PDMS substrate including ECM coating properties (i.e., ligand density and protein tethering) can affect cells and should be investigated [353, 354].

In summary, there are countless avenues to investigate concerning cell mechanobiology and EV potential. A thorough understanding of the mechanoregulatory mechanisms in the context of the cues investigated in this dissertation will be essential to the start of an adaptable and scalable EV biomanufacturing scheme. Despite this, there still remain other obstacles to overcome in the movement of EV medicines from the bench to the bedside. In particular, a standardization of EV isolation and purification protocols is urgently needed as these are incredibly influential on downstream EV analyses and perceived therapeutic abilities [116, 117]. As such, the entire biomanufacturing process will need to be considered early on in the development of an EV formulation in a manner that is both conducive to scalability and unrestrictive of exploratory research.

6.3 Scientific Contributions to the Field and to the Jay Lab

- Determined that flow-derived shear stress augments MSC EV angiogenic activity *in vivo* (Chapter 3).

- Determined that increased mechanical confinement can be used to enhance MSC EV production and alter EV bioactivity (Chapter 4).
- Determined that reduced substrate stiffness can enhance both MSC EV secretion and angiogenic bioactivity (Chapter 5).
- Established photolithography protocols (provided by Drs. Mary Doolin and Kim Stroka).
- Established PDMS micropillar confinement protocol (provided by Drs. Mary Doolin and Kim Stroka).
- Established mouse macrophage LPS-stimulation assay for testing EV bioactivity.
- Optimized endothelial cell tube formation assay for testing EV bioactivity.
- Established tangential flow filtration and size-exclusion chromatography techniques as improved EV isolation strategies.
- Established an updated protocol for EV-depletion.
- Executed collaborations with Dr. Ian White's lab (UMD) and Dr. Steven Prior's lab (UMD).
- Executed collaboration with Dr. Wei Chao (UMB) which resulted in one peer-reviewed publication (see Chapter 6.4).
- Trained and mentored 1 graduate student (Emily Powsner), 2 undergraduate students (Zach Kasica and Lauren Hoorens Van Heyningen), and 1 high school student (Amaya Aranda).

6.4 Peer-Reviewed Journal Publications

- **Kronstadt, S.M.**, D.B. Patel, L.J. Born, D. Levy, M. Lerman, B. Mahadik, S. McLoughlin, A. Fasuyi, L. Fowlkes, L.H. Van Heyningen, A. Aranda, S.N. Abadchi, K.H. Chang, A.T.W. Hsu, S. Bengali, J.W. Harmon, J.P. Fisher, S.M. Jay. 2022. Mesenchymal stem cell culture within perfusion bioreactors incorporating 3D-printed scaffolds enables improved extracellular vesicle yield with preserved bioactivity. Biomaterials. Submitted.
- **Kronstadt, S.M.**, L.H. Van Heyningen, A. Aranda, S.M. Jay. 2022. Assessment of anti-inflammatory bioactivity of extracellular vesicles is susceptible to error via media component contamination. Cytotherapy. Submitted.
- Pottash, A., D. Levy, A. Jeyaram, L. Kuo, **S.M. Kronstadt**, W. Chao, S. Jay. 2022. Combinatorial microRNA loading into extracellular vesicles for increased anti-inflammatory efficacy. Molecular Pharmaceutics. Submitted.
- Paolini, L., M. Monguio-Tortajada, [and 32 others, including **S.M. Kronstadt**]. 2022. Large-scale production of extracellular vesicles: report on the "massivEVs" ISEV workshop. Journal of Extracellular Biology. Under review.
- **Kronstadt, S.M.,** S.M. Jay, A. Jeyaram. 2022. Extracellular vesicle loading via pH-gradient modification. Methods in Molecular Biology. DOI: 10.1007/978-1-0716-2341-1_17.
- **Kronstadt, S.M.**, A.E. Pottash, D. Levy, S. Wang, W. Chao, S.M. Jay. 2021. Therapeutic potential of extracellular vesicles for sepsis treatment. Advanced Therapeutics. DOI: 10.1002/adtp.202000259.

- Shimada, B.K., Y. Yang, J. Zhu, S. Wang, A. Suen, **S.M. Kronstadt**, A. Jeyaram, S.M. Jay, and W. Chao. 2020. Extracellular miR-146a-5p induces cardiac innate immune response and cardiomyocyte dysfunction. ImmunoHorizons. 4 (9): 561-572. DOI: 10.4049/immunohorizons.2000075.
- Jeyaram, A., T.N. Lamichhane, S. Wang, L. Zou, E. Dahal, **S.M. Kronstadt**, D. Levy, B. Parajuli, D.R. Knudsen, W. Chao, and S.M. Jay. 2019. Enhanced loading of functional miRNA cargo via pH gradient modification of extracellular vesicles. Molecular Therapy. 28 (3): 975-985. DOI: 10.1016/j.ymthe.2019.12.007.

Appendix A: Assessment of Anti-Inflammatory Bioactivity of Extracellular Vesicles is Susceptible to Error via Media Component Contamination

A.1 Introduction

With the potential to mirror the functional effects of parental cells and shuttle bioactive cargoes intercellularly, extracellular vesicles (EVs) hold promise as early-stage biomarkers and therapeutic interventions for various diseases as well as proficient drug delivery vehicles [70, 366]. As such, much effort has been expended in exploring the production, isolation, and functional characterization of EVs resulting in various methodologies that differ vastly across individual experiments and phases of research (i.e., preclinical vs clinical) [367]. In terms of EV production, there has been a collective movement to implement dynamic and/or 3D cell culture microenvironments, as these techniques are often more scalable than traditional flask culture and can produce EVs that resemble those within the physiological niche [14]. Specifically, bioreactor-based culture allows for the implementation of physiological parameters, including flow-derived shear stress, and has been shown to significantly increase EV production across numerous studies [15, 147, 169-171, 256, 368-371]. Importantly, the shift from static to dynamic culture is also known to cause dramatic changes in the EV therapeutic profile [116, 166, 169, 170, 256]; in some cases elucidating EV effects that were not present when utilizing traditional flask culture [166]. This phenomenon of altered EV bioactivity can also be observed when implementing different EV isolation

strategies such as tangential flow filtration (TFF), ultracentrifugation (UC), or size-exclusion chromatography (SEC) [116, 117]. Thus, optimizing EV production and isolation methods may be vital in creating an ideal EV formulation for a given application.

Despite the important role that culture conditions and isolation strategies may play, only a couple of studies have explored the combinatorial effects of these techniques on perceived EV bioactivity [116, 372]. In one such study, Haraszti and colleagues demonstrated that EVs from umbilical cord-derived MSCs cultured within a microcarrier-based bioreactor and isolated via TFF were more efficient in delivering functional therapeutic siRNA into neurons than those EVs isolated from the same bioreactor culture using UC. They also show that bioreactor EVs isolated using UC were no more effective in siRNA transfer than EVs from traditional flask culture isolated using UC or TFF [116]. Previous research also cautions over assuming that the EVs are solely responsible for therapeutic activity, as many isolation strategies can result in the co-isolation of process impurities [373]. Demonstrating this is a study by Whitaker et al. in which the co-isolated and non-EV associated VEGF within MSC EV preparations had pro-angiogenic and pro-migratory effects on endothelial cells that could wrongfully be accredited to the EVs [118]. Altogether, these studies emphasize the importance of optimizing both cell culture conditions and isolation methods simultaneously while implementing careful functional assessment to produce the most viable EV therapeutic platform.

As for functional evaluation of EVs, much interest is often paid to EV anti-inflammatory capacity, as inflammatory dysregulation is ubiquitous in many chronic diseases (e.g., sepsis, cancer, and autoimmune disorders) and tissue regeneration issues [374, 375]. Recently, Pacienza and colleagues developed an *in vitro* LPS-stimulated mouse macrophage assay to assess the anti-inflammatory potential of mesenchymal stem cell (MSC)-derived EVs. Notably, results obtained in this *in vitro* assay were able to predict the efficacy of different MSC EV preparations in suppressing LPS-stimulated inflammation in mice [376]. As such, this assay and derivatives of it have been used regularly to test the anti-inflammatory properties of EVs [377-379].

In the present investigation, we examined the combinatorial effects of cell culture conditions (i.e., static vs dynamic) and isolation techniques (i.e., UC vs TFF vs SEC) on the size, morphology, and functional characteristics of EVs from HEK293T cells – a highly scalable source for the production of therapeutic EVs [380]. Surprisingly, depending on culture condition and isolation strategy, HEK293T EVs appeared to exert immunosuppressive effects in an LPS-stimulated mouse macrophage model. We found that this result was most likely due to FBS EV contaminants within the HEK293T EV samples. Our results highlight the importance of recognizing and controlling for potential contaminants in EV preparations when utilizing this assay.

A.2. Methods

A.2.1. Cell Maintenance

Human embryonic kidney cells (HEK293T) were purchased from ATCC (CRL-3216) and cultured in T175 flasks using Dulbecco's Modification of Eagle's Medium (DMEM) [+] 4.5 g/L glucose, L-glutamine, and sodium pyruvate (Corning, 10-013-CV) supplemented with 10% fetal bovine serum (FBS; VWR, 89510-186) and 1% penicillin-streptomycin (P/S; Corning, 30-002-CI). All HEK293T cells used in experiments were between passages 4-7. RAW264.7 mouse macrophages (ATCC, TIB-71) were cultured in T175 flasks with DMEM [+] 4.5 g/L glucose, L-glutamine, and sodium pyruvate (Corning, 10-013-CV) supplemented with 5% FBS and 1% P/S. RAW264.7 at passages 10-13 were used in experiments. Human umbilical vein endothelial cells (HUVECs) pooled from multiple donors (PromoCell; C-12203) were cultured in T75 flasks coated with 0.1% gelatin at 37 $^{\circ}$C for 1 h prior to seeding. HUVECs were maintained in complete endothelial growth medium-2 (EGM2; PromoCell, C-22111) supplemented with 1% P/S. During experiments, HUVECs were cultured in endothelial basal medium-2 (EBM2; PromoCell, C-22221) supplemented with 0.1% FBS and 1% P/S. HUVECs at passages 3 and 4 were used in experiments.

A.2.2.HEK293T Cell Culture Conditions

Flask and Scaffold Culture

As static controls, HEK293T cells were cultured within T75 tissue culture flasks (VWR, BD353136) or a 3D-printed scaffold. The scaffold was printed from a biocompatible acrylate-based material (E-Shell 300; EnvisionTEC) using an EnvisionTEC Perfactory 4 Mini Multilens stereolithography apparatus (EnvisionTEC, Inc., Dearborn, MI, USA). The 12 cm^3 volume construct contained a growth surface area (50 cm^2) with small pillars (1 mm in diameter) that were spaced 2.5 mm apart. This design allowed efficient cell removal and immunofluorescence imaging as well as the facilitation of nutrient and gas transport and a mechanism to control fluid parameters predictably. Following printing, scaffolds were submerged in 99% isopropanol (Pharmco-Aaper, Shelbyville, KY) for 5 min to remove excess resin. The scaffolds were then flushed with fresh 99% isopropanol until all excess resin was removed after which the scaffolds were dried with filtered air. Resin curing was accomplished using 2,000 flashes of broad-spectrum light (Otoflash, EnvisionTEC, Inc.). Scaffolds were then cleaned in 100% ethanol for >30 min to eliminate any remaining contaminants, after which they were placed in fresh 100% ethanol and sterilized in an ultraviolet sterilizer (Taylor Scientific, 17-1703) for 10 min. Rehydration was achieved by soaking the scaffolds in sterile serial dilutions of ethanol to 1X PBS (pH 7.4) for 5 minutes per step (75:25, 50:50, 25:75, 0:100 ethanol:PBS). Rehydrated scaffolds were placed in 100% sterile 1X PBS in at 4°C until use. When ready to use, scaffolds were coated with 3 $\mu g/cm^2$

fibronectin in sterile water at 37˚C for 30 min. Flasks and scaffolds were seeded at a density of 2,500 cell/cm^2 in 15 mL of media.

Perfusion Bioreactor Culture

For the perfusion bioreactor condition, select seeded scaffolds were hooked up to a Masterflex L/S Digital Peristaltic Pump (Cole-Parmer; Vernon Hills, IL, USA) using platinum-cured silicon tubing (Cole-Parmer, EW-95802-04). The scaffolds were operated at a flow rate of 5 mL/min which corresponded to a shear stress value of $3x10^{-3}$ dyn/cm^2 as determined previously by computational fluid modeling via the Flow Simulation add-in for SolidWorks (Dassault Systèmes, Velizy-Villacoublay, France). The set-up allowed the scaffolds to be connected to a media reservoir containing 50 mL of EV-depleted FBS media. The pump and scaffolds were then placed within a cell culture incubator at 37°C with 5% CO_2.

A.2.3. Cell Staining and Imaging

After 24 h culture in the bioreactor, the scaffolds were filled with 4% paraformaldehyde for 15 min at room temperature to fix the HEK293T cells. Scaffolds were then washed three times with 1X PBS and filled with permeabilization buffer (300 µM sucrose, 100 µM sodium chloride, 6 µM magnesium chloride, 20 µM HEPES, and 0.5% Triton-X-100 solution) for 5 min at room temperature. AlexaFluor 488 Phalloidin in PBS (1:100) was used

to stain cell actin and cells were visualized on a Nikon Ti2 Microscope (Nikon, Minato City, Tokyo, Japan).

A.2.4. Media EV-Depletion Protocols

To produce EV-depleted FBS, heat-inactivated FBS was centrifuged at 118,000 × *g* for 16 h and the resulting supernatant was filtered through a 0.2 μm bottle top filter for use in subsequent media supplementation. To produce EV-depleted whole media, DMEM with full supplementation (10% heat-inactivated FBS and 1% P/S) was centrifuged at 118,000 × *g* for 16 h and the supernatant was sterile filtered (0.2 μm) for direct use in ensuing experiments.

A.2.5. EV Isolation Techniques

During experiments, HEK293T culture media was replaced with media made with 10% EV-depleted FBS and 1% P/S (i.e., EV-depleted FBS media) or EV-depleted whole media. Approximately 100 mL of HEK293T conditioned media from each culture condition (i.e., flask, scaffold, or bioreactor) was subjected to a series of differential centrifugation to clear the media of cells as previously described [11]. In brief, conditioned media was first centrifuged at 1,000 × *g* for 10 min to remove any cells that may have detached during collection. The supernatant was then collected and centrifuged at 2,000 × *g* for 20 min to remove any larger cellular debris. This supernatant was then centrifuged at 10,000 × *g* for 30 min to remove any large organelles remaining. The cleared conditioned media was then subjected to the various isolation techniques

described below. Final EV samples were stored at 4°C and were analyzed within three days of collection.

Ultracentrifugation

For ultracentrifugation (UC), the conditioned media was subjected to an additional centrifugation step of 118,000 × *g* for 2 h in a Type 70 Ti ultracentrifuge rotor (Beckman Coulter). The resulting EV pellet was resuspended in 1X PBS and placed into a Nanosep 300 kDa MWCO spin column (Pall, OD300C35) and spun at 8,000 × *g* until all PBS filtered through the membrane (~10-12 min). EVs were washed two more times with 1X PBS, resuspended in 1X PBS, and sterile filtered using a 0.2 μm syringe filter.

Tangential Flow Filtration

Tangential flow filtration (TFF) was performed using a KrosFlo KR2i TFF system (Spectrum Labs, Los Angeles, CA, USA) equipped with a 100 kDa MWCO hollow fiber filter comprised of a modified polyethersulfone membrane (Spectrum Labs, D02-E100-05-N). Prior to processing the cleared conditioned media, the filter was first washed with at least three volumes of 1X PBS to remove the bacteriostatic reagent. Each filter was used no more than five times. To keep a shear rate at 4000 s^{-1}, the flow rate was kept constant at 106 mL/min. All samples were processed at a transmembrane pressure (TMP) of 5 psi. Samples were first concentrated to a volume of 25 mL and then diafiltrated five times in 1X PBS to exchange buffers. Following buffer

exchange, the EVs were concentrated to a volume of 6-9 mL. Further concentration was performed using a 100 MWCO centrifugal concentrator (Corning, 431486) to achieve a final volume of ~0.5 mL. The final EV suspension was sterile filtered using a 0.2 μm syringe filter.

Size-Exclusion Chromatography

EVs were isolated via size-exclusion chromatography (SEC) using qEV Original columns (Izon Science, ICO-35) per the manufacturer's protocol. Briefly, the cleared conditioned media was concentrated to 0.5 mL using the TFF set-up and centrifugal concentrators described in the previous section. After flushing the columns with 1X PBS, 500 μl of the concentrated media was applied to the top of the column and the first four 0.5 mL fractions after the void volume were collected and pooled. The pooled fractions were then concentrated using 100 MWCO centrifugal concentrators to 0.5 mL and sterile filtered (0.2 μm).

A.2.6. Media Testing

To assess the effects of media components, various media formulations were subjected to the aforementioned isolation techniques. Unconditioned media test formulations (i.e., media without exposure to cells) were defined as the following: no cell (media without any cell conditioning), + FBS (media supplemented with EV-depleted FBS), or -FBS (media without FBS). To evaluate the effects of EV-depletion protocols used to remove contaminating

EVs from the FBS components, HEK293T cells cultured in flasks were exposed to either EV-depleted FBS media or EV-depleted whole media as previously described (see Media EV-depletion Protocols section).

A.2.7. EV Characterization

Protein and Particle Quantification

Total protein concentration was determined using BCA methods (G-Biosciences, 786-571) and size distribution as well as particle concentration were assessed using a NanoSight LM10 (Malvern Instruments; Malvern, UK) with Nanoparticle Tracking Analysis (NTA) software version 2.3. For each sample, three 30-second videos were captured with a camera level set at 12. EV samples were diluted to obtain 20-100 particles per frame and at least 200 completed tracks per video to ensure accurate analysis. The detection threshold was set and kept constant across all replicates and samples. The total number of EVs was evaluated using the final resuspension volume and then divided by the number of cells to give final data expressed as total number of EVs per cell.

EV Markers

Western blot analysis was used to determine the presence of specific EV markers as well as the purity of each sample. Based on the BCA results, 7 μg of protein from each EV sample was used for analysis and compared with 7 μg of cell lysate. EV markers were assessed using primary antibodies for Alix (Abcam, ab186429), TSG101 (Abcam, ab125011), and CD63 (Proteintech,

25682-1-AP), while the absence of contaminating proteins were confirmed using antibodies for GAPDH (Cell Signaling Technology, 2118) and calnexin (Cell Signaling Technology, 2679). All primary antibodies were added at a 1:1,000 dilution, excluding GAPDH which was diluted 1:2,000. A 1:10,000 dilution of a goat anti-rabbit secondary (LI-COR Biosciences, 926-32211) was used. Protein bands were imaged using a LI-COR Odyssey CLX Imager and analyzed using the associated software.

Transmission Electron Microscopy

EV morphology was visualized via transmission electron microscopy (TEM) using a negative staining technique. A portion of each EV sample (10 µl) was fixed in a 1:1 solution using 4% EM-grade paraformaldehyde (Electron Microscopy Sciences, 157-4-100) for 30 min at room temperature. A 10 µl droplet of the EV-PFA mixture was then allowed to adsorb to a carbon-coated copper grid (Electron Microscopy Sciences, CF200-Cu-25) for 20 min. After a brief wash using a of a drop of 1X PBS, the EV-coated grid was then placed on a drop of 1% glutaraldehyde (in 1X PBS) for 5 min. The grid was washed 5-7 times (2 min each wash) on deionized water droplets with blotting on filter paper between washes. The grid was then positioned on a droplet of uranyl-acetate replacement stain (Electron Microscopy Sciences, 22405) and allowed to dry completely for 10 min. Once prepared, the grids were imaged at 200 kV on a JEOL JEM 2100 LaB6 TEM.

A.2.8. Bioactivity Assessment

Macrophage Stimulation Assay

To assess the effects of EV isolation technique and culture method on downstream applications, a mouse macrophage stimulation assay was utilized [376, 381]. RAW264.7 mouse macrophages were seeded at 60,000 cells/well in triplicate in a 48-well plate. 24 h later, two groups (i.e., six wells) of the macrophages were pre-treated with just media with PBS (vehicle control). Another group was pretreated using media supplemented with dexamethasone at 1 μg/mL (resuspended in 1X PBS) which served as the positive control (Dex; Sigma-Aldrich, D4902-25 MG). The remaining macrophages were pre-treated with the HEK293T EVs (resuspended in 1X PBS) from the various culture and isolation techniques at 5E9 EVs/mL diluted in cell culture media. After 24 h of incubation, the pre-treatments were removed and the macrophages were washed once with sterile 1X PBS. Cells were then either treated with just media spiked with PBS (vehicle control) or media spiked with lipopolysaccharide at 10 ng/mL (LPS; resuspended in 1X PBS; Sigma-Aldrich, L4391-1MG) for 4 h. The supernatants were then collected from the RAW264.7 macrophages and frozen at -80° C. Levels of secreted IL-6, RANTES, and TNF-α were assessed using the appropriate DuoSet ELISA kit (R&D Systems, DY406, DY478, DY410).

Tube Formation Assay

HUVECs were used to evaluate effects on endothelial tube formation as previously described [227]. In brief, HUVECs were trypsinized, counted, and aliquoted into a tube marked for each treatment that was filled with 2 mL of EBM2 supplemented with 0.1% FBS and 1% P/S. The cells were then pelleted at 220 × *g* after which the supernatant was removed and the cells were aliquoted to a final concentration of 120,000 cells/mL into complete growth media (positive control), basal media (EBM2 plus 0.1% FBS and 1% P/S) devoid of EVs (negative control), or basal media supplemented with EVs (5E9 EVs/mL) and gently but thoroughly resuspended. The treatments were then applied in triplicate at 500 µl per well (i.e., 60,000 cells/well) in a 24-well plate coated with growth factor reduced Matrigel (Corning, 354230). Cells were imaged at 6 h using a Nikon Eclipse Ti2 Microscope and the number of loops formed by the HUVECs was quantified using ImageJ.

Gap Closure Assay

To assess endothelial migration, HUVECs were seeded at 15,000 cells/well in a 0.1% gelatin-coated 96-well plate and allowed to grow to confluency. The monolayer was then disrupted using an AutoScratch (BioTek Instruments; Winooski, VT, USA) to create a cell gap meant to simulate a wound. HUVECs were gently washed with 1X PBS and serum-starved for 2 h via incubation with basal media. Following serum starvation, the media was aspirated and replaced with complete growth media (positive control), basal media (negative control),

or basal media spiked with EVs (5E9 EVs/mL). The cell gap was imaged at 0 h and 20 h using a Nikon Eclipse Ti2 Microscope and the change in the gap area was calculated using ImageJ as previously described [164].

A.2.9. Statistics

Data are presented as mean ± standard error of the mean (SEM). Two-way ANOVAs with Tukey's multiple comparisons tests were used to determine statistical differences ($p < 0.05$) among groups across cell culture conditions and EV isolation techniques in the *in vitro* stimulated macrophage assay. One-way ANOVAs with Tukey's multiple comparisons tests were used to detect statistical differences ($p < 0.05$) among groups in the *in vitro* gap closure assay and tube formation assay. All statistical analyses were performed using Prism 9.1 (GraphPad Software, La Jolla, CA). Notation for significance in figures are as follows: ns – $p > 0.05$: *- $p < 0.05$; ** - $p < 0.01$; *** or ### - $p < 0.001$; **** or ####- $p < 0.0001$).

A.3 Results

A.3.1. Cell culture condition and EV isolation technique have no effect on EV size or morphology

As various factors including cell culture methods and isolation techniques have been shown to influence downstream EV efficacy [382], we set out to dissect the effect of these factors on HEK293T EVs. HEK293T cells were chosen based on their proven ability to be integrated into scalable biotech processes as well as demonstrated ability to be engineered for therapeutic EV production [380,

383]. The EVs that they secreted are also thought to be relatively therapeutically inert, especially when compared with the EVs of other cell types (e.g., mesenchymal stem cells; MSCs) [3, 384, 385]. Thus, analysis of HEK293T EVs in biological assays could reveal confounding factors in commonly used EV production and characterization strategies. In the current study, HEK293T cells were cultured in a 3D-printed, acrylate-based scaffold hooked up to a peristaltic pump and operated at a 5 mL/min flow rate ($3x10^{-3}$ dyn/cm^2), constituting a set-up which will be referred to as the bioreactor. Prior studies in our lab have revealed that this specific flow rate allows adequate cell viability and increases EV production (i.e., EVs per cell) [15]. HEK293T cells were also cultured in static scaffolds and T75 flasks as controls. Conditioned media from the various culture methods were collected and EVs were isolated via ultracentrifugation (UC), tangential flow filtration (TFF), or size exclusion chromatography (SEC) as depicted in **Figure A.1.A**. There were no significant alterations in EV mode size as measured by NTA (Flask UC – 96.9 ± 5.5 nm; Flask TFF – 86.3 ± 6.4 nm; Flask SEC – 90.9 ± 10.1 nm; Scaffold UC – 88.8 ± 6 nm; Scaffold TFF – 92.9 ± 3.4 nm; Scaffold SEC – 90.9 ± 9.5 nm; Bioreactor UC – 98.7 ± 5.6 nm; Bioreactor TFF – 84.2 ± 4 nm; Bioreactor SEC – 90.1 ± 2 nm) (**Figure A.1.B**). Additionally, greater than 90% of the EV population from each sample were well within the range of acceptable exosomal diameter (40 – 200 nm) (**Figure A.1.B**) [34]. Immunoblotting established the presence of specific EV markers (Alix, TSG101, and CD63) and the absence of cellular debris indicators (Calnexin and GAPDH) (**Figure A.1.C**). TEM images showed

no effect of culture or isolation technique on HEK293T EV morphology (**Figure A.1.D**).

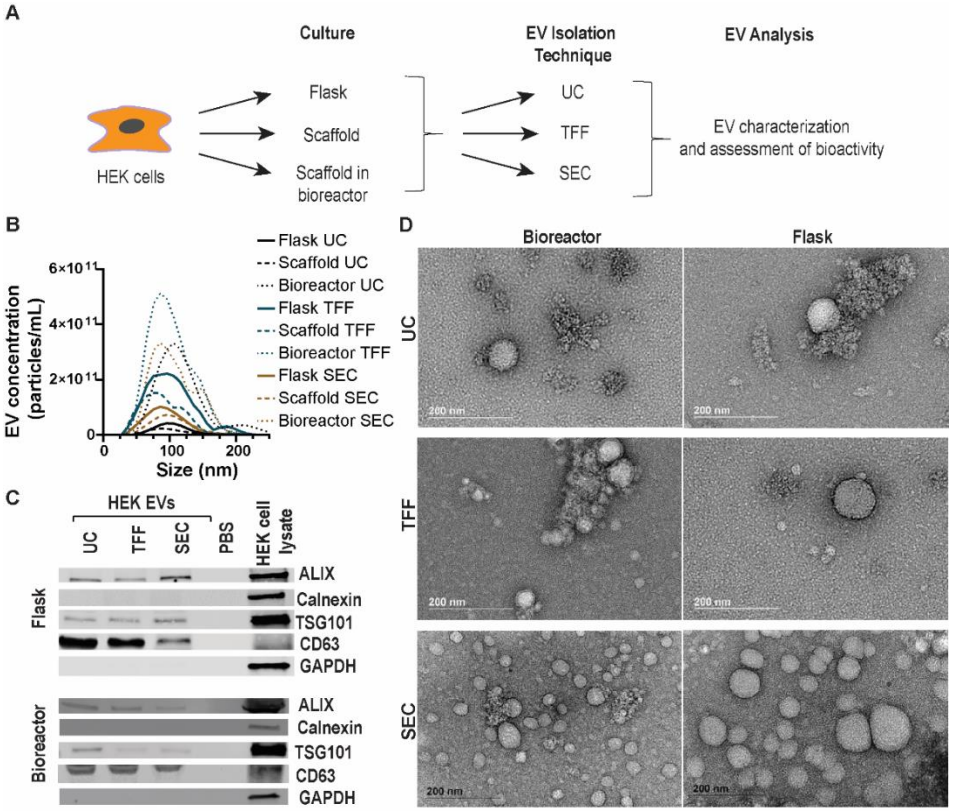


Figure A.1. Culture conditions and isolation techniques do not impart significant effects on size or morphology of HEK293T EVs. (A) Schematic depicting the experimental workflow. (B) Size distribution of HEK293T-derived EVs generated and isolated via the various culture conditions and isolation methods (ultracentrifugation, UC; tangential flow filtration, TFF; size exclusion chromatography, SEC). (C) Immunoblotting of HEK293T EVs from flask and bioreactor conditions isolated via UC, TFF, or SEC for EV-specific markers (CD63, Alix, TSG101) and cell markers (Calnexin and GAPDH). (D) TEM images of HEK293T EVs isolated from the flask and bioreactor culture conditions using each isolation method. Data and images are representative of two independent experiments (N = 2).

A.3.2. Immunomodulatory activity of HEK293T EV preparations is altered by culture condition and isolation method

HEK293T EV isolates prepared using the various culture conditions (i.e., flask, scaffold, or bioreactor) and separation methods (i.e., UC, TFF, or SEC) were assessed in an LPS-stimulated mouse macrophage assay, with final read-outs being the secretion levels of several inflammatory cytokines (i.e., IL-6, RANTES, TNF-α). These cytokines are known to regulate inflammation and are correlated with EV immunomodulatory activity *in vivo* [376, 386, 387]. It was observed that levels of the secreted inflammatory cytokines differed significantly when macrophages were exposed to HEK293T EV preparations from the various culture methods and isolation technique combinations (**Figure A.2**). For every cytokine analyzed, there was a significant interaction of culture technique with isolation method as determined by a two-way ANOVA (IL-6: $p < 0.0001$; RANTES: $p < 0.0001$; TNF-α: $p = 0.0056$). Surprisingly, Tukey's multiple comparison tests revealed that HEK293T EV preparations from every condition, except those from the bioreactor culture isolated using SEC, significantly reduced the levels of IL-6 secretion compared with the LPS-only group (**Figure A.2.A**). A similar trend, although not always significant, was observed in the levels of secreted RANTES (**Figure A.2.B**). Isolating via the UC method in particular produced preparations with a significantly increased ability to suppress the secretion of inflammatory cytokines (**Figure A.2**); an effect that was often lost if cells were cultured within the bioreactor (**Figure**

A.2.B, C). Notably, preparing EV isolates via TFF or SEC weakened the observed suppression of cytokine secretion.

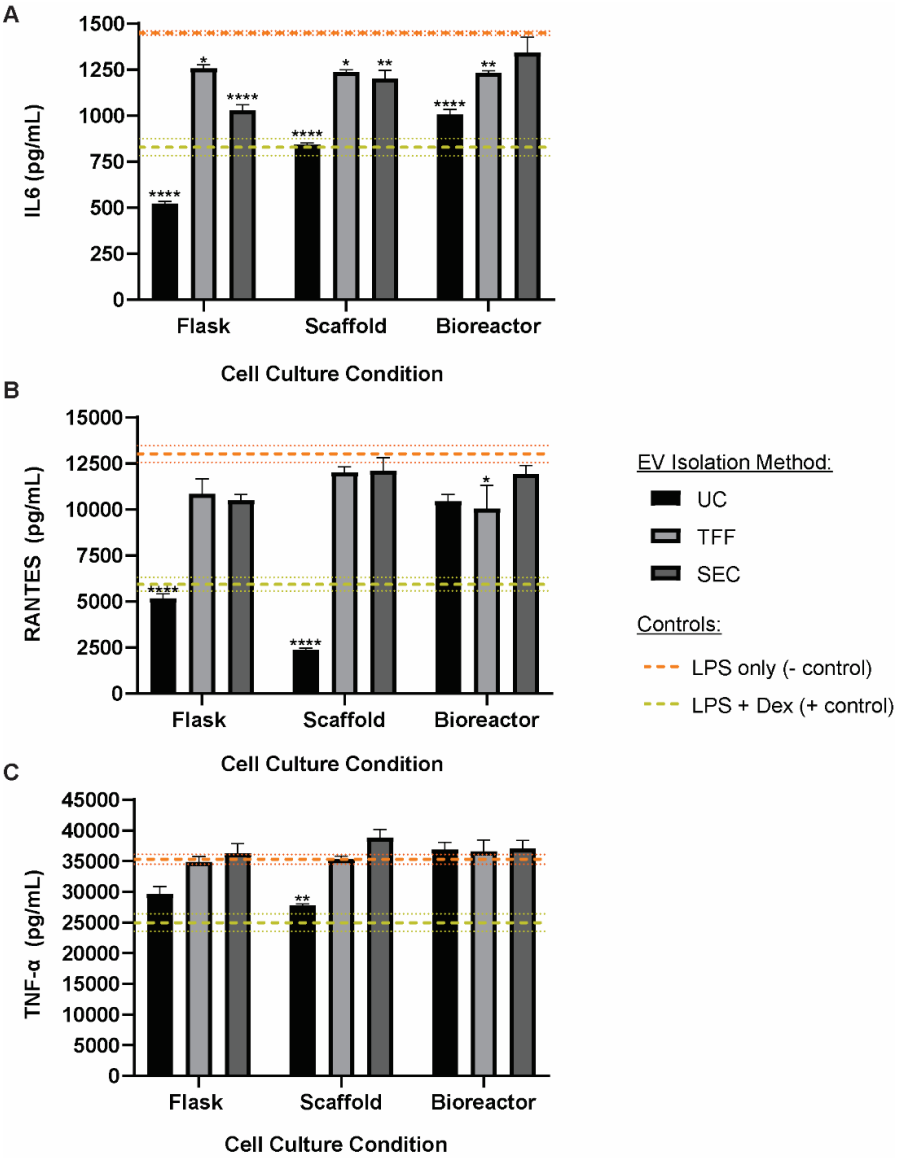


Figure A.2. Culture conditions and isolation techniques alter the immunomodulatory activity of HEK293T EVs. RAW264.7 mouse macrophages were pretreated with either HEK293T EVs from cells within the various culture conditions (i.e., flask, scaffold, or perfusion bioreactor) and isolated using different techniques (i.e., ultracentrifuge – UC, tangential flow filtration – TFF, or size-exclusion chromatography – SEC) or with dexamethasone (Dex) prior to stimulation with lipopolysaccharide (LPS). RAW264.7 supernatants were collected and (A) IL-6, (B) RANTES, and (C) TNF-α secretion was quantified via ELISAs. Data is plotted as mean and error bars represent the standard error of the mean (SEM). Control means are represented as dashed lines with dotted lines representing the SEM. Data includes three technical replicates and data are representative of two independent biological replicates (N = 2). Statistical significance was calculated using a two-way ANOVA using Tukey's multiple comparison tests (*- $p < 0.05$; ** - $p < 0.01$; **** - $p < 0.0001$ compared to LPS negative control).

A.3.3. Media components influence the results of the macrophage stimulation assay

To determine if media components affect the readout of the macrophage stimulation assay, unconditioned media (i.e., media not previously exposed to HEK293T cells) and conditioned media collected from HEK293T cells cultured in flasks were exposed to the various isolation techniques (i.e., UC, TFF, or SEC) and applied to RAW264.7 macrophages prior to LPS stimulation. Interestingly, both unconditioned and conditioned media preparations significantly and similarly reduced the secretion of IL-6 from the stimulated macrophages regardless of isolation technique (**Figure A.3.A**). Analysis of RANTES concentrations reveals a reduction of the cytokine only in the cells treated with the UC-isolated preparations, with a significant reduction in RANTES secretion when treated with the conditioned media (**Figure A.3.B**). However, when looking at TNF-α, the trends readily apparent in the IL-6 concentrations were lost, except for a reduction when isolating with TFF (**Figure A.3.C**).

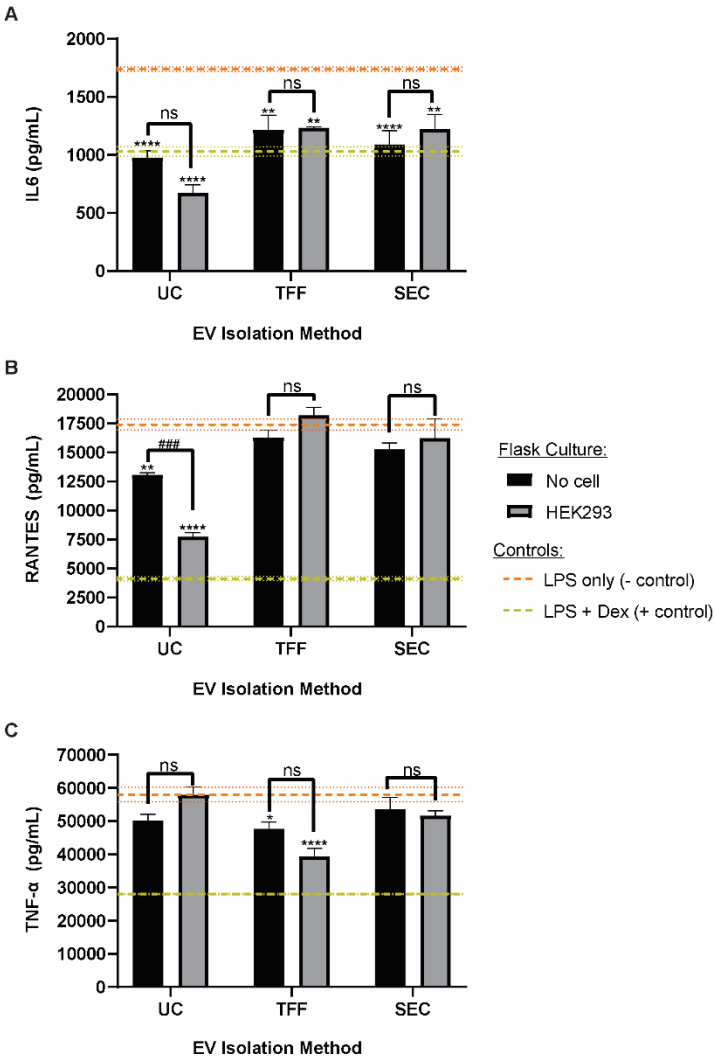


Figure A.3. Unconditioned media subjected to each isolation technique alter cytokine secretion in stimulated macrophages in a similar manner to HEK293T EV preparations. Unconditioned media (i.e., no prior exposure to cells; 'no cell') or media conditioned with HEK293T cells within flasks were exposed to each isolation procedure (i.e., ultracentrifugation – UC, tangential flow filtration – TFF, or size-exclusion chromatography – SEC). Either the resulting preparations or dexamethasone (Dex) were applied to RAW264.7 mouse macrophages prior to stimulation with lipopolysaccharide (LPS). RAW264.7 supernatants were collected and (A) IL-6, (B) RANTES, and (C) TNF-α secretion was quantified via ELISAs. Data is plotted as mean and error bars represent the standard error of the mean (SEM). Control means are represented as dashed lines with dotted lines representing the SEM. Data includes three technical replicates and data are representative of two independent biological replicates (N = 2). Statistical significance was calculated using a two-way ANOVA using Tukey's multiple comparison tests (ns – $p > 0.05$; *- $p < 0.05$; ** - $p < 0.01$; **** - $p < 0.0001$ compared to LPS negative control).

To determine if these results were confined to the stimulated macrophage assay, unconditioned media were isolated via UC and applied in two orthogonal *in vitro* assays. Results showed that in both an endothelial gap closure assay and an endothelial tube formation assay, unconditioned media did not induce any significant response and were similar to the negative control (i.e., basal media) (**Figure A.4**).

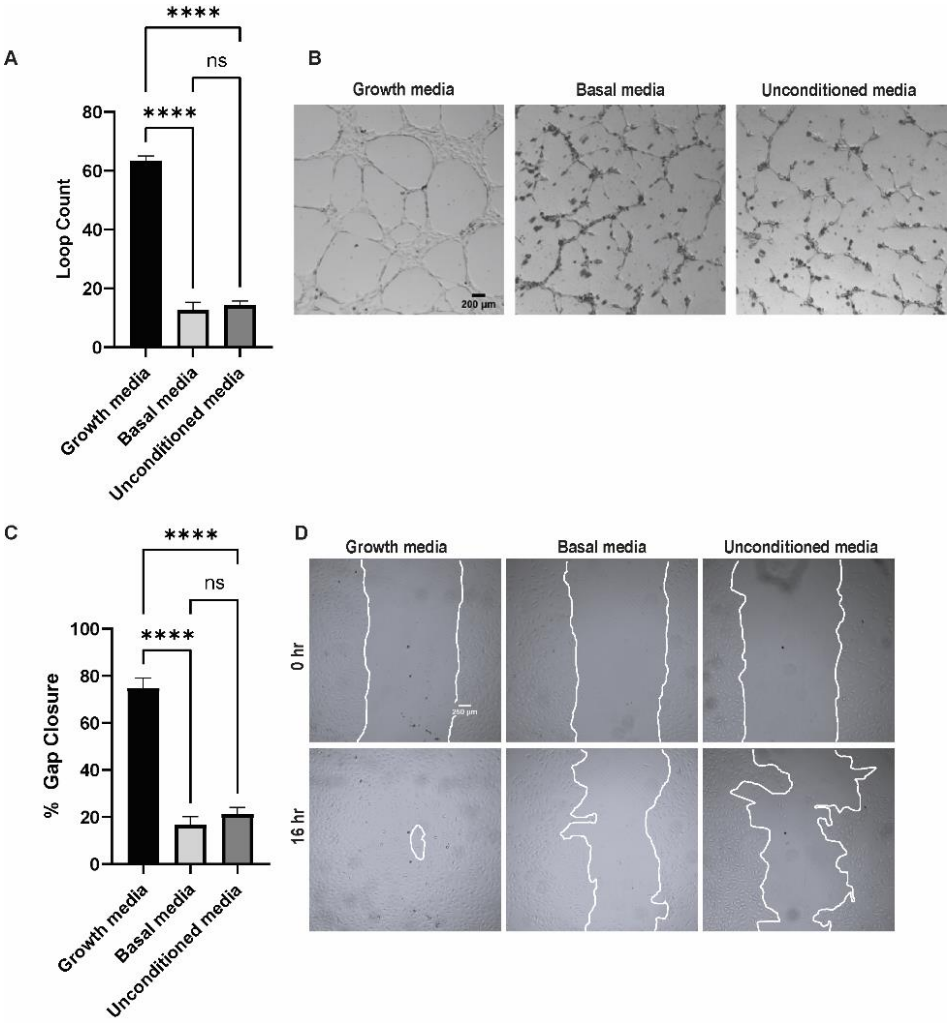


Figure A.4. Unconditioned media do not elicit any significant response in in vitro angiogenic assays. (A) Number of loops formed by human umbilical vein endothelial cells (HUVECs) in a tube formation assay after treatment with growth media (positive control), basal media (negative control), or unconditioned media following exposure to the ultracentrifugation isolation protocol along with (B) the corresponding representative images at 16 hr. (C) Percent gap closure 16 h after treatment with growth media, basal media, or unconditioned media subjected to ultracentrifugation. There were no significant differences between the unconditioned media treatment and the negative control (basal media) in either assay ($p > 0.05$). All images and data are representative of two biological replicates with three technical replicates each. Statistical differences were analyzed using a one-way ANOVA with Tukey's multiple comparisons test (ns – $p > 0.05$, **** - $p < 0.0001$).

To further dissect the observed effects, unconditioned media containing FBS (i.e., + FBS) or unconditioned media without FBS (i.e., - FBS) underwent the UC isolation protocol and were tested in the stimulated macrophage assay. The results revealed that the suppression of IL-6 secretion from macrophages was lost when FBS was absent from the media (**Figure A.5.A**). A similar trend was observed when looking at RANTES levels, but only when using the UC isolation method (**Figure A.5.B**). All patterns of cytokine suppression were diminished when examining TNF-α levels (**Figure A.5.C**). Based on these results, the EV-depletion protocols for media supplementation were examined. Two disparate protocols were followed, and the media tested again in the macrophage assay. In brief, FBS was either depleted of EVs prior to addition into the media (i.e., FBS-depleted) or after being added to the media (i.e., whole media-depleted), subjected to the UC isolation protocol, and applied to macrophages prior to LPS stimulation. Results showed that when whole media was depleted, the secretion of IL-6 from stimulated mouse macrophages was no longer subdued and was statistically similar to the LPS-only control (**Figure A.6**).

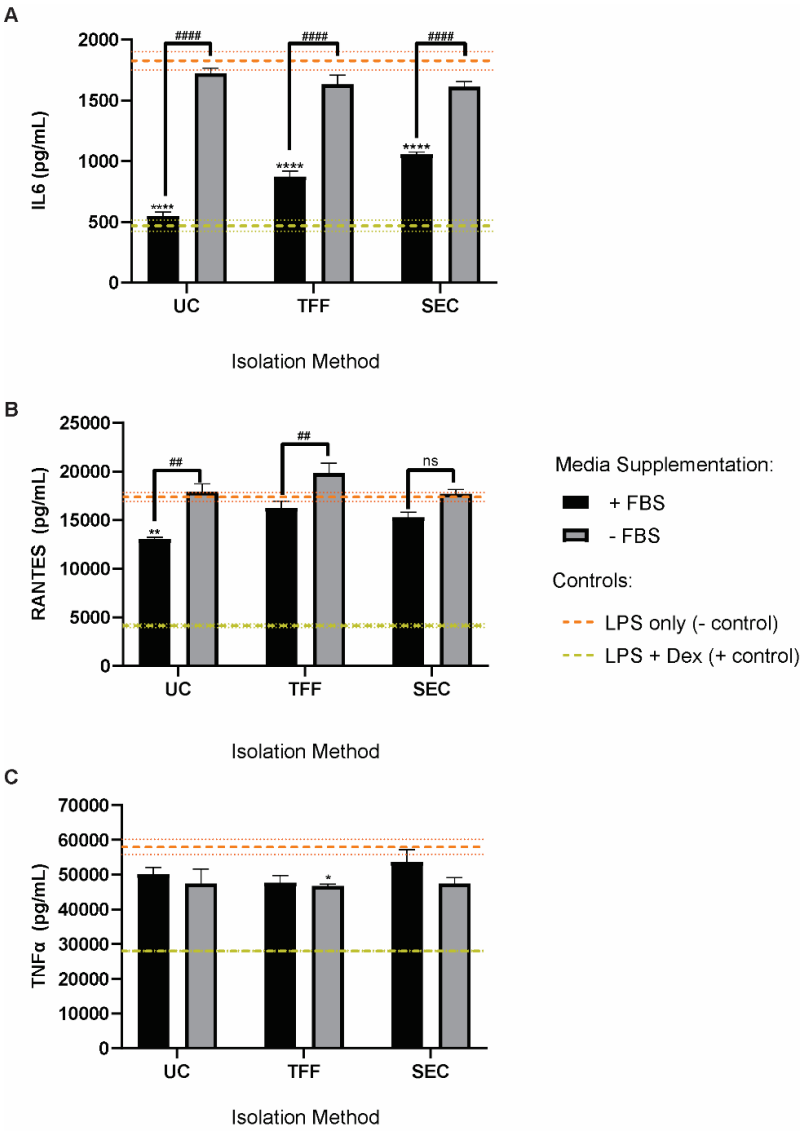


Figure A.5. Fetal bovine serum (FBS) may be responsible for observed immunomodulatory responses of stimulated macrophages. Unconditioned media with FBS (+ FBS) and without FBS (-FBS) were subjected to a routine ultracentrifugation EV isolation protocol and applied to mouse macrophages prior to stimulation with LPS. The concentrations of (A) IL-6, (B) RANTES, and (C) TNF-α were quantified using ELISAs. Data is plotted as mean and error bars represent the standard error of the mean (SEM). Control means are represented as dashed lines with dotted lines representing the SEM. Data includes three technical replicates and data are representative of two independent biological replicates (N = 2). Statistical significance was calculated using a two-way ANOVA using Tukey's multiple comparison tests (ns – $p > 0.05$; *- $p < 0.05$; ** - $p < 0.01$; **** - $p < 0.0001$ compared to LPS negative control; #### - $p < 0.0001$).

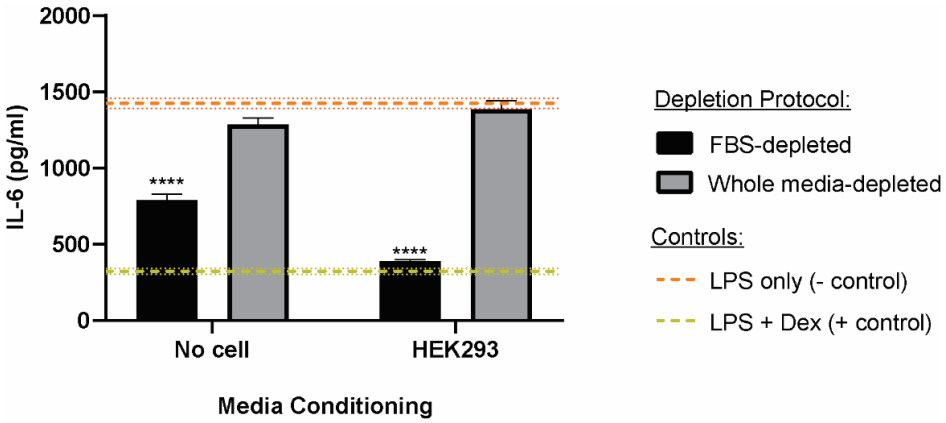


Figure A.6. EV-depletion protocol of media supplements alter the results of the stimulated macrophage assay. FBS was either depleted of contaminating bovine EVs prior to addition to the media (FBS-depleted) or after addition (whole media-depletion), incubated either with (HEK293T) or without cells (no cell), subjected to the ultracentrifugation protocol, and applied to macrophages immediately prior to LPS. When the whole media protocol was used, IL-6 secretion was no longer suppressed. Data is plotted as mean and error bars represent the standard error of the mean (SEM). Control means are represented as dashed lines with dotted lines representing the SEM. Data includes three technical replicates and data are representative of two independent biological replicates (N = 2). Statistical significance was calculated using a two-way ANOVA using Tukey's multiple comparison tests (**** - $p < 0.0001$ compared to LPS negative control).

A.4 Discussion

It is well-known that cell culture parameters (e.g., cell density, passage, media composition, substrate architecture) as well as isolation strategies can significantly impact the molecular composition and therapeutic function of EVs [113, 114, 116, 117, 154, 164, 225, 388-394]. Particularly, this has important downstream implications as movement from the bench to the clinic requires implementing scalable GMP-compliant manufacturing techniques in both EV production (e.g., serum-free media and dynamic bioreactors) and EV isolation (e.g., size-exclusion chromatography), which are often quite different from those utilized in the preclinical setting and can be ever-changing

even through clinical phases [367]. In the present study, we set out to investigate how these various upstream and downstream parameters may interact to alter EV characteristics using HEK293T cells as the EV source based on the proven compatibility of these cells with industry-scale bioprocess operations. To examine upstream parameters, we implemented a 3D-printed scaffold-perfusion bioreactor system previously utilized in our lab and exposed HEK293T cells to low levels of flow-derived shear stress (i.e., $3x10^{-3}$ dyn/cm^2). To examine downstream isolation strategies, we isolated the subsequently secreted HEK293T EVs using the gold-standard technique of ultracentrifugation (UC) and compared it with the more scalable methods of size-exclusion chromatography (SEC) and tangential flow filtration (TFF). Our results suggest that EV size and morphology are not significantly altered when these particular cell culture parameters and isolation strategies are varied (**Figure A.1**). It is important to evaluate both EV size and shape as changes in these characteristics are used as indicators of EV membrane integrity and have been known to be modified by external forces, particularly the shearing involved in high-speed centrifugation [113, 117]. When coupled with membrane markers, size can also be used to suggest possible EV biogenesis routes, as smaller EVs are thought to be derived more so from the endosomal compartment rather than the plasma membrane [395]. Previous research has shown similar results in which EV size and shape are not changed by the culture or isolation methodology used. For example, when comparing UC and TFF isolation methods following traditional flask and 3D microcarrier bioreactor-based culture of umbilical cord-derived MSCs, Haraszti and colleagues found all EV preparations to have similar size distributions [116]. Additionally, prior work in our lab has

demonstrated no significant effect of dynamic culture on such physical parameters of EVs secreted from human dermal microvascular endothelial cells (HDMECs) [15]. However, a study by Sharma et al. showed significant differences in size distributions as well as nanoscale topography (i.e., surface roughness) that was evident across various breast cancer cell-derived EVs that were isolated using four different isolation methods (i.e., ultracentrifugation, density ultracentrifugation, immunoaffinity, precipitation) [122]. The disagreement in results could be attributed to differences in assessment techniques. While the aforementioned studies relied on nanoparticle tracking analysis and transmission electron microscopy, Sharma and colleagues used disparate methods to quantify and assess EV characteristics including atomic force microscopy (AFM), multi-angle light scattering (MALS), direct stochastic optical reconstruction microscopy (dSTORM), and micro-fluidic resistive pore sizing (MRPS). They also measured surface nano-roughness; a dimension rarely evaluated for EVs [396]. Importantly, surface roughness of synthetic nanoparticles has been proven to change the protein corona and subsequently alter their cellular uptake [397]. Although of biological origin, it makes sense that alterations in the surface roughness of EVs may impart similar changes in recipient cell internalization. Altogether these results suggest that, when possible, it is important to utilize orthogonal methods and consider unique characteristics to more rigorously assess EV mechanical parameters to help understand the mechanisms underlying downstream therapeutic effects.

We then assessed whether the culture or isolation techniques alter the bioactivity of HEK293T EVs by applying them in an *in vitro* LPS-stimulated mouse macrophage

model. We found that the EVs, particularly those isolated using ultracentrifugation, significantly reduced the secretion of pro-inflammatory cytokines (i.e., IL-6 and RANTES); an effect that was largely lost when culturing within the bioreactor or isolating using TFF or SEC (**Figure A.2**). As HEK293T EVs are not known to have significant immunomodulatory effects [3], these results were unexpected. Nevertheless, ultracentrifugation is notorious for the co-isolation of proteins and other small molecules which may be imparting the observed therapeutic effect [122, 398-400]. Moreover, previous research in our lab using a similar bioreactor has shown a significant reduction in total protein content per EV [15], which could help explain the loss of the observed effect when using EVs from HEK293T cells cultured within the bioreactor in the present study (**Figure A.2**). This change in protein content in dynamic culture is to be expected as it has been shown that flow can alter the protein corona that forms on nanoparticles [244]. The composition of the EV protein corona under dynamic conditions should be evaluated in future studies.

To confirm whether the HEK293T EVs themselves were truly suppressing cytokine secretion, we focused only on traditional flask culture and assessed the effect of unconditioned media (i.e., media incubated without cells) after being processed using UC, TFF, and SEC. We found that the unconditioned media significantly reduced the IL-6 concentration regardless of isolation technique and lessened the RANTES and TNF-α concentrations particularly when isolating using UC and TFF, respectively (**Figure A.3**). We found that this observation of the unconditioned media having an effect was only present in this specific assay, as there were no significant effects of

unconditioned media subjected to ultracentrifugation in other *in vitro* assays commonly used to assess EV bioactivity (i.e., gap closure and tube formation) (**Figure A.4**). This suggests an interaction between the component(s) of the media and the LPS response in this particular assay. Indeed, fetal bovine serum (FBS), a common reagent for media supplementation, has been shown to alter LPS sensitivity in cell cultures [401] as well alter EV analyses [402]. Thus, we tested unconditioned media without FBS supplementation and found that nearly all treatments were comparable to the LPS control, thus implicating FBS as the component responsible for the cytokine suppression (**Figure A.5**). Interestingly, a previous study by Beninson and Fleshner found that FBS-derived EVs can have an immunosuppressive effect on primary rat macrophages [403]. Inspired by this, we revisited our EV-depletion protocol and found that differences in the methodology used to EV-deplete media can result in drastic differences in cytokine secretion (**Figure A.6**). In the pursuit of understanding the effects of HEK293T EVs in the stimulated macrophage model, we were able to optimize our existing EV-depletion protocol which is a foundational component of the majority of our research.

As EV-based therapies have shown promise in a wide array of applications, there is much interest in the movement of these therapeutics into the clinic. However, successful clinical translation hinges upon the ability to optimize EV therapeutic effects within a scalable, GMP-compliant environment. In our work, we demonstrate an unexpected immunosuppressive effect of HEK293T EVs that differed depending on culture conditions of the HEK293T cells as well as isolation strategies used for the

EVs. This may explain the disparity between studies that report no effect of unmodified HEK293T EVs in their bioactivity assays [144, 235] and others that describe significant immunomodulatory activity [404]. As some culture conditions and isolation methods may be more amenable to scale-up processes than others, it is important to consider these parameters as early as possible to ensure a smooth transition to clinical exploration. We also show that media components from the cell culture may contaminate the separated formulation and alter final EV therapeutic evaluation; a result that further emphasizes the urgency to move to xeno-free, chemically-defined culture conditions and to improve or introduce new downstream separation methods. As identity and purity are major quality considerations to move investigative new drugs into the realm of approved therapeutics [367], this work reiterates the necessity for multiple orthogonal assays as well as the consideration of all controls in order to confirm that any observed effects are truly the result of the experimental EV condition.

Bibliography

[1] J. Galipeau, L. Sensebe. Mesenchymal Stromal Cells: Clinical Challenges and Therapeutic Opportunities. Cell Stem Cell. 2018. 22(6): 824-833.

[2] A. Musial-Wysocka, M. Kot, M. Majka. The Pros and Cons of Mesenchymal Stem Cell-Based Therapies. Cell Transplant. 2019. 28(7): 801-812.

[3] X. Zhu, M. Badawi, S. Pomeroy, D.S. Sutaria, Z. Xie, A. Baek, J. Jiang, O.A. Elgamal, X. Mo, K. Perle, J. Chalmers, T.D. Schmittgen, M.A. Phelps. Comprehensive toxicity and immunogenicity studies reveal minimal effects in mice following sustained dosing of extracellular vesicles derived from HEK293T cells. J Extracell Vesicles. 2017. 6(1): 1324730.

[4] O.M. Elsharkasy, J.Z. Nordin, D.W. Hagey, O.G. de Jong, R.M. Schiffelers, S.E. Andaloussi, P. Vader. Extracellular vesicles as drug delivery systems: Why and how? Adv Drug Deliv Rev. 2020.

[5] L. Alvarez-Erviti, Y. Seow, H. Yin, C. Betts, S. Lakhal, M.J. Wood. Delivery of siRNA to the mouse brain by systemic injection of targeted exosomes. Nat Biotechnol. 2011. 29(4): 341-5.

[6] Y. Liu, D. Li, Z. Liu, Y. Zhou, D. Chu, X. Li, X. Jiang, D. Hou, X. Chen, Y. Chen, Z. Yang, L. Jin, W. Jiang, C. Tian, G. Zhou, K. Zen, J.

Zhang, Y. Zhang, J. Li, C.Y. Zhang. Targeted exosome-mediated delivery of opioid receptor Mu siRNA for the treatment of morphine relapse. Sci Rep. 2015. 5 17543.

[7] R. Gupta, G. Radicioni, S. Abdelwahab, H. Dang, J. Carpenter, M. Chua, P.A. Mieczkowski, J.T. Sheridan, S.H. Randell, M. Kesimer. Intercellular Communication between Airway Epithelial Cells Is Mediated by Exosome-Like Vesicles. Am J Respir Cell Mol Biol. 2019. 60(2): 209-220.

[8] H. Valadi, K. Ekstrom, A. Bossios, M. Sjostrand, J.J. Lee, J.O. Lotvall. Exosome-mediated transfer of mRNAs and microRNAs is a novel mechanism of genetic exchange between cells. Nat Cell Biol. 2007. 9(6): 654-9.

[9] S.M. Kronstadt, A.E. Pottash, D. Levy, S. Wang, W. Chao, S.M. Jay. Therapeutic Potential of Extracellular Vesicles for Sepsis Treatment. Adv Ther (Weinh). 2021. 4(7).

[10] H. Liu, Y. Chen, G. Yin, Q. Xie. Therapeutic prospects of MicroRNAs carried by mesenchymal stem cells-derived extracellular vesicles in autoimmune diseases. Life Sci. 2021. 277 119458.

[11] L.J. Born, K.H. Chang, P. Shoureshi, F. Lay, S. Bengali, A.T.W. Hsu, S.N. Abadchi, J.W. Harmon, S.M. Jay. HOTAIR-Loaded Mesenchymal Stem/Stromal Cell Extracellular Vesicles Enhance

Angiogenesis and Wound Healing. Adv Healthc Mater. 2021. e2002070.

[12] S. Fu, Y. Zhang, Y. Li, L. Luo, Y. Zhao, Y. Yao. Extracellular vesicles in cardiovascular diseases. Cell Death Discov. 2020. 6 68.

[13] B. Sohrabi, B. Dayeri, E. Zahedi, S. Khoshbakht, N. Nezamabadi Pour, H. Ranjbar, A. Davari Nejad, M. Noureddini, B. Alani. Mesenchymal stem cell (MSC)-derived exosomes as novel vehicles for delivery of miRNAs in cancer therapy. Cancer Gene Ther. 2022.

[14] S. Thippabhotla, C. Zhong, M. He. 3D cell culture stimulates the secretion of in vivo like extracellular vesicles. Sci Rep. 2019. 9(1): 13012.

[15] D.B. Patel, C.R. Luthers, M.J. Lerman, J.P. Fisher, S.M. Jay. Enhanced extracellular vesicle production and ethanol-mediated vascularization bioactivity via a 3D-printed scaffold-perfusion bioreactor system. Acta Biomater. 2019. 95 236-244.

[16] S. Ding, P. Kingshott, H. Thissen, M. Pera, P.Y. Wang. Modulation of human mesenchymal and pluripotent stem cell behavior using mechanical and biochemical cues: A review. Biotechnol Bioeng. 2017. 114(2): 260-280.

[17] A. Casado-Diaz, J.M. Quesada-Gomez, G. Dorado. Extracellular Vesicles Derived From Mesenchymal Stem Cells (MSC) in

Regenerative Medicine: Applications in Skin Wound Healing. Front Bioeng Biotechnol. 2020. 8 146.

[18] X. He, Z. Dong, Y. Cao, H. Wang, S. Liu, L. Liao, Y. Jin, L. Yuan, B. Li. MSC-Derived Exosome Promotes M2 Polarization and Enhances Cutaneous Wound Healing. Stem Cells Int. 2019. 2019 7132708.

[19] J. Folkman, A. Moscona. Role of cell shape in growth control. Nature. 1978. 273(5661): 345-9.

[20] J.F. Rupprecht, K.H. Ong, J. Yin, A. Huang, H.H. Dinh, A.P. Singh, S. Zhang, W. Yu, T.E. Saunders. Geometric constraints alter cell arrangements within curved epithelial tissues. Mol Biol Cell. 2017. 28(25): 3582-3594.

[21] J. Liang, S. Gu, X. Mao, Y. Tan, H. Wang, S. Li, Y. Zhou. Endothelial Cell Morphology Regulates Inflammatory Cells Through MicroRNA Transferred by Extracellular Vesicles. Front Bioeng Biotechnol. 2020. 8 369.

[22] M. Liu, D. Wang, S. Gu, B. Tian, J. Liang, Q. Suo, Z. Zhang, G. Yang, Y. Zhou, S. Li. Micro/nano materials regulate cell morphology and intercellular communication by extracellular vesicles. Acta Biomater. 2021. 124 130-138.

[23] M.C. Lampi, C.A. Reinhart-King. Targeting extracellular matrix stiffness to attenuate disease: From molecular mechanisms to clinical trials. Sci Transl Med. 2018. 10(422).

[24] M.S. Samuel, J.I. Lopez, E.J. McGhee, D.R. Croft, D. Strachan, P. Timpson, J. Munro, E. Schroder, J. Zhou, V.G. Brunton, N. Barker, H. Clevers, O.J. Sansom, K.I. Anderson, V.M. Weaver, M.F. Olson. Actomyosin-mediated cellular tension drives increased tissue stiffness and beta-catenin activation to induce epidermal hyperplasia and tumor growth. Cancer Cell. 2011. 19(6): 776-91.

[25] D.J. McGrail, Q.M. Kieu, J.A. Iandoli, M.R. Dawson. Actomyosin tension as a determinant of metastatic cancer mechanical tropism. Phys Biol. 2015. 12(2): 026001.

[26] R.L. Urbano, S. Swaminathan, A.M. Clyne. Stiff Substrates Enhance Endothelial Oxidative Stress in Response to Protein Kinase C Activation. Appl Bionics Biomech. 2019. 2019 6578492.

[27] E. Buzhor, L. Leshansky, J. Blumenthal, H. Barash, D. Warshawsky, Y. Mazor, R. Shtrichman. Cell-based therapy approaches: the hope for incurable diseases. Regen Med. 2014. 9(5): 649-72.

[28] J.R. Ferreira, G.Q. Teixeira, S.G. Santos, M.A. Barbosa, G. Almeida-Porada, R.M. Goncalves. Mesenchymal Stromal Cell Secretome:

Influencing Therapeutic Potential by Cellular Pre-conditioning. Front Immunol. 2018. 9 2837.

[29] M. Wysoczynski, A. Khan, R. Bolli. New Paradigms in Cell Therapy: Repeated Dosing, Intravenous Delivery, Immunomodulatory Actions, and New Cell Types. Circ Res. 2018. 123(2): 138-158.

[30] L. Belov, K.J. Matic, S. Hallal, O.G. Best, S.P. Mulligan, R.I. Christopherson. Extensive surface protein profiles of extracellular vesicles from cancer cells may provide diagnostic signatures from blood samples. J Extracell Vesicles. 2016. 5 25355.

[31] K.P. Hough, L.S. Wilson, J.L. Trevor, J.G. Strenkowski, N. Maina, Y.I. Kim, M.L. Spell, Y. Wang, D. Chanda, J.R. Dager, N.S. Sharma, M. Curtiss, V.B. Antony, M.T. Dransfield, D.D. Chaplin, C. Steele, S. Barnes, S.R. Duncan, J.K. Prasain, V.J. Thannickal, J.S. Deshane. Unique Lipid Signatures of Extracellular Vesicles from the Airways of Asthmatics. Sci Rep. 2018. 8(1): 10340.

[32] L. Margolis, Y. Sadovsky. The biology of extracellular vesicles: The known unknowns. PLoS Biol. 2019. 17(7): e3000363.

[33] C. Thery, K.W. Witwer, E. Aikawa, M.J. Alcaraz, J.D. Anderson, R. Andriantsitohaina, A. Antoniou, T. Arab, F. Archer, G.K. Atkin-Smith, D.C. Ayre, J.M. Bach, D. Bachurski, H. Baharvand, L. Balaj, S. Baldacchino, N.N. Bauer, A.A. Baxter, M. Bebawy, C. Beckham, A.

Bedina Zavec, A. Benmoussa, A.C. Berardi, P. Bergese, E. Bielska, C. Blenkiron, S. Bobis-Wozowicz, E. Boilard, W. Boireau, A. Bongiovanni, F.E. Borras, S. Bosch, C.M. Boulanger, X. Breakefield, A.M. Breglio, M.A. Brennan, D.R. Brigstock, A. Brisson, M.L. Broekman, J.F. Bromberg, P. Bryl-Gorecka, S. Buch, A.H. Buck, D. Burger, S. Busatto, D. Buschmann, B. Bussolati, E.I. Buzas, J.B. Byrd, G. Camussi, D.R. Carter, S. Caruso, L.W. Chamley, Y.T. Chang, C. Chen, S. Chen, L. Cheng, A.R. Chin, A. Clayton, S.P. Clerici, A. Cocks, E. Cocucci, R.J. Coffey, A. Cordeiro-da-Silva, Y. Couch, F.A. Coumans, B. Coyle, R. Crescitelli, M.F. Criado, C. D'Souza-Schorey, S. Das, A. Datta Chaudhuri, P. de Candia, E.F. De Santana, O. De Wever, H.A. Del Portillo, T. Demaret, S. Deville, A. Devitt, B. Dhondt, D. Di Vizio, L.C. Dieterich, V. Dolo, A.P. Dominguez Rubio, M. Dominici, M.R. Dourado, T.A. Driedonks, F.V. Duarte, H.M. Duncan, R.M. Eichenberger, K. Ekstrom, S. El Andaloussi, C. Elie-Caille, U. Erdbrugger, J.M. Falcon-Perez, F. Fatima, J.E. Fish, M. Flores-Bellver, A. Forsonits, A. Frelet-Barrand, F. Fricke, G. Fuhrmann, S. Gabrielsson, A. Gamez-Valero, C. Gardiner, K. Gartner, R. Gaudin, Y.S. Gho, B. Giebel, C. Gilbert, M. Gimona, I. Giusti, D.C. Goberdhan, A. Gorgens, S.M. Gorski, D.W. Greening, J.C. Gross, A. Gualerzi, G.N. Gupta, D. Gustafson, A. Handberg, R.A. Haraszti, P. Harrison, H. Hegyesi, A. Hendrix, A.F. Hill, F.H. Hochberg, K.F. Hoffmann, B. Holder, H. Holthofer, B. Hosseinkhani, G. Hu, Y.

Huang, V. Huber, S. Hunt, A.G. Ibrahim, T. Ikezu, J.M. Inal, M. Isin, A. Ivanova, H.K. Jackson, S. Jacobsen, S.M. Jay, M. Jayachandran, G. Jenster, L. Jiang, S.M. Johnson, J.C. Jones, A. Jong, T. Jovanovic-Talisman, S. Jung, R. Kalluri, S.I. Kano, S. Kaur, Y. Kawamura, E.T. Keller, D. Khamari, E. Khomyakova, A. Khvorova, P. Kierulf, K.P. Kim, T. Kislinger, M. Klingeborn, D.J. Klinke, 2nd, M. Kornek, M.M. Kosanovic, A.F. Kovacs, E.M. Kramer-Albers, S. Krasemann, M. Krause, I.V. Kurochkin, G.D. Kusuma, S. Kuypers, S. Laitinen, S.M. Langevin, L.R. Languino, J. Lannigan, C. Lasser, L.C. Laurent, G. Lavieu, E. Lazaro-Ibanez, S. Le Lay, M.S. Lee, Y.X.F. Lee, D.S. Lemos, M. Lenassi, A. Leszczynska, I.T. Li, K. Liao, S.F. Libregts, E. Ligeti, R. Lim, S.K. Lim, A. Line, K. Linnemannstons, A. Llorente, C.A. Lombard, M.J. Lorenowicz, A.M. Lorincz, J. Lotvall, J. Lovett, M.C. Lowry, X. Loyer, Q. Lu, B. Lukomska, T.R. Lunavat, S.L. Maas, H. Malhi, A. Marcilla, J. Mariani, J. Mariscal, E.S. Martens-Uzunova, L. Martin-Jaular, M.C. Martinez, V.R. Martins, M. Mathieu, S. Mathivanan, M. Maugeri, L.K. McGinnis, M.J. McVey, D.G. Meckes, Jr., K.L. Meehan, I. Mertens, V.R. Minciacchi, A. Moller, M. Moller Jorgensen, A. Morales-Kastresana, J. Morhayim, F. Mullier, M. Muraca, L. Musante, V. Mussack, D.C. Muth, K.H. Myburgh, T. Najrana, M. Nawaz, I. Nazarenko, P. Nejsum, C. Neri, T. Neri, R. Nieuwland, L. Nimrichter, J.P. Nolan, E.N. Nolte-'t Hoen, N. Noren Hooten, L. O'Driscoll, T. O'Grady, A. O'Loghlen, T. Ochiya, M.

Olivier, A. Ortiz, L.A. Ortiz, X. Osteikoetxea, O. Ostergaard, M. Ostrowski, J. Park, D.M. Pegtel, H. Peinado, F. Perut, M.W. Pfaffl, D.G. Phinney, B.C. Pieters, R.C. Pink, D.S. Pisetsky, E. Pogge von Strandmann, I. Polakovicova, I.K. Poon, B.H. Powell, I. Prada, L. Pulliam, P. Quesenberry, A. Radeghieri, R.L. Raffai, S. Raimondo, J. Rak, M.I. Ramirez, G. Raposo, M.S. Rayyan, N. Regev-Rudzki, F.L. Ricklefs, P.D. Robbins, D.D. Roberts, S.C. Rodrigues, E. Rohde, S. Rome, K.M. Rouschop, A. Rughetti, A.E. Russell, P. Saa, S. Sahoo, E. Salas-Huenuleo, C. Sanchez, J.A. Saugstad, M.J. Saul, R.M. Schiffelers, R. Schneider, T.H. Schoyen, A. Scott, E. Shahaj, S. Sharma, O. Shatnyeva, F. Shekari, G.V. Shelke, A.K. Shetty, K. Shiba, P.R. Siljander, A.M. Silva, A. Skowronek, O.L. Snyder, 2nd, R.P. Soares, B.W. Sodar, C. Soekmadji, J. Sotillo, P.D. Stahl, W. Stoorvogel, S.L. Stott, E.F. Strasser, S. Swift, H. Tahara, M. Tewari, K. Timms, S. Tiwari, R. Tixeira, M. Tkach, W.S. Toh, R. Tomasini, A.C. Torrecilhas, J.P. Tosar, V. Toxavidis, L. Urbanelli, P. Vader, B.W. van Balkom, S.G. van der Grein, J. Van Deun, M.J. van Herwijnen, K. Van Keuren-Jensen, G. van Niel, M.E. van Royen, A.J. van Wijnen, M.H. Vasconcelos, I.J. Vechetti, Jr., T.D. Veit, L.J. Vella, E. Velot, F.J. Verweij, B. Vestad, J.L. Vinas, T. Visnovitz, K.V. Vukman, J. Wahlgren, D.C. Watson, M.H. Wauben, A. Weaver, J.P. Webber, V. Weber, A.M. Wehman, D.J. Weiss, J.A. Welsh, S. Wendt, A.M. Wheelock, Z. Wiener, L. Witte, J. Wolfram, A. Xagorari, P.

Xander, J. Xu, X. Yan, M. Yanez-Mo, H. Yin, Y. Yuana, V. Zappulli, J. Zarubova, V. Zekas, J.Y. Zhang, Z. Zhao, L. Zheng, A.R. Zheutlin, A.M. Zickler, P. Zimmermann, A.M. Zivkovic, D. Zocco, E.K. Zuba-Surma. Minimal information for studies of extracellular vesicles 2018 (MISEV2018): a position statement of the International Society for Extracellular Vesicles and update of the MISEV2014 guidelines. J Extracell Vesicles. 2018. 7(1): 1535750.

[34] S. El Andaloussi, I. Mäger, X.O. Breakefield, M.J.A. Wood. Extracellular vesicles: biology and emerging therapeutic opportunities. Nature Reviews Drug Discovery. 2013. 12 347.

[35] I. Huang-Doran, C.Y. Zhang, A. Vidal-Puig. Extracellular Vesicles: Novel Mediators of Cell Communication In Metabolic Disease. Trends Endocrinol Metab. 2017. 28(1): 3-18.

[36] G. van Niel, G. D'Angelo, G. Raposo. Shedding light on the cell biology of extracellular vesicles. Nat Rev Mol Cell Biol. 2018. 19(4): 213-228.

[37] M. Colombo, C. Moita, G. van Niel, J. Kowal, J. Vigneron, P. Benaroch, N. Manel, L.F. Moita, C. Thery, G. Raposo. Analysis of ESCRT functions in exosome biogenesis, composition and secretion highlights the heterogeneity of extracellular vesicles. J Cell Sci. 2013. 126(Pt 24): 5553-65.

[38] H. Kalra, G.P. Drummen, S. Mathivanan. Focus on Extracellular Vesicles: Introducing the Next Small Big Thing. Int J Mol Sci. 2016. 17(2): 170.

[39] H. Shao, H. Im, C.M. Castro, X. Breakefield, R. Weissleder, H. Lee. New Technologies for Analysis of Extracellular Vesicles. Chem Rev. 2018. 118(4): 1917-1950.

[40] T. Juan, M. Furthauer. Biogenesis and function of ESCRT-dependent extracellular vesicles. Semin Cell Dev Biol. 2018. 74 66-77.

[41] Z. Andreu, M. Yanez-Mo. Tetraspanins in extracellular vesicle formation and function. Front Immunol. 2014. 5 442.

[42] V.R. Minciacchi, M.R. Freeman, D. Di Vizio. Extracellular vesicles in cancer: exosomes, microvesicles and the emerging role of large oncosomes. Semin Cell Dev Biol. 2015. 40 41-51.

[43] C.P.R. Xavier, H.R. Caires, M.A.G. Barbosa, R. Bergantim, J.E. Guimaraes, M.H. Vasconcelos. The Role of Extracellular Vesicles in the Hallmarks of Cancer and Drug Resistance. Cells. 2020. 9(5).

[44] P. Samuel, M. Fabbri, D.R.F. Carter. Mechanisms of Drug Resistance in Cancer: The Role of Extracellular Vesicles. Proteomics. 2017. 17(23-24).

[45] L. Han, E.W. Lam, Y. Sun. Extracellular vesicles in the tumor microenvironment: old stories, but new tales. Mol Cancer. 2019. 18(1): 59.

[46] M. Yanez-Mo, P.R. Siljander, Z. Andreu, A.B. Zavec, F.E. Borras, E.I. Buzas, K. Buzas, E. Casal, F. Cappello, J. Carvalho, E. Colas, A. Cordeiro-da Silva, S. Fais, J.M. Falcon-Perez, I.M. Ghobrial, B. Giebel, M. Gimona, M. Graner, I. Gursel, M. Gursel, N.H. Heegaard, A. Hendrix, P. Kierulf, K. Kokubun, M. Kosanovic, V. Kralj-Iglic, E.M. Kramer-Albers, S. Laitinen, C. Lasser, T. Lener, E. Ligeti, A. Line, G. Lipps, A. Llorente, J. Lotvall, M. Mancek-Keber, A. Marcilla, M. Mittelbrunn, I. Nazarenko, E.N. Nolte-'t Hoen, T.A. Nyman, L. O'Driscoll, M. Olivan, C. Oliveira, E. Pallinger, H.A. Del Portillo, J. Reventos, M. Rigau, E. Rohde, M. Sammar, F. Sanchez-Madrid, N. Santarem, K. Schallmoser, M.S. Ostenfeld, W. Stoorvogel, R. Stukelj, S.G. Van der Grein, M.H. Vasconcelos, M.H. Wauben, O. De Wever. Biological properties of extracellular vesicles and their physiological functions. J Extracell Vesicles. 2015. 4 27066.

[47] A. Turchinovich, O. Drapkina, A. Tonevitsky. Transcriptome of Extracellular Vesicles: State-of-the-Art. Front Immunol. 2019. 10 202.

[48] R. Shah, T. Patel, J.E. Freedman. Circulating Extracellular Vesicles in Human Disease. N Engl J Med. 2018. 379(10): 958-966.

[49] P.D. Robbins, A.E. Morelli. Regulation of immune responses by extracellular vesicles. Nat Rev Immunol. 2014. 14(3): 195-208.

[50] D.S. Chulpanova, K.V. Kitaeva, V. James, A.A. Rizvanov, V.V. Solovyeva. Therapeutic Prospects of Extracellular Vesicles in Cancer Treatment. Front Immunol. 2018. 9 1534.

[51] P. Raeven, J. Zipperle, S. Drechsler. Extracellular Vesicles as Markers and Mediators in Sepsis. Theranostics. 2018. 8(12): 3348-3365.

[52] S.Y. Chong, C.K. Lee, C. Huang, Y.H. Ou, C.J. Charles, A.M. Richards, Y.R. Neupane, M.V. Pavon, O. Zharkova, G. Pastorin, J.W. Wang. Extracellular Vesicles in Cardiovascular Diseases: Alternative Biomarker Sources, Therapeutic Agents, and Drug Delivery Carriers. Int J Mol Sci. 2019. 20(13).

[53] H. Xu, S. Jia, H. Xu. Potential therapeutic applications of exosomes in different autoimmune diseases. Clin Immunol. 2019. 205 116-124.

[54] R.C. Friedman, K.K. Farh, C.B. Burge, D.P. Bartel. Most mammalian mRNAs are conserved targets of microRNAs. Genome Res. 2009. 19(1): 92-105.

[55] Z. Liu, A. Sall, D. Yang. MicroRNA: An emerging therapeutic target and intervention tool. Int J Mol Sci. 2008. 9(6): 978-99.

[56] Y. Peng, C.M. Croce. The role of MicroRNAs in human cancer. Signal Transduct Target Ther. 2016. 1 15004.

[57] R. Kumarswamy, I. Volkmann, T. Thum. Regulation and function of miRNA-21 in health and disease. RNA Biol. 2011. 8(5): 706-13.

[58] E.N. Olson. MicroRNAs as therapeutic targets and biomarkers of cardiovascular disease. Sci Transl Med. 2014. 6(239): 239ps3.

[59] A. Wronska, I. Kurkowska-Jastrzebska, G. Santulli. Application of microRNAs in diagnosis and treatment of cardiovascular disease. Acta Physiol (Oxf). 2015. 213(1): 60-83.

[60] M. Mann, A. Mehta, J.L. Zhao, K. Lee, G.K. Marinov, Y. Garcia-Flores, L.F. Lu, A.Y. Rudensky, D. Baltimore. An NF-kappaB-microRNA regulatory network tunes macrophage inflammatory responses. Nat Commun. 2017. 8(1): 851.

[61] M. Hill, N. Tran. Global miRNA to miRNA Interactions: Impacts for miR-21. Trends Cell Biol. 2021. 31(1): 3-5.

[62] X. Ma, L.E. Becker Buscaglia, J.R. Barker, Y. Li. MicroRNAs in NF-kappaB signaling. J Mol Cell Biol. 2011. 3(3): 159-66.

[63] K. Essandoh, G.C. Fan. Role of extracellular and intracellular microRNAs in sepsis. Biochim Biophys Acta. 2014. 1842(11): 2155-2162.

[64] W. Zhou, A.S. Pal, A.Y. Hsu, T. Gurol, X. Zhu, S.E. Wirbisky-Hershberger, J.L. Freeman, A.L. Kasinski, Q. Deng. MicroRNA-223 Suppresses the Canonical NF-kappaB Pathway in Basal Keratinocytes to Dampen Neutrophilic Inflammation. Cell Rep. 2018. 22(7): 1810-1823.

[65] T.H. Lin, J. Pajarinen, L. Lu, A. Nabeshima, L.A. Cordova, Z. Yao, S.B. Goodman. NF-kappaB as a Therapeutic Target in Inflammatory-Associated Bone Diseases. Adv Protein Chem Struct Biol. 2017. 107 117-154.

[66] H. Yu, L. Lin, Z. Zhang, H. Zhang, H. Hu. Targeting NF-kappaB pathway for the therapy of diseases: mechanism and clinical study. Signal Transduct Target Ther. 2020. 5(1): 209.

[67] J. Chen, C. Hu, P. Pan. Extracellular Vesicle MicroRNA Transfer in Lung Diseases. Front Physiol. 2017. 8 1028.

[68] J. Ma, X. Tao, Y. Huang. Silencing microRNA-210 in Hypoxia-Induced HUVEC-Derived Extracellular Vesicles Inhibits Hemangioma. Cerebrovasc Dis. 2020. 1-12.

[69] J. Xu, Y. Feng, A. Jeyaram, S.M. Jay, L. Zou, W. Chao. Circulating Plasma Extracellular Vesicles from Septic Mice Induce Inflammation via MicroRNA- and TLR7-Dependent Mechanisms. J Immunol. 2018. 201(11): 3392-3400.

[70] K. O'Brien, K. Breyne, S. Ughetto, L.C. Laurent, X.O. Breakefield. RNA delivery by extracellular vesicles in mammalian cells and its applications. Nat Rev Mol Cell Biol. 2020. 21(10): 585-606.

[71] L.A. Mulcahy, R.C. Pink, D.R. Carter. Routes and mechanisms of extracellular vesicle uptake. J Extracell Vesicles. 2014. 3.

[72] D.E. Murphy, O.G. de Jong, M. Brouwer, M.J. Wood, G. Lavieu, R.M. Schiffelers, P. Vader. Extracellular vesicle-based therapeutics: natural versus engineered targeting and trafficking. Exp Mol Med. 2019. 51(3): 1-12.

[73] K. O'Brien, S. Ughetto, S. Mahjoum, A.V. Nair, X.O. Breakefield. Uptake, functionality, and re-release of extracellular vesicle-encapsulated cargo. Cell Rep. 2022. 39(2): 110651.

[74] F. Meziani, X. Delabranche, P. Asfar, F. Toti. Bench-to-bedside review: circulating microparticles--a new player in sepsis? Crit Care. 2010. 14(5): 236.

[75] G. Woth, M. Tokes-Fuzesi, T. Magyarlaki, G.L. Kovacs, I. Vermes, D. Muhl. Activated platelet-derived microparticle numbers are elevated in patients with severe fungal (Candida albicans) sepsis. Ann Clin Biochem. 2012. 49(Pt 6): 554-60.

[76] A. Dickhout, R.R. Koenen. Extracellular Vesicles as Biomarkers in Cardiovascular Disease; Chances and Risks. Front Cardiovasc Med. 2018. 5 113.

[77] E. Woith, G. Fuhrmann, M.F. Melzig. Extracellular Vesicles-Connecting Kingdoms. Int J Mol Sci. 2019. 20(22).

[78] A.G. Yates, R.C. Pink, U. Erdbrugger, P.R. Siljander, E.R. Dellar, P. Pantazi, N. Akbar, W.R. Cooke, M. Vatish, E. Dias-Neto, D.C. Anthony, Y. Couch. In sickness and in health: The functional role of extracellular vesicles in physiology and pathology in vivo: Part I: Health and Normal Physiology: Part I: Health and Normal Physiology. J Extracell Vesicles. 2022. 11(1): e12151.

[79] M.L. Mastronardi, H.A. Mostefai, F. Meziani, M.C. Martinez, P. Asfar, R. Andriantsitohaina. Circulating microparticles from septic shock patients exert differential tissue expression of enzymes related to inflammation and oxidative stress. Crit Care Med. 2011. 39(7): 1739-48.

[80] P.S. Prakash, C.C. Caldwell, A.B. Lentsch, T.A. Pritts, B.R. Robinson. Human microparticles generated during sepsis in patients with critical illness are neutrophil-derived and modulate the immune response. J Trauma Acute Care Surg. 2012. 73(2): 401-6; discussion 406-7.

[81] S. Balusu, E. Van Wonterghem, R. De Rycke, K. Raemdonck, S. Stremersch, K. Gevaert, M. Brkic, D. Demeestere, V. Vanhooren, A. Hendrix, C. Libert, R.E. Vandenbroucke. Identification of a novel mechanism of blood-brain communication during peripheral inflammation via choroid plexus-derived extracellular vesicles. EMBO Mol Med. 2016. 8(10): 1162-1183.

[82] B.L. Johnson, 3rd, E.F. Midura, P.S. Prakash, T.C. Rice, N. Kunz, K. Kalies, C.C. Caldwell. Neutrophil derived microparticles increase mortality and the counter-inflammatory response in a murine model of sepsis. Biochim Biophys Acta Mol Basis Dis. 2017. 1863(10 Pt B): 2554-2563.

[83] M. Kojima, J.A. Gimenes-Junior, T.W. Chan, B.P. Eliceiri, A. Baird, T.W. Costantini, R. Coimbra. Exosomes in postshock mesenteric lymph are key mediators of acute lung injury triggering the macrophage activation via Toll-like receptor 4. FASEB J. 2018. 32(1): 97-110.

[84] Z. Yuan, B. Bedi, R.T. Sadikot. Bronchoalveolar Lavage Exosomes in Lipopolysaccharide-induced Septic Lung Injury. J Vis Exp. 2018. (135).

[85] K. Jiang, J. Yang, S. Guo, G. Zhao, H. Wu, G. Deng. Peripheral Circulating Exosome-Mediated Delivery of miR-155 as a Novel

Mechanism for Acute Lung Inflammation. Mol Ther. 2019. 27(10): 1758-1771.

[86] J.R. Wisler, K. Singh, A.R. McCarty, A.S.E. Abouhashem, J.W. Christman, C.K. Sen. Proteomic Pathway Analysis of Monocyte-Derived Exosomes during Surgical Sepsis Identifies Immunoregulatory Functions. Surg Infect (Larchmt). 2020. 21(2): 101-111.

[87] R. Nieuwland, R.J. Berckmans, S. McGregor, A.N. Boing, F.P. Romijn, R.G. Westendorp, C.E. Hack, A. Sturk. Cellular origin and procoagulant properties of microparticles in meningococcal sepsis. Blood. 2000. 95(3): 930-5.

[88] J.J. Li, B. Wang, M.C. Kodali, C. Chen, E. Kim, B.J. Patters, L. Lan, S. Kumar, X. Wang, J. Yue, F.F. Liao. In vivo evidence for the contribution of peripheral circulating inflammatory exosomes to neuroinflammation. J Neuroinflammation. 2018. 15(1): 8.

[89] X. Delabranche, J. Boisrame-Helms, P. Asfar, A. Berger, Y. Mootien, T. Lavigne, L. Grunebaum, F. Lanza, C. Gachet, J.M. Freyssinet, F. Toti, F. Meziani. Microparticles are new biomarkers of septic shock-induced disseminated intravascular coagulopathy. Intensive Care Med. 2013. 39(10): 1695-703.

[90] H. Matsumoto, K. Yamakawa, H. Ogura, T. Koh, N. Matsumoto, T. Shimazu. Enhanced expression of cell-specific surface antigens on endothelial microparticles in sepsis-induced disseminated intravascular coagulation. Shock. 2015. 43(5): 443-9.

[91] M.J. Mooberry, R. Bradford, E.L. Hobl, F.C. Lin, B. Jilma, N.S. Key. Procoagulant microparticles promote coagulation in a factor XI-dependent manner in human endotoxemia. J Thromb Haemost. 2016. 14(5): 1031-42.

[92] Y. Wang, L. Luo, M. Morgelin, H. Thorlacius. Rac1 regulates sepsis-induced formation of platelet-derived microparticles and thrombin generation. Biochem Biophys Res Commun. 2017. 487(4): 887-891.

[93] C. Tripisciano, R. Weiss, T. Eichhorn, A. Spittler, T. Heuser, M.B. Fischer, V. Weber. Different Potential of Extracellular Vesicles to Support Thrombin Generation: Contributions of Phosphatidylserine, Tissue Factor, and Cellular Origin. Sci Rep. 2017. 7(1): 6522.

[94] C. Tripisciano, R. Weiss, S. Karuthedom George, M.B. Fischer, V. Weber. Extracellular Vesicles Derived From Platelets, Red Blood Cells, and Monocyte-Like Cells Differ Regarding Their Ability to Induce Factor XII-Dependent Thrombin Generation. Front Cell Dev Biol. 2020. 8 298.

[95] J.N. Deng, Y.Q. Li, Y. Liu, Q. Li, Y. Hu, J.Q. Xu, T.Y. Sun, L.X. Xie. Exosomes derived from plasma of septic patients inhibit apoptosis of T lymphocytes by down-regulating bad via hsa-miR-7-5p. Biochem Biophys Res Commun. 2019. 513(4): 958-966.

[96] T. Iba, H. Ogura. Role of extracellular vesicles in the development of sepsis-induced coagulopathy. J Intensive Care. 2018. 6 68.

[97] M. Janiszewski, A.O. Do Carmo, M.A. Pedro, E. Silva, E. Knobel, F.R. Laurindo. Platelet-derived exosomes of septic individuals possess proapoptotic NAD(P)H oxidase activity: A novel vascular redox pathway. Crit Care Med. 2004. 32(3): 818-25.

[98] M.H. Gambim, O. do Carmo Ade, L. Marti, S. Verissimo-Filho, L.R. Lopes, M. Janiszewski. Platelet-derived exosomes induce endothelial cell apoptosis through peroxynitrite generation: experimental evidence for a novel mechanism of septic vascular dysfunction. Crit Care. 2007. 11(5): R107.

[99] H.A. Mostefai, J.M. Bourget, F. Meziani, M.C. Martinez, D. Leonetti, A. Mercat, P. Asfar, L. Germain, R. Andriantsitohaina. Interleukin-10 controls the protective effects of circulating microparticles from patients with septic shock on tissue-engineered vascular media. Clin Sci (Lond). 2013. 125(2): 77-85.

[100] X. Mu, X. Wang, W. Huang, R.T. Wang, K. Essandoh, Y. Li, A.M. Pugh, J. Peng, S. Deng, Y. Wang, C.C. Caldwell, T. Peng, K.J. Yu, G.C. Fan. Circulating Exosomes Isolated from Septic Mice Induce Cardiovascular Hyperpermeability Through Promoting Podosome Cluster Formation. Shock. 2018. 49(4): 429-441.

[101] V. Chatterjee, X. Yang, Y. Ma, B. Cha, J.E. Meegan, M. Wu, S.Y. Yuan. Endothelial microvesicles carrying Src-rich cargo impair adherens junction integrity and cytoskeleton homeostasis. Cardiovasc Res. 2020. 116(8): 1525-1538.

[102] D.W. Greening, S.K. Gopal, R. Xu, R.J. Simpson, W. Chen. Exosomes and their roles in immune regulation and cancer. Semin Cell Dev Biol. 2015. 40 72-81.

[103] W. Jian, L. Gu, B. Williams, Y. Feng, W. Chao, L. Zou. Toll-like Receptor 7 Contributes to Inflammation, Organ Injury, and Mortality in Murine Sepsis. Anesthesiology. 2019. 131(1): 105-118.

[104] K. Gao, J. Jin, C. Huang, J. Li, H. Luo, L. Li, Y. Huang, Y. Jiang. Exosomes Derived From Septic Mouse Serum Modulate Immune Responses via Exosome-Associated Cytokines. Front Immunol. 2019. 10 1560.

[105] S.E. Headland, H.R. Jones, L.V. Norling, A. Kim, P.R. Souza, E. Corsiero, C.D. Gil, A. Nerviani, F. Dell'Accio, C. Pitzalis, S.M. Oliani,

L.Y. Jan, M. Perretti. Neutrophil-derived microvesicles enter cartilage and protect the joint in inflammatory arthritis. Sci Transl Med. 2015. 7(315): 315ra190.

[106] G. Leoni, P.A. Neumann, N. Kamaly, M. Quiros, H. Nishio, H.R. Jones, R. Sumagin, R.S. Hilgarth, A. Alam, G. Fredman, I. Argyris, E. Rijcken, D. Kusters, C. Reutelingsperger, M. Perretti, C.A. Parkos, O.C. Farokhzad, A.S. Neish, A. Nusrat. Annexin A1-containing extracellular vesicles and polymeric nanoparticles promote epithelial wound repair. J Clin Invest. 2015. 125(3): 1215-27.

[107] R. Szatanek, J. Baran, M. Siedlar, M. Baj-Krzyworzeka. Isolation of extracellular vesicles: Determining the correct approach (Review). Int J Mol Med. 2015. 36(1): 11-7.

[108] M.Y. Konoshenko, E.A. Lekchnov, A.V. Vlassov, P.P. Laktionov. Isolation of Extracellular Vesicles: General Methodologies and Latest Trends. Biomed Res Int. 2018. 2018 8545347.

[109] A.N. Boing, E. van der Pol, A.E. Grootemaat, F.A. Coumans, A. Sturk, R. Nieuwland. Single-step isolation of extracellular vesicles by size-exclusion chromatography. J Extracell Vesicles. 2014. 3.

[110] J.Z. Nordin, Y. Lee, P. Vader, I. Mager, H.J. Johansson, W. Heusermann, O.P. Wiklander, M. Hallbrink, Y. Seow, J.J. Bultema, J. Gilthorpe, T. Davies, P.J. Fairchild, S. Gabrielsson, N.C. Meisner-

Kober, J. Lehtio, C.I. Smith, M.J. Wood, S. El Andaloussi. Ultrafiltration with size-exclusion liquid chromatography for high yield isolation of extracellular vesicles preserving intact mechanical and functional properties. Nanomedicine. 2015. 11(4): 879-83.

[111] N. Heath, L. Grant, T.M. De Oliveira, R. Rowlinson, X. Osteikoetxea, N. Dekker, R. Overman. Rapid isolation and enrichment of extracellular vesicle preparations using anion exchange chromatography. Sci Rep. 2018. 8(1): 5730.

[112] J.M. Carnino, H. Lee, Y. Jin. Isolation and characterization of extracellular vesicles from Broncho-alveolar lavage fluid: a review and comparison of different methods. Respir Res. 2019. 20(1): 240.

[113] D.D. Taylor, S. Shah. Methods of isolating extracellular vesicles impact down-stream analyses of their cargoes. Methods. 2015. 87 3-10.

[114] D. Buschmann, B. Kirchner, S. Hermann, M. Marte, C. Wurmser, F. Brandes, S. Kotschote, M. Bonin, O.K. Steinlein, M.W. Pfaffl, G. Schelling, M. Reithmair. Evaluation of serum extracellular vesicle isolation methods for profiling miRNAs by next-generation sequencing. J Extracell Vesicles. 2018. 7(1): 1481321.

[115] A. Gamez-Valero, M. Monguio-Tortajada, L. Carreras-Planella, M. Franquesa, K. Beyer, F.E. Borras. Size-Exclusion Chromatography-

based isolation minimally alters Extracellular Vesicles' characteristics compared to precipitating agents. Sci Rep. 2016. 6 33641.

[116] R.A. Haraszti, R. Miller, M. Stoppato, Y.Y. Sere, A. Coles, M.C. Didiot, R. Wollacott, E. Sapp, M.L. Dubuke, X. Li, S.A. Shaffer, M. DiFiglia, Y. Wang, N. Aronin, A. Khvorova. Exosomes Produced from 3D Cultures of MSCs by Tangential Flow Filtration Show Higher Yield and Improved Activity. Mol Ther. 2018. 26(12): 2838-2847.

[117] E.A. Mol, M.J. Goumans, P.A. Doevendans, J.P.G. Sluijter, P. Vader. Higher functionality of extracellular vesicles isolated using size-exclusion chromatography compared to ultracentrifugation. Nanomedicine. 2017. 13(6): 2061-2065.

[118] T.E. Whittaker, A. Nagelkerke, V. Nele, U. Kauscher, M.M. Stevens. Experimental artefacts can lead to misattribution of bioactivity from soluble mesenchymal stem cell paracrine factors to extracellular vesicles. J Extracell Vesicles. 2020. 9(1): 1807674.

[119] D.L.M. Rupert, V. Claudio, C. Lasser, M. Bally. Methods for the physical characterization and quantification of extracellular vesicles in biological samples. Biochim Biophys Acta Gen Subj. 2017. 1861(1 Pt A): 3164-3179.

[120] J.A. Welsh, J.A. Holloway, J.S. Wilkinson, N.A. Englyst. Extracellular Vesicle Flow Cytometry Analysis and Standardization. Front Cell Dev Biol. 2017. 5 78.

[121] G. Midekessa, K. Godakumara, J. Ord, J. Viil, F. Lattekivi, K. Dissanayake, S. Kopanchuk, A. Rinken, A. Andronowska, S. Bhattacharjee, T. Rinken, A. Fazeli. Zeta Potential of Extracellular Vesicles: Toward Understanding the Attributes that Determine Colloidal Stability. ACS Omega. 2020. 5(27): 16701-16710.

[122] S. Sharma, M. LeClaire, J. Wohlschlegel, J. Gimzewski. Impact of isolation methods on the mechanical heterogeneity of single extracellular vesicles. Sci Rep. 2020. 10(1): 13327.

[123] O.P.B. Wiklander, M.A. Brennan, J. Lotvall, X.O. Breakefield, S. El Andaloussi. Advances in therapeutic applications of extracellular vesicles. Sci Transl Med. 2019. 11(492).

[124] M. Kabat, I. Bobkov, S. Kumar, M. Grumet. Trends in mesenchymal stem cell clinical trials 2004-2018: Is efficacy optimal in a narrow dose range? Stem Cells Transl Med. 2020. 9(1): 17-27.

[125] Y. Song, H. Dou, X. Li, X. Zhao, Y. Li, D. Liu, J. Ji, F. Liu, L. Ding, Y. Ni, Y. Hou. Exosomal miR-146a Contributes to the Enhanced Therapeutic Efficacy of Interleukin-1beta-Primed Mesenchymal Stem Cells Against Sepsis. Stem Cells. 2017. 35(5): 1208-1221.

[126] Y. Wang, L. Zhang, Y. Li, L. Chen, X. Wang, W. Guo, X. Zhang, G. Qin, S.H. He, A. Zimmerman, Y. Liu, I.M. Kim, N.L. Weintraub, Y. Tang. Exosomes/microvesicles from induced pluripotent stem cells deliver cardioprotective miRNAs and prevent cardiomyocyte apoptosis in the ischemic myocardium. Int J Cardiol. 2015. 192 61-9.

[127] P. Gangadaran, R.L. Rajendran, H.W. Lee, S. Kalimuthu, C.M. Hong, S.Y. Jeong, S.W. Lee, J. Lee, B.C. Ahn. Extracellular vesicles from mesenchymal stem cells activates VEGF receptors and accelerates recovery of hindlimb ischemia. J Control Release. 2017. 264 112-126.

[128] M. Reis, E. Mavin, L. Nicholson, K. Green, A.M. Dickinson, X.N. Wang. Mesenchymal Stromal Cell-Derived Extracellular Vesicles Attenuate Dendritic Cell Maturation and Function. Front Immunol. 2018. 9 2538.

[129] P. Lai, J. Weng, L. Guo, X. Chen, X. Du. Novel insights into MSC-EVs therapy for immune diseases. Biomark Res. 2019. 7 6.

[130] G. Zheng, R. Huang, G. Qiu, M. Ge, J. Wang, Q. Shu, J. Xu. Mesenchymal stromal cell-derived extracellular vesicles: regenerative and immunomodulatory effects and potential applications in sepsis. Cell Tissue Res. 2018. 374(1): 1-15.

[131] A. Gowen, F. Shahjin, S. Chand, K.E. Odegaard, S.V. Yelamanchili. Mesenchymal Stem Cell-Derived Extracellular Vesicles: Challenges in Clinical Applications. Front Cell Dev Biol. 2020. 8 149.

[132] T.N. Lamichhane, S. Sokic, J.S. Schardt, R.S. Raiker, J.W. Lin, S.M. Jay. Emerging roles for extracellular vesicles in tissue engineering and regenerative medicine. Tissue Eng Part B Rev. 2015. 21(1): 45-54.

[133] T.N. Lamichhane, R.S. Raiker, S.M. Jay. Exogenous DNA Loading into Extracellular Vesicles via Electroporation is Size-Dependent and Enables Limited Gene Delivery. Mol Pharm. 2015. 12(10): 3650-7.

[134] J. Hall, S. Prabhakar, L. Balaj, C.P. Lai, R.A. Cerione, X.O. Breakefield. Delivery of Therapeutic Proteins via Extracellular Vesicles: Review and Potential Treatments for Parkinson's Disease, Glioma, and Schwannoma. Cell Mol Neurobiol. 2016. 36(3): 417-27.

[135] P. Vader, E.A. Mol, G. Pasterkamp, R.M. Schiffelers. Extracellular vesicles for drug delivery. Adv Drug Deliv Rev. 2016. 106(Pt A): 148-156.

[136] D. Ha, N. Yang, V. Nadithe. Exosomes as therapeutic drug carriers and delivery vehicles across biological membranes: current perspectives and future challenges. Acta Pharm Sin B. 2016. 6(4): 287-96.

[137] J.R. Chevillet, Q. Kang, I.K. Ruf, H.A. Briggs, L.N. Vojtech, S.M. Hughes, H.H. Cheng, J.D. Arroyo, E.K. Meredith, E.N. Gallichotte, E.L. Pogosova-Agadjanyan, C. Morrissey, D.L. Stirewalt, F. Hladik, E.Y. Yu, C.S. Higano, M. Tewari. Quantitative and stoichiometric analysis of the microRNA content of exosomes. Proc Natl Acad Sci U S A. 2014. 111(41): 14888-93.

[138] P. Gangadaran, B.C. Ahn. Extracellular Vesicle- and Extracellular Vesicle Mimetics-Based Drug Delivery Systems: New Perspectives, Challenges, and Clinical Developments. Pharmaceutics. 2020. 12(5).

[139] J.V. Ferreira, A.R. Soares, J. Ramalho, C.M. Carvalho, M.H. Cardoso, P. Pintado, A.S. Carvalho, H.C. Beck, R. Mattheisen, M. Zuzarte, H. Girao, G. Van Niel, P. Pereira. LAMP2A Regulates the Loading of Proteins into Exosomes. Science Advances. 2022. 8(12).

[140] D. Zhang, H. Lee, Z. Zhu, J.K. Minhas, Y. Jin. Enrichment of selective miRNAs in exosomes and delivery of exosomal miRNAs in vitro and in vivo. Am J Physiol Lung Cell Mol Physiol. 2017. 312(1): L110-L121.

[141] M.C. Didiot, L.M. Hall, A.H. Coles, R.A. Haraszti, B.M. Godinho, K. Chase, E. Sapp, S. Ly, J.F. Alterman, M.R. Hassler, D. Echeverria, L. Raj, D.V. Morrissey, M. DiFiglia, N. Aronin, A. Khvorova. Exosome-mediated Delivery of Hydrophobically Modified siRNA for Huntingtin mRNA Silencing. Mol Ther. 2016. 24(10): 1836-1847.

[142] S.A.A. Kooijmans, S. Stremersch, K. Braeckmans, S.C. de Smedt, A. Hendrix, M.J.A. Wood, R.M. Schiffelers, K. Raemdonck, P. Vader. Electroporation-induced siRNA precipitation obscures the efficiency of siRNA loading into extracellular vesicles. J Control Release. 2013. 172(1): 229-238.

[143] P.R. Cullis, M.B. Bally, T.D. Madden, L.D. Mayer, M.J. Hope. pH gradients and membrane transport in liposomal systems. Trends Biotechnol. 1991. 9(8): 268-72.

[144] A. Jeyaram, T.N. Lamichhane, S. Wang, L. Zou, E. Dahal, S.M. Kronstadt, D. Levy, B. Parajuli, D.R. Knudsen, W. Chao, S.M. Jay. Enhanced Loading of Functional miRNA Cargo via pH Gradient Modification of Extracellular Vesicles. Mol Ther. 2020. 28(3): 975-985.

[145] M. Alexander, R. Hu, M.C. Runtsch, D.A. Kagele, T.L. Mosbruger, T. Tolmachova, M.C. Seabra, J.L. Round, D.M. Ward, R.M. O'Connell. Exosome-delivered microRNAs modulate the inflammatory response to endotoxin. Nat Commun. 2015. 6 7321.

[146] S.H. Park, H.-J. Choi, S.Y. Lee, J.-S. Han. TLR4-mediated IRAK1 activation induces TNF-α expression via JNK-dependent NF-κB activation in human bronchial epithelial cells. European Journal of Inflammation. 2015. 13(3): 183-195.

[147] D.C. Watson, D. Bayik, A. Srivatsan, C. Bergamaschi, A. Valentin, G. Niu, J. Bear, M. Monninger, M. Sun, A. Morales-Kastresana, J.C. Jones, B.K. Felber, X. Chen, I. Gursel, G.N. Pavlakis. Efficient production and enhanced tumor delivery of engineered extracellular vesicles. Biomaterials. 2016. 105 195-205.

[148] D. Ti, H. Hao, C. Tong, J. Liu, L. Dong, J. Zheng, Y. Zhao, H. Liu, X. Fu, W. Han. LPS-preconditioned mesenchymal stromal cells modify macrophage polarization for resolution of chronic inflammation via exosome-shuttled let-7b. J Transl Med. 2015. 13 308.

[149] J. Li, Y. Lee, H.J. Johansson, I. Mager, P. Vader, J.Z. Nordin, O.P. Wiklander, J. Lehtio, M.J. Wood, S.E. Andaloussi. Serum-free culture alters the quantity and protein composition of neuroblastoma-derived extracellular vesicles. J Extracell Vesicles. 2015. 4 26883.

[150] C. Lo Sicco, D. Reverberi, C. Balbi, V. Ulivi, E. Principi, L. Pascucci, P. Becherini, M.C. Bosco, L. Varesio, C. Franzin, M. Pozzobon, R. Cancedda, R. Tasso. Mesenchymal Stem Cell-Derived Extracellular Vesicles as Mediators of Anti-Inflammatory Effects: Endorsement of Macrophage Polarization. Stem Cells Transl Med. 2017. 6(3): 1018-1028.

[151] Z. Lu, Y. Chen, C. Dunstan, S. Roohani-Esfahani, H. Zreiqat. Priming Adipose Stem Cells with Tumor Necrosis Factor-Alpha

Preconditioning Potentiates Their Exosome Efficacy for Bone Regeneration. Tissue Eng Part A. 2017. 23(21-22): 1212-1220.

[152] H. Namazi, E. Mohit, I. Namazi, S. Rajabi, A. Samadian, E. Hajizadeh-Saffar, N. Aghdami, H. Baharvand. Exosomes secreted by hypoxic cardiosphere-derived cells enhance tube formation and increase pro-angiogenic miRNA. J Cell Biochem. 2018. 119(5): 4150-4160.

[153] M.T. Harting, A.K. Srivastava, S. Zhaorigetu, H. Bair, K.S. Prabhakara, N.E. Toledano Furman, J.V. Vykoukal, K.A. Ruppert, C.S. Cox, Jr., S.D. Olson. Inflammation-Stimulated Mesenchymal Stromal Cell-Derived Extracellular Vesicles Attenuate Inflammation. Stem Cells. 2018. 36(1): 79-90.

[154] M. Palviainen, H. Saari, O. Karkkainen, J. Pekkinen, S. Auriola, M. Yliperttula, M. Puhka, K. Hanhineva, P.R. Siljander. Metabolic signature of extracellular vesicles depends on the cell culture conditions. J Extracell Vesicles. 2019. 8(1): 1596669.

[155] M.R. Showalter, B. Wancewicz, O. Fiehn, J.A. Archard, S. Clayton, J. Wagner, P. Deng, J. Halmai, K.D. Fink, G. Bauer, B. Fury, N.H. Perotti, M. Apperson, J. Butters, P. Belafsky, G. Farwell, M. Kuhn, J.A. Nolta, J.D. Anderson. Primed mesenchymal stem cells package exosomes with metabolites associated with immunomodulation. Biochem Biophys Res Commun. 2019. 512(4): 729-735.

[156] B. Mead, X. Chamling, D.J. Zack, Z. Ahmed, S. Tomarev. TNFalpha-Mediated Priming of Mesenchymal Stem Cells Enhances Their Neuroprotective Effect on Retinal Ganglion Cells. Invest Ophthalmol Vis Sci. 2020. 61(2): 6.

[157] J.M. Cha, E.K. Shin, J.H. Sung, G.J. Moon, E.H. Kim, Y.H. Cho, H.D. Park, H. Bae, J. Kim, O.Y. Bang. Efficient scalable production of therapeutic microvesicles derived from human mesenchymal stem cells. Sci Rep. 2018. 8(1): 1171.

[158] L. Yan, X. Wu. Exosomes produced from 3D cultures of umbilical cord mesenchymal stem cells in a hollow-fiber bioreactor show improved osteochondral regeneration activity. Cell Biol Toxicol. 2020. 36(2): 165-178.

[159] E. Ragni, C. Perucca Orfei, P. De Luca, C. Mondadori, M. Vigano, A. Colombini, L. de Girolamo. Inflammatory priming enhances mesenchymal stromal cell secretome potential as a clinical product for regenerative medicine approaches through secreted factors and EV-miRNAs: the example of joint disease. Stem Cell Res Ther. 2020. 11(1): 165.

[160] S. Kim, S.K. Lee, H. Kim, T.M. Kim. Exosomes Secreted from Induced Pluripotent Stem Cell-Derived Mesenchymal Stem Cells Accelerate Skin Cell Proliferation. Int J Mol Sci. 2018. 19(10).

[161] H. Park, H. Park, D. Mun, J. Kang, H. Kim, M. Kim, S. Cui, S.H. Lee, B. Joung. Extracellular Vesicles Derived from Hypoxic Human Mesenchymal Stem Cells Attenuate GSK3beta Expression via miRNA-26a in an Ischemia-Reperfusion Injury Model. Yonsei Med J. 2018. 59(6): 736-745.

[162] L. Yang, Y. Zhai, Y. Hao, Z. Zhu, G. Cheng. The Regulatory Functionality of Exosomes Derived from hUMSCs in 3D Culture for Alzheimer's Disease Therapy. Small. 2020. 16(3): e1906273.

[163] T.N. Lamichhane, C.A. Leung, L.Y. Douti, S.M. Jay. Ethanol Induces Enhanced Vascularization Bioactivity of Endothelial Cell-Derived Extracellular Vesicles via Regulation of MicroRNAs and Long Non-Coding RNAs. Sci Rep. 2017. 7(1): 13794.

[164] D.B. Patel, K.M. Gray, Y. Santharam, T.N. Lamichhane, K.M. Stroka, S.M. Jay. Impact of cell culture parameters on production and vascularization bioactivity of mesenchymal stem cell-derived extracellular vesicles. Bioeng Transl Med. 2017. 2(2): 170-179.

[165] Y. Yang, R. Knight, P. Stephens, Y. Zhang. Three-dimensional culture of oral progenitor cells: Effects on small extracellular vesicles production and proliferative function. J Oral Pathol Med. 2020. 49(4): 342-349.

[166] A. Jarmalaviciute, V. Tunaitis, U. Pivoraite, A. Venalis, A. Pivoriunas. Exosomes from dental pulp stem cells rescue human dopaminergic neurons from 6-hydroxy-dopamine-induced apoptosis. Cytotherapy. 2015. 17(7): 932-9.

[167] E.S. Kim, K. Kida, J. Mok, Y. Seong, S.Y. Jo, T. Kanaki, M. Horikawa, K.H. Kim, T.M. Kim, T.S. Park, J. Park. Cellhesion VP enhances the immunomodulating potential of human mesenchymal stem cell-derived extracellular vesicles. Biomaterials. 2021. 271 120742.

[168] K.F. Eichholz, I. Woods, M. Riffault, G.P. Johnson, M. Corrigan, M.C. Lowry, N. Shen, M.N. Labour, K. Wynne, L. O'Driscoll, D.A. Hoey. Human bone marrow stem/stromal cell osteogenesis is regulated via mechanically activated osteocyte-derived extracellular vesicles. Stem Cells Transl Med. 2020.

[169] H. Kang, Y.H. Bae, Y. Kwon, S. Kim, J. Park. Extracellular Vesicles Generated Using Bioreactors and their Therapeutic Effect on the Acute Kidney Injury Model. Adv Healthc Mater. 2022. 11(4): e2101606.

[170] S. Guo, L. Debbi, B. Zohar, R. Samuel, R.S. Arzi, A.I. Fried, T. Carmon, D. Shevach, I. Redenski, I. Schlachet, A. Sosnik, S. Levenberg. Stimulating Extracellular Vesicles Production from Engineered Tissues by Mechanical Forces. Nano Lett. 2021. 21(6): 2497-2504.

[171] J. Gobin, G. Muradia, J. Mehic, C. Westwood, L. Couvrette, A. Stalker, S. Bigelow, C.C. Luebbert, F.S. Bissonnette, M.J.W. Johnston, S. Sauve, R.Y. Tam, L. Wang, M. Rosu-Myles, J.R. Lavoie. Hollow-fiber bioreactor production of extracellular vesicles from human bone marrow mesenchymal stromal cells yields nanovesicles that mirrors the immuno-modulatory antigenic signature of the producer cell. Stem Cell Res Ther. 2021. 12(1): 127.

[172] T. Najrana, A. Mahadeo, R. Abu-Eid, E. Kreienberg, V. Schulte, A. Uzun, C. Schorl, L. Goldberg, P. Quesenberry, J. Sanchez-Esteban. Mechanical stretch regulates the expression of specific miRNA in extracellular vesicles released from lung epithelial cells. J Cell Physiol. 2020. 235(11): 8210-8223.

[173] B. Xia, J. Gao, S. Li, L. Huang, L. Zhu, T. Ma, L. Zhao, Y. Yang, K. Luo, X. Shi, L. Mei, H. Zhang, Y. Zheng, L. Lu, Z. Luo, J. Huang. Mechanical stimulation of Schwann cells promote peripheral nerve regeneration via extracellular vesicle-mediated transfer of microRNA 23b-3p. Theranostics. 2020. 10(20): 8974-8995.

[174] F. Zhuang, Q. Shi, W.B. Wang, H. Bao, J. Yan, S. Gao, Z. Liu, Z.L. Jiang, Y.X. Qi. Endothelial microvesicles induced by physiological cyclic stretch inhibit ICAM1-Dependent leukocyte adhesion. Exp Cell Res. 2020. 386(1): 111710.

[175] W. Yu, X. Su, M. Li, W. Wan, A. Li, H. Zhou, F. Xu. Three-dimensional mechanical microenvironment enhanced osteogenic activity of mesenchymal stem cells-derived exosomes. Chemical Engineering Journal. 2021. 417.

[176] L. Zhang, H. Liu, K. Xu, Z. Ling, Y. Huang, Q. Hu, K. Lu, C. Liu, Y. Wang, N. Liu, X. Zhang, B. Xu, J. Wu, S. Chen, G. Zhang, M. Chen. Hypoxia preconditioned renal tubular epithelial cell-derived extracellular vesicles alleviate renal ischaemia-reperfusion injury mediated by the HIF-1alpha/Rab22 pathway and potentially affected by microRNAs. Int J Biol Sci. 2019. 15(6): 1161-1176.

[177] M. Harmati, E. Gyukity-Sebestyen, G. Dobra, L. Janovak, I. Dekany, O. Saydam, E. Hunyadi-Gulyas, I. Nagy, A. Farkas, T. Pankotai, Z. Ujfaludi, P. Horvath, F. Piccinini, M. Kovacs, T. Biro, K. Buzas. Small extracellular vesicles convey the stress-induced adaptive responses of melanoma cells. Sci Rep. 2019. 9(1): 15329.

[178] J.S. Mayo, W.E. Kurata, K.M. O'Connor, L.M. Pierce. Oxidative Stress Alters Angiogenic and Antimicrobial Content of Extracellular Vesicles and Improves Flap Survival. Plast Reconstr Surg Glob Open. 2019. 7(12): e2588.

[179] T. Fukuta, A. Nishikawa, K. Kogure. Low level electricity increases the secretion of extracellular vesicles from cultured cells. Biochem Biophys Rep. 2020. 21 100713.

[180] S. Lenzini, K. Debnath, J.C. Joshi, S.W. Wong, K. Srivastava, X. Geng, I.S. Cho, A. Song, R. Bargi, J.C. Lee, G.C.H. Mo, D. Mehta, J.W. Shin. Cell-Matrix Interactions Regulate Functional Extracellular Vesicle Secretion from Mesenchymal Stromal Cells. ACS Nano. 2021.

[181] S. Andrews, T. Maughon, R. Marklein, S. Stice. Priming of MSCs with inflammation-relevant signals affects extracellular vesicle biogenesis, surface markers, and modulation of T cell subsets. Journal of Immunology and Regenerative Medicine. 2021. 13.

[182] H. Shen, S. Yoneda, Y. Abu-Amer, F. Guilak, R.H. Gelberman. Stem cell-derived extracellular vesicles attenuate the early inflammatory response after tendon injury and repair. J Orthop Res. 2020. 38(1): 117-127.

[183] M.J. Amir K. Varkouhi, Lindsay Ormesher, Stéphane Gagnon, Sakshi Goyal, Razieh Rabani, Claire Masterson, Chris Spring, Paul Z. Chen, Frank X. Gu, Claudia C. dos Santos, Gerard F. Curley, John G. Laffey. Extracellular Vesicles from Interferon-γ–primed Human Umbilical Cord Mesenchymal Stromal Cells Reduce Escherichia coli–induced Acute Lung Injury in Rats. Anesthesiology. 2019. 130 778-790.

[184] R. Xu, F. Zhang, R. Chai, W. Zhou, M. Hu, B. Liu, X. Chen, M. Liu, Q. Xu, N. Liu, S. Liu. Exosomes derived from pro-inflammatory bone marrow-derived mesenchymal stem cells reduce inflammation and

myocardial injury via mediating macrophage polarization. J Cell Mol Med. 2019. 23(11): 7617-7631.

[185] J.A. Kink, M.H. Forsberg, S. Reshetylo, S. Besharat, C.J. Childs, J.D. Pederson, A. Gendron-Fitzpatrick, M. Graham, P.D. Bates, E.G. Schmuck, A. Raval, P. Hematti, C.M. Capitini. Macrophages Educated with Exosomes from Primed Mesenchymal Stem Cells Treat Acute Radiation Syndrome by Promoting Hematopoietic Recovery. Biol Blood Marrow Transplant. 2019. 25(11): 2124-2133.

[186] M. Najar, M. Krayem, N. Meuleman, D. Bron, L. Lagneaux. Mesenchymal Stromal Cells and Toll-Like Receptor Priming: A Critical Review. Immune Netw. 2017. 17(2): 89-102.

[187] A. Gray, R.S. Schloss, M. Yarmush. Donor variability among anti-inflammatory pre-activated mesenchymal stromal cells. Technology (Singap World Sci). 2016. 4(3): 201-215.

[188] M. Francois, R. Romieu-Mourez, M. Li, J. Galipeau. Human MSC suppression correlates with cytokine induction of indoleamine 2,3-dioxygenase and bystander M2 macrophage differentiation. Mol Ther. 2012. 20(1): 187-95.

[189] R. Domenis, A. Cifu, S. Quaglia, C. Pistis, M. Moretti, A. Vicario, P.C. Parodi, M. Fabris, K.R. Niazi, P. Soon-Shiong, F. Curcio. Pro inflammatory stimuli enhance the immunosuppressive functions of

adipose mesenchymal stem cells-derived exosomes. Sci Rep. 2018. 8(1): 13325.

[190] N.C. Noronha, A. Mizukami, C. Caliari-Oliveira, J.G. Cominal, J.L.M. Rocha, D.T. Covas, K. Swiech, K.C.R. Malmegrim. Priming approaches to improve the efficacy of mesenchymal stromal cell-based therapies. Stem Cell Res Ther. 2019. 10(1): 131.

[191] R.S. Waterman, S.L. Tomchuck, S.L. Henkle, A.M. Betancourt. A new mesenchymal stem cell (MSC) paradigm: polarization into a pro-inflammatory MSC1 or an Immunosuppressive MSC2 phenotype. PLoS One. 2010. 5(4): e10088.

[192] A.J. Keung, S. Kumar, D.V. Schaffer. Presentation counts: microenvironmental regulation of stem cells by mechanical and material cues. Annu Rev Cell Dev Biol. 2010. 26 533-56.

[193] A. Maziarz, B. Kocan, M. Bester, S. Budzik, M. Cholewa, T. Ochiya, A. Banas. How electromagnetic fields can influence adult stem cells: positive and negative impacts. Stem Cell Res Ther. 2016. 7(1): 54.

[194] J.Z. Gasiorowski, C.J. Murphy, P.F. Nealey. Mechanical cues and cell behavior: the big impact of little things. Annu Rev Biomed Eng. 2013. 15 155-76.

[195] M. Santoro, S.E. Lamhamedi-Cherradi, B.A. Menegaz, J.A. Ludwig, A.G. Mikos. Flow perfusion effects on three-dimensional culture and

drug sensitivity of Ewing sarcoma. Proc Natl Acad Sci U S A. 2015. 112(33): 10304-9.

[196] T. Ohashi, M. Sato. Remodeling of vascular endothelial cells exposed to fluid shear stress: experimental and numerical approach. Fluid Dynamics Research. 2005. 37(1-2): 40-59.

[197] L. Liu, B. Yu, J. Chen, Z. Tang, C. Zong, D. Shen, Q. Zheng, X. Tong, C. Gao, J. Wang. Different effects of intermittent and continuous fluid shear stresses on osteogenic differentiation of human mesenchymal stem cells. Biomech Model Mechanobiol. 2012. 11(3-4): 391-401.

[198] M.R. Kreke, L.A. Sharp, Y.W. Lee, A.S. Goldstein. Effect of intermittent shear stress on mechanotransductive signaling and osteoblastic differentiation of bone marrow stromal cells. Tissue Eng Part A. 2008. 14(4): 529-37.

[199] D.J. Kota, K.S. Prabhakara, N. Toledano-Furman, D. Bhattarai, Q. Chen, B. DiCarlo, P. Smith, F. Triolo, P.L. Wenzel, C.S. Cox, Jr., S.D. Olson. Prostaglandin E2 Indicates Therapeutic Efficacy of Mesenchymal Stem Cells in Experimental Traumatic Brain Injury. Stem Cells. 2017. 35(5): 1416-1430.

[200] H.J. Lee, M.F. Diaz, A. Ewere, S.D. Olson, C.S. Cox, Jr., P.L. Wenzel. Focal adhesion kinase signaling regulates anti-inflammatory function

of bone marrow mesenchymal stromal cells induced by biomechanical force. Cell Signal. 2017. 38 1-9.

[201] J. Zhou, Y.S. Li, S. Chien. Shear stress-initiated signaling and its regulation of endothelial function. Arterioscler Thromb Vasc Biol. 2014. 34(10): 2191-8.

[202] E.S. Lee, L.S. Boldo, B.O. Fernandez, M. Feelisch, M.C. Harmsen. Suppression of TAK1 pathway by shear stress counteracts the inflammatory endothelial cell phenotype induced by oxidative stress and TGF-beta1. Sci Rep. 2017. 7 42487.

[203] J. Hwang, M.H. Ing, A. Salazar, B. Lassegue, K. Griendling, M. Navab, A. Sevanian, T.K. Hsiai. Pulsatile versus oscillatory shear stress regulates NADPH oxidase subunit expression: implication for native LDL oxidation. Circ Res. 2003. 93(12): 1225-32.

[204] C. Hermann, A.M. Zeiher, S. Dimmeler. Shear stress inhibits H2O2-induced apoptosis of human endothelial cells by modulation of the glutathione redox cycle and nitric oxide synthase. Arterioscler Thromb Vasc Biol. 1997. 17(12): 3588-92.

[205] J. Rossi, P. Jonak, L. Rouleau, L. Danielczak, J.C. Tardif, R.L. Leask. Differential response of endothelial cells to simvastatin when conditioned with steady, non-reversing pulsatile or oscillating shear stress. Ann Biomed Eng. 2011. 39(1): 402-13.

[206] E. Hergenreider, S. Heydt, K. Treguer, T. Boettger, A.J. Horrevoets, A.M. Zeiher, M.P. Scheffer, A.S. Frangakis, X. Yin, M. Mayr, T. Braun, C. Urbich, R.A. Boon, S. Dimmeler. Atheroprotective communication between endothelial cells and smooth muscle cells through miRNAs. Nat Cell Biol. 2012. 14(3): 249-56.

[207] A.C. Vion, B. Ramkhelawon, X. Loyer, G. Chironi, C. Devue, G. Loirand, A. Tedgui, S. Lehoux, C.M. Boulanger. Shear stress regulates endothelial microparticle release. Circ Res. 2013. 112(10): 1323-33.

[208] C. Devue, M. Robillard, P.M. Coly, C. Boulanger, X. Loyer. Endothelial shear stress affects extracellular vesicle release and biodistribution. Archives of Cardiovascular Diseases Supplements. 2020. 12(2-4).

[209] Y. Zheng, Y. Li, G. Liu, X. Qi, X. Cao. MicroRNA-24 inhibits the proliferation and migration of endothelial cells in patients with atherosclerosis by targeting importin-alpha3 and regulating inflammatory responses. Exp Ther Med. 2018. 15(1): 338-344.

[210] A.M. Malek, S.L. Alper, S. Izumo. Hemodynamic shear stress and its role in atherosclerosis. JAMA. 1999. 282(21): 2035-42.

[211] J. Shemesh, I. Jalilian, A. Shi, G. Heng Yeoh, M.L. Knothe Tate, M. Ebrahimi Warkiani. Flow-induced stress on adherent cells in microfluidic devices. Lab Chip. 2015. 15(21): 4114-27.

[212] T.L. Place, F.E. Domann, A.J. Case. Limitations of oxygen delivery to cells in culture: An underappreciated problem in basic and translational research. Free Radic Biol Med. 2017. 113 311-322.

[213] J. Lovecchio, P. Gargiulo, J.L. Vargas Luna, E. Giordano, O.E. Sigurjonsson. A standalone bioreactor system to deliver compressive load under perfusion flow to hBMSC-seeded 3D chitosan-graphene templates. Sci Rep. 2019. 9(1): 16854.

[214] F. Martin-Saavedra, L. Crespo, C. Escudero-Duch, L. Saldana, E. Gomez-Barrena, N. Vilaboa. Substrate Microarchitecture Shapes the Paracrine Crosstalk of Stem Cells with Endothelial Cells and Osteoblasts. Sci Rep. 2017. 7(1): 15182.

[215] G. Valles, F. Bensiamar, L. Crespo, M. Arruebo, N. Vilaboa, L. Saldana. Topographical cues regulate the crosstalk between MSCs and macrophages. Biomaterials. 2015. 37 124-33.

[216] G. Piret, M.-T. Perez, C.N. Prinz. Substrate porosity induces phenotypic alterations in retinal cells cultured on silicon nanowires. RSC Adv. 2014. 4(53): 27888-27897.

[217] M.H. Kim, Y. Sawada, M. Taya, M. Kino-Oka. Influence of surface topography on the human epithelial cell response to micropatterned substrates with convex and concave architectures. J Biol Eng. 2014. 8 13.

[218] M.N. Andalib, Y. Dzenis, H.J. Donahue, J.Y. Lim. Biomimetic substrate control of cellular mechanotransduction. Biomater Res. 2016. 20 11.

[219] R. Singhvi, A. Kumar, G.P. Lopez, G.N. Stephanopoulos, D.I. Wang, G.M. Whitesides, D.E. Ingber. Engineering cell shape and function. Science. 1994. 264(5159): 696-8.

[220] A. Pitaval, Q. Tseng, M. Bornens, M. Thery. Cell shape and contractility regulate ciliogenesis in cell cycle-arrested cells. J Cell Biol. 2010. 191(2): 303-12.

[221] M.W. Klinker, R.A. Marklein, J.L. Lo Surdo, C.H. Wei, S.R. Bauer. Morphological features of IFN-gamma-stimulated mesenchymal stromal cells predict overall immunosuppressive capacity. Proc Natl Acad Sci U S A. 2017. 114(13): E2598-E2607.

[222] R.A. Marklein, J.L. Lo Surdo, I.H. Bellayr, S.A. Godil, R.K. Puri, S.R. Bauer. High Content Imaging of Early Morphological Signatures Predicts Long Term Mineralization Capacity of Human Mesenchymal Stem Cells upon Osteogenic Induction. Stem Cells. 2016. 34(4): 935-47.

[223] S. Rocha, J. Carvalho, P. Oliveira, M. Voglstaetter, D. Schvartz, A.R. Thomsen, N. Walter, R. Khanduri, J.C. Sanchez, A. Keller, C. Oliveira, I. Nazarenko. 3D Cellular Architecture Affects MicroRNA

and Protein Cargo of Extracellular Vesicles. Adv Sci (Weinh). 2019. 6(4): 1800948.

[224] M. Monguio-Tortajada, S. Roura, C. Galvez-Monton, J.M. Pujal, G. Aran, L. Sanjurjo, M. Franquesa, M.R. Sarrias, A. Bayes-Genis, F.E. Borras. Nanosized UCMSC-derived extracellular vesicles but not conditioned medium exclusively inhibit the inflammatory response of stimulated T cells: implications for nanomedicine. Theranostics. 2017. 7(2): 270-284.

[225] Y. Zhang, M. Chopp, Z.G. Zhang, M. Katakowski, H. Xin, C. Qu, M. Ali, A. Mahmood, Y. Xiong. Systemic administration of cell-free exosomes generated by human bone marrow derived mesenchymal stem cells cultured under 2D and 3D conditions improves functional recovery in rats after traumatic brain injury. Neurochem Int. 2017. 111 69-81.

[226] M. Jafarinia, F. Alsahebfosoul, H. Salehi, N. Eskandari, M. Ganjalikhani-Hakemi. Mesenchymal Stem Cell-Derived Extracellular Vesicles: A Novel Cell-Free Therapy. Immunol Invest. 2020. 49(7): 758-780.

[227] D. Levy, A. Jeyaram, L.J. Born, K.-H. Chang, S.N. Abadchi, A.T. Wei Hsu, T. Solomon, A. Aranda, S. Stewart, X. He, J.W. Harmon, S.M. Jay. The Impact of Storage Condition and Duration on Function of

Native and Cargo-Loaded Mesenchymal Stromal Cell Extracellular Vesicles. BioRxiv. 2022.

[228] X. Zhuang, X. Xiang, W. Grizzle, D. Sun, S. Zhang, R.C. Axtell, S. Ju, J. Mu, L. Zhang, L. Steinman, D. Miller, H.G. Zhang. Treatment of brain inflammatory diseases by delivering exosome encapsulated anti-inflammatory drugs from the nasal region to the brain. Mol Ther. 2011. 19(10): 1769-79.

[229] R.O. Elliott, M. He. Unlocking the Power of Exosomes for Crossing Biological Barriers in Drug Delivery. Pharmaceutics. 2021. 13(1).

[230] B. Crivelli, T. Chlapanidas, S. Perteghella, E. Lucarelli, L. Pascucci, A.T. Brini, I. Ferrero, M. Marazzi, A. Pessina, M.L. Torre, G. Italian Mesenchymal Stem Cell. Mesenchymal stem/stromal cell extracellular vesicles: From active principle to next generation drug delivery system. J Control Release. 2017. 262 104-117.

[231] S. Morelli, A. Piscioneri, S. Salerno, L. De Bartolo. Hollow Fiber and Nanofiber Membranes in Bioartificial Liver and Neuronal Tissue Engineering. Cells Tissues Organs. 2021. 1-30.

[232] J. An, J.E.M. Teoh, R. Suntornnond, C.K. Chua. Design and 3D Printing of Scaffolds and Tissues. Engineering. 2015. 1(2): 261-268.

[233] O.G. de Jong, M.C. Verhaar, Y. Chen, P. Vader, H. Gremmels, G. Posthuma, R.M. Schiffelers, M. Gucek, B.W. van Balkom. Cellular

stress conditions are reflected in the protein and RNA content of endothelial cell-derived exosomes. J Extracell Vesicles. 2012. 1.

[234] M.F. Pittenger, D.E. Discher, B.M. Peault, D.G. Phinney, J.M. Hare, A.I. Caplan. Mesenchymal stem cell perspective: cell biology to clinical progress. NPJ Regen Med. 2019. 4 22.

[235] T.N. Lamichhane, A. Jeyaram, D.B. Patel, B. Parajuli, N.K. Livingston, N. Arumugasaamy, J.S. Schardt, S.M. Jay. Oncogene Knockdown via Active Loading of Small RNAs into Extracellular Vesicles by Sonication. Cell Mol Bioeng. 2016. 9(3): 315-324.

[236] Z. Han, C. Peng, J. Yi, Y. Wang, Q. Liu, Y. Yang, S. Long, L. Qiao, Y. Shen. Matrix-assisted laser desorption ionization mass spectrometry profiling of plasma exosomes evaluates osteosarcoma metastasis. iScience. 2021. 24(8): 102906.

[237] Y. Huang, J.Y. Qian, H. Cheng, X.M. Li. Effects of shear stress on differentiation of stem cells into endothelial cells. World J Stem Cells. 2021. 13(7): 894-913.

[238] K.M. Kim, Y.J. Choi, J.H. Hwang, A.R. Kim, H.J. Cho, E.S. Hwang, J.Y. Park, S.H. Lee, J.H. Hong. Shear stress induced by an interstitial level of slow flow increases the osteogenic differentiation of mesenchymal stem cells through TAZ activation. PLoS One. 2014. 9(3): e92427.

[239] A.C. Shieh, M.A. Swartz. Regulation of tumor invasion by interstitial fluid flow. Phys Biol. 2011. 8(1): 015012.

[240] A. Taherian, X. Li, Y. Liu, T.A. Haas. Differences in integrin expression and signaling within human breast cancer cells. BMC Cancer. 2011. 11 293.

[241] C. Alcaino, K. Knutson, P.A. Gottlieb, G. Farrugia, A. Beyder. Mechanosensitive ion channel Piezo2 is inhibited by D-GsMTx4. Channels (Austin). 2017. 11(3): 245-253.

[242] R. Soffe, S. Baratchi, S.Y. Tang, M. Nasabi, P. McIntyre, A. Mitchell, K. Khoshmanesh. Analysing calcium signalling of cells under high shear flows using discontinuous dielectrophoresis. Sci Rep. 2015. 5 11973.

[243] S. Palchetti, V. Colapicchioni, L. Digiacomo, G. Caracciolo, D. Pozzi, A.L. Capriotti, G. La Barbera, A. Lagana. The protein corona of circulating PEGylated liposomes. Biochim Biophys Acta. 2016. 1858(2): 189-96.

[244] D.T. Jayaram, S.M. Pustulka, R.G. Mannino, W.A. Lam, C.K. Payne. Protein Corona in Response to Flow: Effect on Protein Concentration and Structure. Biophys J. 2018. 115(2): 209-216.

[245] J. Phan, P. Kumar, D. Hao, K. Gao, D. Farmer, A. Wang. Engineering mesenchymal stem cells to improve their exosome efficacy and yield for cell-free therapy. J Extracell Vesicles. 2018. 7(1): 1522236.

[246] M. Maumus, P. Rozier, J. Boulestreau, C. Jorgensen, D. Noel. Mesenchymal Stem Cell-Derived Extracellular Vesicles: Opportunities and Challenges for Clinical Translation. Front Bioeng Biotechnol. 2020. 8 997.

[247] M. Mendt, S. Kamerkar, H. Sugimoto, K.M. McAndrews, C.C. Wu, M. Gagea, S. Yang, E.V.R. Blanko, Q. Peng, X. Ma, J.R. Marszalek, A. Maitra, C. Yee, K. Rezvani, E. Shpall, V.S. LeBleu, R. Kalluri. Generation and testing of clinical-grade exosomes for pancreatic cancer. JCI Insight. 2018. 3(8).

[248] D.E. Rodriguez-Fuentes, L.E. Fernandez-Garza, J.A. Samia-Meza, S.A. Barrera-Barrera, A.I. Caplan, H.A. Barrera-Saldana. Mesenchymal Stem Cells Current Clinical Applications: A Systematic Review. Arch Med Res. 2021. 52(1): 93-101.

[249] J. Lembong, M.J. Lerman, T.J. Kingsbury, C.I. Civin, J.P. Fisher. A Fluidic Culture Platform for Spatially Patterned Cell Growth, Differentiation, and Cocultures. Tissue Eng Part A. 2018. 24(23-24): 1715-1732.

[250] B.A. Gonzalez, M. Perez-Nevarez, A. Mirza, M.G. Perez, Y.M. Lin, C.D. Hsu, A. Caobi, A. Raymond, M.E. Gomez Hernandez, F. Fernandez-Lima, F. George, S. Ramaswamy. Physiologically Relevant Fluid-Induced Oscillatory Shear Stress Stimulation of Mesenchymal Stem Cells Enhances the Engineered Valve Matrix Phenotype. Front Cardiovasc Med. 2020. 7 69.

[251] J. Webber, A. Clayton. How pure are your vesicles? J Extracell Vesicles. 2013. 2.

[252] G. Raposo, W. Stoorvogel. Extracellular vesicles: exosomes, microvesicles, and friends. J Cell Biol. 2013. 200(4): 373-83.

[253] M. Piffoux, A. Nicolas-Boluda, V. Mulens-Arias, S. Richard, G. Rahmi, F. Gazeau, C. Wilhelm, A.K.A. Silva. Extracellular vesicles for personalized medicine: The input of physically triggered production, loading and theranostic properties. Adv Drug Deliv Rev. 2019. 138 247-258.

[254] N.C. Gauthier, M.A. Fardin, P. Roca-Cusachs, M.P. Sheetz. Temporary increase in plasma membrane tension coordinates the activation of exocytosis and contraction during cell spreading. Proc Natl Acad Sci U S A. 2011. 108(35): 14467-72.

[255] A.E. Morrell, G.N. Brown, S.T. Robinson, R.L. Sattler, A.D. Baik, G. Zhen, X. Cao, L.F. Bonewald, W. Jin, L.C. Kam, X.E. Guo.

Mechanically induced Ca(2+) oscillations in osteocytes release extracellular vesicles and enhance bone formation. Bone Res. 2018. 6 6.

[256] J. Cao, B. Wang, T. Tang, L. Lv, Z. Ding, Z. Li, R. Hu, Q. Wei, A. Shen, Y. Fu, B. Liu. Three-dimensional culture of MSCs produces exosomes with improved yield and enhanced therapeutic efficacy for cisplatin-induced acute kidney injury. Stem Cell Res Ther. 2020. 11(1): 206.

[257] C.M. Potter, K.H. Lao, L. Zeng, Q. Xu. Role of biomechanical forces in stem cell vascular lineage differentiation. Arterioscler Thromb Vasc Biol. 2014. 34(10): 2184-90.

[258] S.M. Naqvi, L.M. McNamara. Stem Cell Mechanobiology and the Role of Biomaterials in Governing Mechanotransduction and Matrix Production for Tissue Regeneration. Front Bioeng Biotechnol. 2020. 8 597661.

[259] N. Raman, S.A.M. Imran, K.B. Ahmad Amin Noordin, W. Zaman, F. Nordin. Mechanotransduction in Mesenchymal Stem Cells (MSCs) Differentiation: A Review. Int J Mol Sci. 2022. 23(9).

[260] S. Dupont, L. Morsut, M. Aragona, E. Enzo, S. Giulitti, M. Cordenonsi, F. Zanconato, J. Le Digabel, M. Forcato, S. Bicciato, N.

Elvassore, S. Piccolo. Role of YAP/TAZ in mechanotransduction. Nature. 2011. 474(7350): 179-83.

[261] X. Cai, K.C. Wang, Z. Meng. Mechanoregulation of YAP and TAZ in Cellular Homeostasis and Disease Progression. Front Cell Dev Biol. 2021. 9 673599.

[262] Y. Hou, J. Li, S. Guan, F. Witte. The therapeutic potential of MSC-EVs as a bioactive material for wound healing. Engineered Regeneration. 2021. 2 182-194.

[263] Q.L. Zeng, D.W. Liu. Mesenchymal stem cell-derived exosomes: An emerging therapeutic strategy for normal and chronic wound healing. World J Clin Cases. 2021. 9(22): 6218-6233.

[264] C. Merino-Gonzalez, F.A. Zuniga, C. Escudero, V. Ormazabal, C. Reyes, E. Nova-Lamperti, C. Salomon, C. Aguayo. Mesenchymal Stem Cell-Derived Extracellular Vesicles Promote Angiogenesis: Potencial Clinical Application. Front Physiol. 2016. 7 24.

[265] E.R. Bray, R.S. Kirsner, E.V. Badiavas. Mesenchymal Stem Cell-Derived Extracellular Vesicles as an Advanced Therapy for Chronic Wounds. Cold Spring Harb Perspect Biol. 2022.

[266] C. Almeria, S. Kress, V. Weber, D. Egger, C. Kasper. Heterogeneity of mesenchymal stem cell-derived extracellular vesicles is highly

impacted by the tissue/cell source and culture conditions. Cell Biosci. 2022. 12(1): 51.

[267] G.D. Kusuma, A. Li, D. Zhu, H. McDonald, I.M. Inocencio, D.C. Chambers, K. Sinclair, H. Fang, D.W. Greening, J.E. Frith, R. Lim. Effect of 2D and 3D Culture Microenvironments on Mesenchymal Stem Cell-Derived Extracellular Vesicles Potencies. Front Cell Dev Biol. 2022. 10 819726.

[268] M. Rodrigues, N. Kosaric, C.A. Bonham, G.C. Gurtner. Wound Healing: A Cellular Perspective. Physiol Rev. 2019. 99(1): 665-706.

[269] C.D. Paul, W.C. Hung, D. Wirtz, K. Konstantopoulos. Engineered Models of Confined Cell Migration. Annu Rev Biomed Eng. 2016. 18 159-80.

[270] H. Priks, T. Butelmann, A. Illarionov, T.G. Johnston, C. Fellin, T. Tamm, A. Nelson, R. Kumar, P.J. Lahtvee. Physical Confinement Impacts Cellular Phenotypes within Living Materials. ACS Appl Bio Mater. 2020. 3(7): 4273-4281.

[271] M.T. Doolin, R.A. Moriarty, K.M. Stroka. Mechanosensing of Mechanical Confinement by Mesenchymal-Like Cells. Front Physiol. 2020. 11 365.

[272] M.T. Doolin, K.M. Stroka. Integration of Mesenchymal Stem Cells into a Novel Micropillar Confinement Assay. Tissue Eng Part C Methods. 2019. 25(11): 662-676.

[273] E.M. Balzer, Z. Tong, C.D. Paul, W.C. Hung, K.M. Stroka, A.E. Boggs, S.S. Martin, K. Konstantopoulos. Physical confinement alters tumor cell adhesion and migration phenotypes. FASEB J. 2012. 26(10): 4045-56.

[274] Z. Tong, E.M. Balzer, M.R. Dallas, W.C. Hung, K.J. Stebe, K. Konstantopoulos. Chemotaxis of cell populations through confined spaces at single-cell resolution. PLoS One. 2012. 7(1): e29211.

[275] Y. Alapan, M. Younesi, O. Akkus, U.A. Gurkan. Anisotropically Stiff 3D Micropillar Niche Induces Extraordinary Cell Alignment and Elongation. Adv Healthc Mater. 2016. 5(15): 1884-92.

[276] K. Wolf, S. Alexander, V. Schacht, L.M. Coussens, U.H. von Andrian, J. van Rheenen, E. Deryugina, P. Friedl. Collagen-based cell migration models in vitro and in vivo. Semin Cell Dev Biol. 2009. 20(8): 931-41.

[277] S. Busatto, G. Vilanilam, T. Ticer, W.L. Lin, D.W. Dickson, S. Shapiro, P. Bergese, J. Wolfram. Tangential Flow Filtration for Highly Efficient Concentration of Extracellular Vesicles from Large Volumes of Fluid. Cells. 2018. 7(12).

[278] M.T. Doolin, K.M. Stroka. Physical confinement alters cytoskeletal contributions towards human mesenchymal stem cell migration. Cytoskeleton (Hoboken). 2018. 75(3): 103-117.

[279] B. Pontes, P. Monzo, L. Gole, A.L. Le Roux, A.J. Kosmalska, Z.Y. Tam, W. Luo, S. Kan, V. Viasnoff, P. Roca-Cusachs, L. Tucker-Kellogg, N.C. Gauthier. Membrane tension controls adhesion positioning at the leading edge of cells. J Cell Biol. 2017. 216(9): 2959-2977.

[280] M. Li, J. Zheng, T. Wu, Y. He, J. Guo, J. Xu, C. Gao, S. Qu, Q. Zhang, J. Zhao, W. Cheng. Activation of TRPV4 Induces Exocytosis and Ferroptosis in Human Melanoma Cells. Int J Mol Sci. 2022. 23(8).

[281] Y. Sun, B. Wan, R. Wang, B. Zhang, P. Luo, D. Wang, J.J. Nie, D. Chen, X. Wu. Mechanical Stimulation on Mesenchymal Stem Cells and Surrounding Microenvironments in Bone Regeneration: Regulations and Applications. Front Cell Dev Biol. 2022. 10 808303.

[282] M. Bao, J. Xie, A. Piruska, W.T.S. Huck. 3D microniches reveal the importance of cell size and shape. Nat Commun. 2017. 8(1): 1962.

[283] S. Bian, L. Zhang, L. Duan, X. Wang, Y. Min, H. Yu. Extracellular vesicles derived from human bone marrow mesenchymal stem cells promote angiogenesis in a rat myocardial infarction model. J Mol Med (Berl). 2014. 92(4): 387-97.

[284] N. Wang, C. Chen, D. Yang, Q. Liao, H. Luo, X. Wang, F. Zhou, X. Yang, J. Yang, C. Zeng, W.E. Wang. Mesenchymal stem cells-derived extracellular vesicles, via miR-210, improve infarcted cardiac function by promotion of angiogenesis. Biochim Biophys Acta Mol Basis Dis. 2017. 1863(8): 2085-2092.

[285] Y.C. Yeh, E.A. Corbin, S.R. Caliari, L. Ouyang, S.L. Vega, R. Truitt, L. Han, K.B. Margulies, J.A. Burdick. Mechanically dynamic PDMS substrates to investigate changing cell environments. Biomaterials. 2017. 145 23-32.

[286] A.E. Stanton, X. Tong, F. Yang. Varying solvent type modulates collagen coating and stem cell mechanotransduction on hydrogel substrates. APL Bioeng. 2019. 3(3): 036108.

[287] Y. Li, J. Wang, W. Zhong. Regulation and mechanism of YAP/TAZ in the mechanical microenvironment of stem cells (Review). Mol Med Rep. 2021. 24(1).

[288] R.J. Mills, J.E. Frith, J.E. Hudson, J.J. Cooper-White. Effect of geometric challenges on cell migration. Tissue Eng Part C Methods. 2011. 17(10): 999-1010.

[289] J. Ge, L. Guo, S. Wang, Y. Zhang, T. Cai, R.C. Zhao, Y. Wu. The size of mesenchymal stem cells is a significant cause of vascular obstructions and stroke. Stem Cell Rev Rep. 2014. 10(2): 295-303.

[290] P. Bandaru, G. Cefaloni, F. Vajhadin, K. Lee, H.J. Kim, H.J. Cho, M.C. Hartel, S. Zhang, W. Sun, M.J. Goudie, S. Ahadian, M.R. Dokmeci, J. Lee, A. Khademhosseini. Mechanical Cues Regulating Proangiogenic Potential of Human Mesenchymal Stem Cells through YAP-Mediated Mechanosensing. Small. 2020. 16(25): e2001837.

[291] S. Liu, C. Jiang, J. Hu, H. Chen, B. Han, S. Xia. Low-Intensity Pulsed Ultrasound Enhanced Adipose-Derived Stem Cell-Mediated Angiogenesis in the Treatment of Diabetic Erectile Dysfunction through the Piezo-ERK-VEGF Axis. Stem Cells Int. 2022. 2022 6202842.

[292] I. Arnaoutova, J. George, H.K. Kleinman, G. Benton. The endothelial cell tube formation assay on basement membrane turns 20: state of the science and the art. Angiogenesis. 2009. 12(3): 267-74.

[293] S. La Porta, L. Roth, M. Singhal, C. Mogler, C. Spegg, B. Schieb, X. Qu, R.H. Adams, H.S. Baldwin, S. Savant, H.G. Augustin. Endothelial Tie1-mediated angiogenesis and vascular abnormalization promote tumor progression and metastasis. J Clin Invest. 2018. 128(2): 834-845.

[294] M. Bahramsoltani, I. Slosarek, W. De Spiegelaere, J. Plendl. Angiogenesis and collagen type IV expression in different endothelial cell culture systems. Anat Histol Embryol. 2014. 43(2): 103-15.

[295] K.S. Moulton, B.R. Olsen, S. Sonn, N. Fukai, D. Zurakowski, X. Zeng. Loss of collagen XVIII enhances neovascularization and vascular permeability in atherosclerosis. Circulation. 2004. 110(10): 1330-6.

[296] R. Kivela, M. Silvennoinen, M. Lehti, S. Jalava, V. Vihko, H. Kainulainen. Exercise-induced expression of angiogenic growth factors in skeletal muscle and in capillaries of healthy and diabetic mice. Cardiovasc Diabetol. 2008. 7 13.

[297] R. Jaksik, M. Iwanaszko, J. Rzeszowska-Wolny, M. Kimmel. Microarray experiments and factors which affect their reliability. Biol Direct. 2015. 10 46.

[298] Y. Wang, U. Armato, J. Wu. Targeting Tunable Physical Properties of Materials for Chronic Wound Care. Front Bioeng Biotechnol. 2020. 8 584.

[299] C.F. Guimarães, L. Gasperini, A.P. Marques, R.L. Reis. The stiffness of living tissues and its implications for tissue engineering. Nature Reviews Materials. 2020. 5(5): 351-370.

[300] Y. Ji, J. Li, Y. Wei, W. Gao, X. Fu, Y. Wang. Substrate stiffness affects the immunosuppressive and trophic function of hMSCs via modulating cytoskeletal polymerization and tension. Biomater Sci. 2019. 7(12): 5292-5300.

[301] M. Nguyen-Truong, S. Kim, C. Doherty, M. Frederes, K. LeBar, S. Ghosh, P. Hematti, R. Chinnadurai, W.R. Wagner, Z. Wang. Pro-angiogenic Potential of Mesenchymal Stromal Cells Regulated by Matrix Stiffness and Anisotropy Mimicking Right Ventricles. Biomacromolecules. 2022. 23(6): 2353-2361.

[302] M. Nasser, Y. Wu, Y. Danaoui, G. Ghosh. Engineering microenvironments towards harnessing pro-angiogenic potential of mesenchymal stem cells. Mater Sci Eng C Mater Biol Appl. 2019. 102 75-84.

[303] B. Yi, Q. Xu, W. Liu. An overview of substrate stiffness guided cellular response and its applications in tissue regeneration. Bioact Mater. 2022. 15 82-102.

[304] R. Olivares-Navarrete, E.M. Lee, K. Smith, S.L. Hyzy, M. Doroudi, J.K. Williams, K. Gall, B.D. Boyan, Z. Schwartz. Substrate Stiffness Controls Osteoblastic and Chondrocytic Differentiation of Mesenchymal Stem Cells without Exogenous Stimuli. PLoS One. 2017. 12(1): e0170312.

[305] M. Sun, G. Chi, P. Li, S. Lv, J. Xu, Z. Xu, Y. Xia, Y. Tan, J. Xu, L. Li, Y. Li. Effects of Matrix Stiffness on the Morphology, Adhesion, Proliferation and Osteogenic Differentiation of Mesenchymal Stem Cells. Int J Med Sci. 2018. 15(3): 257-268.

[306] R.N. Palchesko, L. Zhang, Y. Sun, A.W. Feinberg. Development of polydimethylsiloxane substrates with tunable elastic modulus to study cell mechanobiology in muscle and nerve. PLoS One. 2012. 7(12): e51499.

[307] J.Y. Park, S.J. Yoo, E.-J. Lee, D.H. Lee, J.Y. Kim, S.-H. Lee. Increased poly(dimethylsiloxane) stiffness improves viability and morphology of mouse fibroblast cells. BioChip Journal. 2010. 4(3): 230-236.

[308] S. Masterton, M. Ahearne. Influence of polydimethylsiloxane substrate stiffness on corneal epithelial cells. R Soc Open Sci. 2019. 6(12): 191796.

[309] Z. Wang, A.A. Volinsky, N.D. Gallant. Crosslinking effect on polydimethylsiloxane elastic modulus measured by custom-built compression instrument. Journal of Applied Polymer Science. 2014. 131(22): n/a-n/a.

[310] J. Liu, H. Zheng, X. Dai, P.S.P. Poh, H.G. Machens, A.F. Schilling. Transparent PDMS Bioreactors for the Fabrication and Analysis of Multi-Layer Pre-vascularized Hydrogels Under Continuous Perfusion. Front Bioeng Biotechnol. 2020. 8 568934.

[311] A.C. Timm, P.G. Shankles, C.M. Foster, M.J. Doktycz, S.T. Retterer. Characterization of extended channel bioreactors for continuous-flow

protein production. Journal of Vacuum Science & Technology B, Nanotechnology and Microelectronics: Materials, Processing, Measurement, and Phenomena. 2015. 33(6).

[312] K. Raj M, S. Chakraborty. PDMS microfluidics: A mini review. Journal of Applied Polymer Science. 2020. 137(27).

[313] A.J. Steward, D.J. Kelly. Mechanical regulation of mesenchymal stem cell differentiation. J Anat. 2015. 227(6): 717-31.

[314] S.W. Wong, S. Lenzini, R. Giovanni, K. Knowles, J.W. Shin. Matrix mechanical cues direct mesenchymal stromal cell functions in immunity. Acta Biomater. 2021. 133 126-138.

[315] M.-H. Wu. Simple poly(dimethylsiloxane) surface modification to control cell adhesion. Surface and Interface Analysis. 2009. 41(1): 11-16.

[316] X.Q. Brown, K. Ookawa, J.Y. Wong. Evaluation of polydimethylsiloxane scaffolds with physiologically-relevant elastic moduli: interplay of substrate mechanics and surface chemistry effects on vascular smooth muscle cell response. Biomaterials. 2005. 26(16): 3123-9.

[317] J.J. Cunningham, J. Nikolovski, J.J. Linderman, D.J. Mooney. Quantification of Fibronectin Adsorption to Silicon-Rubber Cell Culture Substrates. Biotechniques. 2002. 32(4): 876-880.

[318] K. Daliri, K. Pfannkuche, B. Garipcan. Effects of physicochemical properties of polyacrylamide (PAA) and (polydimethylsiloxane) PDMS on cardiac cell behavior. Soft Matter. 2021. 17(5): 1156-1172.

[319] D. Sharma, W. Jia, F. Long, S. Pati, Q. Chen, Y. Qyang, B. Lee, C.K. Choi, F. Zhao. Polydopamine and collagen coated micro-grated polydimethylsiloxane for human mesenchymal stem cell culture. Bioact Mater. 2019. 4 142-150.

[320] T.J. Kim, J. Seong, M. Ouyang, J. Sun, S. Lu, J.P. Hong, N. Wang, Y. Wang. Substrate rigidity regulates Ca2+ oscillation via RhoA pathway in stem cells. J Cell Physiol. 2009. 218(2): 285-93.

[321] J. Seo, J. Kim. Regulation of Hippo signaling by actin remodeling. BMB Rep. 2018. 51(3): 151-156.

[322] J.K. Virdi, P. Pethe. Biomaterials Regulate Mechanosensors YAP/TAZ in Stem Cell Growth and Differentiation. Tissue Eng Regen Med. 2021. 18(2): 199-215.

[323] S. Patwardhan, P. Mahadik, O. Shetty, S. Sen. ECM stiffness-tuned exosomes drive breast cancer motility through thrombospondin-1. Biomaterials. 2021. 279 121185.

[324] M. Tkach, C. Thery. Communication by Extracellular Vesicles: Where We Are and Where We Need to Go. Cell. 2016. 164(6): 1226-1232.

[325] X. Zhang, Y. Wang, X. Wang, B. Zou, J. Mei, X. Peng, Z. Wu. Extracellular vesicles-encapsulated microRNA-10a-5p shed from cancer-associated fibroblast facilitates cervical squamous cell carcinoma cell angiogenesis and tumorigenicity via Hedgehog signaling pathway. Cancer Gene Ther. 2021. 28(5): 529-542.

[326] J. Zhu, S. Du, J. Zhang, G. Huang, L. Dong, E. Ren, D. Liu. microRNA-10a-5p from gastric cancer cell-derived exosomes enhances viability and migration of human umbilical vein endothelial cells by targeting zinc finger MYND-type containing 11. Bioengineered. 2022. 13(1): 496-507.

[327] G.Y. Xiao, C.C. Cheng, Y.S. Chiang, W.T. Cheng, I.H. Liu, S.C. Wu. Exosomal miR-10a derived from amniotic fluid stem cells preserves ovarian follicles after chemotherapy. Sci Rep. 2016. 6 23120.

[328] J. Li, S. Yue, J. Fang, J. Zeng, S. Chen, J. Tian, S. Nie, X. Liu, H. Ding. MicroRNA-10a/b inhibit TGF-beta/Smad-induced renal fibrosis by targeting TGF-beta receptor 1 in diabetic kidney disease. Mol Ther Nucleic Acids. 2022. 28 488-499.

[329] M. Li, L. Liu, W. Zang, Y. Wang, Y. Du, X. Chen, P. Li, J. Li, G. Zhao. miR365 overexpression promotes cell proliferation and invasion by targeting ADAMTS-1 in breast cancer. Int J Oncol. 2015. 47(1): 296-302.

[330] D. Zhang, E. Liu, J. Kang, X. Yang, H. Liu. miR-3613-3p affects cell proliferation and cell cycle in hepatocellular carcinoma. Oncotarget. 2017. 8(54): 93014-93028.

[331] H. Lewis, R. Lance, D. Troyer, H. Beydoun, M. Hadley, J. Orians, T. Benzine, K. Madric, O.J. Semmes, R. Drake, A. Esquela-Kerscher. miR-888 is an expressed prostatic secretions-derived microRNA that promotes prostate cell growth and migration. Cell Cycle. 2014. 13(2): 227-39.

[332] S. Huang, L. Chen. MiR-888 regulates side population properties and cancer metastasis in breast cancer cells. Biochem Biophys Res Commun. 2014. 450(4): 1234-40.

[333] Y. Shi, M. Qiu, Y. Wu, L. Hai. MiR-548-3p functions as an anti-oncogenic regulator in breast cancer. Biomed Pharmacother. 2015. 75 111-6.

[334] Y. Zong, P. Wu, C. Nai, Y. Luo, F. Hu, W. Gao, N. Zhai, T. Xu, D. Li. Effect of MicroRNA-30e on the Behavior of Vascular Smooth Muscle Cells via Targeting Ubiquitin-Conjugating Enzyme E2I. Circ J. 2017. 81(4): 567-576.

[335] X. Lin, Z. Yang, P. Zhang, G. Shao. miR-154 suppresses non-small cell lung cancer growth in vitro and in vivo. Oncol Rep. 2015. 33(6): 3053-60.

[336] S.W. Ferguson, J. Wang, C.J. Lee, M. Liu, S. Neelamegham, J.M. Canty, J. Nguyen. The microRNA regulatory landscape of MSC-derived exosomes: a systems view. Sci Rep. 2018. 8(1): 1419.

[337] C. Zhang, H. Wang, X. Liu, Y. Hu, L. Ding, X. Zhang, Q. Sun, Y. Li. Oncogenic microRNA-411 promotes lung carcinogenesis by directly targeting suppressor genes SPRY4 and TXNIP. Oncogene. 2019. 38(11): 1892-1904.

[338] X. Gong, A. Hu, X. Li, J. He, Z. Wu, X. Zuo, P. Ning. Coordinated expression of vascular endothelial growth factor A and urokinase-type plasminogen activator contributes to classical swine fever virus Shimen infection in macrophages. BMC Vet Res. 2019. 15(1): 82.

[339] C. Wang, C. Li, R. Hao, M.S. Ali Sheikh. miR-559 Inhibits Proliferation, Autophagy, and Angiogenesis of Hepatocellular Carcinoma Cells by Targeting PARD3. Mediators of Inflammation. 2022. 2022 1-9.

[340] J. Bischoff, C. Brasel, B. Kraling, K. Vranovska. E-Selectin is Upregulated in Proliferating Endothelial Cells In Vitro. Microcirculation. 1997. 4(2): 279-287.

[341] J. Luo, G. Paranya, J. Bischoff. Noninflammatory Expression of E-Selectin is Regulated By Cell Growth. Blood. 1999. 93(11): 3785-3791.

[342] J.F. Leeuwenberg, E.F. Smeets, J.J. Neefjes, M.A. Shaffer, T. Cinek, J. T.M., T.J. Ahern, W.A. Buurman. E-Selectin and Intercellular Adhesion Molecule-1 are Released by Activated Human Endothelial Cells In Vitro. Immunology. 1992. 77(4): 543-549.

[343] I.Y. Oh, C.H. Yoon, J. Hur, J.H. Kim, T.Y. Kim, C.S. Lee, K.W. Park, I.H. Chae, B.H. Oh, Y.B. Park, H.S. Kim. Involvement of E-selectin in recruitment of endothelial progenitor cells and angiogenesis in ischemic muscle. Blood. 2007. 110(12): 3891-9.

[344] P. Kumar, M.A. Amin, L.A. Harlow, P.J. Polverini, A.E. Koch. Src and phosphatidylinositol 3-kinase mediate soluble E-selectin-induced angiogenesis. Blood. 2003. 101(10): 3960-8.

[345] A.E. Koch, M.M. Halloran, C.J. Haskell, M.R. Shah, P.J. Polverini. Angiogenesis Mediated By Soluble Forms of E-Selectin and Vascular Cell Adhesion Molecule-1. Nature. 1995. 376(6540): 517-519.

[346] Z. Zhou, C. Lu, S. Meng, L. Dun, N. Yin, H. An, H. Xu, G. Liu, Y. Cai. Silencing of PTGS2 exerts promoting effects on angiogenesis endothelial progenitor cells in mice with ischemic stroke via repression of the NF-kappaB signaling pathway. J Cell Physiol. 2019. 234(12): 23448-23460.

[347] N. Mu, J. Gu, T. Huang, C. Zhang, Z. Shu, M. Li, Q. Hao, W. Li, W. Zhang, J. Zhao, Y. Zhang, L. Huang, S. Wang, X. Jin, X. Xue, W.

Zhang, Y. Zhang. A novel NF-kappaB/YY1/microRNA-10a regulatory circuit in fibroblast-like synoviocytes regulates inflammation in rheumatoid arthritis. Sci Rep. 2016. 6 20059.

[348] S.P. Tabruyn, A.W. Griffioen. A new role for NF-kappaB in angiogenesis inhibition. Cell Death Differ. 2007. 14(8): 1393-7.

[349] I. Matic, M. Antunovic, S. Brkic, P. Josipovic, K.C. Mihalic, I. Karlak, A. Ivkovic, I. Marijanovic. Expression of OCT-4 and SOX-2 in Bone Marrow-Derived Human Mesenchymal Stem Cells during Osteogenic Differentiation. Open Access Maced J Med Sci. 2016. 4(1): 9-16.

[350] J.H. Kim, H.S. Hwang, S.W. Hahm, D.Y. Khang. Hydrophobically recovered and contact printed siloxane oligomers for general-purpose surface patterning. Langmuir. 2010. 26(15): 13015-9.

[351] J.D. Glover, C.E. McLaughlin, M.K. McFarland, J.T. PHam. Extracting Uncrosslinked Material From Low Modulus Sylgard 184 and the Effect on Mechanical Properties. Journal of Polymer Science. 2020. 58(2): 343-351.

[352] V. Vogel, M. Sheetz. Local force and geometry sensing regulate cell functions. Nat Rev Mol Cell Biol. 2006. 7(4): 265-75.

[353] A.E. Stanton, X. Tong, S. Lee, F. Yang. Biochemical Ligand Density Regulates Yes-Associated Protein Translocation in Stem Cells through

Cytoskeletal Tension and Integrins. ACS Appl Mater Interfaces. 2019. 11(9): 8849-8857.

[354] B. Trappmann, J.E. Gautrot, J.T. Connelly, D.G. Strange, Y. Li, M.L. Oyen, M.A. Cohen Stuart, H. Boehm, B. Li, V. Vogel, J.P. Spatz, F.M. Watt, W.T. Huck. Extracellular-matrix tethering regulates stem-cell fate. Nat Mater. 2012. 11(7): 642-9.

[355] R. Seghir, S. Arscott. Extended PDMS Stiffness Range for Flexible Systems. Sensors and Actuators A: Physical. 2015. 230 33-39.

[356] R. De Volder, H. Kong, Biomaterials for Studies in Cellular Mechanotransduction, Mechanobiology of Cell-Cell and Cell-Matrix Interactions2011, pp. 267-277.

[357] J. Zhang, M. Chen, J. Liao, C. Chang, Y. Liu, A.A. Padhiar, Y. Zhou, G. Zhou. Induced Pluripotent Stem Cell-Derived Mesenchymal Stem Cells Hold Lower Heterogeneity and Great Promise in Biological Research and Clinical Applications. Front Cell Dev Biol. 2021. 9 716907.

[358] J.H. Lee, J.Y. Yoon, J.H. Lee, H.H. Lee, J.C. Knowles, H.W. Kim. Emerging biogenesis technologies of extracellular vesicles for tissue regenerative therapeutics. J Tissue Eng. 2021. 12 20417314211019015.

[359] J. Taylor, I. Azimi, G. Monteith, M. Bebawy. Ca(2+) mediates extracellular vesicle biogenesis through alternate pathways in malignancy. J Extracell Vesicles. 2020. 9(1): 1734326.

[360] Y. Wei, W. Li. Calcium, an Emerging Intracellular Messenger for the Hippo Pathway Regulation. Front Cell Dev Biol. 2021. 9 694828.

[361] J.M. Franklin, R.P. Ghosh, Q. Shi, M.P. Reddick, J.T. Liphardt. Concerted localization-resets precede YAP-dependent transcription. Nat Commun. 2020. 11(1): 4581.

[362] S.R. Caliari, S.L. Vega, M. Kwon, E.M. Soulas, J.A. Burdick. Dimensionality and spreading influence MSC YAP/TAZ signaling in hydrogel environments. Biomaterials. 2016. 103 314-323.

[363] D.A. Gaspar, V. Gomide, F.J. Monteiro. The role of perfusion bioreactors in bone tissue engineering. Biomatter. 2012. 2(4): 167-75.

[364] F. Zhao, T.J. Vaughan, L.M. McNamara. Quantification of fluid shear stress in bone tissue engineering scaffolds with spherical and cubical pore architectures. Biomech Model Mechanobiol. 2016. 15(3): 561-77.

[365] K.A. Kilian, B. Bugarija, B.T. Lahn, M. Mrksich. Geometric cues for directing the differentiation of mesenchymal stem cells. Proc Natl Acad Sci U S A. 2010. 107(11): 4872-7.

[366] G. van Niel, G. D'Angelo, G. Raposo, Shedding light on the cell biology of extracellular vehicles, 2017.

[367] E. Rohde, K. Pachler, M. Gimona. Manufacturing and characterization of extracellular vesicles from umbilical cord-derived mesenchymal stromal cells for clinical testing. Cytotherapy. 2019. 21(6): 581-592.

[368] M. de Almeida Fuzeta, N. Bernardes, F.D. Oliveira, A.C. Costa, A. Fernandes-Platzgummer, J.P. Farinha, C.A.V. Rodrigues, S. Jung, R.J. Tseng, W. Milligan, B. Lee, M. Castanho, D. Gaspar, J.M.S. Cabral, C.L. da Silva. Scalable Production of Human Mesenchymal Stromal Cell-Derived Extracellular Vesicles Under Serum-/Xeno-Free Conditions in a Microcarrier-Based Bioreactor Culture System. Front Cell Dev Biol. 2020. 8 553444.

[369] R. Jeske, C. Liu, L. Duke, M.L. Canonicco Castro, L. Muok, P. Arthur, M. Singh, S. Jung, L. Sun, Y. Li. Upscaling human mesenchymal stromal cell production in a novel vertical-wheel bioreactor enhances extracellular vesicle secretion and cargo profile. Bioactive Materials. 2022.

[370] J. Phelps, C. Leonard, S. Shah, R. Krawetz, D.A. Hart, N.A. Duncan, A. Sen. Production of Mesenchymal Progenitor Cell-Derived Extracellular Vesicles in Suspension Bioreactors for Use in Articular Cartilage Repair. Stem Cells Transl Med. 2022. 11(1): 73-87.

[371] J. Wu, D. Wu, G. Wu, H.P. Bei, Z. Li, H. Xu, Y. Wang, D. Wu, H. Liu, S. Shi, C. Zhao, Y. Xu, Y. He, J. Li, C. Wang, X. Zhao, S. Wang. Scale-out production of extracellular vesicles derived from natural killer cells via mechanical stimulation in a seesaw-motion bioreactor for cancer therapy. Biofabrication. 2022. 14(4).

[372] A.C. Andrade, M. Wolf, H.M. Binder, F.G. Gomes, F. Manstein, P. Ebner-Peking, R. Poupardin, R. Zweigerdt, K. Schallmoser, D. Strunk. Hypoxic Conditions Promote the Angiogenic Potential of Human Induced Pluripotent Stem Cell-Derived Extracellular Vesicles. Int J Mol Sci. 2021. 22(8).

[373] M. Popović, A. de Marco. Canonical and selective approaches in exosome purification and their implications for diagnostic accuracy. Translational Cancer Research. 2018. 7(S2): S209-S225.

[374] D. Furman, J. Campisi, E. Verdin, P. Carrera-Bastos, S. Targ, C. Franceschi, L. Ferrucci, D.W. Gilroy, A. Fasano, G.W. Miller, A.H. Miller, A. Mantovani, C.M. Weyand, N. Barzilai, J.J. Goronzy, T.A. Rando, R.B. Effros, A. Lucia, N. Kleinstreuer, G.M. Slavich. Chronic inflammation in the etiology of disease across the life span. Nat Med. 2019. 25(12): 1822-1832.

[375] R. Zhao, H. Liang, E. Clarke, C. Jackson, M. Xue. Inflammation in Chronic Wounds. Int J Mol Sci. 2016. 17(12).

[376] N. Pacienza, R.H. Lee, E.H. Bae, D.K. Kim, Q. Liu, D.J. Prockop, G. Yannarelli. In Vitro Macrophage Assay Predicts the In Vivo Anti-inflammatory Potential of Exosomes from Human Mesenchymal Stromal Cells. Mol Ther Methods Clin Dev. 2019. 13 67-76.

[377] Y. Kuwahara, K. Yoshizaki, H. Nishida, H. Kamishina, S. Maeda, K. Takano, N. Fujita, R. Nishimura, J.I. Jo, Y. Tabata, H. Akiyoshi. Extracellular Vesicles Derived From Canine Mesenchymal Stromal Cells in Serum Free Culture Medium Have Anti-inflammatory Effect on Microglial Cells. Front Vet Sci. 2021. 8 633426.

[378] R. Malvicini, D. Santa-Cruz, G. De Lazzari, A.M. Tolomeo, C. Sanmartin, M. Muraca, G. Yannarelli, N. Pacienza. Macrophage bioassay standardization to assess the anti-inflammatory activity of mesenchymal stromal cell-derived small extracellular vesicles. Cytotherapy. 2022.

[379] Z. Wang, K. Maruyama, Y. Sakisaka, S. Suzuki, H. Tada, M. Suto, M. Saito, S. Yamada, E. Nemoto. Cyclic Stretch Force Induces Periodontal Ligament Cells to Secrete Exosomes That Suppress IL-1beta Production Through the Inhibition of the NF-kappaB Signaling Pathway in Macrophages. Front Immunol. 2019. 10 1310.

[380] J. Kim, Y. Song, C.H. Park, C. Choi. Platform technologies and human cell lines for the production of therapeutic exosomes. Extracellular Vesicles and Circulating Nucleic Acids. 2021.

[381] A.E. Pottash, D. Levy, A. Jeyaram, L. Kuo, S.M. Kronstadt, W. Chao, S.M. Jay. Combinatorial microRNA Loading into Extracellular Vesicles for Anti-Inflammatory Therapy. BioRxiv. 2022.

[382] J.M. Gudbergsson, K.B. Johnsen, M.N. Skov, M. Duroux. Systematic review of factors influencing extracellular vesicle yield from cell cultures. Cytotechnology. 2016. 68(4): 579-92.

[383] E. Tan, C.S.H. Chin, Z.F.S. Lim, S.K. Ng. HEK293 Cell Line as a Platform to Produce Recombinant Proteins and Viral Vectors. Front Bioeng Biotechnol. 2021. 9 796991.

[384] A.F. Saleh, E. Lázaro-Ibáñez, M.A.M. Forsgard, O. Shatnyeva, X. Osteikoetxea, F. Karlsson, N. Heath, M. Ingelsten, J. Rose, J. Harris, M. Mairesse, S.M. Bates, M. Clausen, D. Etal, E. Leonard, M.D. Fellows, N. Dekker, N. Edmunds. Extracellular vesicles induce minimal hepatotoxicity and immunogenicity. Nanoscale. 2019. 11(14): 6990-7001.

[385] Y. Zhang, Z. Hao, P. Wang, Y. Xia, J. Wu, D. Xia, S. Fang, S. Xu. Exosomes from human umbilical cord mesenchymal stem cells enhance fracture healing through HIF-1alpha-mediated promotion of angiogenesis in a rat model of stabilized fracture. Cell Prolif. 2019. 52(2): e12570.

[386] S. Ahmadvand Koohsari, A. Absalan, D. Azadi. Human umbilical cord mesenchymal stem cell-derived extracellular vesicles attenuate experimental autoimmune encephalomyelitis via regulating pro and anti-inflammatory cytokines. Sci Rep. 2021. 11(1): 11658.

[387] F.F. Cruz, Z.D. Borg, M. Goodwin, D. Sokocevic, D.E. Wagner, A. Coffey, M. Antunes, K.L. Robinson, S.A. Mitsialis, S. Kourembanas, K. Thane, A.M. Hoffman, D.H. McKenna, P.R. Rocco, D.J. Weiss. Systemic Administration of Human Bone Marrow-Derived Mesenchymal Stromal Cell Extracellular Vesicles Ameliorates Aspergillus Hyphal Extract-Induced Allergic Airway Inflammation in Immunocompetent Mice. Stem Cells Transl Med. 2015. 4(11): 1302-16.

[388] D.B. Patel, M. Santoro, L.J. Born, J.P. Fisher, S.M. Jay. Towards rationally designed biomanufacturing of therapeutic extracellular vesicles: impact of the bioproduction microenvironment. Biotechnol Adv. 2018. 36(8): 2051-2059.

[389] J.M. Gudbergsson, K. Jonsson, J.B. Simonsen, K.B. Johnsen. Systematic review of targeted extracellular vesicles for drug delivery - Considerations on methodological and biological heterogeneity. J Control Release. 2019. 306 108-120.

[390] C.N. Davis, H. Phillips, J.J. Tomes, M.T. Swain, T.J. Wilkinson, P.M. Brophy, R.M. Morphew. The importance of extracellular vesicle

purification for downstream analysis: A comparison of differential centrifugation and size exclusion chromatography for helminth pathogens. PLoS Negl Trop Dis. 2019. 13(2): e0007191.

[391] G.K. Patel, M.A. Khan, H. Zubair, S.K. Srivastava, M. Khushman, S. Singh, A.P. Singh. Comparative analysis of exosome isolation methods using culture supernatant for optimum yield, purity and downstream applications. Sci Rep. 2019. 9(1): 5335.

[392] J. Van Deun, P. Mestdagh, R. Sormunen, V. Cocquyt, K. Vermaelen, J. Vandesompele, M. Bracke, O. De Wever, A. Hendrix. The impact of disparate isolation methods for extracellular vesicles on downstream RNA profiling. J Extracell Vesicles. 2014. 3.

[393] C.Y. Ng, L.T. Kee, M.E. Al-Masawa, Q.H. Lee, T. Subramaniam, D. Kok, M.H. Ng, J.X. Law. Scalable Production of Extracellular Vesicles and Its Therapeutic Values: A Review. Int J Mol Sci. 2022. 23(14).

[394] D. Freitas, M. Balmana, J. Pocas, D. Campos, H. Osorio, A. Konstantinidi, S.Y. Vakhrushev, A. Magalhaes, C.A. Reis. Different isolation approaches lead to diverse glycosylated extracellular vesicle populations. J Extracell Vesicles. 2019. 8(1): 1621131.

[395] M. Tkach, J. Kowal, C. Thery. Why the need and how to approach the functional diversity of extracellular vesicles. Philos Trans R Soc Lond B Biol Sci. 2018. 373(1737).

[396] J. Woo, S. Sharma, J. Gimzewski. The Role of Isolation Methods on a Nanoscale Surface Structure and its Effect on the Size of Exosomes. J Circ Biomark. 2016. 5 11.

[397] A. Piloni, C.K. Wong, F. Chen, M. Lord, A. Walther, M.H. Stenzel. Surface roughness influences the protein corona formation of glycosylated nanoparticles and alter their cellular uptake. Nanoscale. 2019. 11(48): 23259-23267.

[398] S.M. Langevin, D. Kuhnell, M.A. Orr-Asman, J. Biesiada, X. Zhang, M. Medvedovic, H.E. Thomas. Balancing yield, purity and practicality: a modified differential ultracentrifugation protocol for efficient isolation of small extracellular vesicles from human serum. RNA Biol. 2019. 16(1): 5-12.

[399] J.B. Simonsen. What Are We Looking At? Extracellular Vesicles, Lipoproteins, or Both? Circ Res. 2017. 121(8): 920-922.

[400] M. Auber, D. Frohlich, O. Drechsel, E. Karaulanov, E.M. Kramer-Albers. Serum-free media supplements carry miRNAs that co-purify with extracellular vesicles. J Extracell Vesicles. 2019. 8(1): 1656042.

[401] N. Yang, D.D. Sin, D.R. Dorscheid. Various Factors Affect Lipopolysaccharide Sensitization in Cell Cultures. BioTechniques. 2020. 69 127-132.

[402] B.M. Lehrich, Y. Liang, M.S. Fiandaca. Foetal bovine serum influence on in vitro extracellular vesicle analyses. J Extracell Vesicles. 2021. 10(3): e12061.

[403] L.A. Beninson, M. Fleshner. Exosomes in fetal bovine serum dampen primary macrophage IL-1beta response to lipopolysaccharide (LPS) challenge. Immunol Lett. 2015. 163(2): 187-92.

[404] H. Choi, Y. Kim, A. Mirzaaghasi, J. Heo, Y.N. Kim, J.H. Shin, S. Kim, N.H. Kim, E.S. Cho, J. In Yook, T.H. Yoo, E. Song, P. Kim, E.C. Shin, K. Chung, K. Choi, C. Choi. Exosome-based Delivery of Super-Repressor IκBα Relieves Sepsis-Associated Organ Damage and Mortality Science Advances. 2020. 6(15).